Reactive and resilient: the contrasting behaviour of monazite and titanite during deformation (The Forno-Rosarolo shear zone; Ivrea-Verbano Zone)

Journal:	*Geological Magazine*
Manuscript ID	GEO-2024-3479.R1
Manuscript Type:	Original Article
Date Submitted by the Author:	07-Mar-2025
Complete List of Authors:	Langone, Antonio; University of Pavia, Department of Earth and Environmental Sciences Simonetti, Matteo; Istituto Superiore per la Protezione e la Ricerca Ambientale Dipartimento per il Servizio Geologico d'Italia; Istituto Superiore per la Protezione e la Ricerca Ambientale Dipartimento per il Servizio Geologico d'Italia Corvò, Stefania; University of Pavia, Department of Earth and Environmental Sciences Bonazzi, Mattia; University of Pavia, Department of Earth and Environmental Sciences Maino, Matteo; University of Pavia, Department of Earth and Environmental Sciences Piazolo, Sandra; University of Leeds, School of Earth and Environment Orlando, Andrea; National Research Council, Institute of Geosciences and Earth Resources Braschi, Eleonora; National Research Council, Institute of Geosciences and Earth Resources
Keywords:	Mylonites, monazite, titanite, petrochronology, geochemistry, microstructure, U–(Th)–Pb
Abstract:	Dating the shear zone activity remains challenging and depends on geochronometer reactivity. We investigate the Forno-Rosarolo Shear Zone (Ivrea-Verbano Zone, Italy), developed in the intermediate-low continental crust under amphibolite-facies conditions. Sheared paragneisses and calc-silicates were dated using in-situ U–(Th–)Pb monazite and titanite geochronology. Three monazite generations (MNZI-III) were identified based on microstructural position, internal features, chemical zoning (Th, Y), and isotopic data. Deformation was mainly recorded by MNZII, with high-Y domains yielding Triassic dates (average ages of: 238±8 and 222±8 Ma). Rare, highly fractured or porous MNZIII grains provided younger dates (202±8 to 184±6 Ma). MNZI, abundant in protomylonites, retains regional metamorphism, linking monazite U–Th–Pb data to fabric evolution. Titanite shows different zoning features and chemistry as function of the surrounding mineral assemblage: i) strongly zoned grains are mostly associated with silicate-rich layers; ii) homogeneous grains are generally within the silicate-poor layers. Both types show a decoupling between chemistry, almost completely related to the peak metamorphism, and U–Pb isotopes. Deformation microstructures promoted a total reset of the U–Pb dataset at the beginning of deformation and a subsequent volume diffusion through the grains: the innermost domains of both titanite types provide a Triassic lower intercept age (240±5 Ma) while the rims/tips, locally coinciding with high strained portions, define an alignment of

	isotopic data with a Jurassic lower intercept age (186±6 Ma). This study highlights how combining monazite and titanite geochronology refines the timing and duration of deformation, particularly in large-scale shear zones involving different lithologies.

Reactive and resilient: the contrasting behaviour of monazite and titanite during deformation (The Forno-Rosarolo shear zone; Ivrea-Verbano Zone)

Langone A.[1]*, Simonetti M.[3], Corvò S. [1,2] *, Bonazzi, M.[1,2], Maino, M.[1,2], Orlando, A.,[4] Braschi, E.[4], Piazolo, S.[5]

1 Department of Earth and Environmental Sciences, University of Pavia, Pavia, Italy

2 Institute of Geosciences and Earth Resources of Pavia, C.N.R., Pavia, Italy

3 Geological Survey of Italy, ISPRA, Roma, Italy

4 Institute of Geosciences and Earth Resources of Florence, C.N.R., Firenze, Italy

5 School of Earth and Environment, University of Leeds, Leeds, United Kingdom

*Corresponding author: antonio.langone@unipv.it; stefania.corvo@unipv.it

ABSTRACT

Dating the shear zone activity remains challenging and depends on geochronometer reactivity. We investigate the Forno-Rosarolo Shear Zone (Ivrea-Verbano Zone, Italy), developed in the intermediate-low continental crust under amphibolite-facies conditions. Sheared paragneisses and calc-silicates were dated using in-situ U–(Th–)Pb monazite and titanite geochronology.

Three monazite generations (MNZI-III) were identified based on microstructural position, internal features, chemical zoning (Th, Y), and isotopic data. Deformation was mainly recorded by MNZII, with high-Y domains yielding Triassic dates (average ages of: 238±8 and 222±8 Ma). Rare, highly fractured or porous MNZIII grains provided younger dates (202±8 to 184±6 Ma). MNZI, abundant in protomylonites, retains regional metamorphism, linking monazite U–Th–Pb data to fabric evolution.

Titanite shows different zoning features and chemistry as function of the surrounding mineral assemblage: i) strongly zoned grains are mostly associated with silicate-rich layers; ii) homogeneous grains are generally within the silicate-poor layers. Both types show a decoupling between chemistry, almost completely related to the peak metamorphism, and

U–Pb isotopes. Deformation microstructures promoted a total reset of the U–Pb dataset at the beginning of deformation and a subsequent volume diffusion through the grains: the innermost domains of both titanite types provide a Triassic lower intercept age (240±5 Ma) while the rims/tips, locally coinciding with high strained portions, define an alignment of isotopic data with a Jurassic lower intercept age (186±6 Ma). This study highlights how combining monazite and titanite geochronology refines the timing and duration of deformation, particularly in large-scale shear zones involving different lithologies.

Keywords:

Mylonites, monazite, titanite, petrochronology, geochemistry, microstructure, U–(Th–)Pb

1. INTRODUCTION

Constraining the timing of ductile deformation is crucial for understanding the tectono-metamorphic evolution of intermediate-lower crustal domains in both continental and oceanic crust (e.g., Xypolias, 2010; Oriolo et al., 2018). Mylonites reflect zones of high strain where dominantly ductile deformation has been localized. Mylonitic shear zones occur at all scales in the lithosphere and may provide pathways that localize fluids and secondary alteration (e.g., Beach, 1976; Austrheim, 2013; Kirkland et al., 2023). These rocks may thus preserve key evidence for the kinematics and structure of an orogen as well as of rift-related systems. Dating the evolution of the shear zones has been described as one of the most difficult problems in geochronology (e.g., Oriolo et al., 2018; Kirkland et al., 2023). In addition to the dating of major fabric-forming minerals, *in-situ* geochronology or petrochronology on minor and accessory minerals may provide direct constraints on the timing of deformation (e.g., Piazolo et al., 2012) as it allows linking isotopic dating, microstructures, geochemistry and thermobarometry. In recent years, the combination, simultaneously or not, of isotopic ratios and trace element for accessory and minor minerals with in-situ techniques, opens the possibility to date the small syn-kinematic domains developed on pre-existing grains (e.g., Simonetti et al., 2020, 2021b; Carosi et al., 2022; Moser et al., 2022; Walters et al., 2022; Kirkland et al., 2023; Kavanagh-Lepage et al. 2023; Corvò et al, 2023). Among the accessory minerals, monazite and titanite are the most promising being present in different rock types and, most important being more reactive with respect to other accessory minerals, i.e., zircon. Both chronometers have been shown to develop chemical zoning as function of metamorphic reactions with and without deformation allowing to link the ages to specific geologic events (Engi, 2017; Hetherington et al., 2017; Kohn, 2017; Kohn, et al., 2017).

The usefulness of monazite as a geochronometer is due to its lattice properties allowing it to contain high concentration of Th and U and low amounts of common-Pb (Parrish, 1990). Monazite is common in metapelitic/metapsammitic rocks with Ca-poor and Al-rich bulk compositions at metamorphic conditions above upper greenschist facies (e.g., Spear and Pyle, 2010). Unlike zircon, monazite has a higher reactivity, it is able to preserve isotopic inheritance and to record P-T conditions from prograde to retrograde (e.g., Langone et al., 2011). Monazite may develops chemical zoning that can be linked to a specific metamorphic reaction related to static or dynamic (re)crystallization of both major and accessory rock forming minerals (e.g., Wawrzenitz et al., 2012; Hetherington et al., 2017). In the last years, the combination of *in situ* U-Th-Pb data with the geochemical composition of the dated monazites allowed to establish the timing of complex geologic events (e.g., Shaw et al., 2001; Williams & Jercinovic, 2002; Rasmussen & Muhling 2007; Di Vincenzo et al., 2007; Janots et al., 2012; Wawrzenitz et al., 2012; Williams & Jercinovic, 2012; Didier et al., 2014; Grand'Homme et al., 2016; Kohn, 2016; Regis et al., 2016; Bosse & Villa 2019; Bergemann et al., 2020; Simonetti et al., 2020, 2021b; Schulz, 2021; Carosi et al., 2022). Although monazite can be useful to date tectonic events in rocks from the middle and lower crust

(Erickson et al., 2015; Williams & Jercinovic, 2012, Mottram and Cottle, 2024), it has been documented that monazite is able to record shearing by fluid-assisted dissolution and growth on rims at low amphibolite facies metamorphic condition (e.g., Terry et al., 2000) or even lower metamorphic conditions (e.g., Shaw et al., 2001).

Recently, it has been demonstrated that titanite microstructures can be used to date hyper velocity meteorite impacts (e.g., Papapavlou et al., 2017; McGregor et al., 2021) as well as the activity of ductile shear zones developed within continental crustal rocks (e.g., Gordon et al., 2021; Moser et al., 2022; Kavanagh-Lepage et al., 2023; Corvò et al., 2023). Conversely to monazite, the adoption of titanite as a geochronometer is complicated by two main issues. Firstly, it has a strong affinity for Pb and thus it may incorporate common lead during crystallization (e.g., Kohn, 2017). Consequently, most titanite U–Pb measurements require correction for substantial common Pb before age interpretations, e.g., by regressing less radiogenic and more radiogenic measurements on an inverse isochrons (Tera-Wasserburg diagrams) to derive an age. Secondly, the temperature range for diffusive Pb-loss within the grains is somewhat disputed. Titanite has been traditionally considered as a thermochronometer with closure temperatures of 650°C and 750°C determined experimentally for titanite crystals with 0.5 and 5mm radii, respectively and considering a cooling of about 5°C/Myr (Cherniak, 1993). In contrast with the experimental studies, several studies on natural titanite grains suggest that the U–Pb isotope system may be resistant to volume diffusion at temperature of up to 800°C (Kohn, 2017; Hartnady et al., 2019) providing crystallization ages (and not cooling ages) and referring to titanite as a petrochronometer (e.g., Hartnady et al., 2019; Holder et al., 2019; Olierook et al., 2019; Scibiorski et al., 2019; Kirkland et al., 2020; Gordon et al., 2021; Moser et al., 2022; Walters et al., 2022). Besides these two main issues several authors (e.g., Gordon et al., 2021; Moser et al., 2022; Kavanagh-Lepage et al., 2023; Corvò et al., 2023), highlighted a decoupling between the

U–Pb isotopic system and some trace elements and a strong dependence on the mineral assemblage of the hosting microdomain for titanite during (e.g., Corvò et al., 2023).

In this contribution we aim to assess the robustness and utility of the two geochronometers in deciphering the tectono-metamorphic history of high strain rocks. We present monazite and titanite microstructural, chemical and isotopic data from mylonitic paragneisses and calc-silicates from an extensional shear zone affecting the continental crustal section of the Ivrea-Verbano Zone. This zone is ideally suited for our study since it has been object of detail reconstructions of strain distribution and lithological make-up. It has been shown that both monazite and titanite are present in the main lithologies. Importantly, the zone records different tectono-metamorphic events, the timing of which remains disputed (e.g., Siegesmund et al., 2008; Garde et al., 2015; Simonetti et al., 2023). Here we i) describe the behaviour of monazite and titanite under the same shearing conditions, ii) shed light on the timing of deformation by U-Th-Pb dating of monazite and titanite and on the petrologic evolution of mylonites during deformation, iii) discuss the complementary and contrasting utility of these two geochronometers in dating deformation in mid- to lower crustal rocks.

2. GEOLOGICAL SETTING

The Ivrea-Verbano Zone (IVZ) in north-western Italy represents a cross-section through the middle to lower continental crust of the Southern Alpine basement (Fig. 1A). During the Alpine collision, the IVZ underwent vertical exhumation and open folding, but it escaped the metamorphic overprint (Henk et al., 1997; Rutter et al., 2007; Wolff et al., 2012). The IVZ is delimited by the Insubric Line northward, while south-eastward, it is juxtaposed to the Serie dei Laghi Unit by the Late-Variscan Cossato–Mergozzo–Brissago Line, which is in turn crosscut by the Pogallo Line (Fig. 1A; Boriani et al., 1990).

The IVZ is traditionally subdivided in three main units (Fig. 1A), from NW-SE: i) the mantle peridotites; ii) the Mafic Complex, and iii) a volcano-sedimentary metamorphic sequence, namely the Kinzigite Formation. The latter is considered as the originally upper part of the tilted crustal section made up of a heterogeneous group of metasediments, comprising mainly metapelites with intercalated metabasic rocks (i.e., volcanic sediments and MORB-like lavas) and minor marbles/calc-silicates and quartzites (Zingg, 1990; Schmid, 1993; Quick et al., 2002; Kunz et al., 2014). At a regional scale, peak metamorphic grade decreases from granulite (~900 °C and 900 MPa) to amphibolite facies (~600 °C and ~400 MPa) from NW to SE (Schmid & Wood, 1976; Brodie & Rutter, 1987; Zingg, 1990; Schmid, 1993; Redler et al., 2012; Kunz et al., 2014; Kunz & White, 2019). The highest degree of metamorphic conditions has been recorded by paragneiss septa (i.e., depleted granulite) forming layers within the Mafic Complex (Fig. 1A; Sinigoi et al., 1996; Ewing et al., 2013). The progressive switch at the mid to lower crustal levels from granulite to amphibolite facies is marked by a transition zone of ~1-5 kilometres (Fig. 1B) that experienced extensive migmatization processes (e.g., Redler et al., 2012; Kunz et al., 2014; Carvalho et al., 2019). In the north-eastern part of the IVZ, this transition zone hosts two mylonitic shear zones, namely the Anzola (Brodie and Rutter, 1987; Corvò et al., 2022; 2023) and the Forno-Rosarolo shear zones (Siegesmund et al., 2008; Simonetti et al., 2023). Although described as separate shear zones and often named in different way (see Simonetti et al., 2021a), these structures have been interpreted as a single fault system, with NNE-SSW strike (e.g., Rutter et al., 2007), associated to the Triassic-Jurassic (180-230 Ma) rift-related tectonic (Beltrando et al., 2015; Petri et al., 2019; Simonetti et al., 2023; Corvò et al., 2023). In this time interval, crustal thinning (<10 km thick) was accommodated by several shear zones active during different phases of rifting (Manatschal et al., 2007; Mohn et al., 2012) at different crustal levels (e.g., Beltrando et al., 2015).

3. GEOCHRONOLOGICAL BACKGROUND

Several authors, by using geochronological and/or thermochronological techniques, aimed to constrain the timing of the main geodynamic episodes that characterised the evolution of the crustal section of the IVZ. Here we report a summary of the main tectono-metamorphic event well recorded by both geo- and thermochronometers.

The rare occurrence of Carboniferous (Pennsylvanian) metamorphic (i.e., 316±3 Ma U–Pb on zircon, Ewing et al. 2013, 2015; 311±2 Ma garnet–whole rock Lu–Hf isochrons, Connop et al., 2024) and magmatic ages (i.e., 314 ±5 Ma U–Pb on zircon Klötzli et al., 2014) indicates that the pervasive amphibolite- and granulite-facies mineral parageneses of the IVZ formed after the peak of Variscan compressional deformation and plutonism.

The IVZ recorded mostly tectono-metamorphic and magmatic events during the Permian as documented by dating of different accessory minerals from metamorphic (e.g., Henk et al., 1997; Vavra et al., 1999; Guergouz et al., 2018; Kunz et al., 2018; Williams et al., 2022; Wyatt et al., 2022, Corvò et al., 2024) and magmatic rocks (e.g., Peressini et al., 2007; Karakas et al., 2018). This High-Temperature (HT) event has been confirmed also recently by both in-situ garnet U–Pb dating (Bartoli et al., 2024) and garnet–whole rock Lu–Hf isochrons (Connop et al., 2024) of metamorphic samples across the crustal section. The pervasive amphibolite- and granulite-facies mineral parageneses formed during the Permian lithospheric thinning, well documented across the Alps (e.g., Schuster & Stüwe, 2012).

The geochronological studies performed on metamorphic rocks across the IVZ crustal section revealed also that the HT conditions persisted for several Myr. Thanks to a systematic study of textures, REE content and U–Pb ages of zircon and monazite grains, Guergouz et al. (2018) inferred that the minimum duration for high-temperature metamorphism should be between 20 and 30 Myr. Kunz et al. (2018) dated granulitic rocks by zircon U–Pb and suggested that the HT metamorphic conditions lasted for a longer time interval, up to 60 Myr. A recent study of monazite across the crustal section exposed in the Valle Strona di Omegna reported dates mostly in the range 240–320 Ma with two main peaks at circa 290 and 270 Ma (Williams et al., 2022). According to these authors, the monazite textural and chemical features indicate that these dates record the timing of pre-peak to peak metamorphic conditions. The long-lasting persistency of HT conditions agrees with the model proposed by Schuster & Stüwe (2012) suggesting lithospheric thinning with negligible surface subsidence between 290 and 240 Ma.

Magmatism and deformation associated with the Triassic-Jurassic Tethyan rifting largely overprinted the Permian crustal section (e.g., Beltrando et al., 2015). A review of both geochronological and thermochronological Triassic-Jurassic data has been recently published (Simonetti et al., 2021a). Here we synthetize isotopic data related to post Permian deformation events recorded by the IVZ crustal section. One of the oldest studies focused on deformation was provided by Brodie et al. (1989) by dating with Ar-Ar method syn-kinematic hornblende from mylonitic amphibolites of the Anzola shear zone (Fig. 1A). These authors obtained two ages at 215±5 Ma and 210±5 Ma that were interpreted by the authors in terms of the effects of grain-size reduction on the closure temperature for argon in hornblende and help further to chart the cooling history of the rocks. The activity of the Anzola Shear Zone has been recently constrained by Corvò et al. (2023) by U–Pb petrochronology of titanite from mylonites consisting of alternating amphibolites and calc-silicates. These authors obtained a Jurassic lower intercept age (188 ± 2 Ma) from rims/tips of titanite grains showing different chemistry and a major concentration of dislocations with respect to the inner domains. The Jurassic deformation was also recorded at different crustal levels by rocks showing different metamorphic conditions. The most prominent rifting-related structure in the southern portion of the IVZ is the Pogallo Line, which is interpreted as a low-angle normal fault that accommodated thinning (Hodges & Fountain, 1984) between Triassic and Jurassic age (ca. 210 and 170 Ma; Zingg, 1990; Mulch et al., 2002; Wolff et al., 2012) under decreasing temperatures from amphibolite- to greenschist-facies conditions. In the northern sector of the IVZ, Late Triassic to Early Jurassic ductile shear zones developed within (ultra)mafic rocks of the lower crust (U–Pb zircon data, Langone et al., 2018; hornblende Ar-Ar data, Boriani & Villa, 1997 of mylonitic metagabbro in Val Cannobina) and mantle peridotites (e.g., U–Pb zircon data, Corvò et al., 2020) under upper-amphibolite to granulite facies conditions (Brodie, 1981; Kenkmann, 2000; Kenkmann and Dresen, 2002; Degli Alessandrini, 2018; Langone et al., 2018).

3. METHODS

3.1 Sampling strategy

For geochronology, we selected metapelites showing different microstructural features (protomylonitic and mylonitic fabric) and composition (biotite-rich and biotite-poor) for monazite dating and a calc-silicate sample for titanite dating (Table 1). All the samples are coming from the transition between the high-strain and the low strain zones of the shear zone (Simonetti et al., 2023). Monazite samples were collected from one outcrop along the road whereas titanite-bearing sample is coming from another outcrop along the river, about 150m southward (Fig. 1B). Monazite was analysed within six thin sections from a biotite-poor (VSDO-13B) and two biotite-rich paragneisses (VSDO-13A and VSDO-13M; Fig. 2; Table 1).

Titanite was studied on different thin sections of mylonitic calc-silicates. The analyses were carried out in a (50 µm-thick) thin section of a representative sample (VSDO-12R2B; Table 1; Fig. 3). The samples were oriented on the field and thin sections are made parallel to the mineral lineation and perpendicular to the main foliation, therefore along the XZ plane of the finite strain ellipsoid.

3.2 Monazite and titanite chemistry

Thin sections were polished, C-coated and inspected using a Scanning Electron Microscope (SEM; Mira3, TESCAN) hosted at Earth and Environmental Sciences Department of Pavia University, in order to observe monazite and titanite microstructural position, internal features and zoning in Back-Scattered Electron (BSE).

The composition and zoning of monazite grains were characterized by acquiring X-ray maps (for P, Ca, Y, La, Ce, Pr, Nd, Sm, Eu, Gd, Th and U) and chemical analyses with a JEOL 8200 Super Probe electron microprobe hosted at the University of Milano (Italy) and a CAMECA SX-Five microprobe hosted in the Service CAMPARIS Sorbonne University (Paris). An accelerating voltage of 15 kV, a beam current of 5 and of 150 nA (respectively for chemical analysis and X-ray maps) and a spot size of 1 μm were used for the JEOL 8200 Super Probe. The CAMECA SX-Five microprobe was set at 15 kV, a beam current of 5 and of 230 nA for the maps. Monazite formula, normalised to 16 oxygens, were obtained with an in-house excel spreadsheet. Results are provided in Table S1 (Supplementary Material).

X-ray compositional maps (Si, Ti, Al, Ca, Fe, F, Zr, Nb, La, Ce, Nd) and chemical analyses (Si, Ti, Al, Fe, Mn, Ca, Na, P, Zr, Nb, La, Ce, Nd, Cl, and F) of titanite were acquired with a JEOL 8230 Super Probe electron microprobe hosted at the University of Florence (Italy). An accelerating voltage of 15 kV, a beam current of 20 and of 100 nA (respectively for chemical analysis and X-ray maps) and a spot size of 1 μm were used for chemical analyses, whereas variable spot size was considered according to map size for the compositional map. Titanite stoichiometry was calculated using the method of Oberti et al. (1981). Results are provided in Table S2 (Supplementary Material).

3.3 Imaging and quantitative microstructural analysis (EBSD)

In order to analyse the microstructural features, several monazite and titanite grains from the studied samples were selected for obtaining Electron-Backscattered Diffraction (EBSD) maps in thin section using the FEI Quanta 650 FEG–ESEM (with Oxford X–max 80 SDD

EDS, Oxford/HKL Nordleys EBSD system and Aztec software) at the LEMAS, University of Leeds, UK. A working distance of 20 mm, a 70° stage tilt, accelerating voltage of 20 kV and a step size of 0.5-1 μm were used for analyses. Post processing included correcting for wild spikes and down to a 5 nearest neighbour zero solutions correction. Quantitative orientation analyses are presented by maps, pole and dislocation analysis methods using AztecCrystal 2.2 (Oxford Instruments). Pole figures (PF) for monazite and titanite crystallographic system (monoclinic; (100), (010), (001), lower hemisphere projection on plane XZ), and misorientation profiles tendentially from core to rim or from the low to high distorted domains across the grains are used to assess orientation changes locally and within whole grains. So called Grain Reference Orientation Deviation (GROD) maps are presented to highlight the pattern and degree of lattice distortions inside grains. These colour-coded maps show the change in crystal orientation with respect to its average orientation. Lattice distortions within deformed grains were quantified by calculation of the local dislocation density using the “Weighted Burgers vector” (WBV) analysis following the approach described by Wheeler et al. (2009; 2024) and Timms et al. (2019). Specifically, we performed a loop around the area of titanite grains where the LA-ICP-MS spot analyses was taken. The derived dislocation density value refers to the number of geometrically necessary dislocations that are needed to accommodate the measured lattice distortion over the area in which the LA-ICP-MS spot was taken.

3.4 Monazite and titanite U-(Th-)Pb dating

Monazite and titanite U-(Th-)Pb dating was carried out using a laser ablation, inductively coupled, plasma mass spectrometry (LA-ICP-MS) at CNR-Istituto di Geoscienze e Georisorse U.O. Pavia (Italy). Analytical details, with the technical/methodological parameters following the PlasmaAge recommendation, are reported within Table S3 (Supplementary Material).

The large size of titanite grains/domains allowed us to collect simultaneously trace element concentrations and U-Th-Pb isotopes. Trace element concentrations were calculated using SiO_2 as the internal standard and the concentration of 29.8 wt.%, average obtained from EMPA analyses. NIST610 was used as primary reference materials, MKED-1 and TTN150 (Klemme et al., 2008) were analysed as quality control. The relative standard deviation for MKED-1 is better than 18% and concentrations are typically within better than 5% for Zr, Nb, Nd, Sm, Tb, Dy, Ho, Er, Tm, Hf, Th, and U; better than 11% for Al, Ti, Mn, Fe, Pr, Eu, Gd, Yb, Lu and Pb of expected values for 'MKED-1' (Spandler et al., 2016). Vanadium, Y, La, and Ce are less accurate (21-13%).

Moacir monazite (Cruz et al., 1996; Seydoux-Guillaume et al., 2002a,b; Gasquet et al., 2010) and MKED-1 titanite (Spandler et al. 2016) were used as the primary standards for U-(Th-)Pb dating and were run every ~ 10 unknowns. Precision and accuracy are reported within Table S3 (Supplementary Material).

The software GLITTER ® was used for data reduction (van Achterbergh et al., 2001) of both isotopic ratio and trace elements. IsoplotR (Vermeesch, 2018) was used for representing isotopic data of both monazite and titanite; ages are provided together with the 2sigma uncertainties. Monazite data with discordance higher than 5% and/or a spot overlap were excluded to avoid data bias. The $^{238}U/^{206}Pb$ and $^{207}Pb/^{206}Pb$ isotopic ratios for each analysis are presented uncorrected for common lead in Tera-Wasserburg concordia diagram using IsoplotR (Vermeesch, 2018).

Full analytical results are for monazite and titanite are reported as Supplementary Material Table S4 and S5, respectively.

3.5 Zr-in-titanite thermometer

The Zr-in titanite thermometer of Hayden et al. (2008) was used to calculate titanite temperatures. Uncertainties for the are given at 2σ, propagated assuming ± 0.1 GPa for pressure estimates, 2σ variation of the Zr concentration in titanite and the 2σ uncertainties given by the authors for their calibration of the thermometer (see Cruz-Uribe et al., 2014). Temperature estimates are reported in Table S5 (Supplementary Material).

4.FIELD OBSERVATIONS AND GENERAL PETROGRAPHY

The Forno-Rosarolo Shear Zone (FRSZ), also known as Rosarolo Shear Zone (Siegesmund et al., 2008), crops out in the IVZ section of the Strona di Omegna valley between the Rosarolo and Forno villages (Fig. 1B). It was recently mapped and characterised in detail by Simonetti et al. (2023). It is a NE-SW-oriented shear zone with a thickness of about 500m. Mylonitic foliation is subvertical, in places steeply dipping toward the NW. A sinistral top-to-the-SW sense of shear is well highlighted by the presence of δ- and σ-type porphyroclasts, shear boudins, flanking structures and winged inclusions in all the involved lithologies (Simonetti et al. 2023). The FRSZ developed in a narrow area described as the transition zone between the amphibolite- and granulite-facies metamorphic rocks (Redler et al., 2012; Kunz et al., 2014). Several lithologies are involved in the deformation, in particular paragneisses, metabasites, and locally calc-silicates (Simonetti et al., 2023). The margins of the shear zone are characterised by two low-strain domains (Fig. 1B), with different thickness, made by anastomosed protomylonites and mylonites layers surrounding weakly deformed lenses, whereas the high-strain core (Fig. 1B) consists of alternating mylonites and ultramylonites. The sheared rocks are characterised by a foliation-oriented NE-SW and dipping at variable angle, between 42° and 88°, toward the NW and a mineral lineation plunging at moderate angle toward the NE (Fig. 1B).

The protomylonitic biotite-poor paragneiss is coarse grained and consists of quartz, feldspars, sillimanite, garnet and minor biotite (Fig. 2A). Rutile, zircon, monazite, oxides and sulphides are accessories. Intracrystalline deformation is recognizable in all major phases.

Feldspars show undulose extinction and deformation lamellae, they are only locally fractured, and biotite shows kinks of the cleavage. Quartz is coarse-grained and present lobate grain boundaries and window and pinning structures. Sometimes chessboard extinction microstructure is also present. Locally, quartz-rich domains are characterised by a gradual grain size reduction and by the presence of both subgrains and new grains forming a “core and mantle structure” around larger grains. The prismatic sections of sillimanite show undulose extinction. These rocks are affected by intense fracturing and veining at high angle with respect to the foliation. Fractures and veins are generally closely spaced and crosscut the grains. This late brittle event promoted the replacement of the primary assemblage by secondary minerals such as chlorite, white mica, epidote, ilmenite. Monazite occurs in different textural positions: totally or partially enclosed within garnet or sillimanite porphyroblasts (Fig. 2D), within or among recrystallized quartz grains. Rarely monazite shows jagged contours as evidence for partial replaced by allanite (Fig. S1, Supplementary Material) but locally it is affected by intense fracturing.

Protomylonitic biotite-rich paragneisses are characterised by biotite, sillimanite, garnet, feldspars and quartz (Fig. 2B, E). Monazite, zircon, rutile, and graphite are common accessories. These paragneisses show a migmatitic texture overprinted by a well-defined foliation marked by layers of elongated biotite and large sillimanite prisms with subordinate quartz-feldspathic layers (Fig. 2B, E). This foliation wraps around rounded to elliptical garnet grains which contain numerous inclusions of matrix-forming minerals (Fig. 2B, E).

Feldspars generally show evidence of ductile deformation such as undulose extinction and deformation lamellae. Quartz is coarse-grained and presents lobate grain boundaries. Locally window and pinning structures and deformation lamellae can be recognized. Some grains also display chessboard extinction microstructure.

Sillimanite prisms show undulose extinction and deformation bands whereas the cleavage of biotite is kinked. Sillimanite fish, asymmetric mantled porphyroclasts and S-C-C’ fabric occur indicating a sinistral top-to-the-SW sense of shear. Brittle features are rare as well as the occurrence of secondary minerals such as chlorite after biotite and garnet, ilmenite after rutile.

Mylonitic paragneisses from the high strain zone show the same mineral assemblage of those from the low strain zone but differ for a more apparent mylonitic fabric (Fig. 2C, F). The foliation is marked by alternating melanocratic and leucocratic layers. The formers are made mainly of biotite and sillimanite whereas the leucocratic ones consist of quartz and feldspars (Fig. 2C, F). As porphyroclasts we observed mainly garnet, sillimanite and feldspars. Garnet occurs as rounded or elongated grains parallel to the foliation and, compared to less deformed rocks, it experienced an apparent grain size reduction (Fig. 2C, F). Sillimanite occurring in basal section commonly forms fish-shaped porphyroclasts rarely replaced at the edges by retrograde white-mica. The prismatic sections are generally elongated parallel to the foliation and show evidence for both ductile deformation, such as undulose extinction and kinking, and brittle deformation such as necking and fractures. Also in these samples monazite is rarely partially replacement by allanite growing syn-kinematically (Fig. S1, Supplementary Material).

Calc-silicates are well exposed in a small outcrop along the river (Fig. 1B). They are characterised by large (up to few centimetres) whitish clasts containing feldspars and mafic minerals (clinopyroxene and amphibole) surrounded by a greyish fine-grained matrix (Fig. 3A, B). At the microscale they show a well-developed foliation and mylonitic fabric (Fig. 3A-H). The largest porphyroclasts are made of feldspars whereas clinopyroxene and garnet are smaller (Fig. 3A-H). Calc-silicate shows a compositional layering consisting of calcite-rich layers alternating with layers richer in silicates (Fig. 3A, B). The latter are generally thinner and are made of plagioclase, quartz, green-amphibole and biotite with rare or minor calcite (Fig. 3C, D). Due to the low modal abundance of calcite, they can be defined as carbonate-bearing calc-silicate layers. The thicker calcite-rich layers contain (sub)rounded to elliptical grains of clinopyroxene and feldspars; anhedral garnet, locally showing a poikiloblastic texture, are also common (Fig. 3E-H). Titanite is an abundant accessory mineral whereas allanite and zircon are less common (Fig. 3G). Feldspars and clinopyroxene show evidence for intracrystalline deformation such as undulose extinction; deformation twins are well recognizable within plagioclase (Fig. 3D, F, H). Thin ribbons of recrystallized quartz are also common in the carbonate-bearing calc-silicate layers (Fig. 3D, H). Features indicative of brittle deformation are also common: major minerals as well as titanite and allanite show fractures, locally associated to a small displacement of fragments. Fractures are filled by secondary minerals such as calcite, chlorite and epidote. Retrograde replacement of primary mineral assemblage is not only localised along fractures; within the calcite poor layers, clinozoisite is abundant and generally replaces feldspars.

5. MONAZITE

5.1 Monazite composition

We identified a total of 32 monazite grains in the biotite-rich paragneisses and 4 monazite grains in the biotite-poor paragneisses (Table S6, Supplementary Material). Results of EPMA analysis are reported in Table S1 (Supplementary Material). The monazite grains analysed are rare earth element (REE) phosphate with Ce as the dominant REE (Fig. 4) and thus they can be classified as monazite-(Ce) according to Linthout (2007). Monazites from protomylonites are characterised, on average, by a higher huttonite component (Fig. 4) due to the increase of Th and U with respect to Ca + Si following the solid solution between cheralite ($Ca(Th,U)(PO_4)_2$) and huttonite $(Th,U)SiO_4$ end-members (Förster, 1998; Linthout, 2007).

Among the analysed elements, Nd, Y, and La show apparent variations as function of the rock fabric. While Y and La are on average higher within monazite from mylonites, Nd has an opposite trend (Fig. 4B-C; Table S1). The Th/U ratio does not change significantly within the two different sheared rocks (Fig. 4C; Table S1) and it has values comparable to those reported for monazite within granulites exposed in the Valle Strona di Omegna (Williams et al., 2022; Fig. 4D).

5.2 Monazite textural position and zoning

Protomylonite: Biotite-poor paragneiss (VSDO-13B1)

Here we selected 4 monazite grains (Mnz1a, Mnz4a, Mnz6a and Mnz6b) that are among grains of major rock-forming minerals or included within a sillimanite porphyroblast (Fig. 5, Table S6).

Mnz1a and 6b have an elongated shape whereas Mnz6a has a more irregular shape with cuspate terminations. All these grains are characterised by a large Th-rich core surrounded by thin rims/edges with lower Th content. Y is generally homogeneous within the large core and tends to be higher in the outermost domains (a few µm) of the grains (Fig. 5A-B). Mnz4a is stubby (Fig. 5B) and differs from the other grains since it shows opposite zoning features: on one side, towards the foliation, high-Th and low-Y domains occur. This grain is also characterised by intense fractures that crosscut the entire grain, and it has numerous fine-grained pores/inclusions aligned almost parallel to the main fractures (Fig. 5B).

Protomylonite: Biotite-rich paragneisses (VSDO-13A1)

In sample VSDO-13A1 a total of 9 grains were characterised by X-ray maps: 8 grains are located along the main foliation and 1 is included in garnet (Table S6).

The monazite grains located along the main foliation show a variable size and shape (TableS6), and all presents apparent chemical zoning for Y and Th (Fig. 5A-D and S2; Table S1). The most common zoning pattern consists of large cores richer in Th and poorer in Y surrounded by thinner irregular rims richer in Y and poorer in Th (e.g., Mnz6b Fig. 5C and Mnz2a, 8a, Fig. S2). The Th distribution in the internal domains is irregular and locally riches concentrations up to 12wt.% (ThO_2). Locally Y-rich bands alternate with Th-rich ones (e.g., Mnz4a, Fig. 5B). Monazite grains totally or partially enclosed within garnet are characterised by a patchy zoning of both Y and Th (e.g., Mnz7a, Fig. 5D). Less commonly Y is almost homogeneously distributed within the grain whereas Th looks oscillating (e.g., Mnz1a Fig. 5A).

Mylonites: paragneisses

Sheared paragneisses *(VSDO-13M1, VSDO-13M2 and VSDO-13M4)* contain abundant monazite grains. Twenty-three grains were selected as representative of different textural positions and were fully characterised (EPMA chemical analyses and X-ray maps; Table S1): 13 are located along the main foliation, 3 are in the strain shadow around porphyroclasts, 4 are in contact with garnet and 3 are totally or partially included within garnet porphyroclasts (Table S6). Some of these monazite features are shown in Fig. 5 and S2. The X-ray maps of selected monazite grains revealed that monazite shows three main different zoning patterns.

i) Ten of the analysed twenty-three grains do not show a clear core-rim zoning and are locally characterised by internal domains poorer in Y and external domain richer Y (e.g., Mnz7, VSDO-13M1; Mnz7 VSDO-13M2; Mnz14, VSDO-13M4, Fig. 5E). In these grains Y and Th are correlated.

ii) Seven of the analysed twenty-three grains show irregular shapes with inner domains richer in Y and external domains Y-depleted. In these grains the zoning pattern of Th is not apparently correlated with Y (e.g., Mnz6, VSDO-13M1; Mnz4 VSDO-13M4, Fig. 5H).

iii) Five of the analysed twenty-three grains are elongated (high aspect ratio) and show richer Y cores and poorer Y rims/tips (Mnz15, Mnz11 and Mn10 VSDO-13M2, Fig. 5F-G). Also, in these grains the zoning pattern of Th is not apparently correlated with Y.

A patchy distribution of both Th and Y was observed for one grain partially included within garnet (e.g., Mnz15, VSDO-13M4).

5.3 Monazite quantitative orientation data

Four monazite grains from the studied samples were analysed by EBSD (Fig. 6). Two from the protomylonitic paragneiss (Mnz2a, Mnz6B, VSDO-13A1) and two from the mylonitic paragneiss (Mnz1, Mnz2, VSDO-13M1). All monazite grains show significant distortions (up to 12°) regardless of the degree of strain intensity of the two different samples. However, monazite grains from mylonites show higher degree of distortions strongly localised at the rims/tips of the grain with respect to those from protomylonites. In all grains, the systematic orientation of the main grain (blue colour) with little changes of distortions towards the rims (red colour) is highlighted not only by EBSD maps but also by the profile and pole figures (Mnz2a, Mnz2; Fig. 6A, D). The single blue points in pole figures emphasise the occurrence of neoblasts (e.g., Mnz6B, Mnz1; Fig. 6B, C).

Monazite from the protomylonite (VSDO-13A1) shows slightly continuous and discontinuous increasing lattice distortions from core to rim (around 5-8°; Fig. 6A, B). The higher degree of distortion is focused on the rim/tips (Mnz2A; Fig. 6A) and locally, when changes in orientation due to the occurrence of grain boundaries occurred (Mnz6B; Fig. 6B).

Monazite from the mylonite (VSDO-13M1) presents significant lattice distortions especially focused on the rim/tips (up to 12°; Fig. 6C, D). These locally developed into distinct neoblasts (Mnz1; Fig. 6C) or are reached from the continuous increasing of distortions from core to rim (Mnz2; Fig. 6D).

5.4 Monazite U-Th-Pb dating

Protomylonites

A total of eighty-eight analyses were performed on 12 monazite grains within the protomylonites (4 grains from the biotite-poor sample; Fig. 7A-B; Tab. S4). Sixty-three data resulted concordant (% of concordance >95%) for both $^{206}Pb/^{238}U$ vs $^{207}Pb/^{235}U$ and $^{206}Pb/^{238}U$ vs $^{208}Pb/^{232}Th$ systematics in the range of 314±6 Ma to 184±6 Ma. The dominant Carboniferous-Permian dates (57% of the total dataset) were obtained mostly from cores of monazite occurring within the foliation and from one grain enclosed within garnet. These grains are characterised by both cores to rim zoning features (low-Y cores or inner domains surrounded by high Y rims and/or external domains) or patchy zoning (Figs. 7B, S3). The Triassic data (33% of the total dataset) were obtained mostly from high-Y external portions (Fig. 7B) whereas the youngest Jurassic dates were obtained from one high-Y grain occurring as satellite around a larger grain (Fig. S3), a high-Y rim of a monazite with patchy zoning and a Y-rich domain of a grain showing numerous fractures and pores (e.g., Mnz4a, VSDO13-B1).

Mylonites

A total of eighty-eight analyses were performed on 21 monazite grains within the mylonites (Fig. 7A-B; Tab. S4). Sixty-one $^{206}Pb/^{238}U$ data resulted concordant (% of concordance >95%) with respect to both $^{207}Pb/^{235}U$ and $^{208}Pb/^{232}Th$ data. Although dates show a huge spread from 290 ± 14 Ma to 188 ± 6 Ma they fall mostly in the Triassic period (36 data, 59% of the entire dataset). The minor Carboniferous-Permian dates (8 data, 13% of the entire dataset) were obtained mostly from cores of monazite occurring within the foliation and from two grains partially or totally enclosed within garnet. These grains are characterised by both cores to rim zoning features (low-Y cores or inner domains surrounded by high Y rims and/or external domains) or patchy zoning. The Triassic and Jurassic dates (53 data, 87% of the entire dataset) were obtained from high-Y rims surrounding low-Y cores and from high-Y elongated or anhedral grains along the foliation (Fig. 7B, S4).

6 TITANITE

6.1 Titanite textural position

Titanite is found generally as elongated grains aligned with the foliation (Fig. 8) with dimensions up to 600x250 μm. Locally, small grains occur as satellites around larger titanite grains (Fig. 8A, B). Rarely titanite is observed within clinopyroxene porphyroclasts (e.g., Ttn11; Fig. 8H). Two sets of fractures were observed within titanite (Fig. 8), one set is parallel to the cleavage and the second one is generally at high angle with respect to the foliation and crosscut the entire grains. In this latter case, fractures are filled by secondary minerals such as chlorite, albite, epidote, ilmenite. In titanite inclusions of feldspars, calcite, chlorite, epidote, apatite, zircon and rarely rutile were observed. Trails of small inclusions/pore are also common (Fig. 8).

6.2 Titanite zoning, chemistry and thermometry

Based on textural and chemical features titanite can be subdivided in two main types. Type "Z" titanite is apparently zoned in BSE images with darker tips/terminations and brighter cores (Fig. 8A-D). Rarely, the darker domains are more extended, partially enveloping the grain (Fig. 8B-D). Locally, zoning features are crosscut by brighter parallel bands reflecting twins (Fig. 8B-D). Type "Z" titanite occurs generally within the silicate-rich layers. Type "unZ" titanite is relatively unzoned in BSE images (Fig. 8E- G) and occurs mostly within the calcite-rich layers. Both types can coexist within the same textural site within a distance of a few microns (Fig. 8G, H) at the boundary between the two compositional layers (i.e., calcite-rich and silicate-rich layers). The apparent chemical differences between the two types of titanite have been further documented by X-ray maps of both types (Figs. S5 and S6). According to the X-ray maps of two selected grains of type "Z" titanite large cores with higher La_2O_3,

Ce_2O_3 and Nd_2O_3 and Nb_2O_5 are surrounded by thinner rims/tips with lower REE (Fig. S5). The distribution of elements within the cores is indicative of a sector zoning.

Quantitative chemical analyses of titanite are reported in Table S2 and Fig. 9A-B. Type “unZ” titanite grains have on average lower TiO_2 (35.9±0.7 wt.%) and Fe_2O_3 (0.34±0.04 wt.%) contents with respect to zoned titanite (TiO_2=36.6±0.6 wt.%; Fe_2O_3=0.39±0.05 wt.%) and higher Al_2O_3 content (2.5±0.3 vs 2.0±0.3 wt.%; Fig. 9A). The CaO content of type “Z” titanite is highly scattered and on average lower (27.8±0.5 wt.%) than the CaO content of unzoned titanite (28.2±0.2 wt.%; Fig. 9B). Analogously, fluorine is on average higher for the type “unZ” titanite with respect to type “Z” (0.76±0.07 vs 0.59±0.07 wt.%; Fig. 9B).

Fourteen titanite grains were analysed for trace element composition confirming significant differences between the two types of titanite (zoned vs unzoned) and from core to rims of zoned titanite grains. The normalised REE patterns reveal that the two different types of titanite show similar trends with LREE fractionated over HREE (Fig. 9C-D). This is particularly apparent for type “Z” titanite (Fig. 9C), and one type “unZ” grain characterised by a significant depletion of HREE (e.g., Ttn23; Fig. 9D). Type “Z” titanite differs also for a more pronounced negative Eu anomaly that is weak or absent for homogeneous titanite (Fig. 9C, D). Type “Z” titanite grains are characterised also by a more pronounced intragrain variation of the REE patterns (Fig. 9C). Generally, the dark external domains have LREE lower than 10000 times CI whereas the bright inner domains have LREE higher than 10000 times CI (Fig. 9C, E).

Zirconium has an opposite trend with respect to REE (Fig. 9E) being on average higher within inner domains of type “unZ” homogeneous titanite grains with respect to type “Z” titanite (Zr<1600 ppm). This difference is much more apparent for the dark external domains of type “Z” titanite where Zr is <500 ppm (Fig. 9E). The two types of titanite are well distinguishable in terms of Nd contents. The type “unZ” grains are generally poorer in Nd (<1000 ppm) with respect to type “Z” titanite (Fig. 9E).

By adopting the Zr-in-titanite thermometer of Hayden et al. (2008) the obtained temperatures range from 741 to 866°C for type “Z” titanite and from 744 to 919°C for type “unZ” titanite. The external domains of both types of titanite are systematically poorer in Zr content and thus provide lower temperatures with respect to the internal domains (Fig. 9F). The obtained temperature values overlap the peak temperature conditions estimated from the surrounding metabasite and metapelitic rocks equilibrated under high-grade metamorphic conditions (e.g., Kunz & White, 2019; Fig. 9F).

6.3 Titanite quantitative orientation data

Seventeen titanite grains were analysed with EBSD; we present four representative grains in terms of deformation and type (type “Z” Fig. 10A-D, type “unZ”, Fig. 10-H). Most of the analysed grains show at least one set of polysynthetic straight to slightly kinked twin lamellae (e.g. Fig. 10). The twins have a thickness of about 0.5 μm, cross the grain and terminate against grain boundaries with a disorientation from the host grain by ~74°/<102> in accordance with previous studies (Timms et al., 2019; McGregor et al., 2021; Corvò et al. 2023).

While twins are common for the two studied titanite type grains ("Z" and “unZ”), the other deformation features differ between them.

Type “Z” titanite shows lattice distortions up to 21° focused to rims/tips (10 grains; ttn2, ttn4, ttn5, ttn7, ttn10, ttn23, ttn24 ttn34, ttn27, Ttn40; Fig. 10A-D), whereas type “unZ” titanite has diffuse and weak (<5°) intracrystalline lattice distortions (six grains; ttn18, ttn19, ttn3, ttn16, ttn25, ttn26; Fig. 10E-H). One exceptional elongated grain (ttn17) exhibits fragmented (domino like) texture with stepped variation of the distortion angle and minor subgrains (Fig. 10H). Quantification of the local dislocation density (measured as Weighted Burgers vector, hereafter WBV) for type “Z” and type “unZ” grains provides average values for laser spot analyses of 0.0043 μm^{-1} and 0.0018 μm^{-1}, respectively (Tab. S5). Overall, for both titanite types, deformation and orientation changes do not perfectly overlap the chemical zoning.

6.4 Titanite U–Pb dating

A total of 73 petrochronological analyses were performed on 14 grains within a mylonitic calc-silicate (VSDO-12R2B). Results are summarised in Tab. S5 and Fig. 11. The U–Pb data are dispersed on the Tera-Wasserburg diagram defining a large U–Pb field suggesting ternary mixing between different common Pb values and multiple radiogenic Pb components. In order to interpret the U–Pb data, we looked for alignment of the isotopic data correlated with textural position, chemistry and/or deformation microstructure (i.e., dislocations density) for each titanite type, namely type “Z” and type “unZ” (Fig. 11).

By considering the average dislocation density calculated for each U–Pb analytical spot, no clear correlations are apparent (Fig. 11A, B). A weak correlation with ΣLREE and isotopic data is appreciable especially for zoned titanite (type “Z”; Fig. 11C). The analytical spots collected from domains richer in LREE are generally located to the left of the data population (Fig. 11C, D).

The location of the analysis spots shows a slight systematic in the TW diagram (Fig. 11E, F): external domains/tips of both types show a good alignment on the TW defining a lower intercept at 186 ± 6 Ma (Fig. 11G). The entire dataset is bounded by another regression line mostly coinciding with the innermost domains of both zoned and homogeneous titanite grains. This regression line has a lower intercept age at 240 ± 5 Ma. The U–Pb data between the two regression lines refer to cores and intermediate positions (Fig. 11E-G).

7. DISCUSSION

7.1 Behaviour of monazite as function of the deformation fabric

As shown in the Kernel Density Estimation plots of Fig. 12A, the distribution of concordant data of monazite grains within protomylonites range broadly from Carboniferous-Permian (52% of the data) to Triassic (48% of the data) with rare Jurassic dates. This spread is partially overlapping the monazite radiometric data from unsheared metamorphic rocks collected along the Valle Strona di Omegna crustal section (Fig. 12B; Henk et al., 1997; Guergouz et al., 2018; Williams et al., 2022; Wyatt et al., 2022). Conversely, the distribution of U–Th–Pb concordant data of monazite grains within mylonites is tighter being almost made by Triassic-Jurassic dates (85% of the data; Fig. 12A) which are scarce in previous studies of unsheared metamorphic rocks from the same crustal section (Fig. 12B).

These different distributions of U–Th–Pb concordant data between monazite from protomylonites and mylonites are correlated with textures, microstructure and chemistry (zoning features). Monazite grains from protomylonites have stubby or rounded shapes (low aspect ratio) and are generally larger with respect to monazite from mylonites (Fig. 5, Table S6). They are generally characterised by large homogeneous cores surrounded by thin rims with lobate boundaries towards the cores (Fig. 5). Conversely, within mylonites monazite grains show higher aspect ratios (highly elongated grains), chemical zoning revealed more complex features with larger rims/tips over cores or and/or opposite chemical trends from core to rims with respect monazite from protomylonites (Fig. 5). These results are generally consistent with the microstructural results that show higher degree of distortions strongly localised at the rims/tips of the monazite grains from mylonites with respect to those from protomylonites (Fig. 6).

7.2 Presence of three distinct monazite generations

Combining textural features with chemical data, X-ray maps and isotopic data we recognized three generations of monazite. The main features of the three different generations are schematized in Figure 13A.

The first generation of monazite (MNZI) is defined by grains partially or totally included within garnet porphyroclasts (shielding effect) and domains of monazite occurring along the foliation. MNZI grains/domains are more abundant within protomylonites (Figs., 7 and 13A) and are associated with Carboniferous-Permian concordant dates (314-250 Ma). Monazite grains from mylonites partially enclosed within garnet were also able to locally preserve old dates but often discordant (e.g., Janots et al., 2008). The preservation of old dates within the foliation is a common feature of sheared rocks (e.g., Langone et al., 2011) and highlights the heterogeneous behaviour of monazite (or more generally of geochronometers) as function of the hosting microdomain and shear partitioning. MNZI grains/domains are generally characterized by patchy zoning of both Th and Y and/or cores poorer in Y with respect to the rims/ external domains. The patchy zoning of both Th and Y is probably the result of an aggregation of small monazite grains in lower-amphibolite facies rock, pseudomorph after (probable) allanite (e.g., Skrzypek et al., 2018; Williams et al., 2018). The low Y cores of MNZI grains lying along the foliation or in contact with matrix-forming minerals (Fig. 13A) formed likely during or after garnet growth that is able to fractionate Y as well as HREE (e.g., Rubatto et al., 2006; Taylor et al., 2014).

The second generation of monazite (MNZII) refers to rims/domains with higher Y concentrations (MNZIIa, Fig. 13A) with respect to cores or adjacent domains (i.e., MNZI). MNZIIa domains are characterised by lobate, inward-penetrating shapes with sharp contact with the inner domains suggesting the migration of a reaction front. These features have been suggested as criteria for identify the Coupled Dissolution-Precipitation process (CDP; Putnis, 2009; Harlov et al., 2011; Varga et al., 2020) and have been attributed to the inward progression of fluids/melts changing chemistry and or isotopic record (Putnis, 2009; Weinberg et al., 2020, Varga et al. 2020). MNZIIa rims/domains are common within protomylonites but are more developed within mylonitic samples where they can be the 2/3 of the grain (Figs. 5, 7, 13A). The isotopic data relative to the MNZIIa define a Triassic cluster of concordant dates (weighted average of 222 ± 8 Ma). The second generation of monazite is not only restricted to domains of replacement but also is seen as whole grains with elongated shapes (high aspect ratio) and high Y content almost homogeneously distributed along the grain or with low Y “tips” (MNZIIb on Fig.13A). Monazite grains with these features were observed exclusively within mylonites and provided Triassic dates (weighted average of 238 ± 8 Ma; Figs. 7, 13A). The internal, external and isotopic features suggest a syn-kinematic development of MNZIIb grains/domains whose ages are related to a specific tectonic event (e.g., Williams & Jercinovic, 2002). The observed textural and internal features suggest that the Y-rich MNZIIb grains are probably the result of a more pervasive CDP process that, as well as for MNZIIa, it may reflect a period of monazite formation coevally with the breakdown of garnet (releasing Y). The higher proportion of MNZII over MNZI within mylonites is correlated with a more intense garnet break-down (Fig. 13A) as documented by grain size reduction and shaping of garnet becoming smaller, elliptic or rounded. The Y released during garnet break-down is thus incorporated within the external domains (MNZIIa) and/or grains (MNZIIb) of monazite formed by CDP.

The last generation of monazite (MNZIII) is defined by a few grains/domains providing mostly Jurassic concordant dates (nine data; dates ranging from 202±8 to 184±6 Ma; Fig. 13A). MNZIII grains/domains were observed mainly within protomylonites (e.g., Mnz4a, VSDO-13B1; Mnz6c, VSDO-13A1; Mnz8c, VSDO-13A2; Fig. 5 and S1) and rarely within mylonites (Mnz9, VSDO-13M1 in Fig. S1; Fig. 13A). MNZIII is mostly defined by small, isolated grains occurring as satellites around larger grains and by domains of grains characterised by i) numerous fractures and/or ii) anhedral shapes and/or iii) numerous pores. The relatively large spread of dates and the presence of interconnected nano- and micro-porosity, as well as fractures, are markers that can indicate a late interaction with fluid (e.g., Harlov et al., 2011) and/or a partial replacement of monazite by a nanomixture of the different monazite generations (e.g., Grand’Homme et al., 2016; Hentschel et al., 2020).

The observed generations of monazite do not show well defined age clusters being the concordant U–Th–Pb smeared from Carboniferous to Jurassic (Figs. 7 and 12A). This is more apparent for protomylonitic samples. In order to explain this continuous distribution of the concordant U–Th–Pb data two possible phenomena can be argued: i) the physical mixing of domains with different ages within the grain and/or ii) the partial resetting of monazite during subsequent events. Weinberg et al. (2020) studied monazite in migmatites and suggested that the physical mixing had not influence on the age spread that was mainly controlled by the fact that the radiogenic Pb was not completely removed during the CDP reactions occurred during the younger events (Seydoux-Guillaume et al., 2003). Therefore, we here interpret the observed dates distribution within sheared rocks as reflecting inheritance from the regional HT metamorphism (MNZI), the development of syn-shearing domains/grains by CDP during Triassic (MNZII, 238±8 – 222±8 Ma), the late alteration of monazite grains/domains (MNZIII) during Jurassic by interaction with fluids locally promoted by intracrystalline deformation.

7.3 Titanite heterogeneity controlled by the local environment

Two types of titanite were recognized within the calc-silicate sample: i) titanite characterised by an apparent zoning, higher REE content and lying mostly within calcite-poor layers (type “Z” titanite); ii) homogeneous titanite with lower REE contents and occurring preferentially within calcite-rich layers (type “unZ” titanite). The main features of the two titanite types are schematized in Figure 13B.

The occurrence of these two distinct types of titanite within the same thin section suggests that the calc-silicate sample is made of different protoliths, i.e., siliciclastic/volcanoclastic and carbonate/marl (Fig. 13B). The same observation has been recently made by Corvò et al. (2022; 2023) for titanite within mylonitic rocks from the Anzola Shear Zone from the adjacent Ossola valley (Fig. 1A). In these rocks the chemistry of titanite together with the

719 mineral assemblages suggests the presence of alternating layers made of amphibolites and
720 calc-silicates, i.e. former siliciclastic/volcanoclastic and carbonate/marl layers, respectively.
721 The local environment exerted a fundamental role also on the deformation features recorded
722 by titanite (Fig. 13B). While deformation twinning is common for both “Z” and “unZ” types,
723 titanite grains from calcite-poor portions (type “Z”) show higher lattice distortions (up to 21°)
724 focused to rims/tips with respect to “unZ” titanite from calcite-rich portions. A similar
725 correlation between microstructure and the composition of the microdomain hosting titanite
726 has been described for the banded (amphibolites – calc-silicates) mylonites of the Anzola
727 Shear Zone exposed in the adjacent Ossola valley (Fig. 1A; Corvò et al., 2023).
728

729 ***7.4 Petrogenesis of titanite vs U–Pb record: a decoupling between chemistry and***
730 ***isotopes***

731 Figure 13B summarizes the suggested petrogenetic evolution of titanite as well as the
732 observed microstructures and the isotopic record. Titanite is occurring within the matrix and
733 is also included within clinopyroxene porphyroclasts (Fig. 8H). In both cases it shows the
734 same zoning and chemical features. These observations suggest that titanite formed at least
735 coevally with the peak metamorphic assemblage during the Permian high-temperature
736 regional metamorphism. Since the occurrence of sphene in metamorphic rocks is strongly
737 controlled by bulk composition (Frost et al., 2001), the composite nature of our sample, i.e.,
738 former siliciclastic/volcanoclastic and carbonate/marl layers, would imply different
739 metamorphic reactions for the formation of titanite. According to phase relations diagram for
740 calcite-bearing rocks titanite could be produced and stable at high temperatures and $X(H_2O)$
741 conditions during regional metamorphism by reactions involving calcite, quartz, rutile ±
742 clino/zoisite (e.g., Frost et al., 2001; Kohn, 2017). Within the silicate-rich layers, the
743 formation of titanite during metamorphism needs further reactants such as chlorite,
744 clinopyroxene, amphibole, plagioclase and ilmenite (e.g., Frost et al., 2001; Kohn, 2017).

The reactions involving the above-mentioned reactants may explain the formation of titanite observed within both calcite-poor and calcite-rich domains of the studied sample during the HT regional metamorphism. The apparent zoning consisting of a depletion of LREE, Y and Zr in the external portions of type “Z” titanite can be explained by two alternative processes. This feature is compatible with the occurrence of large allanite (LREE-rich epidote) grains grown almost coevally with titanite within the silicate-rich layers (Fig. 3G). Alternatively, the LREE depletion of the external domains for titanite could be related by the occurrence of clinozoisite developed during deformation (Fig. 3H). The lack of an apparent zoning within type “unZ” titanite and the occurrence of clinozoisite within both layers suggest that the observed zoning is a primary feature due to the formation of allanite almost coevally with titanite (stage2 on Fig. 13B).

The pre-shear mineral assemblages of both calcite-poor and calcite-rich layers contain garnet. The observed REE pattern for titanite may be useful to unravel the genetic relationships between garnet and titanite. The lack of a significant and general HREE fractionation for the analysed titanite grains (Fig. 9C, D) indicate that titanite probably predates garnet formation. Alternatively, the possible HREE fractionation exerted by garnet coeval or predating titanite is extremely local (e.g., Ttn23, Fig. 9D). According to the P-T-X(CO_2) modelling of Rapa et al. (2017) for both calcite-poor and calcite-rich domains of calc-silicates from Himalaya, different episodes of titanite growth are predicted before the formation of garnet-bearing assemblages. These observations are more compatible with our first hypothesis of a garnet postdating titanite. Summarizing, the observed titanite grains are the result of different metamorphic reactions, as function of the hosting microdomains, producing allanite almost coevally with titanite (stage 2 on Fig.13B) and predating garnet during regional HT metamorphism. This petrogenetic reconstruction is coherent with the Zr-in-titanite temperature estimates obtained for internal domains of titanite indicating high temperature conditions (919 ± 82 – 746 ± 50°C). These temperatures overlap, or are even higher than, the peak temperatures estimated from the adjacent mafic and pelitic metamorphic rocks (Fig. 9; Kunz & White 2019). Even though, the titanite rims provided lower temperature with respect to the cores (850 ± 57 – 741 ± 49°C) these remain still significantly higher with respect to the qualitative (syn-kinematic mineral assemblages suggest epidote-bearing amphibolite facies conditions) and quantitative estimates of temperature conditions of deformation (<700°C; Simonetti et al., 2023).

Contrarily to monazite showing three distinct generations it has not been possible to define different generations for titanite combining U–Pb isotopes with chemistry and microstructures (Fig. 13B). The U–Pb data obtained from titanite are bounded by two regression lines with lower intercept ages at 240±5 and 186±6 Ma (Fig. 11; 13B). These two regression lines are correlated with textural position being the oldest related to the cores and the youngest linked to the rims/tips of titanite. The time interval framed by the two regression lines does not fit with (postdate) the main peaks of the Permian regional high-temperature metamorphism that has been constrained, in extreme detail, with zircon (Ewing et al., 2013; Kunz et al., 2018), monazite (Williams et al., 2022; Wyatt et al., 2022) and garnet (Connop et al., 2024; Bartoli et al., 2024) along the same crustal section (Fig. 12B). The oldest possible intercept age from the innermost portion of titanite grains points to Triassic (*TTNII*? in Fig. 13B) indicating that this accessory mineral was not able to clearly retain the age of crystallisation (*TTNI?* in Fig. 13B). The Triassic lower intercept age obtained from the innermost titanite domains could thus reflect: i) the crystallization/cooling age, or ii) a total reset of the isotopic system within a pre-existing grain. As discussed above, titanite formed during the Permiam regional metamorphism, coevally with the first generation of monazite (MNZI in Fig. 13A) therefore the first hypothesis is unlikely. The studied crustal levels experienced high temperature conditions for a long-time interval causing a spread of the zircon (Ewing et al., 2013; Kunz et al., 2018) and monazite ages (Williams et al., 2022; Wyatt et al., 2022). At these temperatures the U–Pb system of zircon and monazite was partially reset whereas within titanite it was completely open until Triassic. Alternatively, a Triassic event caused a total reset of the titanite U–Pb record. The U–Pb data distribution strongly correlated with the position within the grain of titanite could reflect a volume diffusion process enhanced by deformation twins (e.g. Bonamici et al., 2015; Moser et al., 2022; Corvò et al., 2023; Kavanagh-Lepage et al., 2023) that are common features of both titanite types (Fig. 13B). At the high temperature stage of shearing the development of deformation twins promoted the evacuation of the radiogenic ions (e.g., Kavanagh-Lepage et al., 2023). The oldest lower intercept age obtained from the inner portions of titanite is partially overlapping the age of syn-kinematic monazite (i.e., MNZII: 222±8 and 238±8 Ma). This observation supports the alternative interpretation of the old lower intercept age marks the beginning of deformation. The U–Pb lower intercept age obtained from the external domains (rims/tips) partially showing evidence for intracrystalline deformation (localised higher dislocation density) of both titanite types (TTNIII in Fig. 13B) may thus reflect the end of volume diffusive loss of Pb and a localized deformation-induced isotopic reset (Stearns et al., 2015; Moser et al., 2022). Recently, Corvò et al. (2023) reported the same interpretation for titanite grains within the Anzola Shear Zone, that can be considered as the NE prolongation of the shear zone studied in this work.

In summary, titanite preserved the internal features (chemistry and zoning) from the Permian regional metamorphic event while the U–Pb data have no memory of it, recording mostly the deformation-induced resetting and volume diffusion. Several authors have recently described similar features studying titanite in sheared rocks (Kavanagh-Lepage et al., 2023; Corvò et al., 2023): deformation influenced the U–Pb system without promoting significant modification of titanite chemistry (geochemical decoupling).

7.5 Complementary behaviour of monazite and titanite

Combining the chemical, isotopic and microstructural features we recognised a contrasting behaviour of monazite and titanite that likely provided complementary information (Figs. 11-13). The former experienced an intense reactivity (CDP) during Triassic with the involvement of garnet (e.g., Y-enriched rims/domains/grains; MNZII on Fig. 13A). Locally, it developed internal features (chemistry, fractures, pores) suggesting a fluid assisted phase of isotopic perturbance during Jurassic (MNZIII on Fig. 13A). Monazite was also able to substantially preserve the age information relative to the prograde HT metamorphism, resulting thus partially resilient to the subsequent deformation events (MNZI on Fig. 13A).

Titanite on the contrary was almost chemically unreactive during deformation preserving the zoning features developed during the prograde metamorphism (chemical resiliency). On the other hand, titanite has not retained the age of the Permian HT metamorphism (TTNI? on Fig. 13B), as documented by monazite in this work and from literature (Bartoli et al., 2024; Cannop et al., 2024; Wyatt et al., 2022; Williams et al., 2022; Henk et al., 1997). A similar decoupling between chemistry and U–Pb isotopic data has been already described for titanite in amphibolite and calc-silicate (Holder & Hacker 2019; Kavanagh-Lepage et al., 2023; Corvò et al., 2023). Titanite demonstrated a more pronounced intracrystalline deformation, with respect to monazite, as documented by deformation twins across the grains and the localization of dislocations at rims/tips. These features could be responsible for the observed decoupling, allowing more efficiently the mobility of U and Pb isotopes (along the dislocation boundaries, e.g., Bonamici et al., 2015) with respect to the other trace elements. Moreover, in presence of abundant silicates surrounding titanite the deformation at the rim/tips is generally more intense and thus the U–Pb data of these domains might reflect both volume diffusion and recrystallization.

Combining the complementary information from the two investigated geochronometers and thanks to their different behaviour during shearing it has been possible to reconstruct the timing of the shear zone activity otherwise only partially recorded.

7.6 Regional implications: rift-related shear zone activity from Middle Triassic (Ladinian) to Early Jurassic (Sinemurian)

The Forno-Rosarolo shear zone developed within metasedimentary rocks characterised by metamorphic conditions at the transition between granulite and amphibolite facies (Redler et al., 2012; Kunz et al., 2014; Kunz & White, 2019; Simonetti et al., 2023). Deformation overprinted mainly paragneisses and metabasites, which experienced extensive partial melting during Permian time. Petrographic and microstructural observation on mylonitic paragneisses suggest that deformation developed under amphibolite facies conditions (~650 °C and ~0.55GPa; Simonetti et al., 2023). The rare occurrence of chlorite at the expense of biotite and the sillimanite replacement by white mica indicate that mylonites were poorly affected by green-schist retrograde overprint (Simonetti et al., 2023).

Integrating the U–Th–Pb data with textural, microstructural and chemical features of monazite, the activity of the shear zone can be constrained from two monazite generations. The main one, MNZII, documents the amphibolite facies ductile shearing with formation of tiny, syn-kinematic Y-rich monazite grains (238±8 Ma) and Y-rich rims (222±8 Ma) around old cores (MNZI: 314-250 Ma). This Triassic event represents the beginning of a syn-rift deformation that has been recorded at different crustal levels within the IVZ (e.g., Langone et al., 2018). During the late stage of the amphibolite-facies deformation, the interplay between deformation and fluids promoted the formation of the third generation of monazite (MNZIII; from 202±8 to 184±6 Ma) within sheared paragneisses and the formation of the rims/tips of titanite within the mylonitic calc-silicates (TTNIII; lower intercept age at 186±6 Ma). Both the last generation of monazite and the rim/tips of titanite can be attributed to the end of deformation under amphibolite facies condition across the Triassic-Jurassic boundary. It is interesting to note that recently a similar conclusion has been suggested by

Corvò et al. (2023) for the Anzola Shear Zone from the adjacent Ossola valley, i.e. a northeast prolongation of the studied shear zone.

8. CONCLUSIONS

The activity of the shear zone has been constrained at the Triassic-Jurassic time by combining geochemical and U–(Th)–Pb data from monazite and titanite within sheared migmatitic paragneisses and calc-silicates, respectively.

Monazite chemical and isotopic signature is directly affected by its deformation history. In protomylonitic paragneisses monazite preferentially retained ages related to the regional HT metamorphism (resiliency) whereas in mylonites it was more able to record the deformation events (reactivity). The Y-rich syn-kinematic domains/grains of monazite formed during Triassic (238 ± 8 – 222 ± 8 Ma) due to a CDP process coevally with the breakdown of garnet (releasing Y).

On the contrary, although titanite was almost chemically unreactive during deformation (resiliency), its U–Pb isotopic system was not able to retain the Permian regional metamorphism. The U–Pb data are correlated with textural and microstructural features. The titanite innermost domains provide a Triassic lower intercept age (240 ± 5 Ma) indicating a total isotopic reset at the beginning of deformation. This was favoured by the occurrence of deformation twins across the titanite grains acting as preferential pathways for the U and Pb isotopes. The rims/tips of titanite, partially overlapping the zone of accumulation of dislocations, define a Jurassic lower intercept age at 186±6 Ma. The entire U–Pb dataset is thus reflecting the combined effect of a deformation-induced volume diffusion and recrystallization.

The reconstructed timing of deformation suggests a strong causal relationship to the Triassic-Jurassic rifting event leading to the opening of the Alpine Tethys that affected the

Adria continental crust. Hence, mid crustal shear zones such as the one studied played a fundamental role in accommodating deformation.

Our study shows that combining age information from different geochronometers within different protoliths and/or showing different fabric (i.e., protomylonitic and mylonitic) allows to unveil the details of shear zone activity.

Acknowledgement

The following projects partially funded this research: PRIN2017 “Micro to Macro - how to unravel the nature of the large magmatic events” (20178LPCPW- Langone Antonio); Fondazione Cariplo, project "MADAM", grant n° 2024-0348 (Stefania Corvò).

References

AUSTRHEIM, H., 2013. Fluid and deformation induced metamorphic processes around Moho beneath continent collision zones: examples from the exposed root zone of the Caledonian mountain belt, W-Norway. *Tectonophysics* **609**, 620–635.

BARTOLI, O., LEOJ.MILLONIG, L.J., CARVALHO, B.B., MARSCHALL, H.R., GERDES, A., 2024. The Age of Granulite-Facies Metamorphism in the Ivrea–Verbano Zone (NW Italy) Determined Through In Situ U–Pb Dating of Garnet. *Journal of Petrology*, **65**, https://doi.org/10.1093/petrology/egae083

BEACH, A. 1976. The interrelations of fluid transport, deformation, geochemistry and heat flow in early Proterozoic shear zones in the Lewisian complex. *Philosophical Transactions for the Royal Society of London*. Series A, Mathematical and Physical Sciences, 569-604.

BELTRANDO, M., STOCKLI, D. F., DECARLIS, A., & MANATSCHAL, G. 2015. A crustal-scale view at rift localization along the fossil Adriatic margin of the Alpine Tethys preserved in NW Italy. *Tectonics*, **34(9)**, 1927–1951. https://doi.org/10.1002/2015TC003973

BERGEMANN, C. A., GNOS, E., BERGER, A., JANOTS, E., & WHITEHOUSE, M. J. 2020. Dating tectonic activity in the Lepontine Dome and Rhone-Simplon Fault regions through hydrothermal monazite-(Ce). *Solid Earth*, **11(1)**, 199–222. https://doi.org/10.5194/se-11-199-2020

BERTOLANI, M. 1968. Sguardo generale alla petrografia della Valle S trona (Novara). Guida all'escursione. Schweizerische Miner, Petr, Mitt, 48, 314-328.

BONAMICI, C.E., FANNING, C.M., KOZDON, R., FOURNELLE, J.H., VALLEY, J.W., 2015. Combined oxygen-isotope and U-Pb zoning studies of titanite: new criteria for age preservation. *Chemical Geology* **398**, 70–84. https://doi.org/10.1016/j.chemgeo.2015.02.002

BORIANI, A., BURLINI, L., & SACCHI, R. 1990. The Cossato-Mergozzo-Brissago Line and the Pogallo Line (Southern Alps, Northern Italy) and their relationships with the late-Hercynian magmatic and metamorphic events. Tectonophysics, 182(1–2), 91–102. https://doi.org/10.1016/0040-1951(90)90344-8

BORIANI, A. C., & VILLA, I. M. 1997. Geochronology of regional metamorphism in the Ivrea-Verbano Zone and Serie dei Laghi, Italian Alps. *Schweiz. Mineral., Petrogr. Mitt.* **77**, 381-401. https://doi.org/10.5169/SEALS-58492

BOSSE, V., & VILLA, I. M. 2019. Petrochronology and hygrochronology of tectono-metamorphic events. *Gondwana Research*, **71**, 76-90.

BRODIE, K. H. 1981. Variation in amphibole and plagioclase composition with deformation. *Tectonophysics*, **78(1–4)**, 385–402. https://doi.org/10.1016/0040-1951(81)90021-4

BRODIE, K. H., & RUTTER, E. H. 1987. Deep crustal extensional faulting in the Ivrea Zone of Northern Italy. *Tectonophysics*, **140(2–4)**, 193–212. https://doi.org/10.1016/0040-1951(87)90229-0

BRODIE, K. H., RUTTER, E. H., & REX, D. 1989. On the age of deep crustal extensional faulting in the Ivrea zone, northern Italy. *Geological Society, London, Special Publications*, **45**, 203–210. https://doi.org/10.1144/GSL.SP.1989.045.01.11

CAROSI, R., MONTOMOLI, C., IACCARINO, S., BENETTI, B., PETROCCIA, A., & SIMONETTI, M. 2022. Constraining the Timing of Evolution of Shear Zones in Two Collisional Orogens: Fusing Structural Geology and Geochronology. *Geosciences*, **12(6)**, 231. https://doi.org/10.3390/geosciences12060231

CARVALHO, B. B., BARTOLI, O., FERRI, F., CESARE, B., FERRERO, S., REMUSAT, L., CAPIZZI, L. S., & POLI, S., 2019. Anatexis and fluid regime of the deep continental crust: New clues from melt and fluid inclusions in metapelitic migmatites from Ivrea Zone (NW Italy). *Journal of Metamorphic Geology*, **37(7)**, 951–975. https://doi.org/10.1111/jmg.12463

975 CHERNIAK, D. J., 1993. Lead diffusion in titanite and preliminary results on the effects of radiation damage on Pb transport. *Chemical Geology*, **110(1–3)**, 177–194. https://doi.org/10.1016/0009-2541(93)90253-F

978

979 CONNOP, C.H., SMYE, A.J., GARBER, J.M., MOSER, A.C., CADDICK, M.J., VERVOORT, J.D., 2024. Assembly of lower continental crust: A garnet Lu-Hf petrochronological investigation of the Ivrea-Verbano Zone, Italy. *Earth Planet. Sci. Lett.,* **634**, https://doi.org/10.1016/j.epsl.2024.118677

983

984 CORVÒ, S., LANGONE, A., PADRÓN-NAVARTA, J. A., TOMMASI, A., & ZANETTI, A. 2020. Porphyroclasts: Source and Sink of Major and Trace Elements During Deformation-Induced Metasomatism (Finero, Ivrea-Verbano Zone, Italy). *Geosciences*, **10(5)**, 196. https://doi.org/10.3390/geosciences10050196

988

989 CORVÒ, S., MAINO, M., PIAZOLO, S., SENO, S., & LANGONE, A. 2022. Role of inherited compositional and structural heterogeneity in shear zone development at mid-low levels of the continental crust (the Anzola shear zone; Ivrea-Verbano Zone, Southern Alps). *Lithos*, **422–423**, 106745. https://doi.org/10.1016/j.lithos.2022.106745

993

994 CORVÒ S., MAINO M., PIAZOLO S., KYLANDER-CLARK A. R.C., SENO S., LANGONE A. 2023. Crystal plasticity and fluid availability govern the ability of titanite to record the age of deformation. *Earth and Planetary Science Letters*, **620(C)**, 118349. https://doi.org/10.1016/j.epsl.2023.118349

998

CORVÒ, S., KYLANDER-CLARK, A. R., & LANGONE, A. 2024. Titanite petrochronological data across the continental crust section exposed in Val d'Ossola (Ivrea-Verbano Zone, Italy). *Data in Brief*, **56**, https://doi.org/10.1016/j.dib.2024.110804.

CRUZ, M.J., CUNHA, J.C., MERLET, C. & SABATÉ, P., 1996. Datação punctual das monazitas das região de Itambé, Bahia, através da microssonda electrônica. XXXIX Congresso Brasileiro de Geologia, vol. 2 Sociedade Brasileira de Geologià-Núcleo, Bahià-Segipe, pp. 206–209.

CRUZ-URIBE, A.M., FEINEMAN, M.D., ZACK, T. & BARTH, M. 2014. Metamorphic reaction rates at ~650-800°C from diffusion of niobium in rutile. *Geochim. Cosmochim. Ac.*, **130**, 63-77, https://doi.org/10.1016/j.gca.2013.12.015

DEGLI ALESSANDRINI, G. 2018. Deformation mechanisms and strain localization in the mafic continental lower crust. School Geogr. Earth Environ. Sci. Univ. Plymouth. Published thesis.

DIDIER, A., BOSSE, V., CHERNEVA, Z., GAUTIER, P., GEORGIEVA, M., PAQUETTE, J. L., & GERDJIKOV, I. 2014. Syn-deformation fluid-assisted growth of monazite during renewed high-grade metamorphism in metapelites of the Central Rhodope (Bulgaria, Greece). *Chemical Geology*, **381**, 206-222.

DI VINCENZO, G., CAROSI, R., PALMERI, R., & TIEPOLO, M. 2007. A comparative U-Th-Pb (zircon-monazite) and 40Ar-39Ar (muscovite-biotite) study of shear zones in northern Victoria Land (Antarctica): Implications for geochronology and localized reworking of the

Ross Orogen. *Journal of Metamorphic Geology*, **25(6)**, 605–630. https://doi.org/10.1111/j.1525-1314.2007.00717.x

ENGI, M. (2017). Petrochronology Based on REE-Minerals: Monazite, Allanite, Xenotime, Apatite. *Reviews in Mineralogy and Geochemistry*, **83(1)**, 365–418. https://doi.org/10.2138/rmg.2017.83.12

ERICKSON, T. M., PEARCE, M. A., TAYLOR, R. J. M., TIMMS, N. E., CLARK, C., REDDY, S. M., & BUICK, I. S. 2015. Deformed monazite yields high-temperature tectonic ages. *Geology*, **43(5)**, 383–386. https://doi.org/10.1130/G36533.1

EWING, T. A., HERMANN, J., & RUBATTO, D. 2013. The robustness of the Zr-in-rutile and Ti-in-zircon thermometers during high-temperature metamorphism (Ivrea-Verbano Zone, northern Italy). *Contributions to Mineralogy and Petrology*, **165(4)**, 757–779. https://doi.org/10.1007/s00410-012-0834-5

EWING, T. A., RUBATTO, D., BELTRANDO, M., & HERMANN, J. 2015. Constraints on the thermal evolution of the Adriatic margin during Jurassic continental break-up: U–Pb dating of rutile from the Ivrea–Verbano Zone, Italy. *Contributions to Mineralogy and Petrology*, **169(4)**, 44. https://doi.org/10.1007/s00410-015-1135-6

FÖRSTER, H.-J. 1998. The chemical composition of REE-Y-Th-U-rich accessory minerals in peraluminous granites of the Erzgebirge-Fichtelgebirge region, Germany; Part I, The monazite-(Ce)-brabantite solid solution series. *American Mineralogist*, **83(3–4)**, 259–272. https://doi.org/10.2138/am-1998-3-409

FROST, B. R., CHAMBERLAIN, K. R., & SCHUMACHER, J. C. 2001. Sphene (titanite): Phase relations and role as a geochronometer. *Chemical Geology*, **172(1–2)**, 131–148. https://doi.org/10.1016/S0009-2541(00)00240-0

GARDE, A.A., BORIANI, A., SØRENSEN, E.V., 2015. Crustal modelling of the Ivrea–Verbano zone in northern Italy re-examined: coseismic cataclasis versus extensional shear zones and sideways rotation. *Tectonophysics,* **662**, 291–311. https://doi.org/10.1016/j.tecto.2015.04.003

GORDON, S. M., KIRKLAND, C. L., REDDY, S. M., BLATCHFORD, H. J., WHITNEY, D. L., TEYSSIER, C., EVANS, N. J., & MCDONALD, B. J. 2021. Deformation-enhanced recrystallization of titanite drives decoupling between U-Pb and trace elements. *Earth and Planetary Science Letters*, **560**, 116810. https://doi.org/10.1016/j.epsl.2021.116810

GRAND'HOMME, A., JANOTS, E., SEYDOUX-GUILLAUME, A.-M., GUILLAUME, D., BOSSE, V., MAGNIN, V., 2016. Partial resetting of the U-Th-Pb systems in experimentally altered monazite: Nanoscale evidence of incomplete replacement. Geology G37770.1.

GUERGOUZ, C., MARTIN, L., VANDERHAEGHE, O., THÉBAUD, N., & FIORENTINI, M. 2018. Zircon and monazite petrochronologic record of prolonged amphibolite to granulite facies metamorphism in the Ivrea-Verbano and Strona-Ceneri Zones, NW Italy. *Lithos*, **308–309**, 1–18. https://doi.org/10.1016/j.lithos.2018.02.014

HARLOV, D. E., WIRTH, R., & HETHERINGTON, C. J. 2011. Fluid-mediated partial alteration in monazite: The role of coupled dissolution–reprecipitation in element redistribution and mass transfer. *Contributions to Mineralogy and Petrology*, **162(2)**, 329–348. https://doi.org/10.1007/s00410-010-0599-7

HARTNADY, M. I. H., KIRKLAND, C. L., CLARK, C., SPAGGIARI, C. V., SMITHIES, R. H., EVANS, N. J., & MCDONALD, B. J. 2019. Titanite dates crystallization: Slow Pb diffusion during super-solidus re-equilibration. *Journal of Metamorphic Geology*, **37(6)**, 823–838. https://doi.org/10.1111/jmg.12489

HAYDEN, L.A., WATSON, E.B. & WARK, D.A. 2008. A thermobarometer for sphene (titanite). *Contrib. Mineral. Petrol.*, **155**, 529–540, DOI 10.1007/s00410-007-0256-y

HENTSCHEL, F., JANOTS, E., TREPMANN, C.A., MAGNIN, V., LANARI, P., 2020. Corona formation around monazite and xenotime during greenschist-facies metamorphism and deformation. Eur. J. Mineral. 32, 521–544.

HENK, A., FRANZ, L., TEUFEL, S., & ONCKEN, O. 1997. Magmatic Underplating, Extension, and Crustal Reequilibration: Insights From A Cross-Section Through the Ivrea Zone and Strona-Ceneri Zone, Northern Italy. *The Journal of Geology*, **105(3)**, 367–378. https://doi.org/10.1086/515932

HETHERINGTON, C. J., BACKUS, E. L., MCFARLANE, C. R. M., FISHER, C. M., & PEARSON, D. G. 2017. Origins of Textural, Compositional, and Isotopic Complexity in Monazite and Its Petrochronological Analysis. In *Microstructural Geochronology Planetary Records Down to Atom Scale* (eds. D. E. Moser, F. Corfu, J. R. Darling, S. M. Reddy, & K. Tait), Geophysical Monograph Series, pp. 63–90. John Wiley & Sons, Inc. https://doi.org/10.1002/9781119227250.ch3

HODGES, K. V., & FOUNTAIN, D. M. 1984. Pogallo Line, South Alps, northern Italy: An intermediate crustal level, low-angle normal fault? *Geology*, **12**, 151-155.

HOLDER, R. M., & HACKER, B. R. (2019). Fluid-driven resetting of titanite following ultrahigh-temperature metamorphism in southern Madagascar. *Chemical Geology*, **504**, 38–52. https://doi.org/10.1016/j.chemgeo.2018.11.017

HOLDER, R. M., HACKER, B. R., SEWARD, G. G. E., & KYLANDER-CLARK, A. R. C. 2019. Interpreting titanite U–Pb dates and Zr thermobarometry in high-grade rocks: Empirical constraints on elemental diffusivities of Pb, Al, Fe, Zr, Nb, and Ce. *Contributions to Mineralogy and Petrology*, **174(5)**, 42. https://doi.org/10.1007/s00410-019-1578-2

JANOTS, E., BERGER, A., GNOS, E., WHITEHOUSE, M., LEWIN, E., PEQKE, T., 2012. Constraints on fluid evolution during metamorphism from U–Th–Pb systematics in Alpine hydrothermal monazite. Chem. Geol. 326–327, 61–71.

JANOTS, E., ENGI, M., BERGER, A., ALLAZ, J., SCHWARZ, J.-O., SPANDLER, C., 2008. Prograde metamorphic sequence of REE minerals in pelitic rocks of the Central Alps: implications for allanite-monazite-xenotime phase relations from 250 to 610 degrees C. J. Metamorph. Geol. 26, 509–526.

KARAKAS, O., WOTZLAW, J.F., GUILLONG, M., ULMER, P., BRACK, P., ECONOMOS, R., BERGANTZ, G. W., SINIGOI, S., BACHMANN, O., 2019. The pace of crustal-scale magma accretion and differentiation beneath silicic caldera volcanoes. *Geology* **47**, 719–723.

KAVANAGH-LEPAGE, C., GERVAIS, F., LARSON, K., GRAZIANI, R., & MOUKHSIL, A. 2023. Deformation induced decoupling between U-Pb and trace elements in titanite revealed through petrochronology and study of localized deformation. *Geoscience Frontiers*, **14(2)**, 101496. https://doi.org/10.1016/j.gsf.2022.101496

KENKMANN, T. 2000. Processes controlling the shrinkage of porphyroclasts in gabbroic shear zones. *Journal of Structural Geology*, **22(4)**, 471–487. https://doi.org/10.1016/S0191-8141(99)00177-7

KENKMANN, T., & DRESEN, G. 2002. Dislocation microstructure and phase distribution in a lower crustal shear zone – an example from the Ivrea-Zone, Italy. *International Journal of Earth Sciences*, **91(3)**, 445–458. https://doi.org/10.1007/s00531-001-0236-9

KIRKLAND, C.L., YAKYMCHUK, C., GARDINER, N.J., SZILAS, K., HOLLIS, J., OLIEROOK, H., STEENFELT, A. 2020. Titanite petrochronology linked to phase equilibrium modelling constrains tectono-thermal events in the Akia Terrane, West Greenland. *Chemical Geology* **536**, 119467

KIRKLAND, C. L., OLIEROOK, H. K. H., DANIŠÍK, M., LIEBMANN, J., HOLLIS, J., RIBEIRO, B. V., & RANKENBURG, K. 2023. Dating mylonitic overprinting of ancient rocks. *Communications Earth & Environment,* **4(1)**, 47. https://doi.org/10.1038/s43247-023-00709-5

KLEMME, S., PROWATKE, S., MÜNKER, C., MAGEE, C.W., LAHAYE, Y., ZACK, T., KASEMANN, S.A., CABATO, E.J.A. & KAESER, B. 2008. Synthesis and Preliminary

Characterisation of New Silicate, Phosphate and Titanite Reference Glasses. *Geostandards and Geoanalytical Research*, **32**, 1, 39-54

KLÖTZLI, U.S., SINIGOI, S., QUICK, J.E., DEMARCHI, G., TASSINARI, C.C., SATO, K., GÜNES, Z., 2014. Duration of igneous activity in the Sesia Magmatic System and implications for high-temperature metamorphism in the Ivrea–Verbano deep crust. *Lithos* **206**,19–33.

KOHN, M. J. 2016. Metamorphic chronology—a tool for all ages: Past achievements and future prospects. *American Mineralogist*, **101(1)**, 25–42. https://doi.org/10.2138/am-2016-5146

KOHN, M. J. 2017. Titanite Petrochronology. *Reviews in Mineralogy and Geochemistry*, **83(1)**, 419–441. https://doi.org/10.2138/rmg.2017.83.13

KOHN, M. J., ENGI, M., LANARI, P., & SWAINSON, I. (Eds.). (2017). *Petrochronology: Methods and applications*. The Mineralogical Society of America.

KUNZ, B. E., JOHNSON, T. E., WHITE, R. W., & REDLER, C. 2014. Partial melting of metabasic rocks in Val Strona di Omegna, Ivrea Zone, northern Italy. *Lithos*, **190–191**, 1–12. https://doi.org/10.1016/j.lithos.2013.11.015

KUNZ, B. E., REGIS, D., & ENGI, M. 2018. Zircon ages in granulite facies rocks: Decoupling from geochemistry above 850 °C? *Contributions to Mineralogy and Petrology*, **173(3)**, 26. https://doi.org/10.1007/s00410-018-1454-5

KUNZ, B. E., & WHITE, R. W. 2019. Phase equilibrium modelling of the amphibolite to granulite facies transition in metabasic rocks (Ivrea Zone, NW Italy). *Journal of Metamorphic Geology*, **37(7)**, 935–950. https://doi.org/10.1111/jmg.12478

LANGONE, A., BRAGA, R., MASSONNE, H.-J., & TIEPOLO, M. 2011. Preservation of old (prograde metamorphic) U–Th–Pb ages in unshielded monazite from the high-pressure paragneisses of the Variscan Ulten Zone (Italy). *Lithos*, **127(1–2)**, 68–85. https://doi.org/10.1016/j.lithos.2011.08.007

LANGONE, A., ZANETTI, A., DACZKO, N. R., PIAZOLO, S., TIEPOLO, M., & MAZZUCCHELLI, M. 2018. Zircon U-Pb Dating of a Lower Crustal Shear Zone: A Case Study From the Northern Sector of the Ivrea-Verbano Zone (Val Cannobina, Italy). *Tectonics*, **37(1)**, 322–342. https://doi.org/10.1002/2017TC004638

LINTHOUT, K. 2007. Tripartite division of the system 2REEPO4—CaTh(po4)2 – 2ThSiO4, discreditation of brabantite, and recognition of cheralite as the name for members dominated by CaTh(PO4)2. *The Canadian Mineralogist*, **45(3)**, 503–508. https://doi.org/10.2113/gscanmin.45.3.503

MANATSCHAL, G., MÜNTENER, O., LAVIER, L. L., MINSHULL, T. A., & PÉRON-PINVIDIC, G. 2007. Observations from the Alpine Tethys and Iberia–Newfoundland margins pertinent to the interpretation of continental breakup. *Geological Society, London, Special Publications*, **282(1)**, 291–324. https://doi.org/10.1144/SP282.14

MCDONOUGH, W.F. & SUN, S.S. 1995. The composition of the Earth. *Chem. Geol.,* **120 (3–4)**, 223–253.

MCGREGOR, M., ERICKSON, T. M., SPRAY, J. G., & WHITEHOUSE, M. J. 2021. High-resolution EBSD and SIMS U–Pb geochronology of zircon, titanite, and apatite: Insights from the Lac La Moinerie impact structure, Canada. *Contributions to Mineralogy and Petrology*, **176(10)**, 76. https://doi.org/10.1007/s00410-021-01828-y

MOHN, G., MANATSCHAL, G., BELTRANDO, M., MASINI, E., & KUSZNIR, N. 2012. Necking of continental crust in magma-poor rifted margins: Evidence from the fossil Alpine Tethys margins: Necking Of Continental Crust. *Tectonics*, **31(1)**, https://doi.org/10.1029/2011TC002961

MOSER, A. C., HACKER, B. R., GEHRELS, G. E., SEWARD, G. G. E., KYLANDER-CLARK, A. R. C., & GARBER, J. M. 2022. Linking titanite U–Pb dates to coupled deformation and dissolution–reprecipitation. *Contributions to Mineralogy and Petrology*, **177(3)**, 42. https://doi.org/10.1007/s00410-022-01906-9

MOTTRAM, C.M. & COTTLE J.M., 2024. An electron backscatter diffraction study of monazite: Linking the time-deformation path. *Chemical Geology* **663**, 122238

MULCH, A., COSCA, M., & HANDY, M. 2002. In-situ UV-laser 40Ar/39Ar geochronology of a micaceous mylonite: An example of defect-enhanced argon loss. *Contributions to Mineralogy and Petrology*, **142(6)**, 738–752. https://doi.org/10.1007/s00410-001-0325-6

OBERTI, R., SMITH, D.C., ROSSI, G. & CAUCIA, F., (1981). The crystal-chemistry of high-aluminium titanites. *Eur. J. Mineral.*, 777–792.

OLIEROOK, H. K. H., TAYLOR, R. J. M., ERICKSON, T. M., CLARK, C., REDDY, S. M., KIRKLAND, C. L., JAHN, I., & BARHAM, M. 2019. Unravelling complex geologic histories using U–Pb and trace element systematics of titanite. *Chemical Geology*, **504**, 105–122. https://doi.org/10.1016/j.chemgeo.2018.11.004

ORIOLO, S., WEMMER, K., OYHANTÇABAL, P., FOSSEN, H., SCHULZ, B., & SIEGESMUND, S. 2018. Geochronology of shear zones – A review. *Earth-Science Reviews*, **185**, 665–683. https://doi.org/10.1016/j.earscirev.2018.07.007

PAPAPAVLOU, K., DARLING, J. R., STOREY, C. D., LIGHTFOOT, P. C., MOSER, D. E., & LASALLE, S., 2017. Dating shear zones with plastically deformed titanite: New insights into the orogenic evolution of the Sudbury impact structure (Ontario, Canada). *Precambrian Research*, **291**, 220–235. https://doi.org/10.1016/j.precamres.2017.01.007

PARRISH, R. R. 1990. U–Pb dating of monazite and its application to geological problems. *Canadian Journal of Earth Sciences*, **27(11)**, 1431–1450. https://doi.org/10.1139/e90-152

PERESSINI, G., QUICK, J.E., SINIGOI, S., HOFMANN, A.W., FANNING, M., 2007. Duration of a large mafic intrusion and heat transfer in the lower crust: a SHRIMP U-Pb zircon study in the Ivrea-Verbano Zone (Western Alps, Italy). *J. Petrol.* **48**, 1185–1218.

PETRI, B., DURETZ, T., MOHN, G., SCHMALHOLZ, S. M., KARNER, G. D., & MÜNTENER, O. 2019. Thinning mechanisms of heterogeneous continental lithosphere. *Earth and Planetary Science Letters*, **512**, 147–162. https://doi.org/10.1016/j.epsl.2019.02.007

PIAZOLO, S., AUSTRHEIM, H. & WHITEHOUSE, M. 2012. Brittle-ductile microfabrics in naturally deformed zircon: deformation mechanisms and consequences for U–Pb dating. *American Mineralogist*, **97(10)**, 1544–1563.

PUTNIS, A., JANSSEN, A., JAMTVEIT, B., & PUTNIS, C. V., 2009. Reaction-induced fracturing during replacement reactions. Geochimica et Cosmochimica Acta Supplement, **73**, A1061.

QUICK, J. E., SINIGOI, S., SNOKE, A. W., KALAKAY, T. J., MAYER, A., & PERESSINI, G. 2002. Geologic map of the southern Ivrea-Verbano zone, northwestern Italy. https://doi.org/10.3133/i2776

RAPA, G., GROPPO, C., ROLFO, F., PETRELLI, M., MOSCA, P., & PERUGINI, D., 2017. Titanite-bearing calc-silicate rocks constrain timing, duration and magnitude of metamorphic CO_2 degassing in the Himalayan belt. *Lithos*, **292–293**, 364–378. https://doi.org/10.1016/j.lithos.2017.09.024

RASMUSSEN, B., & MUHLING, J. R. 2007. Monazite begets monazite: Evidence for dissolution of detrital monazite and reprecipitation of syntectonic monazite during low-grade regional metamorphism. *Contributions to Mineralogy and Petrology*, **154(6)**, 675–689. https://doi.org/10.1007/s00410-007-0216-6

REDLER, C., JOHNSON, T. E., WHITE, R. W., & KUNZ, B. E. 2012. Phase equilibrium constraints on a deep crustal metamorphic field gradient: Metapelitic rocks from the Ivrea Zone (NW Italy). *Journal of Metamorphic Geology,* **30(3)**, 235–254. https://doi.org/10.1111/j.1525-1314.2011.00965.x

REGIS, D., WARREN, C. J., MOTTRAM, C. M., & ROBERTS, N. M. W. 2016. Using monazite and zircon petrochronology to constrain the P—T—T evolution of the middle crust in the Bhutan Himalaya. *Journal of Metamorphic Geology*, **34(6)**, 617–639. https://doi.org/10.1111/jmg.12196

RUBATTO, D., HERMANN, J., & BUICK, I. S. 2006. Temperature and Bulk Composition Control on the Growth of Monazite and Zircon During Low-pressure Anatexis (Mount Stafford, Central Australia). *Journal of Petrology*, **47(10)**, 1973–1996. https://doi.org/10.1093/petrology/egl033

RUTTER, E., BRODIE, K., JAMES, T., & BURLINI, L. 2007. Large-scale folding in the upper part of the Ivrea-Verbano zone, NW Italy. *Journal of Structural Geology*, **29(1)**, 1–17. https://doi.org/10.1016/j.jsg.2006.08.013

SCHMID, R., & WOOD, B. J. 1976. Phase relationships in granulitic metapelites from the Ivrea-Verbano zone (Northern Italy). *Contributions to Mineralogy and Petrology*, **54(4)**, 255–279. https://doi.org/10.1007/BF00389407

SCHMID, S. M. 1993. Ivrea Zone and Adjacent Southern Alpine Basement. *In Pre-Mesozoic Geology in the Alps* (eds J. F. von Raumer & F. Neubauer), pp. 567–583. Springer Berlin Heidelberg. https://doi.org/10.1007/978-3-642-84640-3_33

SCHULZ, B. 2021. Petrochronology of Monazite-Bearing Garnet Micaschists as a Tool to Decipher the Metamorphic Evolution of the Alpine Basement. *Minerals*, **11(9)**, 981. https://doi.org/10.3390/min11090981

SCHUSTER, R., STÜWE, K., 2021. Permian metamorphic event in the Alps. *Geology*, **36**, 603-606.

SCIBIORSKI, E., KIRKLAND, C. L., KEMP, A. I. S., TOHVER, E., & EVANS, N. J. 2019. Trace elements in titanite: A potential tool to constrain polygenetic growth processes and timing. *Chemical Geology*, **509**, 1–19. https://doi.org/10.1016/j.chemgeo.2019.01.006

SEYDOUX-GUILLAUME, A.-M., GONCALVES, P., WIRTH, R., & DEUTSCH, A. 2003. Transmission electron microscope study of polyphase and discordant monazites: Site-specific specimen preparation using the focused ion beam technique. *Geology*, **31(11)**, 973. https://doi.org/10.1130/G19582.1

SEYDOUX-GUILLAUME, A. M., PAQUETTE, J. L., WIEDENBECK, M., MONTEL, J. M., & HEINRICH, W. 2002. Experimental resetting of the U–Th–Pb systems in monazite. Chemical Geology, 191(1-3), 165-181. https://doi.org/10.1016/S0009-2541(02)00155-9

SHAW, C. A., KARLSTROM, K. E., WILLIAMS, M. L., JERCINOVIC, M. J., & MCCOY, A. M. 2001. Electron-microprobe monazite dating of ca. 1.71–1.63 Ga and ca. 1.45–1.38 Ga deformation in the Homestake shear zone, Colorado: Origin and early evolution of a persistent intracontinental tectonic zone. *Geology*, **29(8)**, 739. https://doi.org/10.1130/0091-7613(2001)029<0739:EMMDOC>2.0.CO;2

SIEGESMUND, S., LAYER, P., DUNKL, I., VOLLBRECHT, A., STEENKEN, A., WEMMER, K., & AHRENDT, H. 2008. Exhumation and deformation history of the lower crustal section of the Valstrona di Omegna in the Ivrea Zone, southern Alps. *Geological Society, London, Special Publications*, **298(1)**, 45–68. https://doi.org/10.1144/SP298.3

SIMONETTI, M., CAROSI, R., MONTOMOLI, C., COTTLE, J. M., & LAW, R. D. 2020. Transpressive Deformation in the Southern European Variscan Belt: New Insights From the Aiguilles Rouges Massif (Western Alps). *Tectonics*, **39(6)**. https://doi.org/10.1029/2020TC006153

SIMONETTI, M., CAROSI, R., MONTOMOLI, C., LAW, R. D., & COTTLE, J. M. 2021b. Unravelling the development of regional-scale shear zones by a multidisciplinary approach: The case study of the Ferriere-Mollières Shear Zone (Argentera Massif, Western Alps). *Journal of Structural Geology*, **149**, 104399. https://doi.org/10.1016/j.jsg.2021.104399

SIMONETTI, M., LANGONE, A., CORVÒ, S., & BONAZZI, M. 2021a. Triassic-Jurassic rift-related deformation and temperature-time evolution of the fossil Adriatic margin: a review from Ossola and Strona di Omegna valleys (Ivrea-Verbano Zone). *Ofioliti*, **46(2)**. https://doi.org/10.4454/ofioliti.v46i2.544

SIMONETTI, M., LANGONE, A., BONAZZI, M., CORVÒ, S., & MAINO, M. 2023. Tectono-metamorphic evolution of a post-variscan mid-crustal shear zone in relation to the Tethyan rifting (Ivrea-Verbano Zone, Southern Alps). *Journal of Structural Geology*, **173**, 104896. https://doi.org/10.1016/j.jsg.2023.104896

SINIGOI, S., QUICK, J. E., MAYER, A., & BUDAHN, J. 1996. Influence of stretching and density contrasts on the chemical evolution of continental magmas: An example from the

Ivrea-Verbano Zone. *Contributions to Mineralogy and Petrology*, **123(3)**, 238–250. https://doi.org/10.1007/s004100050153

SKRZYPEK, E., KATO, T., KAWAKAMI, T., SAKATA, S., HATTORI, K., HIRATA, T., & IKEDA, T. 2018. Monazite behaviour and time-scale of metamorphic processes along a low-pressure/high-temperature field gradient (Ryoke Belt, SW Japan). *Journal of Petrology*, **59(6)**, 1109-1144.

SPANDLER, C., HAMMERLI, J., SHA, P., HILBERT-WOLF, H., HU, Y., ROBERTS, E., & SCHMITZ, M. 2016. MKED1: a new titanite standard for in situ analysis of Sm–Nd isotopes and U–Pb geochronology. *Chemical Geology*, **425**, 110-126.

SPEAR, F. S., & PYLE, J. M. 2010. Theoretical modeling of monazite growth in a low-Ca metapelite. *Chemical Geology*, **273(1–2)**, 111–119. https://doi.org/10.1016/j.chemgeo.2010.02.016

STACEY, J.S., & KRAMERS, J.D., 1975. Approximation of terrestrial lead isotope evolution by a two-stage model. *Earth Planet Sci Lett* **26**, 207–221.

STEARNS, M.A., HACKER, B.R., RATSCHBACHER, L., RUTTE, D. & KYLANDER-CLARK, A.R.C., 2015. Titanite petrochronology of the Pamir gneiss domes: implications for middle to deep crust exhumation and titanite closure to Pb and Zr diffusion. *Tectonics* **34(4)**, 784–802. https://doi.org/10.1002/2014TC003774

TAYLOR, R. J. M., CLARK, C., FITZSIMONS, I. C. W., SANTOSH, M., HAND, M., EVANS, N., & MCDONALD, B. 2014. Post-peak, fluid-mediated modification of granulite facies zircon and monazite in the Trivandrum Block, southern India. *Contributions to Mineralogy and Petrology*, **168(2)**, 1044. https://doi.org/10.1007/s00410-014-1044-0

TERRY, M. P., ROBINSON, P., HAMILTON, M. A., & JERCINOVIC, M. J. 2000. Monazite geochronology of UHP and HP metamorphism, deformation, and exhumation, Nordøyane, Western Gneiss Region, Norway. *American Mineralogist*, **85(11–12)**, 1651–1664. https://doi.org/10.2138/am-2000-11-1208

TIMMS, N.E., PEARCE, M.A., ERICKSON, T.M., CAVOSIE, A.J., RAE, A.S., WHEELER, J., WITTMANN, A., FERRIÈERE, L., POELCHAU, M.H., TOMIOKA, N., COLLINS, G.S., GULICK, P.S., RASMUSSEN, C. & MORGAN, J.V., 2019. New shock microstructures in titanite (CaTi-SiO5) from the peak ring of the Chicxulub impact structure, Mexico. *Contrib. Mineral. Petrol.* **174 (5)**, 1–23.

VAN ACTHERBERGH, E. 2001. Data reduction software for LA-ICP-MS. Laser Ablation-ICP-mass spectrometry in the earth sciences: principles and applications, 239-243.

VARGA, J., RAIMONDO, T., DACZKO, N. R., & ADAM, J. 2020. Experimental alteration of monazite in granitic melt: Variable U–Th–Pb and REE mobility during melt-mediated coupled dissolution-precipitation. *Chemical Geology*, **544**, 119602. https://doi.org/10.1016/j.chemgeo.2020.119602

VAVRA, G., SCHMID, R., & GEBAUER, D. 1999. Internal morphology, habit and U-Th-Pb microanalysis of amphibolite-to-granulite facies zircons: Geochronology of the Ivrea Zone (Southern Alps). *Contributions to Mineralogy and Petrology*, **134(4)**, 380–404. https://doi.org/10.1007/s004100050492

VERMEESCH, P. 2018. IsoplotR: A free and open toolbox for geochronology. *Geoscience Frontiers*, **9(5)**, 1479–1493. https://doi.org/10.1016/j.gsf.2018.04.001

WALTERS, J. B., CRUZ-URIBE, A. M., SONG, W. J., GERBI, C., & BIELA, K. 2022. Strengths and limitations of in situ U–Pb titanite petrochronology in polymetamorphic rocks: An example from western Maine, USA. *Journal of Metamorphic Geology*, **40(6)**, 1043–1066. https://doi.org/10.1111/jmg.12657

WAWRZENITZ, N., KROHE, A., RHEDE, D., & ROMER, R. L. 2012. Dating rock deformation with monazite: The impact of dissolution precipitation creep. *Lithos*, **134–135**, 52–74. https://doi.org/10.1016/j.lithos.2011.11.025

WEINBERG, R. F., WOLFRAM, L. C., NEBEL, O., HASALOVÁ, P., ZÁVADA, P., KYLANDER-CLARK, A. R. C., & BECCHIO, R. 2020. Decoupled U-Pb date and chemical zonation of monazite in migmatites: The case for disturbance of isotopic systematics by coupled dissolution-reprecipitation. *Geochimica et Cosmochimica Acta*, **269**, 398–412. https://doi.org/10.1016/j.gca.2019.10.024

WHEELER, J., MARIANI, E., PIAZOLO, S., PRIOR, D.J., TRIMBY, P. & DRURY, M.R., 2009. The weighted Burgers vector: a new quantity for constraining dislocation densities and types using Electron Backscatter Diffraction on 2D sections through crystalline materials. *J. Microsc.* **233 (3)**, 482–494.

WHEELER, J., PIAZOLO, S., PRIOR, D.J., TRIMBY, P. & TIELKE, J.A., 2024. Using crystal-lattice distortion data for geological investigations: the weighted Burgers vector method. *Journal of Structural Geology* **179**, 105040

WHITNEY, D.L. & EVANS, B.W., 2010. Abbreviations for names of rock-forming minerals. *Am. Mineral*. **95 (1)**, 185–187.

WILLIAMS, M. A., KELSEY, D. E., & RUBATTO, D. 2022. Thorium zoning in monazite: A case study from the Ivrea–Verbano zone, NW Italy. *Journal of Metamorphic Geology*, **40(6)**, 1015–1042. https://doi.org/10.1111/jmg.12656

WILLIAMS, M. A., KELSEY, D. E., BAGGS, T., HAND, M., & ALESSIO, K. L. 2018. Thorium distribution in the crust: Outcrop and grain-scale perspectives. *Lithos*, **320**, 222-235.

WILLIAMS, M. L., & JERCINOVIC, M. J. 2002. Microprobe monazite geochronology: Putting absolute time into microstructural analysis. *Journal of Structural Geology*, **24**(6–7), 1013–1028. https://doi.org/10.1016/S0191-8141(01)00088-8

WILLIAMS, M. L., & JERCINOVIC, M. J. 2012. Tectonic interpretation of metamorphic tectonites: Integrating compositional mapping, microstructural analysis and *in situ* monazite dating. *Journal of Metamorphic Geology*, **30(7)**, 739–752. https://doi.org/10.1111/j.1525-1314.2012.00995.x

WOLFF, R., DUNKL, I., KIESSELBACH, G., WEMMER, K., & SIEGESMUND, S. 2012. Thermochronological constraints on the multiphase exhumation history of the Ivrea-Verbano

Zone of the Southern Alps. *Tectonophysics*, **579**, 104–117. https://doi.org/10.1016/j.tecto.2012.03.019

WYATT, D. C., SMYE, A. J., GARBER, J. M., & HACKER, B. R. 2022. Assembly and Tectonic Evolution of Continental Lower Crust: Monazite Petrochronology of the Ivrea-Verbano Zone (Val Strona di Omegna). *Tectonics*, **41(3)**. https://doi.org/10.1029/2021TC006841

XYPOLIAS, P. 2010. Vorticity analysis in shear zones: a review of methods and applications. *Journal of structural Geology*, 32(12), 2072-2092.

ZINGG, A. (1990). The Ivrea Crustal Cross-Section (Northern Italy and Southern Switzerland). In *Exposed Cross-Sections of the Continental Crust* (eds M. H. Salisbury & D. M. Fountain), pp. 1–19. Springer Netherlands. https://doi.org/10.1007/978-94-009-0675-4_1

Figure Captions

Fig. 1 – Geological sketch map of the Ivrea-Verbano Zone, modified after Ewing et al. (2015), Simonetti et al. (2021a; 2023) and Corvò et al. (2022). In A) the locations of Triassic-Jurassic shear zones (in red) dated by U–Pb method are after Langone et al., 2018 (Finero area) and Corvò et al., 2023 (Anzola area). The studied area is delimited by the black box. B) Schematic structural and geological map of the Forno-Rosarolo shear zone (modified after Bertolani 1968 and Simonetti et al., 2023) with location of samples analysed for the geochronology.

Fig. 2 – Thin section scans (A-C) of sheared paragneisses and BSE images (D-F) showing some textural and petrographic details. Dashed white boxes on BSE images in D-F, enclose some monazite grains whose internal zoning is shown in Figure 5. Mineral abbreviations after Whitney and Evans (2010).

Fig. 3 – Thin section scans (A-B) of sheared calc-silicates with thin silicate-rich layers highlighted by the dashed bracket on the left side of each image. Microphotographs show the main petrographic and textural

features under both plane (C, E) and crossed (D, F) polarised lights of calcite-poor (C, D) and calcite-rich layers (E, F). The BSE image in G highlights the presence of large allanite grain close to titanite. The microphotograph in H shows the occurrence or retrograde clinozoisite under both plane (left side) and crossed (right side) polarised lights.

Fig. 4 – Mineral chemistry of monazite from mylonites (red squares) and protomylonites (blue circles). A) Monazite composition and classification according to Linthout (2007), B) Y (a.p.f.u.) versus La (a.p.f.u.), C) Th/U versus Nd (a.p.f.u.). D) Th/U ratio of monazite from metasedimentary rocks with different metamorphic degree from the Valle Strona di Omegna after Williams et al. (2022).

Fig. 5 – BSE and chemical X-ray maps (Y, Th) of monazite grains within proto- and mylonitic paragneisses (A-H). The textural position of each monazite grain is reported within the Y-map. The locations of monazite in A and B are reported in Fig. 2D, locations of monazite grains in D and F are shown in Fig. 2E and 2F, respectively.

Fig. 6 – Representative Y maps and microstructural features of monazite within A, B) protomylonitic (A, B) and mylonitic (C, D) paragneisses. Microstructural features are shown as relative crystallographic orientation maps (GROD angle map), misorientation profile diagrams (a-b) and pole figure plots for (001) to highlight degrees of distortion across the monazite grain. The numbered white circles represent the LA-ICP-MS spot analyses performed on monazite grains numbered according to the U–Pb analyses reported in Tables S4. It is interesting to note that there is no overlap between Y-zoning and increasing distortions. Both maps and plots show the increasing distortions focused on the rim/tips of the grains. Pole figures are plotted in lower hemisphere, equal area projections in the sample x-y-z reference frame. The colours of point in pole figures reflect the colours of the GROD angle map. Black arrows highlight the way of dispersions.

Fig. 7 – Summary of concordant monazite U–Th–Pb data for protomylonitic and mylonitic paragneisses organised in ascending order for each sample. The length of boxes represents the apparent ages with the 2σ uncertainty. Data are coloured as function of the textural position (A) and the Y content of the relative analytical spot (B). The weighted average of two clusters obtained from specific grains/domains are also reported in A). The location of the analytical spots is shown on the X-ray maps and BSE images.

Fig. 8 – High contrast BSE images of titanite within calc-silicates showing textural and internal features. A-D) Type “Z” (Zoned) titanite consisting of large brighter cores surrounded by thin darker asymmetric rims. Small titanite grains occurring as satellites close to the large grains are shown in A and B. E-G) Type “unZ” (unzoned)

1516 titanite without apparent zoning. In both Types, fractures (yellow arrows) at high angle with respect to the foliation are common. Two sets of twins are highlighted by green and purple arrows and are more pronounced within the Type Z titanite. H) BSE Image of a textural site showing the location of titanite grains within the matrix reported in G), and a grain included within a clinopyroxene porphyroclast. The inset is the high contrast BSE image of this included grain.

Fig. 9 – Diagrams of titanite chemistry showing the differences between the two main Types. A) TiO_2 (wt.%) vs Al_2O_3 (wt.%), B) CaO (wt.%) vs F (wt.%). The grey areas enclose the data from the two Types. C) and D) Chondrite-normalized REE patterns of Type "Z" and "unZ", respectively (chondrite values from McDonough and Sun, 1995). For comparison, the Chondrite-normalized REE patterns of titanite grains from sheared amphibolite and calc-silicate layers from the Anzola Shear Zone are reported in grey (Corvò et al., 2023). E) Nd (ppm) vs Zr (ppm), F) Temperature (°C) estimate according to the Zr-in-titanite thermometry (calibration of Hyden et al., 2008). The grey shaded box indicates the Temperature conditions for the regional metamorphism obtained by Kunz and White (2019) with P-T pseudosection calculations for unsheared metabasic and metapelitic rocks at the boundary of the shear zone.

Fig. 10 – BSE and microstructural features of titanite within calc-silicates (sample VSDO-12R2) in Cal-poor calc-silicates (A-D; Type "Z") layers and Cal-rich calc-silicates (E-H; Type "unZ"). Microstructural features are shown as relative crystallographic orientation maps (GROD angle map), misorientation profile diagrams (a-b) and pole figure plots for (100), (010), (001) showing the orientation of titanite grain, grain boundaries, subgrains and twins. The numbered white circles represent the LA-ICP-MS spot analyses performed on titanite grains numbered according to the U–Pb analyses reported in Table S5. It is interesting to note that there is no overlap between BSE-zoning and increasing distortions. While titanites Type "Z" show the increase of distortions focused on the rim/tips of the grains, titanites Type "unZ" show little degree of distortion spread across the whole grain. Pole figures are plotted in lower hemisphere, equal area projections in the sample x-y-z reference frame. The colours of point in pole figures reflect the colours of the GROD angle map. Black arrows highlight the way of dispersions.

Fig. 11 – Tera-Wasserburg diagrams of titanite U–Pb data from Type "Z" (A, C, E) and Type "unZ" (B, D, F) from sample VSDO-12R2. Each ellipse represents a U–Pb datapoint and is coloured as function of: the relative microstructure, defined as the Weighted Burger Vector (A, B); the ΣLREE (C, D) and its position within the grain, i.e., core vs rim (E, F). G) Cumulative Tera-Wasserburg diagram for both titanite types showing the regression lines anchored to Stacey and Kramers (1975) common Pb ratios considering the U–Pb data from

the innermost cores (green filled ellipses) and outermost rims/tips (red filled ellipses) of titanite grains. The relative lower intercept ages are also reported. The datapoints delimited by a dashed line were not included in the calculation of the intercept ages.

Fig. 12 – Kernel Density Estimation (KDE) of U–(Th–)Pb monazite data for sheared (A; this work) and unsheared (B; from literature data) metasedimentary rocks exposed in Val d'Ossola di Omegna. A) $^{206}Pb/^{238}U$ monazite dates for mylonitic (reddish filled KDE curve and datapoints) and protomylonitic (bluish filled KDE curve and datapoints) samples. The grey bands represent the lower intercept ages and relative uncertainties obtained for the titanite from the sheared calc-silicate (this work).

Data points (small circles below the curve) in B) refer to: a) $^{208}Pb/^{232}Th$ monazite dates from amphibolite- to granulite-facies metasediments, after Wyatt et al. (2022); b) $^{206}Pb/^{238}U$ corrected monazite dates from amphibolite- to granulite facies metasediments, after Williams et al. (2022); c) $^{207}Pb/^{206}Pb$ monazite data from amphibolite-facies metasediment, after Guergouz et al. (2018); d) monazite U–Pb ages, after Henk et al. (1997).

Fig. 13 – Synoptic summary of different generations of monazite (A) within protomylonitic and mylonitic paragneisses and titanite (B) within mylonitic calc-silicates. For each generation the main microstructures, chemical zoning features and U–Pb data are reported as well as the main mineral assemblages.

Supplementary materials

Figures Supplementary

Fig. S1 – BSE images of monazite from different samples showing replacement textures with allanite growth.

Fig. S2 – BSE images and chemical X-ray maps (Y, Th) of monazite grains within proto- and mylonitic paragneisses.

Fig. S3 – U–Th–Pb data of monazite within protomylonites from each analysed grain (left column) and ordered (right column). Box high is the 2σ uncertainty. On the diagrams of the left column the concordance between the two U–Pb systems is shown by a colour code reported on the top of the column; the unfilled boxes are the $^{208}Pb/^{232}Th$ data. The textural position of the grain is also shown as well as information about the chemistry.

The diagrams on the right column highlight isotopic data concordant (green filled boxes) and discordant (unfilled and dashed boxes) for the three systems.

Fig. S4 – U–Th–Pb data of monazite within mylonites from each analysed grain (left column) and ordered (right column). Box high is the 2σ uncertainty. On the diagrams of the left column the concordance between the two U–Pb systems is shown by a colour code reported on the top of the column; the unfilled boxes are the $^{208}Pb/^{232}Th$ data. The textural position of the grain is also shown as well as information about the chemistry. The diagrams on the right column highlight isotopic data concordant (green filled boxes) and discordant (unfilled and dashed boxes) for the three systems.

Fig. S5 – BSE and X-ray maps of zoned (Type “Z”) titanites within calc-silicate. The darker shade on the BSE image or cold colours in the X-ray maps for the external domains indicate lower content of LREE. The coloured scale of the X-ray maps represents the intensity of the characteristic X-ray emission for each elements.

Fig. S6 – BSE and X-ray maps of zoned (Type “unZ”) titanites within calc-silicate. The coloured scale of the X-ray maps represents the intensity of the characteristic X-ray emission for each element.

Tables Supplementary

Tab. S1 - EPMA (major and minor elements) chemical results for monazite.

Tab. S2 - Monazite textural features.

Tab. S3 – LA-ICP-MS U–(Th–)Pb data analytical details.

Tab. S4 – U–Th–Pb monazite data.

Tab. S5 - EPMA (major and minor elements) chemical results for titanite.

Tab. S6 - U–Pb and trace elements titanite data.

Table 1 - Summary of mineral assemblage, accessory minerals, type of fabric and analysed minerals for the studied samples.

Sample name (coordinates)	Rock type	Mineral assemblage (accessory minerals)	Type of fabric	Analysed accessory mineral for geochronology
VSDO-13B *(45.932198, 8.290887)*	biotite-poor paragneiss	Sil, Grt, Qz, Pl, Kfs, Bt (Mnz, Rt, Zrn)	protomylonitic fabric	monazite
VSDO-13A *(45.932198, 8.290887)*	biotite-rich paragneisses	Bt, Sil, Grt, Qz, Pl, Kfs (Mnz, Rt, Zrn)	protomylonitic fabric	monazite
VSDO-13M1; VSDO-13M2; VSDO-13M4; *(45.932412, 8.292021)*	biotite-rich paragneisses	Bt, Sil, Grt, Qz, Pl, Kfs (Mnz, Rt, Zrn)	mylonitic (locally ultramylonitic) fabric	monazite
VSDO-12R2B *(45.930638, 8.292250)*	calc-silicate	Cal, Pl, Kfs, Amp, Cpx, Bt, Bt ± Grt, Scp, Aln (Ttn, Zrn, Ap)	mylonitic fabric	titanite

Table S1 - EPMA Monazite

Microprobe Lab	MILANO	MILANO	MILANO	MILANO
Sample	VSDO-13B1	VSDO-13B1	VSDO-13B1	VSDO-13B1
Mnz#	MNZ6A-1	MNZ6A-2	MNZ6A-3	MNZ6A-4
Textural Position	Rim	Int	Int	Core
(wt%)				
P2O5	30.04	29.92	30.38	30.17
SiO2	0.22	0.42	0.41	0.19
ThO2	5.24	8.58	8.24	6.29
UO2	0.31	0.33	0.31	0.30
La2O3	13.13	11.68	11.83	13.27
Ce2O3	28.46	26.30	26.17	27.23
Pr2O3	3.12	2.52	2.74	2.98
Nd2O3	12.71	12.82	12.12	11.65
Sm2O3	1.80	2.22	2.02	2.16
Gd2O3	1.09	1.41	1.45	1.34
Dy2O5	0.04	0.00	0.00	0.08
Y2O3	**0.12**	**0.16**	**0.05**	**0.38**
CaO	1.19	1.69	1.82	1.37
Total	97.47	98.05	97.54	97.40
(a.p.f.u.)				
P	1.01	1.00	1.01	1.01
Si	0.01	0.02	0.02	0.01
Th	0.05	0.08	0.07	0.06
U	0.00	0.00	0.00	0.00
La	0.19	0.17	0.17	0.19
Ce	0.41	0.38	0.38	0.39
Pr	0.05	0.04	0.04	0.04
Nd	0.18	0.18	0.17	0.16
Sm	0.02	0.03	0.03	0.03
Gd	0.01	0.02	0.02	0.02
Dy	0.00	0.00	0.00	0.00
Y	0.00	0.00	0.00	0.01
Ca	0.05	0.07	0.08	0.06
∑ IV	1.02	1.02	1.03	1.02
∑ IX	0.97	0.97	0.96	0.97
CAT4O	1.99	1.99	1.99	1.99
Mnz	93.64	90.30	89.68	92.86
Cher.	5.44	7.88	8.54	6.31
Hutt.	0.92	1.82	1.77	0.83
summ	100	100	100	100

MILANO VSDO-13B1 MNZ6A-5 Core	MILANO VSDO-13B1 MNZ6A-6 Rim	MILANO VSDO-13B1 MNZ6B-1 Rim	MILANO VSDO-13B1 MNZ6B-2 Int	MILANO VSDO-13B1 MNZ6B-3 Int
30.04	29.74	30.25	30.23	30.06
0.16	0.22	0.18	0.24	0.32
5.95	5.38	4.62	5.46	7.42
0.29	0.38	0.28	0.25	0.19
13.37	12.99	13.47	12.93	12.51
27.23	28.14	28.88	28.69	26.92
2.73	3.04	2.95	3.12	2.88
12.09	13.09	12.62	12.50	12.57
1.97	2.14	2.11	2.12	1.74
1.66	1.36	1.31	1.29	1.45
0.20	0.05	0.03	0.16	0.02
0.39	**0.15**	**0.12**	**0.12**	**0.12**
1.29	1.15	0.94	1.17	1.55
97.37	97.83	97.75	98.28	97.76
1.01	1.00	1.01	1.01	1.01
0.01	0.01	0.01	0.01	0.01
0.05	0.05	0.04	0.05	0.07
0.00	0.00	0.00	0.00	0.00
0.20	0.19	0.20	0.19	0.18
0.40	0.41	0.42	0.41	0.39
0.04	0.04	0.04	0.04	0.04
0.17	0.19	0.18	0.18	0.18
0.03	0.03	0.03	0.03	0.02
0.02	0.02	0.02	0.02	0.02
0.00	0.00	0.00	0.00	0.00
0.01	0.00	0.00	0.00	0.00
0.05	0.05	0.04	0.05	0.07
1.02	1.01	1.02	1.02	1.02
0.97	0.98	0.97	0.97	0.97
1.99	1.99	1.99	1.99	1.99
93.39	93.84	94.97	93.68	91.43
5.93	5.24	4.26	5.31	7.18
0.67	0.92	0.77	1.00	1.39
100	100	100	100	100

MILANO VSDO-13B1 MNZ6B-4 Core	MILANO VSDO-13B1 MNZ6B-5 Core	MILANO VSDO-13B1 MNZ6B-6 Int	MILANO VSDO-13B1 MNZ6B-7 Rim	MILANO VSDO-13B1 MNZ4A-1 Rim
30.19	30.05	30.45	29.77	30.15
0.16	0.13	0.15	0.18	0.26
5.60	5.73	5.54	5.94	3.76
0.21	0.17	0.15	0.29	0.15
12.71	12.82	13.11	13.03	14.99
27.21	27.98	27.86	27.24	28.76
2.95	3.15	2.87	3.18	3.16
12.59	12.75	13.08	12.76	11.06
1.86	2.30	2.26	2.10	1.68
1.47	1.49	1.36	1.51	1.44
0.00	0.17	0.22	0.15	0.20
0.14	**0.14**	**0.16**	**0.18**	**0.64**
1.25	1.26	1.18	1.25	0.78
96.33	98.13	98.40	97.58	97.03
1.02	1.01	1.01	1.00	1.01
0.01	0.00	0.01	0.01	0.01
0.05	0.05	0.05	0.05	0.03
0.00	0.00	0.00	0.00	0.00
0.19	0.19	0.19	0.19	0.22
0.40	0.41	0.40	0.40	0.42
0.04	0.05	0.04	0.05	0.05
0.18	0.18	0.18	0.18	0.16
0.03	0.03	0.03	0.03	0.02
0.02	0.02	0.02	0.02	0.02
0.00	0.00	0.00	0.00	0.00
0.00	0.00	0.00	0.00	0.01
0.05	0.05	0.05	0.05	0.03
1.03	1.01	1.02	1.01	1.02
0.96	0.98	0.97	0.98	0.97
1.99	1.99	1.99	1.99	1.99
93.48	93.73	93.97	93.52	95.38
5.83	5.74	5.38	5.73	3.54
0.69	0.53	0.65	0.75	1.08
100	100	100	100	100

MILANO VSDO-13B1 MNZ4A-2 Rim	MILANO VSDO-13B1 MNZ4A-3 Core	MILANO VSDO-13B1 MNZ4A-4 Core	MILANO VSDO-13B1 MNZ4A-5 Rim	MILANO VSDO-13B1 MNZ4A-6 Rim
29.92	30.07	29.51	29.83	29.79
0.29	0.22	0.40	0.47	0.31
6.78	4.33	7.94	4.98	3.53
0.17	0.14	0.42	0.90	0.77
12.43	13.07	12.55	13.04	13.69
27.42	27.69	26.88	26.89	28.90
3.09	3.16	2.86	3.35	3.49
12.87	12.51	11.26	11.85	11.83
1.69	2.38	1.72	2.16	2.20
1.21	1.90	1.32	1.80	1.55
0.23	0.37	0.21	0.46	0.15
0.05	**1.19**	**0.09**	**0.82**	**0.86**
1.34	0.92	1.60	1.04	0.74
97.49	97.95	96.77	97.58	97.80
1.01	1.01	1.00	1.00	1.00
0.01	0.01	0.02	0.02	0.01
0.06	0.04	0.07	0.04	0.03
0.00	0.00	0.00	0.01	0.01
0.18	0.19	0.19	0.19	0.20
0.40	0.40	0.39	0.39	0.42
0.04	0.05	0.04	0.05	0.05
0.18	0.18	0.16	0.17	0.17
0.02	0.03	0.02	0.03	0.03
0.02	0.02	0.02	0.02	0.02
0.00	0.00	0.00	0.01	0.00
0.00	0.02	0.00	0.02	0.02
0.06	0.04	0.07	0.04	0.03
1.02	1.01	1.02	1.02	1.01
0.97	0.98	0.97	0.97	0.98
1.99	1.99	1.99	1.99	1.99
92.55	94.96	90.74	93.32	95.42
6.21	4.12	7.52	4.71	3.31
1.24	0.92	1.74	1.97	1.28
100	100	100	100	100

MILANO VSDO-13B1 MNZ4A-7 Rim	MILANO VSDO-13B1 MNZ4A-8 Rim	MILANO VSDO-13B1 MNZ4A-9 Rim	MILANO VSDO-13B1 MNZ4A-10 Rim	MILANO VSDO-13B1 MNZ1A-1 Rim
29.75	30.09	29.47	29.99	29.66
0.20	0.22	0.37	0.26	0.40
4.75	4.56	7.03	5.36	9.12
0.25	0.13	0.26	0.24	0.19
13.34	13.72	12.76	13.35	11.66
28.35	27.18	27.29	28.29	25.74
2.97	2.91	2.75	3.26	2.79
12.40	12.05	12.89	12.28	12.13
1.96	2.14	1.88	1.76	1.81
1.17	1.76	0.89	0.99	1.12
0.20	0.40	0.05	0.00	0.26
0.38	**1.19**	**0.05**	**0.26**	**0.06**
1.04	0.95	1.43	1.07	1.78
96.77	97.29	97.13	97.10	96.72
1.01	1.01	1.00	1.01	1.00
0.01	0.01	0.01	0.01	0.02
0.04	0.04	0.06	0.05	0.08
0.00	0.00	0.00	0.00	0.00
0.20	0.20	0.19	0.20	0.17
0.42	0.39	0.40	0.41	0.38
0.04	0.04	0.04	0.05	0.04
0.18	0.17	0.18	0.17	0.17
0.03	0.03	0.03	0.02	0.02
0.02	0.02	0.01	0.01	0.01
0.00	0.01	0.00	0.00	0.00
0.01	0.03	0.00	0.01	0.00
0.04	0.04	0.06	0.05	0.08
1.02	1.02	1.01	1.02	1.02
0.98	0.97	0.98	0.97	0.97
1.99	1.99	1.99	1.99	1.99
94.38	94.81	91.80	94.00	89.75
4.76	4.28	6.61	4.90	8.48
0.86	0.91	1.60	1.09	1.77
100	100	100	100	100

MILANO VSDO-13B1 MNZ1A-2 Int	MILANO VSDO-13B1 MNZ1A-3 Rim	MILANO VSDO-13B1 MNZ1A-4 Core	MILANO VSDO-13B1 MNZ1A-5 Core	MILANO VSDO-13B1 MNZ1A-6 Rim
30.05	29.69	30.17	29.97	29.88
0.11	0.22	0.17	0.25	0.31
5.98	6.21	6.18	6.21	7.42
0.26	0.16	0.18	0.24	0.23
12.37	12.50	12.60	12.59	12.08
27.26	27.39	27.08	27.05	26.72
3.07	2.73	3.30	3.27	2.90
12.74	13.13	12.47	12.89	12.28
2.18	2.28	2.06	2.20	2.10
1.63	1.57	1.60	1.33	1.36
0.01	0.14	0.26	0.00	0.17
0.12	**0.13**	**0.14**	**0.04**	**0.15**
1.37	1.35	1.33	1.39	1.53
97.16	97.50	97.54	97.42	97.14
1.01	1.00	1.01	1.01	1.01
0.00	0.01	0.01	0.01	0.01
0.05	0.06	0.06	0.06	0.07
0.00	0.00	0.00	0.00	0.00
0.18	0.18	0.18	0.18	0.18
0.40	0.40	0.39	0.39	0.39
0.04	0.04	0.05	0.05	0.04
0.18	0.19	0.18	0.18	0.17
0.03	0.03	0.03	0.03	0.03
0.02	0.02	0.02	0.02	0.02
0.00	0.00	0.00	0.00	0.00
0.00	0.00	0.00	0.00	0.00
0.06	0.06	0.06	0.06	0.07
1.02	1.01	1.02	1.02	1.02
0.97	0.98	0.97	0.97	0.97
1.99	2.00	1.99	1.99	1.99
93.20	92.89	93.13	92.54	91.49
6.34	6.19	6.14	6.39	7.14
0.47	0.92	0.73	1.07	1.36
100	100	100	100	100

MILANO VSDO-13B1 MNZ1A-7 Int	MILANO VSDO-13B1 MNZ1A-8 Int	MILANO VSDO-13B1 MNZ1A-9 Rim	MILANO VSDO-13B1 MNZ1A-10 Rim	MILANO VSDO-13B1 MNZ1A-11 Int
30.08	30.32	29.70	29.70	29.74
0.13	0.15	0.43	0.34	0.24
5.49	5.78	8.86	8.65	6.51
0.08	0.32	0.15	0.31	0.24
13.06	13.04	12.02	11.93	12.55
28.09	27.79	25.94	25.98	27.29
3.45	2.88	2.44	3.18	2.94
12.72	12.73	13.01	12.29	12.70
2.06	1.91	2.00	1.84	1.98
1.50	1.78	1.42	1.05	1.33
0.18	0.00	0.10	0.00	0.08
0.08	**0.16**	**0.15**	**0.14**	**0.02**
1.15	1.24	1.65	1.69	1.42
98.08	98.11	97.88	97.09	97.04
1.01	1.01	1.00	1.00	1.01
0.01	0.01	0.02	0.01	0.01
0.05	0.05	0.08	0.08	0.06
0.00	0.00	0.00	0.00	0.00
0.19	0.19	0.18	0.18	0.18
0.41	0.40	0.38	0.38	0.40
0.05	0.04	0.04	0.05	0.04
0.18	0.18	0.18	0.18	0.18
0.03	0.03	0.03	0.03	0.03
0.02	0.02	0.02	0.01	0.02
0.00	0.00	0.00	0.00	0.00
0.00	0.00	0.00	0.00	0.00
0.05	0.05	0.07	0.07	0.06
1.01	1.02	1.02	1.02	1.02
0.98	0.97	0.98	0.97	0.98
1.99	1.99	1.99	1.99	1.99
94.22	93.66	90.41	90.53	92.38
5.24	5.68	7.71	7.99	6.57
0.54	0.66	1.89	1.48	1.05
100	100	100	100	100

MILANO VSDO-13B1 MNZ1A-12 Rim	MILANO VSDO-13B1 MNZ1A-13 Core		MILANO VSDO-13A1 MNZ2A-1 Rim	MILANO VSDO-13A1 MNZ2A-2 Rim
30.00	29.11		30.47	29.56
0.22	0.53		0.13	0.08
5.92	8.90		3.29	2.77
0.11	0.14		0.27	0.18
13.59	11.62		15.21	15.67
28.00	26.17		28.78	27.99
2.99	2.78		3.21	3.00
11.91	12.29		11.66	11.04
2.12	1.89		1.85	1.88
1.42	1.15		1.71	1.46
0.16	0.14		0.12	0.24
0.41	**0.22**		**0.29**	**0.24**
1.30	1.68		0.76	2.45
98.15	96.62		97.76	96.56
1.00	0.99		1.02	1.00
0.01	0.02		0.01	0.00
0.05	0.08		0.03	0.03
0.00	0.00		0.00	0.00
0.20	0.17		0.22	0.23
0.41	0.39		0.42	0.41
0.04	0.04		0.05	0.04
0.17	0.18		0.16	0.16
0.03	0.03		0.03	0.03
0.02	0.02		0.02	0.02
0.00	0.00		0.00	0.00
0.01	0.00		0.01	0.01
0.06	0.07		0.03	0.10
1.01	1.01		1.02	1.00
0.98	0.98		0.97	1.02
1.99	1.99		1.99	2.03
93.20	89.78		96.01	89.22
5.89	7.90		3.42	10.46
0.91	2.32		0.56	0.32
100	100		100	100

MILANO VSDO-13A1 MNZ2A-3 Mantle	MILANO VSDO-13A1 MNZ2A-4 Core	MILANO VSDO-13A1 MNZ2A-5 Core	MILANO VSDO-13A1 MNZ2A-6 Core	MILANO VSDO-13A1 MNZ2A-7 Core
30.60	29.98	29.46	30.03	29.90
0.09	0.26	0.76	0.32	0.27
2.63	4.74	4.66	4.96	4.99
0.17	0.18	0.21	0.07	0.30
16.59	14.89	14.39	15.24	15.42
29.50	28.19	30.29	29.30	28.98
3.03	3.16	3.82	2.95	3.47
11.69	11.97	13.17	11.78	12.07
1.87	1.48	1.22	1.59	1.47
1.73	1.16	0.41	1.01	0.70
0.11	0.15	0.13	0.00	0.00
0.47	**0.56**	**0.00**	**0.12**	**0.06**
0.54	1.01	0.54	0.97	0.97
99.03	97.73	99.06	98.34	98.61
1.01	1.01	0.98	1.00	1.00
0.00	0.01	0.03	0.01	0.01
0.02	0.04	0.04	0.04	0.04
0.00	0.00	0.00	0.00	0.00
0.24	0.22	0.21	0.22	0.22
0.42	0.41	0.44	0.42	0.42
0.04	0.05	0.05	0.04	0.05
0.16	0.17	0.19	0.17	0.17
0.03	0.02	0.02	0.02	0.02
0.02	0.02	0.01	0.01	0.01
0.00	0.00	0.00	0.00	0.00
0.01	0.01	0.00	0.00	0.00
0.02	0.04	0.02	0.04	0.04
1.02	1.02	1.01	1.02	1.01
0.97	0.98	0.98	0.98	0.98
1.99	1.99	1.99	1.99	1.99
97.26	94.35	94.51	94.34	94.53
2.38	4.54	2.38	4.33	4.36
0.36	1.10	3.11	1.34	1.12
100	100	100	100	100

MILANO VSDO-13A1 MNZ2A-8 Rim	MILANO VSDO-13A1 MNZ2A-9 Rim	MILANO VSDO-13A1 MNZ2A-10 Core	MILANO VSDO-13A1 MNZ6B-1 Rim	MILANO VSDO-13A1 MNZ6B-2 Rim
26.85	29.23	29.80	29.85	30.31
2.36	0.62	0.29	0.27	0.31
11.40	5.21	4.42	7.10	6.73
0.11	0.10	0.26	0.19	0.24
12.40	14.10	16.12	13.41	12.97
27.32	29.32	29.42	26.40	26.33
2.93	3.16	3.06	2.74	2.95
12.29	12.60	11.39	11.84	12.23
0.89	1.16	1.21	1.93	2.16
0.53	0.94	0.60	1.37	1.59
0.02	0.35	0.13	0.21	0.12
0.03	**0.11**	**0.15**	**0.38**	**0.39**
0.68	0.77	1.00	1.53	1.43
97.82	97.66	97.85	97.21	97.76
0.92	0.99	1.00	1.01	1.01
0.10	0.02	0.01	0.01	0.01
0.11	0.05	0.04	0.06	0.06
0.00	0.00	0.00	0.00	0.00
0.19	0.21	0.24	0.20	0.19
0.41	0.43	0.43	0.38	0.38
0.04	0.05	0.04	0.04	0.04
0.18	0.18	0.16	0.17	0.17
0.01	0.02	0.02	0.03	0.03
0.01	0.01	0.01	0.02	0.02
0.00	0.00	0.00	0.00	0.00
0.00	0.00	0.00	0.01	0.01
0.03	0.03	0.04	0.07	0.06
1.02	1.01	1.01	1.02	1.02
0.97	0.98	0.98	0.98	0.97
1.99	1.99	2.00	1.99	1.99
86.94	93.95	94.34	91.77	92.08
3.07	3.45	4.45	7.09	6.60
9.99	2.60	1.21	1.15	1.32
100	100	100	100	100

MILANO VSDO-13A1 MNZ6B-3 Core	MILANO VSDO-13A1 MNZ6B-4 Mantle	MILANO VSDO-13A1 MNZ6B-5 Core	MILANO VSDO-13A1 MNZ6B-6 Mantle	MILANO VSDO-13A1 MNZ6B-7 Mantle
30.31	28.99	28.68	28.18	26.98
0.21	0.89	1.16	1.30	2.30
6.29	7.75	7.60	7.70	12.26
0.10	0.15	0.19	0.14	0.10
13.27	12.32	12.64	12.45	11.74
27.65	27.40	27.62	28.10	25.88
2.83	3.04	3.18	3.18	2.53
12.81	13.45	13.35	13.84	12.00
1.93	1.83	1.58	1.63	1.02
1.25	0.65	0.71	0.46	0.82
0.16	0.00	0.00	0.00	0.00
0.10	**0.03**	**0.03**	**0.00**	**0.03**
1.42	1.10	0.84	0.77	0.98
98.32	97.59	97.58	97.74	96.64
1.01	0.98	0.97	0.96	0.93
0.01	0.04	0.05	0.05	0.09
0.06	0.07	0.07	0.07	0.11
0.00	0.00	0.00	0.00	0.00
0.19	0.18	0.19	0.19	0.18
0.40	0.40	0.41	0.41	0.39
0.04	0.04	0.05	0.05	0.04
0.18	0.19	0.19	0.20	0.18
0.03	0.03	0.02	0.02	0.01
0.02	0.01	0.01	0.01	0.01
0.00	0.00	0.00	0.00	0.00
0.00	0.00	0.00	0.00	0.00
0.06	0.05	0.04	0.03	0.04
1.02	1.02	1.02	1.01	1.03
0.97	0.97	0.97	0.98	0.96
1.99	1.99	1.99	1.99	1.99
92.65	91.18	91.26	91.10	85.45
6.47	5.02	3.80	3.45	4.55
0.88	3.80	4.93	5.45	10.00
100	100	100	100	100

MILANO VSDO-13A1 MNZ6B-8 Mantle	MILANO VSDO-13A1 MNZ6B-9 Mantle	MILANO VSDO-13A1 MNZ6B-10 Core	MILANO VSDO-13A1 MNZ6B-11 Mantle	MILANO VSDO-13A1 MNZ6B-12 Core
28.02	28.30	29.95	28.38	27.97
1.19	1.22	0.32	1.09	0.18
7.23	9.64	6.84	9.56	6.84
0.01	0.24	0.22	0.13	0.14
13.18	12.29	12.28	12.69	12.57
28.61	27.72	27.38	26.74	27.37
3.20	2.89	3.04	3.15	2.71
12.94	12.53	12.63	13.14	12.49
1.22	1.14	1.87	1.20	1.82
0.38	0.33	1.37	0.60	0.82
0.00	0.06	0.08	0.00	0.05
0.00	**0.06**	**0.18**	**0.04**	**0.02**
0.70	1.08	1.42	1.37	1.45
96.68	97.51	97.57	98.09	94.43
0.97	0.97	1.01	0.97	0.99
0.05	0.05	0.01	0.04	0.01
0.07	0.09	0.06	0.09	0.06
0.00	0.00	0.00	0.00	0.00
0.20	0.18	0.18	0.19	0.19
0.43	0.41	0.40	0.39	0.42
0.05	0.04	0.04	0.05	0.04
0.19	0.18	0.18	0.19	0.19
0.02	0.02	0.03	0.02	0.03
0.01	0.00	0.02	0.01	0.01
0.00	0.00	0.00	0.00	0.00
0.00	0.00	0.00	0.00	0.00
0.03	0.05	0.06	0.06	0.06
1.01	1.02	1.02	1.01	1.00
0.98	0.98	0.97	0.99	1.01
1.99	1.99	1.99	2.00	2.00
91.78	89.71	92.09	89.12	92.39
3.17	5.01	6.55	6.25	6.83
5.06	5.28	1.36	4.63	0.79
100	100	100	100	100

MILANO VSDO-13A1 MNZ6B-13 Mantle	MILANO VSDO-13A1 MNZ6B-14 Mantle	MILANO VSDO-13A1 MNZ6B-15 Rim	MILANO VSDO-13A1 MNZ6B-16 Mantle	MILANO VSDO-13A1 MNZ6B-17 Mantle
28.65	27.87	30.14	27.78	28.56
1.08	1.55	0.32	1.75	1.17
7.39	8.04	6.93	8.96	6.83
0.19	0.07	0.32	0.00	0.17
12.10	12.92	13.20	12.62	12.84
27.71	28.50	27.13	28.39	28.15
3.12	3.23	2.82	3.19	3.05
13.46	12.84	11.80	13.11	13.05
1.80	1.13	1.54	0.93	1.74
0.80	0.58	1.52	0.34	1.04
0.09	0.00	0.10	0.09	0.04
0.00	**0.00**	**0.33**	**0.00**	**0.00**
0.88	0.62	1.32	0.69	0.78
97.27	97.35	97.47	97.84	97.42
0.98	0.96	1.01	0.95	0.97
0.04	0.06	0.01	0.07	0.05
0.07	0.07	0.06	0.08	0.06
0.00	0.00	0.00	0.00	0.00
0.18	0.19	0.19	0.19	0.19
0.41	0.42	0.39	0.42	0.41
0.05	0.05	0.04	0.05	0.04
0.19	0.19	0.17	0.19	0.19
0.02	0.02	0.02	0.01	0.02
0.01	0.01	0.02	0.00	0.01
0.00	0.00	0.00	0.00	0.00
0.00	0.00	0.01	0.00	0.00
0.04	0.03	0.06	0.03	0.03
1.02	1.02	1.02	1.02	1.02
0.97	0.97	0.96	0.97	0.97
1.99	1.99	1.99	1.99	1.99
91.39	90.69	92.47	89.57	91.58
4.01	2.78	6.14	3.11	3.50
4.60	6.53	1.39	7.33	4.92
100	100	100	100	100

MILANO VSDO-13A1 MNZ6B-18 Core	MILANO VSDO-13A1 MNZ6B-19 Mantle	MILANO VSDO-13A1 MNZ6B-20 Rim	MILANO VSDO-13A1 MNZ6B-21 Rim	MILANO VSDO-13A1 MNZ6B-22 Rim
30.11	29.40	29.98	30.27	30.14
0.18	0.74	0.23	0.34	0.22
6.11	9.21	6.92	6.86	6.19
0.25	0.11	0.23	0.25	0.26
12.16	12.00	12.92	12.63	12.56
27.89	26.62	26.58	27.03	26.45
3.03	2.77	3.08	3.11	2.67
13.25	12.53	12.04	12.19	12.11
1.84	1.57	2.01	2.02	1.81
1.09	0.55	1.54	1.25	1.24
0.11	0.35	0.26	0.14	0.69
0.14	**0.12**	**0.37**	**0.41**	**1.81**
1.27	1.69	1.46	1.42	1.37
97.43	97.66	97.62	97.93	97.52
1.01	0.99	1.01	1.01	1.01
0.01	0.03	0.01	0.01	0.01
0.06	0.08	0.06	0.06	0.06
0.00	0.00	0.00	0.00	0.00
0.18	0.18	0.19	0.18	0.18
0.41	0.39	0.39	0.39	0.38
0.04	0.04	0.04	0.04	0.04
0.19	0.18	0.17	0.17	0.17
0.03	0.02	0.03	0.03	0.02
0.01	0.01	0.02	0.02	0.02
0.00	0.00	0.00	0.00	0.01
0.00	0.00	0.01	0.01	0.04
0.05	0.07	0.06	0.06	0.06
1.02	1.02	1.02	1.02	1.02
0.97	0.97	0.98	0.97	0.98
1.99	1.99	1.99	1.99	1.99
93.35	88.98	92.25	91.99	92.80
5.86	7.84	6.74	6.54	6.26
0.79	3.18	1.01	1.48	0.94
100	100	100	100	100

MILANO VSDO-13A1 MNZ6B-23 Rim	MILANO VSDO-13A1 MNZ6B-24 Mantle	MILANO VSDO-13A1 MNZ6C-1 Rim	MILANO VSDO-13A1 MNZ6C-2 Mantle	MILANO VSDO-13A1 MNZ6C-3 Mantle
29.86	29.13	29.55	27.54	28.49
0.32	0.88	0.54	1.87	1.21
7.15	8.92	7.55	10.03	7.26
0.25	0.26	0.15	0.13	0.09
12.44	12.20	12.58	12.39	12.61
27.20	27.02	27.51	27.69	28.36
2.91	2.88	2.82	3.30	3.12
12.00	12.46	12.20	12.44	13.77
2.04	1.68	1.60	0.90	1.43
1.41	0.68	0.85	0.48	0.66
0.29	0.00	0.00	0.05	0.06
0.39	**0.03**	**0.20**	**0.09**	**0.00**
1.48	1.41	1.40	0.81	0.77
97.75	97.54	96.95	97.71	97.84
1.00	0.98	1.00	0.94	0.97
0.01	0.03	0.02	0.08	0.05
0.06	0.08	0.07	0.09	0.07
0.00	0.00	0.00	0.00	0.00
0.18	0.18	0.19	0.18	0.19
0.39	0.40	0.40	0.41	0.42
0.04	0.04	0.04	0.05	0.05
0.17	0.18	0.17	0.18	0.20
0.03	0.02	0.02	0.01	0.02
0.02	0.01	0.01	0.01	0.01
0.00	0.00	0.00	0.00	0.00
0.01	0.00	0.00	0.00	0.00
0.06	0.06	0.06	0.04	0.03
1.02	1.02	1.02	1.02	1.02
0.98	0.97	0.97	0.97	0.98
1.99	1.99	1.99	1.99	1.99
91.80	89.66	91.14	88.43	91.44
6.81	6.54	6.50	3.66	3.47
1.39	3.79	2.36	7.91	5.09
100	100	100	100	100

MILANO VSDO-13A1 MNZ6C-4 Core	MILANO VSDO-13A1 MNZ6C-5 Core	MILANO VSDO-13A1 MNZ6C-6 Mantle	MILANO VSDO-13A1 MNZ6C-7 Core	MILANO VSDO-13A1 MNZ6A-1 Rim
29.96	30.01	28.03	29.85	29.82
0.38	0.25	1.30	0.23	0.25
7.30	7.05	7.57	7.53	7.02
0.27	0.14	0.10	0.16	0.21
12.27	12.23	13.02	12.16	12.84
26.84	27.14	28.79	27.37	27.16
2.98	2.82	2.93	2.93	3.19
13.31	13.40	13.06	12.96	11.73
1.85	2.01	1.48	2.02	1.79
1.23	1.20	0.54	0.88	1.14
0.22	0.18	0.00	0.00	0.17
0.05	**0.17**	**0.00**	**0.00**	**0.36**
1.51	1.52	0.73	1.61	1.43
98.17	98.12	97.54	97.69	97.11
1.00	1.00	0.96	1.00	1.01
0.01	0.01	0.05	0.01	0.01
0.07	0.06	0.07	0.07	0.06
0.00	0.00	0.00	0.00	0.00
0.18	0.18	0.19	0.18	0.19
0.39	0.39	0.43	0.40	0.40
0.04	0.04	0.04	0.04	0.05
0.19	0.19	0.19	0.18	0.17
0.03	0.03	0.02	0.03	0.02
0.02	0.02	0.01	0.01	0.02
0.00	0.00	0.00	0.00	0.00
0.00	0.00	0.00	0.00	0.01
0.06	0.06	0.03	0.07	0.06
1.02	1.01	1.01	1.01	1.02
0.98	0.98	0.98	0.98	0.97
1.99	1.99	2.00	1.99	1.99
91.45	91.97	91.28	91.57	92.29
6.93	6.97	3.26	7.46	6.65
1.62	1.06	5.47	0.98	1.07
100	100	100	100	100

MILANO VSDO-13A1 MNZ6A-2 Mantle	MILANO VSDO-13A1 MNZ6A-3 Rim	MILANO VSDO-13A1 MNZ6A-4 Core	MILANO VSDO-13A1 MNZ6A-5 Mantle	MILANO VSDO-13A1 MNZ6A-6 Rim
27.98	29.69	28.18	29.15	29.96
1.42	0.25	1.32	0.72	0.31
7.54	7.27	9.43	8.57	6.23
0.10	0.33	0.23	0.09	0.25
12.66	12.08	12.51	12.38	12.46
28.45	27.01	27.53	26.75	27.45
3.51	3.12	2.77	2.92	2.97
13.45	12.72	12.40	12.66	13.41
1.03	2.10	1.40	1.53	1.92
0.65	1.17	0.63	0.89	1.00
0.17	0.09	0.00	0.00	0.19
0.00	**0.16**	**0.00**	**0.15**	**0.15**
0.55	1.55	1.13	1.40	1.27
97.53	97.54	97.53	97.21	97.57
0.96	1.00	0.96	0.99	1.01
0.06	0.01	0.05	0.03	0.01
0.07	0.07	0.09	0.08	0.06
0.00	0.00	0.00	0.00	0.00
0.19	0.18	0.19	0.18	0.18
0.42	0.39	0.41	0.39	0.40
0.05	0.05	0.04	0.04	0.04
0.19	0.18	0.18	0.18	0.19
0.01	0.03	0.02	0.02	0.03
0.01	0.02	0.01	0.01	0.01
0.00	0.00	0.00	0.00	0.00
0.00	0.00	0.00	0.00	0.00
0.02	0.07	0.05	0.06	0.05
1.02	1.01	1.02	1.02	1.02
0.98	0.98	0.98	0.97	0.97
1.99	1.99	1.99	1.99	1.99
91.53	91.75	89.16	90.38	92.82
2.49	7.17	5.19	6.49	5.85
5.98	1.08	5.65	3.14	1.34
100	100	100	100	100

MILANO VSDO-13A1 MNZ6A-7 Rim	MILANO VSDO-13A1 MNZ6A-8 Rim	MILANO VSDO-13A1 MNZ6A-9 Rim	MILANO VSDO-13A1 MNZ6A-10 Core	MILANO VSDO-13A1 MNZ6A-11 Rim
29.17	29.40	28.53	28.79	30.02
0.50	0.49	0.89	0.96	0.25
7.00	7.37	8.86	7.36	7.02
0.18	0.15	0.18	0.20	0.22
12.80	12.73	12.80	13.03	13.08
27.16	26.70	26.41	27.98	27.16
2.86	2.86	2.73	3.13	2.97
12.50	12.40	11.90	12.96	11.84
1.96	1.62	1.44	1.68	1.93
1.05	1.23	1.28	0.67	1.64
0.09	0.20	0.34	0.00	0.16
0.51	**0.48**	**0.22**	**0.00**	**0.34**
1.23	1.34	1.31	0.96	1.36
97.01	96.97	96.89	97.71	97.99
0.99	1.00	0.98	0.98	1.01
0.02	0.02	0.04	0.04	0.01
0.06	0.07	0.08	0.07	0.06
0.00	0.00	0.00	0.00	0.00
0.19	0.19	0.19	0.19	0.19
0.40	0.39	0.39	0.41	0.39
0.04	0.04	0.04	0.05	0.04
0.18	0.18	0.17	0.19	0.17
0.03	0.02	0.02	0.02	0.03
0.01	0.02	0.02	0.01	0.02
0.00	0.00	0.00	0.00	0.00
0.01	0.01	0.00	0.00	0.01
0.05	0.06	0.06	0.04	0.06
1.01	1.02	1.01	1.02	1.02
0.98	0.98	0.98	0.98	0.97
1.99	1.99	1.99	1.99	1.99
92.22	91.66	90.08	91.61	92.63
5.64	6.22	6.07	4.34	6.28
2.13	2.13	3.85	4.05	1.08
100	100	100	100	100

MILANO VSDO-13A1 MNZ6A-12 Rim	MILANO VSDO-13A1 MNZ6A-13 Mantle	MILANO VSDO-13A1 MNZ6A-14 Mantle	MILANO VSDO-13A1 MNZ6A-15 Rim	MILANO VSDO-13A1 MNZ6A-16 Rim
29.75	27.63	28.21	29.83	29.57
0.27	1.38	1.45	0.30	0.29
6.40	8.25	7.93	7.18	6.73
0.38	0.24	0.09	0.16	0.14
12.65	12.54	12.87	12.71	13.24
26.88	28.81	28.85	26.76	26.62
3.27	3.54	3.34	2.61	2.79
12.13	13.25	13.45	11.76	12.15
1.94	1.01	1.25	1.97	2.03
1.36	0.30	0.53	1.47	1.51
0.23	0.00	0.00	0.00	0.29
0.28	**0.00**	**0.00**	**0.29**	**0.37**
1.34	0.78	0.61	1.52	1.39
96.89	97.73	98.58	96.57	97.11
1.01	0.95	0.96	1.01	1.00
0.01	0.06	0.06	0.01	0.01
0.06	0.08	0.07	0.07	0.06
0.00	0.00	0.00	0.00	0.00
0.19	0.19	0.19	0.19	0.20
0.39	0.43	0.42	0.39	0.39
0.05	0.05	0.05	0.04	0.04
0.17	0.19	0.19	0.17	0.17
0.03	0.01	0.02	0.03	0.03
0.02	0.00	0.01	0.02	0.02
0.00	0.00	0.00	0.00	0.00
0.01	0.00	0.00	0.01	0.01
0.06	0.03	0.03	0.07	0.06
1.02	1.01	1.02	1.02	1.01
0.97	0.99	0.98	0.97	0.98
1.99	2.00	1.99	1.99	1.99
92.61	90.71	91.25	91.56	92.37
6.21	3.51	2.71	7.12	6.38
1.18	5.78	6.04	1.32	1.25
100	100	100	100	100

MILANO VSDO-13A1 MNZ6A-17 Mantle	MILANO VSDO-13A1 MNZ6A-18 Rim	MILANO VSDO-13A1 MNZ6A-19 Core	MILANO VSDO-13A1 MNZ6A-20 Core	MILANO VSDO-13A1 MNZ6A-21 Core
25.77	28.67	28.47	29.94	28.58
2.68	0.37	1.07	0.20	0.92
14.41	6.83	7.08	6.19	7.09
0.24	0.27	0.08	0.19	0.16
10.99	12.64	13.23	12.14	12.59
25.40	26.72	28.64	28.03	28.20
2.18	3.05	3.43	3.03	2.87
11.47	12.02	13.11	13.20	13.12
0.82	1.66	1.47	2.08	1.49
0.56	1.11	0.60	0.90	0.98
0.00	0.03	0.07	0.11	0.01
0.33	**0.79**	**0.05**	**0.08**	**0.06**
1.12	1.29	0.76	1.28	0.93
95.96	95.44	98.07	97.36	97.00
0.91	0.99	0.97	1.01	0.98
0.11	0.02	0.04	0.01	0.04
0.14	0.06	0.06	0.06	0.07
0.00	0.00	0.00	0.00	0.00
0.17	0.19	0.20	0.18	0.19
0.39	0.40	0.42	0.41	0.42
0.03	0.05	0.05	0.04	0.04
0.17	0.18	0.19	0.19	0.19
0.01	0.02	0.02	0.03	0.02
0.01	0.01	0.01	0.01	0.01
0.00	0.00	0.00	0.00	0.00
0.01	0.02	0.00	0.00	0.00
0.05	0.06	0.03	0.05	0.04
1.02	1.01	1.01	1.02	1.01
0.97	0.99	0.98	0.97	0.98
1.99	2.00	2.00	1.99	1.99
82.95	92.37	92.10	93.23	91.83
5.28	6.00	3.42	5.92	4.26
11.77	1.63	4.48	0.85	3.91
100	100	100	100	100

MILANO VSDO-13A1 MNZ6A-22 Mantle	MILANO VSDO-13A1 MNZ6A-23 Core	MILANO VSDO-13A1 MNZ6A-24 Core	MILANO VSDO-13A1 MNZ6A-25 Core	MILANO VSDO-13A1 MNZ7A-1 Rim
28.51	29.78	28.00	29.04	29.00
1.17	0.20	1.52	0.84	0.93
7.33	7.17	9.84	7.94	7.24
0.18	0.22	0.33	0.09	0.02
12.89	12.61	12.30	12.70	13.81
28.58	27.03	27.30	27.43	28.23
3.11	2.85	3.19	2.75	3.11
13.28	12.87	12.38	12.93	12.50
1.35	1.90	1.16	1.64	1.47
0.59	1.30	0.41	0.86	0.91
0.10	0.18	0.00	0.00	0.00
0.04	**0.13**	**0.00**	**0.00**	**0.02**
0.73	1.51	1.03	1.13	1.01
97.86	97.75	97.46	97.35	98.26
0.97	1.00	0.96	0.99	0.98
0.05	0.01	0.06	0.03	0.04
0.07	0.06	0.09	0.07	0.07
0.00	0.00	0.00	0.00	0.00
0.19	0.19	0.18	0.19	0.20
0.42	0.39	0.40	0.40	0.41
0.05	0.04	0.05	0.04	0.05
0.19	0.18	0.18	0.19	0.18
0.02	0.03	0.02	0.02	0.02
0.01	0.02	0.01	0.01	0.01
0.00	0.00	0.00	0.00	0.00
0.00	0.00	0.00	0.00	0.00
0.03	0.06	0.04	0.05	0.04
1.02	1.01	1.02	1.02	1.02
0.98	0.98	0.97	0.97	0.98
1.99	1.99	1.99	1.99	1.99
91.81	92.16	88.72	91.18	91.56
3.27	6.97	4.74	5.20	4.55
4.92	0.87	6.54	3.62	3.89
100	100	100	100	100

MILANO VSDO-13A1 MNZ7A-2 Rim	MILANO VSDO-13A1 MNZ7A-3 Mantle	MILANO VSDO-13A1 MNZ7A-4 Core	MILANO VSDO-13A1 MNZ7A-5 Core	MILANO VSDO-13A1 MNZ7A-6 Mantle
29.49	30.06	29.56	29.64	29.26
0.26	0.19	0.28	0.33	0.66
4.85	4.08	4.37	4.01	4.17
0.27	0.45	0.32	0.51	0.25
14.12	13.54	15.11	14.01	13.92
28.09	27.49	29.62	28.16	28.95
2.90	2.98	3.27	3.38	3.15
12.06	11.73	12.30	12.02	12.20
1.87	1.72	1.32	1.83	1.88
1.32	1.42	0.77	1.77	1.54
0.17	0.60	0.08	0.43	0.43
0.31	**1.80**	**0.03**	**0.71**	**0.75**
1.03	0.94	0.83	0.90	0.57
96.74	97.00	97.87	97.70	97.72
1.00	1.01	1.00	1.00	0.99
0.01	0.01	0.01	0.01	0.03
0.04	0.04	0.04	0.04	0.04
0.00	0.00	0.00	0.00	0.00
0.21	0.20	0.22	0.21	0.20
0.41	0.40	0.43	0.41	0.42
0.04	0.04	0.05	0.05	0.05
0.17	0.17	0.18	0.17	0.17
0.03	0.02	0.02	0.03	0.03
0.02	0.02	0.01	0.02	0.02
0.00	0.01	0.00	0.01	0.01
0.01	0.04	0.00	0.01	0.02
0.04	0.04	0.04	0.04	0.02
1.01	1.02	1.01	1.01	1.01
0.98	0.97	0.99	0.98	0.98
1.99	1.99	2.00	2.00	1.99
94.22	94.96	95.10	94.63	94.77
4.67	4.25	3.73	4.02	2.52
1.11	0.79	1.17	1.36	2.72
100	100	100	100	100

MILANO VSDO-13A1 MNZ7A-7 Rim	MILANO VSDO-13A1 MNZ7A-8 Rim	MILANO VSDO-13A1 MNZ7A-9 Core	MILANO VSDO-13A1 MNZ7A-10 Rim	MILANO VSDO-13A1 MNZ7A-11 Mantle
29.80	29.73	29.90	28.90	29.45
0.32	0.24	0.28	0.69	0.48
4.76	4.76	4.25	4.50	4.68
0.28	0.39	0.36	0.46	0.15
14.25	14.03	14.33	14.20	14.16
28.53	28.45	28.77	29.32	28.39
3.01	2.77	2.84	3.20	3.35
12.30	12.37	12.37	12.56	12.23
1.67	1.80	1.79	1.72	1.92
1.47	1.61	1.47	0.92	1.29
0.22	0.25	0.37	0.00	0.14
0.34	**0.31**	**0.91**	**0.26**	**0.42**
0.85	0.98	0.95	0.56	0.85
97.80	97.69	98.58	97.28	97.51
1.00	1.00	1.00	0.98	0.99
0.01	0.01	0.01	0.03	0.02
0.04	0.04	0.04	0.04	0.04
0.00	0.00	0.00	0.00	0.00
0.21	0.21	0.21	0.21	0.21
0.41	0.41	0.42	0.43	0.41
0.04	0.04	0.04	0.05	0.05
0.17	0.18	0.17	0.18	0.17
0.02	0.02	0.02	0.02	0.03
0.02	0.02	0.02	0.01	0.02
0.00	0.00	0.00	0.00	0.00
0.01	0.01	0.02	0.01	0.01
0.04	0.04	0.04	0.02	0.04
1.02	1.01	1.01	1.01	1.01
0.98	0.98	0.99	0.98	0.98
1.99	1.99	2.00	1.99	1.99
94.78	94.54	94.68	94.64	94.17
3.86	4.43	4.18	2.49	3.80
1.36	1.03	1.14	2.88	2.02
100	100	100	100	100

MILANO VSDO-13A1 MNZ7A-12 Mantle	MILANO VSDO-13A1 MNZ7A-13 Mantle	MILANO VSDO-13A1 MNZ7A-14 Rim	MILANO VSDO-13A1 MNZ7A-15 Rim	MILANO VSDO-13A1 MNZ7B-1 Rim
30.01	30.00	29.56	29.23	30.09
0.33	0.29	0.27	0.49	0.15
4.29	4.54	4.38	5.22	3.68
0.31	0.38	0.33	0.19	0.37
14.14	13.44	13.88	14.15	13.91
28.25	27.40	28.12	28.30	26.57
3.13	2.88	3.12	3.24	2.78
12.11	12.16	11.88	12.02	11.56
1.79	1.98	1.87	1.79	2.43
1.62	1.52	1.52	1.11	2.34
0.32	0.25	0.26	0.03	0.50
1.35	**1.49**	**0.37**	**0.36**	**1.66**
0.85	0.96	0.94	0.98	0.92
98.50	97.28	96.50	97.11	96.95
1.00	1.01	1.01	0.99	1.01
0.01	0.01	0.01	0.02	0.01
0.04	0.04	0.04	0.05	0.03
0.00	0.00	0.00	0.00	0.00
0.21	0.20	0.21	0.21	0.20
0.41	0.40	0.41	0.42	0.39
0.04	0.04	0.05	0.05	0.04
0.17	0.17	0.17	0.17	0.16
0.02	0.03	0.03	0.02	0.03
0.02	0.02	0.02	0.01	0.03
0.00	0.00	0.00	0.00	0.01
0.03	0.03	0.01	0.01	0.04
0.04	0.04	0.04	0.04	0.04
1.01	1.02	1.02	1.01	1.02
0.98	0.97	0.98	0.98	0.97
1.99	1.99	1.99	2.00	1.99
94.90	94.47	94.56	93.51	95.24
3.75	4.32	4.30	4.42	4.14
1.35	1.20	1.14	2.07	0.62
100	100	100	100	100

MILANO VSDO-13A1 MNZ7B-2 Rim	MILANO VSDO-13A1 MNZ7B-3 Core	MILANO VSDO-13A1 MNZ7B-4 Core	MILANO VSDO-13A1 MNZ7B-5 Core	MILANO VSDO-13A1 MNZ7B-6 Core
30.04	29.82	29.44	29.82	30.01
0.08	0.34	0.29	0.36	0.32
3.67	4.26	4.32	4.34	4.10
0.39	0.42	0.39	0.61	0.44
13.79	13.93	13.82	13.86	14.25
26.40	28.54	28.15	28.21	28.31
2.68	3.17	3.06	3.03	2.94
11.42	12.13	12.13	11.56	12.30
2.66	2.12	2.01	1.86	2.01
2.51	1.28	1.26	1.17	1.52
0.96	0.39	0.10	0.41	0.25
1.95	**0.63**	**0.22**	**0.98**	**0.38**
0.94	0.87	1.35	0.86	0.92
97.50	97.91	96.54	97.07	97.75
1.01	1.00	1.00	1.00	1.01
0.00	0.01	0.01	0.01	0.01
0.03	0.04	0.04	0.04	0.04
0.00	0.00	0.00	0.01	0.00
0.20	0.20	0.20	0.20	0.21
0.38	0.41	0.41	0.41	0.41
0.04	0.05	0.04	0.04	0.04
0.16	0.17	0.17	0.16	0.17
0.04	0.03	0.03	0.03	0.03
0.03	0.02	0.02	0.02	0.02
0.01	0.01	0.00	0.01	0.00
0.04	0.01	0.00	0.02	0.01
0.04	0.04	0.06	0.04	0.04
1.01	1.01	1.01	1.02	1.02
0.98	0.98	0.99	0.97	0.97
1.99	1.99	2.00	1.99	1.99
95.46	94.66	92.72	94.55	94.52
4.21	3.91	6.05	3.91	4.12
0.33	1.44	1.23	1.54	1.36
100	100	100	100	100

MILANO VSDO-13A1 MNZ7B-7 Rim	MILANO VSDO-13A1 MNZ7B-8 Rim	MILANO VSDO-13A1 MNZ7B-9 Core	MILANO VSDO-13A1 MNZ7B-10 Rim	MILANO VSDO-13A1 MNZ7B-11 Rim
29.60	29.86	30.31	29.90	29.18
0.26	0.30	0.31	0.45	0.67
4.29	4.04	4.45	4.86	4.74
0.38	0.37	0.58	0.17	0.12
13.99	13.97	14.19	13.71	13.94
28.32	27.42	28.38	27.48	30.08
3.24	3.20	2.96	3.17	3.76
12.01	11.39	12.37	11.97	12.98
1.89	1.50	1.86	1.81	1.03
1.42	1.09	1.09	1.59	0.86
0.05	0.52	0.48	0.38	0.26
0.28	**2.35**	**0.33**	**1.56**	**0.15**
0.90	0.90	0.98	0.83	0.52
96.64	96.92	98.28	97.88	98.29
1.01	1.00	1.01	1.00	0.99
0.01	0.01	0.01	0.02	0.03
0.04	0.04	0.04	0.04	0.04
0.00	0.00	0.01	0.00	0.00
0.21	0.20	0.21	0.20	0.21
0.42	0.40	0.41	0.40	0.44
0.05	0.05	0.04	0.05	0.05
0.17	0.16	0.17	0.17	0.18
0.03	0.02	0.03	0.02	0.01
0.02	0.01	0.01	0.02	0.01
0.00	0.01	0.01	0.00	0.00
0.01	0.05	0.01	0.03	0.00
0.04	0.04	0.04	0.04	0.02
1.02	1.01	1.02	1.02	1.01
0.98	0.98	0.97	0.97	0.98
1.99	1.99	1.99	1.99	1.99
94.79	94.75	94.29	94.43	94.91
4.09	4.00	4.42	3.70	2.32
1.12	1.26	1.29	1.87	2.77
100	100	100	100	100

MILANO VSDO-13A1 MNZ7B-12 Core	MILANO VSDO-13A1 MNZ7B-13 Core	MILANO VSDO-13A1 MNZ7B-14 Rim		MILANO VSDO-13A2 MNZ8A-1 Mantle
29.64	30.01	29.72		30.07
0.27	0.42	0.41		0.30
4.44	4.25	4.70		5.14
0.55	0.44	0.41		0.43
13.98	14.05	14.31		14.18
28.40	27.69	28.54		27.50
3.13	3.41	3.09		3.40
12.17	11.96	12.00		11.86
1.94	2.06	2.05		1.93
1.44	1.65	1.34		1.54
0.24	0.49	0.30		0.14
0.34	**0.79**	**0.16**		**0.43**
0.92	0.90	1.00		1.14
97.46	98.12	98.04		98.07
1.00	1.00	1.00		1.00
0.01	0.02	0.02		0.01
0.04	0.04	0.04		0.05
0.00	0.00	0.00		0.00
0.21	0.20	0.21		0.21
0.42	0.40	0.41		0.40
0.05	0.05	0.04		0.05
0.17	0.17	0.17		0.17
0.03	0.03	0.03		0.03
0.02	0.02	0.02		0.02
0.00	0.01	0.00		0.00
0.01	0.02	0.00		0.01
0.04	0.04	0.04		0.05
1.01	1.02	1.01		1.02
0.98	0.97	0.98		0.98
1.99	1.99	1.99		1.99
94.72	94.23	93.79		93.58
4.15	4.02	4.49		5.16
1.13	1.75	1.71		1.26
100	100	100		100

MILANO VSDO-13A2 MNZ8A-2 core	MILANO VSDO-13A2 MNZ8A-3 Mantle	MILANO VSDO-13A2 MNZ8A-4 Mantle	MILANO VSDO-13A2 MNZ8A-5 Mantle	MILANO VSDO-13A2 MNZ8A-6 Mantle
29.97	29.47	27.35	29.99	27.70
0.28	0.43	1.99	0.23	1.43
5.16	5.72	9.14	5.31	7.82
0.38	0.17	0.07	0.36	0.07
13.95	13.91	12.95	14.09	13.42
28.60	28.57	28.65	27.26	28.41
3.30	3.15	3.26	3.16	3.10
12.39	12.19	12.53	11.97	12.40
1.68	1.74	0.72	2.35	1.17
0.98	0.70	0.18	1.91	0.63
0.00	0.00	0.00	0.10	0.15
0.08	**0.01**	**0.04**	**0.49**	**0.00**
1.08	1.05	0.49	1.08	0.60
97.84	97.11	97.37	98.30	96.89
1.01	1.00	0.94	1.00	0.96
0.01	0.02	0.08	0.01	0.06
0.05	0.05	0.08	0.05	0.07
0.00	0.00	0.00	0.00	0.00
0.20	0.21	0.19	0.21	0.20
0.41	0.42	0.43	0.39	0.42
0.05	0.05	0.05	0.05	0.05
0.18	0.17	0.18	0.17	0.18
0.02	0.02	0.01	0.03	0.02
0.01	0.01	0.00	0.03	0.01
0.00	0.00	0.00	0.00	0.00
0.00	0.00	0.00	0.01	0.00
0.05	0.04	0.02	0.05	0.03
1.02	1.02	1.02	1.01	1.01
0.97	0.98	0.97	0.98	0.98
1.99	1.99	1.99	1.99	1.99
93.94	93.37	89.39	94.15	91.26
4.89	4.79	2.23	4.89	2.71
1.17	1.84	8.39	0.96	6.03
100	100	100	100	100

MILANO VSDO-13A2 MNZ8A-7 Core	MILANO VSDO-13A2 MNZ8A-8 Mantle	MILANO VSDO-13A2 MNZ8A-9 Core	MILANO VSDO-13A2 MNZ8A-10 Mantle	MILANO VSDO-13A2 MNZ8A-11 Rim
29.69	29.75	29.67	29.83	27.44
0.23	0.36	0.42	0.29	1.87
4.61	4.67	4.97	4.66	8.96
0.79	0.17	0.27	0.09	0.09
13.44	13.77	14.32	14.54	13.05
28.29	28.04	28.75	27.86	28.19
3.33	3.19	2.83	3.14	3.39
12.39	11.59	12.34	11.69	12.38
1.75	1.53	1.97	1.41	0.75
1.29	1.39	0.99	1.67	0.40
0.08	0.61	0.00	0.37	0.00
0.10	**1.47**	**0.10**	**1.27**	**0.00**
1.11	0.94	1.03	0.90	0.47
97.10	97.49	97.66	97.72	96.98
1.01	1.00	1.00	1.00	0.95
0.01	0.01	0.02	0.01	0.08
0.04	0.04	0.04	0.04	0.08
0.01	0.00	0.00	0.00	0.00
0.20	0.20	0.21	0.21	0.20
0.41	0.41	0.42	0.40	0.42
0.05	0.05	0.04	0.05	0.05
0.18	0.16	0.18	0.17	0.18
0.02	0.02	0.03	0.02	0.01
0.02	0.02	0.01	0.02	0.01
0.00	0.01	0.00	0.00	0.00
0.00	0.03	0.00	0.03	0.00
0.05	0.04	0.04	0.04	0.02
1.01	1.01	1.02	1.01	1.02
0.98	0.98	0.98	0.98	0.97
1.99	1.99	1.99	1.99	1.99
93.96	94.27	93.60	94.75	89.91
5.06	4.22	4.62	4.03	2.14
0.97	1.51	1.77	1.22	7.95
100	100	100	100	100

MILANO VSDO-13A2 MNZ8A-12 Rim	MILANO VSDO-13A2 MNZ8A-13 Mantle	MILANO VSDO-13A2 MNZ8B-1 Rim	MILANO VSDO-13A2 MNZ8B-2 Mantle	MILANO VSDO-13A2 MNZ8B-3 Mantle
30.23	29.57	29.73	29.26	29.57
0.29	0.31	0.17	0.22	0.21
5.45	4.55	4.59	5.34	3.23
0.24	0.09	0.26	0.25	0.30
13.60	14.08	13.36	13.95	14.28
26.82	28.20	26.75	27.88	29.90
2.66	3.09	2.72	2.94	3.50
11.50	11.86	11.69	11.75	12.90
2.08	1.60	1.98	2.21	1.85
1.96	1.17	1.58	1.43	1.29
0.16	0.48	0.65	0.29	0.07
0.65	**1.17**	**2.12**	**0.37**	**0.09**
1.11	0.94	0.97	1.13	0.68
96.75	97.11	96.57	97.03	97.87
1.02	1.00	1.01	1.00	1.00
0.01	0.01	0.01	0.01	0.01
0.05	0.04	0.04	0.05	0.03
0.00	0.00	0.00	0.00	0.00
0.20	0.21	0.20	0.21	0.21
0.39	0.41	0.39	0.41	0.44
0.04	0.04	0.04	0.04	0.05
0.16	0.17	0.17	0.17	0.18
0.03	0.02	0.03	0.03	0.03
0.03	0.02	0.02	0.02	0.02
0.00	0.01	0.01	0.00	0.00
0.01	0.02	0.05	0.01	0.00
0.05	0.04	0.04	0.05	0.03
1.03	1.01	1.01	1.01	1.01
0.96	0.98	0.98	0.99	0.99
1.98	2.00	1.99	2.00	2.00
93.59	94.49	94.87	93.91	96.12
5.14	4.20	4.41	5.15	3.02
1.27	1.31	0.72	0.94	0.86
100	100	100	100	100

MILANO VSDO-13A2 MNZ8B-4 Mantle	MILANO VSDO-13A2 MNZ8B-5 Rim	MILANO VSDO-13A2 MNZ8B-6 Mantle	MILANO VSDO-13A2 MNZ8B-7 Mantle	MILANO VSDO-13A2 MNZ8B-8 Core
29.67	29.69	29.65	29.55	29.47
0.15	0.13	0.23	0.19	0.22
3.03	4.71	5.44	5.13	4.73
0.05	0.18	0.27	0.25	0.86
14.44	13.69	14.11	13.82	13.46
30.23	27.22	27.47	27.48	27.92
3.61	2.65	2.44	3.31	3.00
12.68	11.71	11.78	11.91	11.93
1.99	1.75	2.28	1.98	2.18
1.00	1.75	1.57	1.68	2.00
0.00	0.35	0.41	0.52	0.14
0.17	**1.70**	**0.49**	**0.60**	**0.52**
0.68	1.02	1.20	1.04	1.10
97.70	96.55	97.34	97.47	97.53
1.00	1.01	1.00	1.00	1.00
0.01	0.01	0.01	0.01	0.01
0.03	0.04	0.05	0.05	0.04
0.00	0.00	0.00	0.00	0.01
0.21	0.20	0.21	0.20	0.20
0.44	0.40	0.40	0.40	0.41
0.05	0.04	0.04	0.05	0.04
0.18	0.17	0.17	0.17	0.17
0.03	0.02	0.03	0.03	0.03
0.01	0.02	0.02	0.02	0.03
0.00	0.00	0.01	0.01	0.00
0.00	0.04	0.01	0.01	0.01
0.03	0.04	0.05	0.04	0.05
1.01	1.01	1.01	1.01	1.01
0.99	0.98	0.98	0.99	0.99
2.00	1.99	2.00	2.00	2.00
96.39	94.80	93.58	94.46	94.08
3.01	4.64	5.47	4.73	4.97
0.61	0.56	0.96	0.81	0.95
100	100	100	100	100

MILANO VSDO-13A2 MNZ8B-9 Core	MILANO VSDO-13A2 MNZ8B-10 Core	MILANO VSDO-13A2 MNZ8B-11 Core	MILANO VSDO-13A2 MNZ8B-12 Mantle	MILANO VSDO-13A2 MNZ8B-13 Mantle
29.86	29.72	30.06	27.97	27.29
0.25	0.18	0.14	1.46	2.06
4.27	5.04	2.91	6.97	9.17
0.60	0.99	0.58	0.00	0.19
13.78	13.50	14.08	13.93	13.03
27.90	27.56	29.25	29.00	28.89
3.00	3.19	3.53	3.50	3.20
12.23	11.82	12.34	13.27	12.70
2.16	1.67	2.24	1.02	0.69
1.39	1.44	1.36	0.00	0.27
0.36	0.51	0.06	0.00	0.10
0.65	**0.64**	**0.21**	**0.00**	**0.00**
1.03	1.24	0.81	0.54	0.51
97.49	97.51	97.57	97.66	98.09
1.00	1.00	1.01	0.96	0.93
0.01	0.01	0.01	0.06	0.08
0.04	0.05	0.03	0.06	0.08
0.01	0.01	0.01	0.00	0.00
0.20	0.20	0.21	0.21	0.19
0.41	0.40	0.43	0.43	0.43
0.04	0.05	0.05	0.05	0.05
0.17	0.17	0.17	0.19	0.18
0.03	0.02	0.03	0.01	0.01
0.02	0.02	0.02	0.00	0.00
0.00	0.01	0.00	0.00	0.00
0.01	0.01	0.00	0.00	0.00
0.04	0.05	0.03	0.02	0.02
1.01	1.01	1.02	1.02	1.02
0.98	0.98	0.98	0.98	0.98
1.99	2.00	1.99	2.00	1.99
94.28	93.57	95.79	91.59	89.16
4.66	5.65	3.62	2.37	2.29
1.06	0.78	0.59	6.04	8.55
100	100	100	100	100

MILANO	MILANO	MILANO	MILANO	MILANO
VSDO-13A2	VSDO-13A2	VSDO-13A2	VSDO-13A2	VSDO-13A2
MNZ8B-14	MNZ8B-15	MNZ8B-16	MNZ8B-17	MNZ8B-18
Mantle	Mantle	Mantle	Core	Mantle
27.07	26.73	28.50	30.13	29.77
1.82	2.22	0.95	0.14	0.38
8.76	10.56	5.72	3.14	5.24
0.18	0.20	0.19	0.37	0.20
13.34	12.89	13.72	14.67	14.42
28.52	27.86	29.93	29.66	27.38
3.07	3.19	3.10	3.10	2.81
12.94	12.46	12.76	13.05	11.83
0.74	0.61	0.81	2.07	1.83
0.41	0.49	0.40	1.02	1.44
0.16	0.05	0.00	0.02	0.08
0.02	**0.01**	**0.00**	**0.19**	**0.66**
0.42	0.60	0.65	0.68	1.01
97.44	97.87	96.73	98.24	97.06
0.94	0.92	0.98	1.01	1.00
0.07	0.09	0.04	0.01	0.02
0.08	0.10	0.05	0.03	0.05
0.00	0.00	0.00	0.00	0.00
0.20	0.19	0.20	0.21	0.21
0.43	0.42	0.44	0.43	0.40
0.05	0.05	0.05	0.04	0.04
0.19	0.18	0.18	0.18	0.17
0.01	0.01	0.01	0.03	0.03
0.01	0.01	0.01	0.01	0.02
0.00	0.00	0.00	0.00	0.00
0.00	0.00	0.00	0.00	0.01
0.02	0.03	0.03	0.03	0.04
1.01	1.01	1.02	1.01	1.02
0.98	0.98	0.98	0.98	0.97
2.00	2.00	1.99	1.99	1.99
90.46	87.99	93.06	96.41	93.76
1.89	2.69	2.95	3.02	4.61
7.64	9.32	3.99	0.57	1.62
100	100	100	100	100

MILANO VSDO-13A2 MNZ8B-19 Core	MILANO VSDO-13A2 MNZ8B-20 Mantle	MILANO VSDO-13A2 MNZ8B-21 Mantle	MILANO VSDO-13A2 MNZ8B-22 Rim	MILANO VSDO-13A2 MNZ8C-1 Rim
30.05	29.77	29.82	29.69	29.90
0.22	0.22	0.24	0.20	0.28
4.14	5.37	3.26	5.29	6.10
0.73	0.18	0.31	0.21	0.48
13.93	13.56	14.10	14.00	13.65
28.61	27.77	29.89	27.53	26.94
3.09	2.80	3.18	3.19	2.83
12.14	11.79	12.63	11.71	11.52
1.83	2.18	2.13	1.95	2.21
1.67	1.59	1.04	1.46	2.03
0.12	0.21	0.00	0.21	0.38
0.52	**0.46**	**0.07**	**0.51**	**0.60**
0.95	1.14	0.69	1.09	1.26
98.00	97.04	97.36	97.03	98.18
1.01	1.01	1.01	1.01	1.00
0.01	0.01	0.01	0.01	0.01
0.04	0.05	0.03	0.05	0.05
0.01	0.00	0.00	0.00	0.00
0.20	0.20	0.21	0.21	0.20
0.41	0.41	0.44	0.40	0.39
0.04	0.04	0.05	0.05	0.04
0.17	0.17	0.18	0.17	0.16
0.02	0.03	0.03	0.03	0.03
0.02	0.02	0.01	0.02	0.03
0.00	0.00	0.00	0.00	0.00
0.01	0.01	0.00	0.01	0.01
0.04	0.05	0.03	0.05	0.05
1.02	1.02	1.02	1.01	1.01
0.98	0.98	0.98	0.98	0.98
1.99	1.99	1.99	1.99	1.99
94.80	93.82	95.87	94.18	93.09
4.27	5.22	3.11	4.97	5.72
0.93	0.96	1.02	0.85	1.19
100	100	100	100	100

MILANO VSDO-13A2 MNZ8C-2 Core	MILANO VSDO-13A2 MNZ8C-3 Core	MILANO VSDO-13A2 MNZ8C-4 Core	MILANO VSDO-13A2 MNZ8C-5 Mantle	MILANO VSDO-13A2 MNZ8C-6 Mantle
27.66	27.12	27.52	29.77	29.47
1.81	2.18	1.71	0.26	0.53
9.15	10.38	8.76	5.80	5.63
0.00	0.20	0.17	0.29	0.04
13.42	12.31	12.88	13.84	13.95
28.70	27.80	28.31	26.89	28.42
3.29	2.90	3.27	2.87	3.40
12.49	12.42	12.51	11.58	12.44
0.77	0.99	0.98	2.31	1.49
0.24	0.50	0.53	1.39	0.98
0.00	0.00	0.00	0.34	0.34
0.07	**0.00**	**0.03**	**0.75**	**0.73**
0.65	0.68	0.62	1.23	0.78
98.25	97.49	97.29	97.32	98.19
0.94	0.93	0.95	1.00	0.99
0.07	0.09	0.07	0.01	0.02
0.08	0.10	0.08	0.05	0.05
0.00	0.00	0.00	0.00	0.00
0.20	0.18	0.19	0.20	0.20
0.42	0.41	0.42	0.39	0.41
0.05	0.04	0.05	0.04	0.05
0.18	0.18	0.18	0.16	0.18
0.01	0.01	0.01	0.03	0.02
0.00	0.01	0.01	0.02	0.01
0.00	0.00	0.00	0.00	0.00
0.00	0.00	0.00	0.02	0.02
0.03	0.03	0.03	0.05	0.03
1.02	1.02	1.02	1.01	1.01
0.98	0.97	0.98	0.98	0.98
1.99	1.99	1.99	1.99	1.99
89.55	87.68	89.95	93.30	94.31
2.91	3.09	2.82	5.62	3.49
7.54	9.23	7.23	1.09	2.20
100	100	100	100	100

MILANO VSDO-13A2 MNZ8C-7 Core	MILANO VSDO-13A2 MNZ8C-8 Rim	MILANO VSDO-13A2 MNZ8C-9 Rim		PARIS VSDO-13M1 MNZ7-1 Mantle
27.62	30.19	29.19		29.42
1.99	0.24	0.24		0.26
10.54	5.58	5.37		5.00
0.10	0.16	0.23		0.16
12.42	13.74	14.29		13.95
28.01	27.44	26.83		28.20
3.18	3.07	2.51		2.89
12.43	11.63	11.23		10.97
0.61	2.25	2.58		2.05
0.49	1.40	1.91		1.03
0.06	0.18	0.00		
0.19	**0.48**	**0.58**		**0.60**
0.72	1.20	1.07		1.01
98.37	97.56	96.03		95.77
0.94	1.01	1.00		1.01
0.08	0.01	0.01		0.01
0.10	0.05	0.05		0.05
0.00	0.00	0.00		0.00
0.18	0.20	0.21		0.21
0.41	0.40	0.40		0.42
0.05	0.04	0.04		0.04
0.18	0.16	0.16		0.16
0.01	0.03	0.04		0.03
0.01	0.02	0.03		0.01
0.00	0.00	0.00		0.00
0.00	0.01	0.01		0.01
0.03	0.05	0.05		0.04
1.02	1.02	1.01		1.02
0.97	0.97	0.98		0.97
1.99	1.99	1.99		1.99
88.37	93.50	94.04		94.20
3.25	5.47	4.92		4.67
8.38	1.03	1.05		1.14
100	100	100		100

PARIS VSDO-13M1 MNZ7-2 Core	PARIS VSDO-13M1 MNZ7-3 Core	PARIS VSDO-13M1 MNZ7-4 Core	PARIS VSDO-13M1 MNZ7-5 Core	PARIS VSDO-13M1 MNZ7-6 Rim
29.47	29.06	29.36	29.51	29.68
0.31	0.31	0.32	0.34	0.32
4.79	4.40	5.71	4.68	5.00
0.11	0.43	0.10	0.43	0.06
13.75	15.22	13.94	14.24	13.95
28.94	27.77	29.07	27.99	27.53
3.46	2.99	3.14	3.25	3.40
12.58	11.60	11.93	11.87	12.02
2.11	2.13	1.99	2.12	2.32
0.94	1.03	0.94	0.83	1.07
0.11	**0.34**	**0.09**	**0.20**	**0.41**
0.90	0.84	1.07	0.87	0.96
97.76	96.32	98.13	96.35	96.73
1.00	1.00	0.99	1.00	1.01
0.01	0.01	0.01	0.01	0.01
0.04	0.04	0.05	0.04	0.05
0.00	0.00	0.00	0.00	0.00
0.20	0.23	0.21	0.21	0.21
0.42	0.41	0.43	0.41	0.40
0.05	0.04	0.05	0.05	0.05
0.18	0.17	0.17	0.17	0.17
0.03	0.03	0.03	0.03	0.03
0.01	0.01	0.01	0.01	0.01
0.00	0.00	0.00	0.00	0.00
0.00	0.01	0.00	0.00	0.01
0.04	0.04	0.05	0.04	0.04
1.01	1.01	1.01	1.02	1.02
0.98	0.98	0.99	0.97	0.97
2.00	1.99	2.00	1.99	1.99
94.63	94.86	93.80	94.53	94.24
4.07	3.82	4.86	4.01	4.39
1.30	1.32	1.34	1.46	1.38
100	100	100	100	100

PARIS VSDO-13M1 MNZ7-7 Core	PARIS VSDO-13M1 MNZ7-8 Core	PARIS VSDO-13M1 MNZ8-1 Mantle	PARIS VSDO-13M1 MNZ8-2 Mantle	PARIS VSDO-13M1 MNZ8-3 Core
29.32	29.57	29.12	29.45	29.55
0.34	0.35	0.34	0.31	0.29
4.68	4.18	5.03	5.04	4.99
0.38	0.35	0.10	0.20	0.15
14.37	14.71	13.41	13.89	14.04
28.51	28.02	28.46	27.22	26.91
3.05	3.73	2.94	3.48	3.07
11.93	11.21	11.26	11.48	11.89
2.26	1.85	2.43	2.64	2.81
1.03	0.67	1.70	2.11	1.13
0.18	**0.25**	**0.43**	**0.43**	**0.41**
0.88	0.80	1.02	1.03	0.98
96.92	95.70	96.24	97.27	96.26
1.00	1.01	1.00	1.00	1.01
0.01	0.01	0.01	0.01	0.01
0.04	0.04	0.05	0.05	0.05
0.00	0.00	0.00	0.00	0.00
0.21	0.22	0.20	0.21	0.21
0.42	0.41	0.42	0.40	0.40
0.04	0.05	0.04	0.05	0.04
0.17	0.16	0.16	0.16	0.17
0.03	0.03	0.03	0.04	0.04
0.01	0.01	0.02	0.03	0.02
0.00	0.00	0.00	0.00	0.00
0.00	0.01	0.01	0.01	0.01
0.04	0.03	0.04	0.04	0.04
1.01	1.02	1.01	1.01	1.02
0.98	0.96	0.99	0.98	0.97
1.99	1.99	2.00	2.00	1.99
94.59	94.79	93.88	94.03	94.25
3.97	3.71	4.66	4.67	4.52
1.44	1.50	1.46	1.30	1.23
100	100	100	100	100

PARIS VSDO-13M1 MNZ8-4 Core	PARIS VSDO-13M1 MNZ8-5 Core	PARIS VSDO-13M1 MNZ8-6 Mantle	PARIS VSDO-13M1 MNZ8-7 Mantle	PARIS VSDO-13M1 MNZ9-1 Rim
29.26	29.31	29.33	29.30	29.01
0.86	0.29	0.29	0.30	0.38
5.33	5.27	5.52	5.94	5.18
0.20	0.15	0.19	0.01	0.14
13.76	13.84	14.86	14.95	13.08
26.63	27.31	26.28	25.02	25.71
2.52	2.99	3.51	2.70	3.16
11.20	10.55	11.00	11.10	10.20
2.24	2.51	2.89	1.92	2.02
1.03	1.67	1.94	1.51	1.22
0.61	**0.92**	**0.49**	**2.15**	**1.86**
1.09	1.04	1.06	1.12	1.04
95.46	96.08	97.66	96.74	93.80
1.00	1.00	1.00	1.00	1.01
0.03	0.01	0.01	0.01	0.02
0.05	0.05	0.05	0.05	0.05
0.00	0.00	0.00	0.00	0.00
0.20	0.21	0.22	0.22	0.20
0.39	0.40	0.39	0.37	0.39
0.04	0.04	0.05	0.04	0.05
0.16	0.15	0.16	0.16	0.15
0.03	0.03	0.04	0.03	0.03
0.01	0.02	0.03	0.02	0.02
0.00	0.00	0.00	0.00	0.00
0.01	0.02	0.01	0.05	0.04
0.05	0.04	0.05	0.05	0.05
1.03	1.01	1.01	1.01	1.02
0.95	0.98	0.99	0.99	0.96
1.99	1.99	2.00	2.00	1.99
91.27	93.97	94.00	93.60	93.40
5.01	4.77	4.79	5.12	4.92
3.72	1.26	1.21	1.28	1.67
100	100	100	100	100

PARIS VSDO-13M1 MNZ9-2 Core	PARIS VSDO-13M1 MNZ9-3 Core	PARIS VSDO-13M1 MNZ9-4 Core	PARIS VSDO-13M1 MNZ9-5 Rim	PARIS VSDO-13M1 MNZ9-6 Core
29.61	29.50	29.75	29.73	29.62
0.35	0.33	0.31	0.26	0.32
6.27	5.65	5.24	5.54	5.31
0.09	0.16	0.14	0.10	0.09
13.56	13.52	14.11	13.78	13.70
27.76	28.58	27.85	25.43	28.85
3.37	3.38	3.34	3.40	2.77
12.04	11.45	11.35	10.45	11.55
2.32	1.62	2.01	2.06	2.33
0.45	0.70	1.11	1.33	1.46
0.15	**0.32**	**0.36**	**2.40**	**0.78**
1.22	1.08	1.05	1.08	1.13
97.33	96.58	96.65	95.65	97.94
1.00	1.00	1.01	1.01	1.00
0.01	0.01	0.01	0.01	0.01
0.06	0.05	0.05	0.05	0.05
0.00	0.00	0.00	0.00	0.00
0.20	0.20	0.21	0.20	0.20
0.41	0.42	0.41	0.37	0.42
0.05	0.05	0.05	0.05	0.04
0.17	0.16	0.16	0.15	0.16
0.03	0.02	0.03	0.03	0.03
0.01	0.01	0.01	0.02	0.02
0.00	0.00	0.00	0.00	0.00
0.00	0.01	0.01	0.05	0.02
0.05	0.05	0.05	0.05	0.05
1.02	1.02	1.02	1.02	1.01
0.98	0.97	0.97	0.97	0.99
1.99	1.99	1.99	1.99	2.00
92.91	93.61	93.83	93.90	93.64
5.58	4.98	4.84	5.00	5.04
1.51	1.41	1.33	1.10	1.31
100	100	100	100	100

PARIS VSDO-13M1 MNZ9-7 Core	PARIS VSDO-13M1 MNZ2-1 Rim	PARIS VSDO-13M1 MNZ2-2 Core	PARIS VSDO-13M1 MNZ2-3 Core	PARIS VSDO-13M1 MNZ2-4 Core
29.72	29.74	29.67	29.72	29.49
0.32	0.29	0.28	0.28	0.39
5.28	4.28	4.33	4.23	6.24
0.15	0.36	0.34	0.36	0.07
13.90	12.93	14.61	13.86	15.77
28.79	27.87	28.46	28.44	25.90
3.59	2.81	2.50	3.17	2.96
11.73	12.93	12.91	12.85	10.93
1.90	1.93	1.96	2.23	1.91
1.23	1.19	0.94	1.09	0.46
0.27	**0.25**	**0.14**	**0.23**	**0.74**
1.06	0.87	0.92	0.92	1.10
98.18	95.71	97.05	97.57	95.99
1.00	1.01	1.00	1.00	1.00
0.01	0.01	0.01	0.01	0.02
0.05	0.04	0.04	0.04	0.06
0.00	0.00	0.00	0.00	0.00
0.20	0.19	0.22	0.20	0.23
0.42	0.41	0.42	0.42	0.38
0.05	0.04	0.04	0.05	0.04
0.17	0.19	0.18	0.18	0.16
0.03	0.03	0.03	0.03	0.03
0.02	0.02	0.01	0.01	0.01
0.00	0.00	0.00	0.00	0.00
0.01	0.01	0.00	0.00	0.02
0.05	0.04	0.04	0.04	0.05
1.01	1.03	1.02	1.01	1.02
0.98	0.96	0.98	0.98	0.97
1.99	1.98	1.99	1.99	1.99
93.91	94.71	94.66	94.68	93.21
4.76	4.03	4.15	4.14	5.10
1.33	1.26	1.19	1.19	1.69
100	100	100	100	100

PARIS VSDO-13M1 MNZ2-5 Core	PARIS VSDO-13M1 MNZ2-6 Rim	PARIS VSDO-13M1 MNZ1-1 Rim	PARIS VSDO-13M1 MNZ1-2 Core	PARIS VSDO-13M1 MNZ1-3 Core
29.42	29.69	29.95	29.56	29.69
0.28	0.26	0.27	0.29	0.34
4.38	4.62	5.41	4.92	4.79
0.39	0.25	0.20	0.16	0.23
13.96	14.03	13.94	14.01	14.20
29.14	28.27	27.15	28.98	29.13
3.81	2.74	3.18	3.36	3.17
12.21	11.72	11.04	12.23	12.70
2.24	2.67	2.46	2.23	2.09
0.61	1.90	1.53	0.20	0.38
0.10	**0.38**	**0.50**	**0.09**	**0.22**
0.93	0.97	1.09	0.96	0.95
97.46	97.77	96.92	96.99	97.89
1.00	1.00	1.01	1.00	1.00
0.01	0.01	0.01	0.01	0.01
0.04	0.04	0.05	0.04	0.04
0.00	0.00	0.00	0.00	0.00
0.21	0.21	0.20	0.21	0.21
0.43	0.41	0.40	0.42	0.42
0.06	0.04	0.05	0.05	0.05
0.17	0.17	0.16	0.17	0.18
0.03	0.04	0.03	0.03	0.03
0.01	0.03	0.02	0.00	0.01
0.00	0.00	0.00	0.00	0.00
0.00	0.01	0.01	0.00	0.00
0.04	0.04	0.05	0.04	0.04
1.01	1.01	1.02	1.01	1.01
0.99	0.98	0.97	0.98	0.98
2.00	1.99	1.99	1.99	1.99
94.65	94.55	93.79	94.40	94.32
4.19	4.38	5.04	4.38	4.27
1.15	1.08	1.17	1.22	1.41
100	100	100	100	100

PARIS VSDO-13M1 MNZ1-4 Core	PARIS VSDO-13M1 MNZ1-5 Core	PARIS VSDO-13M1 MNZ6-1 Rim	PARIS VSDO-13M1 MNZ6-2 Rim	PARIS VSDO-13M1 MNZ6-3 Core
29.66	29.66	29.71	29.76	29.92
0.27	0.29	0.25	0.25	0.23
5.29	5.53	4.99	5.02	4.92
0.14	0.24	0.13	0.20	0.25
14.17	13.93	13.90	13.94	13.55
28.45	29.16	26.99	27.12	27.67
4.13	3.73	2.61	3.11	3.15
11.96	11.98	10.66	11.40	11.00
2.41	2.31	2.42	2.26	2.22
0.64	1.06	1.42	1.13	1.40
0.05	**0.13**	**0.67**	**0.80**	**1.07**
1.05	1.08	1.07	1.06	1.02
98.70	99.60	95.06	96.78	96.79
1.00	0.99	1.02	1.01	1.01
0.01	0.01	0.01	0.01	0.01
0.05	0.05	0.05	0.05	0.04
0.00	0.00	0.00	0.00	0.00
0.21	0.20	0.21	0.21	0.20
0.41	0.42	0.40	0.40	0.40
0.06	0.05	0.04	0.05	0.05
0.17	0.17	0.15	0.16	0.16
0.03	0.03	0.03	0.03	0.03
0.01	0.01	0.02	0.01	0.02
0.00	0.00	0.00	0.00	0.00
0.00	0.00	0.01	0.02	0.02
0.04	0.05	0.05	0.05	0.04
1.01	1.00	1.03	1.02	1.02
0.99	0.99	0.96	0.97	0.97
2.00	2.00	1.99	1.99	1.99
94.15	93.99	93.87	94.02	94.31
4.73	4.81	5.02	4.88	4.69
1.13	1.20	1.11	1.09	1.00
100	100	100	100	100

PARIS VSDO-13M1 MNZ6-4 Core	PARIS VSDO-13M1 MNZ6-5 Rim	PARIS VSDO-13M1 MNZ6-6 Rim	PARIS VSDO-13M1 MNZ6-7 Core	PARIS VSDO-13M1 MNZ6-8 Core
29.97	29.30	29.20	29.47	29.44
0.27	0.37	0.22	0.33	0.39
5.68	6.46	4.95	3.94	6.28
0.11	0.03	0.23	0.37	0.30
14.45	15.16	13.07	13.23	12.73
26.21	26.43	26.29	28.15	27.66
3.26	2.40	3.01	3.23	3.38
9.96	10.53	11.37	13.48	11.70
2.18	1.95	2.27	2.67	1.84
1.57	1.34	1.69	1.04	0.55
2.52	**1.37**	**1.48**	**0.12**	**0.13**
1.15	1.16	1.15	0.77	1.20
98.12	96.62	95.41	97.12	95.58
1.00	1.00	1.00	1.00	1.01
0.01	0.01	0.01	0.01	0.02
0.05	0.06	0.05	0.04	0.06
0.00	0.00	0.00	0.00	0.00
0.21	0.22	0.20	0.20	0.19
0.38	0.39	0.39	0.41	0.41
0.05	0.04	0.04	0.05	0.05
0.14	0.15	0.17	0.19	0.17
0.03	0.03	0.03	0.04	0.03
0.02	0.02	0.02	0.01	0.01
0.00	0.00	0.00	0.00	0.00
0.05	0.03	0.03	0.00	0.00
0.05	0.05	0.05	0.03	0.05
1.01	1.01	1.01	1.02	1.02
0.98	0.98	0.98	0.98	0.97
1.99	1.99	1.99	1.99	1.99
93.69	93.07	93.75	95.12	92.66
5.18	5.33	5.30	3.50	5.65
1.13	1.59	0.95	1.38	1.69
100	100	100	100	100

PARIS VSDO-13M1 MNZ5-1 Rim	PARIS VSDO-13M1 MNZ5-2 Core	PARIS VSDO-13M1 MNZ5-3 Core	PARIS VSDO-13M1 MNZ5-4 Rim	PARIS VSDO-13M1 MNZ5-5 Mantle
29.92	30.02	30.33	24.46	29.73
0.25	0.25	0.23	11.74	0.31
4.90	4.57	4.46	4.35	3.99
0.12	0.13	0.09	0.12	0.33
14.07	13.64	15.52	12.43	14.73
25.99	26.45	26.47	24.34	29.55
3.20	3.11	2.61	2.80	3.25
11.30	10.74	11.03	9.42	11.85
2.52	2.00	1.90	1.68	2.24
1.28	0.97	1.14	0.76	0.78
0.65	**2.42**	**2.08**	**0.96**	**0.33**
1.02	0.97	0.93	1.01	0.77
95.89	95.98	97.67	94.66	97.88
1.02	1.01	1.01	0.77	1.00
0.01	0.01	0.01	0.44	0.01
0.04	0.04	0.04	0.04	0.04
0.00	0.00	0.00	0.00	0.00
0.21	0.20	0.23	0.17	0.22
0.38	0.39	0.38	0.33	0.43
0.05	0.05	0.04	0.04	0.05
0.16	0.15	0.16	0.13	0.17
0.03	0.03	0.03	0.02	0.03
0.02	0.01	0.01	0.01	0.01
0.00	0.00	0.00	0.00	0.00
0.01	0.05	0.04	0.02	0.01
0.04	0.04	0.04	0.04	0.03
1.03	1.02	1.02	1.21	1.01
0.96	0.96	0.97	0.80	0.98
1.98	1.99	1.99	2.01	1.99
94.13	94.44	94.80	59.99	95.25
4.78	4.46	4.22	3.38	3.45
1.09	1.09	0.98	36.63	1.31
100	100	100	100	100

PARIS VSDO-13M1 MNZ10-1 Rim	PARIS VSDO-13M1 MNZ10-2 Mantle	PARIS VSDO-13M1 MNZ10-3 Mantle	PARIS VSDO-13M1 MNZ10-4 Core	PARIS VSDO-13M1 MNZ10-5 Core
29.99	30.15	30.20	29.40	29.95
0.30	0.35	0.28	0.76	0.25
4.92	5.14	5.14	10.07	5.56
0.12	0.18	0.10	0.01	0.33
13.97	15.10	13.99	10.67	12.53
26.54	27.84	27.43	25.75	26.00
2.85	2.87	3.28	3.24	2.77
10.45	10.41	10.42	13.76	12.23
2.06	1.98	2.40	2.13	2.36
1.21	1.45	2.04	0.64	1.34
1.20	**1.53**	**0.97**	**0.13**	**0.10**
1.04	1.03	1.07	1.60	1.28
94.76	98.76	98.24	98.15	94.70
1.02	1.00	1.01	0.99	1.02
0.01	0.01	0.01	0.03	0.01
0.04	0.05	0.05	0.09	0.05
0.00	0.00	0.00	0.00	0.00
0.21	0.22	0.20	0.16	0.19
0.39	0.40	0.40	0.37	0.38
0.04	0.04	0.05	0.05	0.04
0.15	0.15	0.15	0.20	0.18
0.03	0.03	0.03	0.03	0.03
0.02	0.02	0.03	0.01	0.02
0.00	0.00	0.00	0.00	0.00
0.03	0.03	0.02	0.00	0.00
0.04	0.04	0.05	0.07	0.06
1.03	1.02	1.02	1.02	1.03
0.95	0.98	0.97	0.97	0.95
1.98	1.99	1.99	1.99	1.98
93.78	93.93	93.93	89.21	92.81
4.91	4.62	4.88	7.48	6.09
1.31	1.44	1.18	3.31	1.11
100	100	100	100	100

PARIS VSDO-13M1 MNZ10-6 Core	PARIS VSDO-13M1 MNZ10-7 Mantle	PARIS VSDO-13M1 MNZ10-8		PARIS VSDO-13M2 MNZ10-1 Rim
29.63	29.97	29.66		29.66
0.56	0.28	0.36		0.24
8.36	5.13	5.03		5.56
0.13	0.26	0.15		0.22
11.64	14.98	14.48		14.23
26.63	25.89	26.34		25.36
3.27	2.62	2.59		3.01
14.20	11.34	11.33		10.95
2.31	2.23	2.29		2.13
0.45	1.72	1.90		1.35
0.11	**1.47**	**1.10**		**1.32**
1.47	1.07	1.66		1.11
99.07	97.10	97.25		95.79
0.99	1.01	1.00		1.01
0.02	0.01	0.01		0.01
0.08	0.05	0.05		0.05
0.00	0.00	0.00		0.00
0.17	0.22	0.21		0.21
0.39	0.38	0.38		0.37
0.05	0.04	0.04		0.04
0.20	0.16	0.16		0.16
0.03	0.03	0.03		0.03
0.01	0.02	0.03		0.02
0.00	0.00	0.00		0.00
0.00	0.03	0.02		0.03
0.06	0.05	0.07		0.05
1.01	1.02	1.01		1.02
0.98	0.97	0.99		0.96
1.99	1.99	2.00		1.99
90.92	93.94	91.14		93.76
6.71	4.89	7.38		5.21
2.37	1.17	1.48		1.03
100	100	100		100

PARIS	PARIS	PARIS	PARIS	PARIS
VSDO-13M2	VSDO-13M2	VSDO-13M2	VSDO-13M2	VSDO-13M2
MNZ10-2	MNZ10-3	MNZ10-4	MNZ10-5	MNZ10-6
Mantle	Core	Core	Rim	Core
29.88	29.82	29.31	29.64	29.97
0.24	0.23	0.37	0.23	0.24
5.43	5.44	6.86	5.49	5.39
0.09	0.15	0.00	0.19	0.11
13.27	12.91	14.13	14.72	14.10
24.57	24.97	27.14	25.97	24.73
3.44	2.89	2.95	3.06	2.92
10.43	10.52	10.05	10.63	10.07
1.91	1.99	2.18	2.30	1.79
1.18	1.68	0.87	1.48	1.81
2.50	**3.01**	**1.23**	**1.09**	**2.24**
1.06	1.08	1.18	1.07	1.05
94.65	95.25	96.69	96.15	94.62
1.02	1.01	1.00	1.01	1.02
0.01	0.01	0.01	0.01	0.01
0.05	0.05	0.06	0.05	0.05
0.00	0.00	0.00	0.00	0.00
0.20	0.19	0.21	0.22	0.21
0.36	0.37	0.40	0.38	0.36
0.05	0.04	0.04	0.04	0.04
0.15	0.15	0.14	0.15	0.14
0.03	0.03	0.03	0.03	0.02
0.02	0.02	0.01	0.02	0.02
0.00	0.00	0.00	0.00	0.00
0.05	0.06	0.03	0.02	0.05
0.05	0.05	0.05	0.05	0.05
1.03	1.02	1.01	1.02	1.03
0.95	0.96	0.98	0.97	0.95
1.98	1.99	1.99	1.99	1.98
93.92	93.93	92.94	94.06	93.97
5.00	5.06	5.48	4.95	4.97
1.08	1.02	1.58	0.99	1.05
100	100	100	100	100

PARIS VSDO-13M2 MNZ10-7 Mantle	PARIS VSDO-13M2 MNZ11-1 Rim	PARIS VSDO-13M2 MNZ11-2 Manlte	PARIS VSDO-13M2 MNZ11-3 Core	PARIS VSDO-13M2 MNZ11-4 Core
29.95	29.53	29.87	30.06	30.08
0.24	0.39	0.21	0.24	0.22
5.40	6.62	5.15	5.05	4.50
0.08	0.06	0.01	0.07	0.10
14.30	14.59	15.67	14.92	14.17
26.74	26.50	28.04	26.82	27.31
3.15	2.86	3.42	2.84	3.03
10.75	10.26	10.69	10.63	10.76
1.90	1.92	1.54	1.74	2.05
1.66	1.23	1.05	1.08	1.38
2.55	**1.13**	**0.71**	**2.28**	**2.60**
1.05	1.14	1.08	0.99	0.94
98.73	96.78	97.43	97.50	98.00
1.00	1.00	1.00	1.01	1.01
0.01	0.02	0.01	0.01	0.01
0.05	0.06	0.05	0.05	0.04
0.00	0.00	0.00	0.00	0.00
0.21	0.22	0.23	0.22	0.21
0.39	0.39	0.41	0.39	0.39
0.05	0.04	0.05	0.04	0.04
0.15	0.15	0.15	0.15	0.15
0.03	0.03	0.02	0.02	0.03
0.02	0.02	0.01	0.01	0.02
0.00	0.00	0.00	0.00	0.00
0.05	0.02	0.02	0.05	0.05
0.04	0.05	0.05	0.04	0.04
1.01	1.02	1.01	1.02	1.01
0.99	0.97	0.98	0.97	0.98
2.00	1.99	1.99	1.99	1.99
94.29	93.01	94.24	94.49	94.88
4.71	5.28	4.87	4.51	4.21
1.00	1.70	0.89	1.00	0.90
100	100	100	100	100

PARIS VSDO-13M2 MNZ11-5 Mantle	PARIS VSDO-13M2 MNZ15-1 Rim	PARIS VSDO-13M2 MNZ15-2 Core	PARIS VSDO-13M2 MNZ15-3 Mantle	PARIS VSDO-13M2 MNZ15-4 Rim
30.30	29.94	30.22	29.77	29.36
0.20	0.26	0.23	0.41	0.54
4.35	5.40	5.06	6.75	6.28
0.16	0.10	0.08	0.00	0.00
13.58	15.11	15.08	15.17	16.23
26.78	27.50	26.72	28.18	28.66
2.95	3.25	2.95	2.92	3.32
10.16	10.60	10.30	10.68	10.40
2.37	2.10	1.87	2.00	1.29
1.84	0.78	1.47	0.83	0.19
2.88	**0.63**	**1.97**	**1.08**	**0.26**
0.87	1.07	1.00	1.21	0.97
97.01	97.18	97.27	98.99	97.52
1.01	1.01	1.01	0.99	0.99
0.01	0.01	0.01	0.02	0.02
0.04	0.05	0.05	0.06	0.06
0.00	0.00	0.00	0.00	0.00
0.20	0.22	0.22	0.22	0.24
0.39	0.40	0.39	0.41	0.42
0.04	0.05	0.04	0.04	0.05
0.14	0.15	0.15	0.15	0.15
0.03	0.03	0.03	0.03	0.02
0.02	0.01	0.02	0.01	0.00
0.00	0.00	0.00	0.00	0.00
0.06	0.01	0.04	0.02	0.01
0.04	0.05	0.04	0.05	0.04
1.02	1.02	1.02	1.01	1.01
0.97	0.97	0.97	0.99	0.98
1.99	1.99	1.99	2.00	1.99
95.21	93.99	94.46	92.91	93.29
3.97	4.89	4.55	5.38	4.40
0.83	1.11	1.00	1.71	2.30
100	100	100	100	100

PARIS VSDO-13M2 MNZ6-1 Rim	PARIS VSDO-13M2 MNZ6-2 Core	PARIS VSDO-13M2 MNZ6-3 Rim	PARIS VSDO-13M2 MNZ7-1 Rim	PARIS VSDO-13M2 MNZ7-2 Core
29.84	29.77	29.61	30.11	30.49
0.19	0.24	0.28	0.21	0.19
5.51	6.03	7.10	3.89	4.23
0.08	0.50	0.13	0.10	0.23
16.00	14.43	14.10	16.76	15.85
27.52	28.07	27.44	29.00	27.14
3.31	2.97	2.86	3.34	3.31
10.25	10.84	11.27	10.48	10.36
1.75	1.66	1.89	1.66	2.10
0.84	0.74	1.29	0.74	1.51
0.80	**0.56**	**0.58**	**0.63**	**1.92**
1.15	1.35	1.38	0.79	0.92
97.58	97.43	98.16	97.93	99.04
1.01	1.00	1.00	1.01	1.01
0.01	0.01	0.01	0.01	0.01
0.05	0.05	0.06	0.03	0.04
0.00	0.00	0.00	0.00	0.00
0.23	0.21	0.21	0.24	0.23
0.40	0.41	0.40	0.42	0.39
0.05	0.04	0.04	0.05	0.05
0.15	0.15	0.16	0.15	0.14
0.02	0.02	0.03	0.02	0.03
0.01	0.01	0.02	0.01	0.02
0.00	0.00	0.00	0.00	0.00
0.02	0.01	0.01	0.01	0.04
0.05	0.06	0.06	0.03	0.04
1.01	1.01	1.01	1.02	1.02
0.98	0.98	0.99	0.98	0.97
1.99	1.99	2.00	1.99	1.99
93.96	92.80	92.49	95.60	95.14
5.22	6.18	6.31	3.53	4.07
0.81	1.02	1.20	0.88	0.78
100	100	100	100	100

PARIS VSDO-13M2 MNZ7-3 Rim	PARIS VSDO-13M2 MNZ7-4 Core	PARIS VSDO-13M2 MNZ7-5 Core	PARIS VSDO-13M2 MNZ7-6 Rim
30.20	30.28	30.38	30.23
0.24	0.22	0.20	0.30
3.86	4.66	4.50	6.76
0.02	0.02	0.10	0.04
17.03	16.49	15.19	15.74
31.50	29.03	30.35	27.93
3.42	3.02	2.97	2.71
10.70	10.08	10.89	10.81
1.40	1.64	1.68	1.54
0.57	1.18	0.69	0.88
0.16	**0.27**	**0.34**	**0.71**
0.68	0.93	0.99	1.26
99.75	97.83	98.52	99.37
1.00	1.01	1.01	1.00
0.01	0.01	0.01	0.01
0.03	0.04	0.04	0.06
0.00	0.00	0.00	0.00
0.25	0.24	0.22	0.23
0.45	0.42	0.44	0.40
0.05	0.04	0.04	0.04
0.15	0.14	0.15	0.15
0.02	0.02	0.02	0.02
0.01	0.02	0.01	0.01
0.00	0.00	0.00	0.00
0.00	0.01	0.01	0.01
0.03	0.04	0.04	0.05
1.01	1.02	1.02	1.01
0.99	0.97	0.97	0.98
2.00	1.99	1.99	1.99
96.08	94.89	94.70	93.08
2.96	4.20	4.45	5.67
0.96	0.91	0.85	1.25
100	100	100	100

PARIS	PARIS	PARIS	PARIS	PARIS
VSDO-13M4	VSDO-13M4	VSDO-13M4	VSDO-13M4	VSDO-13M4
MNZ14-1	MNZ14-2	MNZ14-3	MNZ14-4	MNZ14-5
Rim	Core	Core	Core	Core
30.02	29.97	29.55	30.30	29.78
0.43	0.51	0.52	0.27	0.44
5.13	5.32	5.64	4.77	5.02
0.32	0.36	0.36	0.12	0.31
14.17	12.75	13.09	12.61	13.62
28.03	28.88	27.66	27.04	28.37
3.30	3.19	3.99	2.96	3.34
12.74	11.78	11.98	12.51	12.35
2.06	2.16	2.32	2.27	2.19
1.01	1.08	1.24	1.55	1.14
0.52	**0.32**	**0.36**	**0.84**	**0.25**
0.88	0.88	0.92	0.96	0.85
98.80	97.30	98.17	97.01	97.66
1.00	1.01	1.00	1.02	1.00
0.02	0.02	0.02	0.01	0.02
0.05	0.05	0.05	0.04	0.05
0.00	0.00	0.00	0.00	0.00
0.21	0.19	0.19	0.18	0.20
0.40	0.42	0.40	0.39	0.41
0.05	0.05	0.06	0.04	0.05
0.18	0.17	0.17	0.18	0.18
0.03	0.03	0.03	0.03	0.03
0.01	0.01	0.02	0.02	0.02
0.00	0.00	0.00	0.00	0.00
0.01	0.01	0.01	0.02	0.01
0.04	0.04	0.04	0.04	0.04
1.02	1.03	1.02	1.03	1.02
0.97	0.96	0.97	0.95	0.97
1.99	1.98	1.99	1.98	1.99
94.25	93.79	93.64	94.36	94.31
3.95	4.02	4.17	4.46	3.84
1.80	2.19	2.19	1.18	1.85
100	100	100	100	100

PARIS VSDO-13M4 MNZ14-6 Mantle	PARIS VSDO-13M4 MNZ14-7 Rim	PARIS VSDO-13M4 MNZ9-1 Mantle	PARIS VSDO-13M4 MNZ9-2 Rim	PARIS VSDO-13M4 MNZ9-3 Core
30.00	30.30	29.89	30.20	29.90
0.32	0.24	0.29	0.23	0.20
5.26	5.67	6.47	4.84	5.59
0.09	0.23	0.06	0.12	0.44
14.02	14.71	13.27	13.92	12.64
28.64	27.49	27.85	27.65	26.60
3.16	3.05	3.59	3.16	3.27
11.90	11.62	12.64	11.09	11.62
2.01	2.11	1.96	2.25	2.19
0.76	1.45	0.75	1.48	1.29
0.22	**0.98**	**0.10**	**1.04**	**1.01**
1.06	1.17	1.27	0.96	1.24
97.51	99.55	98.35	97.24	96.54
1.01	1.00	1.00	1.01	1.01
0.01	0.01	0.01	0.01	0.01
0.05	0.05	0.06	0.04	0.05
0.00	0.00	0.00	0.00	0.00
0.21	0.21	0.19	0.20	0.19
0.42	0.39	0.40	0.40	0.39
0.05	0.04	0.05	0.05	0.05
0.17	0.16	0.18	0.16	0.17
0.03	0.03	0.03	0.03	0.03
0.01	0.02	0.01	0.02	0.02
0.00	0.00	0.00	0.00	0.00
0.00	0.02	0.00	0.02	0.02
0.05	0.05	0.05	0.04	0.05
1.02	1.01	1.01	1.02	1.02
0.97	0.98	0.98	0.96	0.97
1.99	1.99	1.99	1.99	1.99
93.84	93.79	92.97	94.63	93.34
4.83	5.21	5.79	4.39	5.78
1.34	1.01	1.24	0.98	0.88
100	100	100	100	100

PARIS VSDO-13M4 MNZ9-4 Eim	PARIS VSDO-13M4 MNZ9-5 Core	PARIS VSDO-13M4 MNZ13-1 Rim	PARIS VSDO-13M4 MNZ13-2 Core	PARIS VSDO-13M4 MNZ13-3 Mantle
30.05	29.63	30.14	30.15	29.83
0.26	0.43	0.21	0.20	0.25
4.93	6.35	5.01	4.74	4.86
0.15	0.61	0.11	0.16	0.13
14.39	12.88	13.99	13.86	14.26
27.46	25.70	28.10	25.50	27.79
3.09	2.98	3.06	2.48	3.30
12.73	11.81	11.72	10.24	12.66
2.46	2.59	2.15	2.03	2.22
1.30	1.37	1.44	1.73	1.03
1.21	**1.59**	**1.14**	**2.50**	**0.31**
1.05	1.18	1.04	0.96	0.95
99.33	97.49	98.13	95.38	98.13
1.00	1.00	1.01	1.02	1.00
0.01	0.02	0.01	0.01	0.01
0.04	0.06	0.04	0.04	0.04
0.00	0.01	0.00	0.00	0.00
0.21	0.19	0.20	0.20	0.21
0.39	0.37	0.41	0.37	0.40
0.04	0.04	0.04	0.04	0.05
0.18	0.17	0.16	0.15	0.18
0.03	0.04	0.03	0.03	0.03
0.02	0.02	0.02	0.02	0.01
0.00	0.00	0.00	0.00	0.00
0.03	0.03	0.02	0.05	0.01
0.04	0.05	0.04	0.04	0.04
1.01	1.02	1.01	1.03	1.01
0.99	0.98	0.98	0.95	0.98
2.00	1.99	1.99	1.98	1.99
94.33	92.77	94.44	94.61	94.67
4.62	5.41	4.67	4.51	4.28
1.05	1.82	0.90	0.88	1.05
100	100	100	100	100

PARIS VSDO-13M4 MNZ13-4 Core	PARIS VSDO-13M4 MNZ13-5 Core	PARIS VSDO-13M4 MNZ13-6 Core	PARIS VSDO-13M4 MNZ13-7 Mantle	PARIS VSDO-13M4 MNZ8-1 Rim
30.10	30.04	30.20	29.83	30.31
0.28	0.23	0.24	0.22	0.26
4.12	5.17	4.69	4.61	4.52
0.18	0.14	0.12	0.05	0.21
13.71	13.46	14.48	14.00	13.07
27.96	24.58	25.94	27.15	27.25
2.80	2.55	2.56	3.24	3.32
12.90	10.85	9.60	13.00	12.50
2.57	1.89	1.89	2.25	2.33
1.36	1.63	1.26	0.88	1.12
0.37	**2.62**	**2.60**	**0.51**	**0.99**
0.83	1.06	1.07	0.96	0.98
97.85	95.01	95.70	96.78	97.29
1.01	1.02	1.02	1.01	1.02
0.01	0.01	0.01	0.01	0.01
0.04	0.05	0.04	0.04	0.04
0.00	0.00	0.00	0.00	0.00
0.20	0.20	0.21	0.21	0.19
0.41	0.36	0.38	0.40	0.39
0.04	0.04	0.04	0.05	0.05
0.18	0.16	0.14	0.19	0.18
0.04	0.03	0.03	0.03	0.03
0.02	0.02	0.02	0.01	0.01
0.00	0.00	0.00	0.00	0.00
0.01	0.06	0.06	0.01	0.02
0.04	0.05	0.05	0.04	0.04
1.02	1.03	1.03	1.02	1.03
0.97	0.95	0.95	0.97	0.96
1.99	1.98	1.98	1.99	1.99
95.06	93.99	93.98	94.68	94.45
3.76	5.01	4.96	4.40	4.46
1.18	1.00	1.06	0.93	1.09
100	100	100	100	100

PARIS VSDO-13M4 MNZ8-2 Core	PARIS VSDO-13M4 MNZ8-3 Core	PARIS VSDO-13M4 MNZ8-4 Core	PARIS VSDO-13M4 MNZ8-5 Rim	PARIS VSDO-13M4 MNZ11-1 Rim
29.86	30.02	30.00	29.72	30.43
0.31	0.26	0.29	0.23	0.24
5.94	6.63	7.73	4.15	5.29
0.03	0.07	0.04	0.16	0.18
14.45	14.00	14.05	13.25	14.27
29.29	26.32	27.00	27.56	28.70
3.40	3.17	3.28	3.39	3.18
12.59	10.78	11.03	12.67	12.12
1.95	1.55	1.79	2.48	2.13
0.73	0.54	0.81	1.74	1.17
0.18	**0.66**	**0.43**	**1.04**	**0.70**
1.13	1.35	1.53	0.92	1.03
100.16	95.86	98.38	97.81	99.46
0.99	1.02	1.00	1.00	1.00
0.01	0.01	0.01	0.01	0.01
0.05	0.06	0.07	0.04	0.05
0.00	0.00	0.00	0.00	0.00
0.21	0.21	0.20	0.19	0.21
0.42	0.39	0.39	0.40	0.41
0.05	0.05	0.05	0.05	0.05
0.18	0.15	0.16	0.18	0.17
0.03	0.02	0.02	0.03	0.03
0.01	0.01	0.01	0.02	0.02
0.00	0.00	0.00	0.00	0.00
0.00	0.01	0.01	0.02	0.01
0.05	0.06	0.06	0.04	0.04
1.00	1.03	1.02	1.01	1.01
1.00	0.96	0.98	0.98	0.98
2.00	1.98	1.99	2.00	1.99
93.76	92.45	91.68	94.91	94.43
4.97	6.41	7.07	4.11	4.60
1.27	1.14	1.25	0.98	0.98
100	100	100	100	100

PARIS VSDO-13M4 MNZ11-2 Core	PARIS VSDO-13M4 MNZ11-3 Rim	PARIS VSDO-13M4 MNZ11-4 Core	PARIS VSDO-13M4 MNZ11-5 Core	PARIS VSDO-13M4 MNZ11-6 Rim
30.05	30.44	30.42	30.25	30.32
0.31	0.25	0.22	0.21	0.24
5.21	5.15	4.69	5.21	4.82
0.04	0.12	0.12	0.12	0.15
16.43	14.50	14.48	14.99	15.03
28.01	27.28	26.82	28.27	27.51
2.73	2.99	2.69	2.45	2.98
10.82	11.77	10.43	11.77	11.25
1.39	1.89	2.17	2.28	2.27
0.42	1.56	1.23	1.58	1.24
0.40	**0.76**	**2.43**	**0.69**	**0.80**
0.95	1.08	1.01	1.12	1.05
96.73	98.47	97.13	99.25	97.72
1.01	1.01	1.01	1.00	1.01
0.01	0.01	0.01	0.01	0.01
0.05	0.05	0.04	0.05	0.04
0.00	0.00	0.00	0.00	0.00
0.24	0.21	0.21	0.22	0.22
0.41	0.39	0.39	0.41	0.40
0.04	0.04	0.04	0.03	0.04
0.15	0.17	0.15	0.16	0.16
0.02	0.03	0.03	0.03	0.03
0.01	0.02	0.02	0.02	0.02
0.00	0.00	0.00	0.00	0.00
0.01	0.02	0.05	0.01	0.02
0.04	0.05	0.04	0.05	0.04
1.02	1.02	1.02	1.01	1.02
0.96	0.97	0.96	0.98	0.97
1.99	1.99	1.99	1.99	1.99
94.28	94.07	94.48	94.16	94.24
4.38	4.88	4.59	4.97	4.73
1.34	1.04	0.94	0.87	1.03
100	100	100	100	100

PARIS VSDO-13M4 MNZ6-1 Core	PARIS VSDO-13M4 MNZ6-2 Core	PARIS VSDO-13M4 MNZ6-3 Mantle	PARIS VSDO-13M4 MNZ5-1	PARIS VSDO-13M4 MNZ5-2 Rim
29.71	29.46	29.33	29.87	29.85
0.29	0.33	0.25	0.21	0.19
6.30	7.07	5.37	5.35	4.71
0.07	0.06	0.09	0.13	0.11
13.64	13.15	13.74	14.03	14.56
28.58	28.45	27.86	26.10	26.88
3.22	3.41	3.02	2.87	3.19
11.76	11.32	11.51	10.40	11.43
1.86	1.79	2.25	2.06	1.73
0.30	0.62	1.04	1.69	0.82
0.12	**0.15**	**0.47**	**2.61**	**2.06**
1.28	1.40	1.16	1.06	1.01
97.23	97.47	96.54	97.30	97.25
1.00	1.00	1.00	1.01	1.01
0.01	0.01	0.01	0.01	0.01
0.06	0.06	0.05	0.05	0.04
0.00	0.00	0.00	0.00	0.00
0.20	0.19	0.20	0.21	0.21
0.42	0.42	0.41	0.38	0.39
0.05	0.05	0.04	0.04	0.05
0.17	0.16	0.17	0.15	0.16
0.03	0.02	0.03	0.03	0.02
0.00	0.01	0.01	0.02	0.01
0.00	0.00	0.00	0.00	0.00
0.00	0.00	0.01	0.06	0.04
0.05	0.06	0.05	0.05	0.04
1.02	1.01	1.01	1.01	1.01
0.98	0.98	0.98	0.98	0.98
1.99	2.00	2.00	1.99	1.99
92.88	92.15	93.60	94.25	94.62
5.86	6.42	5.34	4.85	4.57
1.25	1.43	1.06	0.90	0.81
100	100	100	100	100

PARIS VSDO-13M4 MNZ5-3 Core	PARIS VSDO-13M4 MNZ5-4 Rim	PARIS VSDO-13M4 MNZ5-5 Rim	PARIS VSDO-13M4 MNZ12-1 Rim	PARIS VSDO-13M4 MNZ12-2 Rim
29.40	29.45	29.32	29.81	29.60
0.36	0.22	0.21	0.29	0.29
6.58	5.11	5.03	6.79	6.65
0.02	0.14	0.16	0.07	0.00
14.47	14.81	15.10	14.56	14.50
26.32	26.86	26.99	25.34	27.11
2.29	2.93	3.25	2.71	3.35
10.45	10.74	11.07	10.86	10.46
1.97	2.12	2.27	1.86	1.73
1.26	1.33	1.42	1.12	0.92
1.76	**0.79**	**0.67**	**1.05**	**1.28**
1.22	1.05	1.04	1.25	1.25
96.67	95.92	96.59	95.72	97.70
1.00	1.01	1.00	1.01	1.00
0.01	0.01	0.01	0.01	0.01
0.06	0.05	0.05	0.06	0.06
0.00	0.00	0.00	0.00	0.00
0.21	0.22	0.22	0.22	0.21
0.39	0.40	0.40	0.37	0.40
0.03	0.04	0.05	0.04	0.05
0.15	0.15	0.16	0.16	0.15
0.03	0.03	0.03	0.03	0.02
0.02	0.02	0.02	0.01	0.01
0.00	0.00	0.00	0.00	0.00
0.04	0.02	0.01	0.02	0.03
0.05	0.05	0.04	0.05	0.05
1.01	1.02	1.01	1.02	1.01
0.98	0.97	0.99	0.96	0.98
1.99	1.99	2.00	1.99	1.99
92.82	94.18	94.39	92.84	93.07
5.63	4.88	4.72	5.89	5.70
1.55	0.94	0.89	1.27	1.23
100	100	100	100	100

PARIS VSDO-13M4 MNZ12-3 Core	PARIS VSDO-13M4 MNZ12-4 Core	PARIS VSDO-13M4 MNZ12-5 Mantle	PARIS VSDO-13M4 MNZ12-6 Mantle	PARIS VSDO-13M4 MNZ12-7 Rim
29.65	29.37	29.48	29.64	29.80
0.34	0.34	0.22	0.23	0.22
7.25	7.05	5.46	5.39	5.88
0.02	0.03	0.10	0.16	0.04
14.43	13.86	14.48	14.47	14.23
25.71	25.51	26.55	26.10	26.83
2.43	2.61	3.36	3.25	2.93
10.72	11.17	11.10	11.34	10.96
1.99	1.90	1.92	2.13	1.82
1.14	1.12	1.21	1.40	1.02
1.34	**1.28**	**0.84**	**0.82**	**1.09**
1.34	1.32	1.11	1.11	1.23
96.64	95.53	96.68	96.92	96.99
1.00	1.00	1.01	1.01	1.01
0.01	0.01	0.01	0.01	0.01
0.07	0.06	0.05	0.05	0.05
0.00	0.00	0.00	0.00	0.00
0.21	0.21	0.22	0.21	0.21
0.38	0.38	0.39	0.38	0.39
0.04	0.04	0.05	0.05	0.04
0.15	0.16	0.16	0.16	0.16
0.03	0.03	0.03	0.03	0.03
0.02	0.01	0.02	0.02	0.01
0.00	0.00	0.00	0.00	0.00
0.03	0.03	0.02	0.02	0.02
0.06	0.06	0.05	0.05	0.05
1.02	1.02	1.02	1.02	1.02
0.97	0.97	0.98	0.97	0.97
1.99	1.99	1.99	1.99	1.99
92.29	92.33	93.90	93.87	93.37
6.24	6.17	5.15	5.13	5.68
1.47	1.49	0.94	1.00	0.95
100	100	100	100	100

PARIS VSDO-13M4 MNZ4-1 Mantle	PARIS VSDO-13M4 MNZ4-2 Rim	PARIS VSDO-13M4 MNZ4-3 Mantle	PARIS VSDO-13M4 MNZ4-4 Core	PARIS VSDO-13M4 MNZ4-5 Mantle
30.10	30.15	29.95	30.25	30.28
0.19	0.22	0.24	0.23	0.21
4.53	5.09	4.96	4.98	4.73
0.17	0.05	0.01	0.05	0.14
14.15	14.87	13.84	15.12	14.58
26.76	27.29	27.18	27.15	26.94
3.30	3.36	3.05	2.72	2.48
9.48	10.42	10.62	10.81	10.40
1.65	1.95	1.68	1.84	1.95
1.47	1.15	1.22	1.36	1.44
2.81	**1.80**	**2.12**	**2.07**	**2.32**
0.97	1.04	0.99	0.98	0.95
95.93	97.59	96.13	97.97	96.98
1.01	1.01	1.01	1.01	1.01
0.01	0.01	0.01	0.01	0.01
0.04	0.05	0.04	0.04	0.04
0.00	0.00	0.00	0.00	0.00
0.21	0.22	0.20	0.22	0.21
0.39	0.39	0.40	0.39	0.39
0.05	0.05	0.04	0.04	0.04
0.13	0.15	0.15	0.15	0.15
0.02	0.03	0.02	0.02	0.03
0.02	0.02	0.02	0.02	0.02
0.00	0.00	0.00	0.00	0.00
0.06	0.04	0.05	0.04	0.05
0.04	0.04	0.04	0.04	0.04
1.02	1.02	1.02	1.02	1.02
0.97	0.98	0.97	0.97	0.96
1.99	1.99	1.99	1.99	1.99
94.73	94.39	94.43	94.63	94.75
4.44	4.69	4.56	4.42	4.35
0.83	0.92	1.02	0.95	0.90
100	100	100	100	100

PARIS VSDO-13M4 MNZ4-6 Core	PARIS VSDO-13M4 MNZ4-7 Rim	PARIS VSDO-13M4 MNZ4-8 Rim	PARIS VSDO-13M4 MNZ15-1 Mantle	PARIS VSDO-13M4 MNZ15-2 Core
30.29	29.77	30.20	30.01	29.70
0.22	0.25	0.25	0.25	0.29
5.43	5.04	5.24	5.08	5.17
0.11	0.09	0.07	0.19	0.01
14.43	14.45	14.92	13.49	13.95
25.76	27.17	26.86	26.72	27.59
2.47	3.08	3.09	3.20	3.48
10.42	10.40	10.50	10.59	11.97
1.94	2.04	1.64	2.23	2.18
1.65	1.29	1.11	1.79	0.88
1.97	**1.86**	**1.96**	**2.39**	**0.47**
1.10	1.07	1.01	1.09	0.97
96.11	97.26	97.16	97.70	96.73
1.02	1.00	1.01	1.01	1.01
0.01	0.01	0.01	0.01	0.01
0.05	0.05	0.05	0.05	0.05
0.00	0.00	0.00	0.00	0.00
0.21	0.21	0.22	0.20	0.21
0.37	0.40	0.39	0.39	0.40
0.04	0.04	0.04	0.05	0.05
0.15	0.15	0.15	0.15	0.17
0.03	0.03	0.02	0.03	0.03
0.02	0.02	0.01	0.02	0.01
0.00	0.00	0.00	0.00	0.00
0.04	0.04	0.04	0.05	0.01
0.05	0.05	0.04	0.05	0.04
1.03	1.01	1.02	1.02	1.02
0.96	0.98	0.97	0.98	0.97
1.98	1.99	1.99	1.99	1.99
93.93	94.12	94.31	94.05	94.31
5.11	4.84	4.62	4.90	4.44
0.96	1.04	1.08	1.04	1.25
100	100	100	100	100

PARIS VSDO-13M4 MNZ15-3 Core	PARIS VSDO-13M4 MNZ15-4 Core	PARIS VSDO-13M4 MNZ15-5 Core	PARIS VSDO-13M4 MNZ15-6 Core	PARIS VSDO-13M4 MNZ15-7 Mantle
29.81	29.57	29.79	29.70	29.63
0.25	0.34	0.28	0.27	0.25
5.25	4.61	5.57	4.55	5.00
0.29	0.54	0.57	0.04	0.15
13.40	12.47	12.77	13.41	14.56
27.39	25.16	27.44	28.96	25.79
3.07	3.66	3.75	3.48	3.41
11.09	12.46	11.92	12.53	10.76
2.54	2.78	2.39	2.19	1.95
2.11	1.49	1.17	1.19	1.38
1.51	**1.46**	**0.52**	**0.31**	**2.18**
1.08	0.92	1.23	0.94	1.05
97.84	96.20	97.56	97.58	96.25
1.00	1.01	1.00	1.00	1.00
0.01	0.01	0.01	0.01	0.01
0.05	0.04	0.05	0.04	0.05
0.00	0.00	0.01	0.00	0.00
0.20	0.19	0.19	0.20	0.21
0.40	0.37	0.40	0.42	0.38
0.04	0.05	0.05	0.05	0.05
0.16	0.18	0.17	0.18	0.15
0.03	0.04	0.03	0.03	0.03
0.03	0.02	0.02	0.02	0.02
0.00	0.00	0.00	0.00	0.00
0.03	0.03	0.01	0.01	0.05
0.05	0.04	0.05	0.04	0.05
1.01	1.02	1.01	1.01	1.01
0.99	0.97	0.98	0.98	0.98
2.00	1.99	1.99	1.99	1.99
94.07	94.26	93.22	94.66	94.16
4.87	4.26	5.61	4.21	4.78
1.06	1.48	1.17	1.13	1.06
100	100	100	100	100

PARIS VSDO-13M4 MNZ15-8 Rim	PARIS VSDO-13M4 MNZ10-1	PARIS VSDO-13M4 MNZ10-2	PARIS VSDO-13M4 MNZ10-3	PARIS VSDO-13M4 MNZ10-4
29.92	30.14	30.15	29.83	30.10
0.23	0.21	0.20	0.25	0.28
5.18	5.01	4.74	4.86	4.12
0.22	0.11	0.16	0.13	0.18
12.68	13.99	13.86	14.26	13.71
27.01	28.10	25.50	27.79	27.96
3.60	3.06	2.48	3.30	2.80
11.38	11.72	10.24	12.66	12.90
2.27	2.15	2.03	2.22	2.57
0.84	1.44	1.73	1.03	1.36
2.82	**1.14**	**2.50**	**0.31**	**0.37**
1.09	1.04	0.96	0.95	0.83
98.49	98.12	94.57	97.60	97.16
1.00	1.01	1.02	1.00	1.01
0.01	0.01	0.01	0.01	0.01
0.05	0.04	0.04	0.04	0.04
0.00	0.00	0.00	0.00	0.00
0.18	0.20	0.20	0.21	0.20
0.39	0.41	0.37	0.40	0.41
0.05	0.04	0.04	0.05	0.04
0.16	0.16	0.15	0.18	0.18
0.03	0.03	0.03	0.03	0.04
0.01	0.02	0.02	0.01	0.02
0.00	0.00	0.00	0.00	0.00
0.06	0.02	0.05	0.01	0.01
0.05	0.04	0.04	0.04	0.04
1.01	1.01	1.03	1.01	1.02
0.98	0.98	0.95	0.98	0.97
2.00	1.99	1.98	1.99	1.99
94.14	94.44	94.61	94.67	95.06
4.88	4.67	4.51	4.28	3.76
0.98	0.90	0.88	1.05	1.18
100	100	100	100	100

PARIS VSDO-13M4 MNZ10-5	PARIS VSDO-13M4 MNZ10-6	PARIS VSDO-13M4 MNZ10-7
30.04	30.20	29.83
0.23	0.24	0.22
5.17	4.69	4.61
0.14	0.12	0.05
13.46	14.48	14.00
24.58	25.94	27.15
2.55	2.56	3.24
10.85	9.60	13.00
1.89	1.89	2.25
1.63	1.26	0.88
2.62	**2.60**	**0.51**
1.06	1.07	0.96
94.23	94.65	96.70
1.02	1.02	1.01
0.01	0.01	0.01
0.05	0.04	0.04
0.00	0.00	0.00
0.20	0.21	0.21
0.36	0.38	0.40
0.04	0.04	0.05
0.16	0.14	0.19
0.03	0.03	0.03
0.02	0.02	0.01
0.00	0.00	0.00
0.06	0.06	0.01
0.05	0.05	0.04
1.03	1.03	1.02
0.95	0.95	0.97
1.98	1.98	1.99
93.99	93.98	94.68
5.01	4.96	4.40
1.00	1.06	0.93
100	100	100

Table S2 - EPMA Titanite

Ttn#	Ttn2		Ttn5			Ttn6
Ttn type	zoned		zoned			zoned
Analysis #	30	31	32	33	34	35
position	core	rim	core	rim	core	intermediate
(wt%)						
SiO2	29.72	30.30	30.08	30.41	30.02	29.74
TiO2	36.01	36.90	35.86	36.93	35.80	35.57
Al2O3	1.97	1.67	2.32	1.74	2.08	2.04
FeO	0.37	0.36	0.35	0.35	0.41	0.42
Fe2O3	0.41	0.40	0.39	0.39	0.45	0.47
MnO	0.05	0.05	0.11	0.05	0.13	0.08
CaO	26.93	27.62	27.53	28.23	27.21	27.10
Na2O	0.01	0.01	0.02	0.00	0.00	0.00
P2O5	0.06	0.04	0.05	0.04	0.11	0.16
ZrO2	0.06	0.00	0.12	0.01	0.12	0.09
Nb2O5	0.17	0.14	0.11	0.12	0.21	0.25
La2O3	0.23	0.02	0.20	0.00	0.23	0.27
Ce2O3	1.03	0.13	0.72	0.12	0.90	1.02
Nd2O3	0.70	0.17	0.27	0.15	0.48	0.70
Cl	0.00	0.00	0.00	0.00	0.00	0.00
F	0.46	0.59	0.67	0.63	0.53	0.50
Total	97.77	97.97	98.41	98.78	98.23	97.96
O≡Cl,F	0.19	0.25	0.28	0.26	0.22	0.21
Total-O≡Cl,F	97.58	97.72	98.13	98.52	98.01	97.75
(a.p.f.u.)						
Si	1.00	1.01	1.00	1.00	1.00	1.00
Ti	0.91	0.92	0.90	0.92	0.90	0.90
Al	0.08	0.07	0.09	0.07	0.08	0.08
Fe	0.01	0.01	0.01	0.01	0.01	0.01
Mn	0.00	0.00	0.00	0.00	0.00	0.00
Ca	0.97	0.98	0.98	1.00	0.97	0.98
Na	0.00	0.00	0.00	0.00	0.00	0.00
P	0.00	0.00	0.00	0.00	0.00	0.00
Zr	0.00	0.00	0.00	0.00	0.00	0.00
Nb	0.00	0.00	0.00	0.00	0.00	0.00
La	0.00	0.00	0.00	0.00	0.00	0.00
Ce	0.01	0.00	0.01	0.00	0.01	0.01
Nd	0.01	0.00	0.00	0.00	0.01	0.01
Cl	0.00	0.00	0.00	0.00	0.00	0.00
F	0.05	0.06	0.07	0.07	0.06	0.05
Total	3.05	3.06	3.07	3.07	3.06	3.06
F+Cl	0.02	0.03	0.04	0.03	0.03	0.03
Tot-(F+Cl)	3.03	3.03	3.04	3.04	3.03	3.03
XTtn	0.911	0.925	0.899	0.922	0.906	0.907
XAl,Fe-F	0.049	0.062	0.071	0.066	0.056	0.054

	TTn7			Ttn7bis			Ttn
	zoned			zoned			zor
36	37	38	39	40	42	59	
rim	core	rim	core	rim	new grain	core	
30.27	30.10	30.34	29.74	30.37	30.26	30.74	
36.99	36.37	37.09	36.18	37.17	37.72	35.93	
1.67	2.09	1.65	2.23	1.74	1.64	2.41	
0.35	0.39	0.42	0.42	0.31	0.27	0.33	
0.39	0.43	0.47	0.46	0.34	0.30	0.36	
0.06	0.06	0.11	0.15	0.09	0.10	0.06	
28.19	27.32	28.03	27.11	27.98	28.39	28.42	
0.02	0.01	0.03	0.02	0.01	0.01	0.01	
0.03	0.08	0.02	0.12	0.04	0.05	0.03	
0.00	0.11	0.00	0.05	0.02	0.00	0.52	
0.14	0.15	0.14	0.27	0.26	0.12	0.09	
0.06	0.25	0.02	0.15	0.00	0.01	0.00	
0.10	0.87	0.06	0.87	0.14	0.12	0.12	
0.19	0.50	0.13	0.66	0.32	0.07	0.12	
0.00	0.00	0.00	0.00	0.00	0.00	0.00	
0.61	0.57	0.58	0.55	0.55	0.61	0.75	
98.67	98.87	98.61	98.52	99.01	99.38	99.51	
0.26	0.24	0.24	0.23	0.23	0.26	0.31	
98.41	98.63	98.37	98.28	98.77	99.12	99.20	
1.00	1.00	1.00	0.99	1.00	0.99	1.01	
0.92	0.91	0.92	0.91	0.92	0.93	0.89	
0.07	0.08	0.06	0.09	0.07	0.06	0.09	
0.01	0.01	0.01	0.01	0.01	0.01	0.01	
0.00	0.00	0.00	0.00	0.00	0.00	0.00	
1.00	0.97	0.99	0.97	0.99	1.00	1.00	
0.00	0.00	0.00	0.00	0.00	0.00	0.00	
0.00	0.00	0.00	0.00	0.00	0.00	0.00	
0.00	0.00	0.00	0.00	0.00	0.00	0.01	
0.00	0.00	0.00	0.00	0.00	0.00	0.00	
0.00	0.00	0.00	0.00	0.00	0.00	0.00	
0.00	0.01	0.00	0.01	0.00	0.00	0.00	
0.00	0.01	0.00	0.01	0.00	0.00	0.00	
0.00	0.00	0.00	0.00	0.00	0.00	0.00	
0.06	0.06	0.06	0.06	0.06	0.06	0.08	
3.07	3.06	3.06	3.06	3.06	3.07	3.08	
0.03	0.03	0.03	0.03	0.03	0.03	0.04	
3.04	3.03	3.03	3.03	3.03	3.03	3.04	
0.925	0.907	0.924	0.901	0.924	0.929	0.897	
0.064	0.059	0.060	0.058	0.058	0.063	0.078	

ı35			Ttn43		
ıed			zoned		
60	65	66	67	68	
rim	core	core	rim	rim	*average*
30.53	29.78	30.07	30.54	30.41	*30.2*
36.97	36.16	36.01	37.29	36.99	*36.6*
2.00	2.27	2.31	1.72	1.95	*2.0*
0.34	0.27	0.34	0.37	0.30	*0.4*
0.37	0.30	0.38	0.41	0.34	*0.39*
0.03	0.04	0.09	0.04	0.03	*0.1*
28.38	27.13	27.76	28.45	27.99	*27.8*
0.01	0.00	0.00	0.01	0.00	*0.01*
0.04	0.22	0.08	0.01	0.08	*0.07*
0.03	0.00	0.09	0.00	0.01	*0.07*
0.13	0.04	0.07	0.03	0.05	*0.14*
0.00	0.24	0.13	0.02	0.04	*0.10*
0.03	0.99	0.74	0.03	0.32	*0.46*
0.01	0.72	0.52	0.14	0.28	*0.34*
0.00	0.01	0.00	0.00	0.00	*0.00*
0.67	0.52	0.66	0.63	0.60	*0.59*
99.16	98.41	98.86	99.27	99.05	*98.7*
0.28	0.22	0.28	0.27	0.25	*0.2*
98.88	98.19	98.58	99.01	98.80	*98.4*
1.00	1.00	1.00	1.00	1.00	*1.0*
0.91	0.91	0.90	0.92	0.92	*0.9*
0.08	0.09	0.09	0.07	0.08	*0.1*
0.01	0.01	0.01	0.01	0.01	*0.0*
0.00	0.00	0.00	0.00	0.00	*0.0*
1.00	0.97	0.99	1.00	0.99	*1.0*
0.00	0.00	0.00	0.00	0.00	*0.0*
0.00	0.00	0.00	0.00	0.00	*0.0*
0.00	0.00	0.00	0.00	0.00	*0.0*
0.00	0.00	0.00	0.00	0.00	*0.0*
0.00	0.00	0.00	0.00	0.00	*0.0*
0.00	0.01	0.01	0.00	0.00	*0.0*
0.00	0.01	0.01	0.00	0.00	*0.0*
0.00	0.00	0.00	0.00	0.00	*0.0*
0.07	0.05	0.07	0.07	0.06	*0.1*
3.07	3.06	3.08	3.07	3.06	*3.1*
0.03	0.03	0.03	0.03	0.03	*0.0*
3.04	3.03	3.04	3.04	3.03	*3.0*
0.913	0.904	0.900	0.923	0.916	*0.91*
0.070	0.055	0.069	0.066	0.062	*0.06*

	Ttn15		Ttn25	Ttn26	Ttn27
	unzoned		unzoned	unzoned	unzoned
	43	44	45	46	47
std.dev	core	rim	core	core	core
0.3	30.16	30.34	30.45	30.36	30.14
0.6	36.88	36.97	35.75	35.56	36.16
0.3	2.18	1.88	2.45	2.47	2.50
0.0	0.21	0.30	0.29	0.31	0.27
0.05	0.23	0.33	0.32	0.34	0.30
0.0	0.13	0.06	0.04	0.05	0.03
0.5	28.39	28.32	28.20	28.41	28.20
0.01	0.00	0.01	0.00	0.00	0.00
0.05	0.07	0.03	0.02	0.04	0.02
0.12	0.00	0.00	0.51	0.44	0.00
0.07	0.05	0.05	0.11	0.09	0.07
0.11	0.06	0.03	0.00	0.04	0.08
0.41	0.12	0.11	0.15	0.08	0.07
0.24	0.05	0.06	0.10	0.13	0.00
0.00	0.00	0.00	0.01	0.00	0.02
0.07	0.70	0.69	0.73	0.82	0.75
0.5	99.00	98.84	98.80	98.78	98.31
0.0	0.30	0.29	0.31	0.34	0.32
0.5	98.70	98.55	98.49	98.44	97.99
0.0	0.99	1.00	1.00	1.00	1.00
0.0	0.91	0.92	0.89	0.88	0.90
0.0	0.08	0.07	0.10	0.10	0.10
0.0	0.01	0.01	0.01	0.01	0.01
0.0	0.00	0.00	0.00	0.00	0.00
0.0	1.00	1.00	1.00	1.00	1.00
0.0	0.00	0.00	0.00	0.00	0.00
0.0	0.00	0.00	0.00	0.00	0.00
0.0	0.00	0.00	0.01	0.01	0.00
0.0	0.00	0.00	0.00	0.00	0.00
0.0	0.00	0.00	0.00	0.00	0.00
0.0	0.00	0.00	0.00	0.00	0.00
0.0	0.00	0.00	0.00	0.00	0.00
0.0	0.00	0.00	0.00	0.00	0.00
0.0	0.07	0.07	0.08	0.09	0.08
0.0	3.08	3.08	3.08	3.09	3.09
0.0	0.04	0.04	0.04	0.04	0.04
0.0	3.04	3.04	3.04	3.05	3.05
0.01	0.910	0.919	0.896	0.894	0.896
0.01	0.073	0.072	0.077	0.086	0.078

Ttn28	Ttn29	Ttn28	Ttn30		Ttn31		Ttn
unzoned	unzoned	unzoned	unzoned		unzoned		unzc
48	49	50	51	52	53	54	55
core	core	core	core	rim	core	rim	core
30.19	30.34	30.18	30.66	30.27	30.53	30.50	30.05
35.64	35.04	35.21	35.57	36.72	35.86	36.26	35.88
2.38	2.87	2.68	2.66	2.07	2.56	2.35	2.64
0.32	0.26	0.33	0.32	0.32	0.30	0.30	0.35
0.36	0.29	0.37	0.35	0.36	0.34	0.33	0.39
0.04	0.02	0.07	0.05	0.06	0.02	0.02	0.09
28.29	28.06	28.20	28.17	28.19	28.62	28.34	28.22
0.01	0.01	0.00	0.00	0.01	0.02	0.02	0.01
0.02	0.02	0.04	0.04	0.04	0.02	0.04	0.01
0.47	0.31	0.47	0.31	0.06	0.18	0.01	0.00
0.08	0.09	0.10	0.11	0.08	0.08	0.07	0.00
0.05	0.03	0.05	0.05	0.00	0.06	0.05	0.01
0.12	0.10	0.16	0.18	0.13	0.16	0.22	0.02
0.09	0.07	0.07	0.16	0.10	0.05	0.16	0.03
0.00	0.00	0.00	0.00	0.00	0.02	0.00	0.00
0.71	0.80	0.79	0.81	0.70	0.78	0.70	0.96
98.41	98.04	98.33	99.08	98.75	99.25	99.04	98.29
0.30	0.34	0.33	0.34	0.29	0.33	0.29	0.40
98.11	97.70	98.00	98.74	98.45	98.91	98.74	97.88
1.00	1.01	1.00	1.01	1.00	1.00	1.00	0.99
0.89	0.87	0.88	0.88	0.91	0.89	0.90	0.89
0.09	0.11	0.10	0.10	0.08	0.10	0.09	0.10
0.01	0.01	0.01	0.01	0.01	0.01	0.01	0.01
0.00	0.00	0.00	0.00	0.00	0.00	0.00	0.00
1.00	1.00	1.00	0.99	1.00	1.01	1.00	1.00
0.00	0.00	0.00	0.00	0.00	0.00	0.00	0.00
0.00	0.00	0.00	0.00	0.00	0.00	0.00	0.00
0.01	0.01	0.01	0.00	0.00	0.00	0.00	0.00
0.00	0.00	0.00	0.00	0.00	0.00	0.00	0.00
0.00	0.00	0.00	0.00	0.00	0.00	0.00	0.00
0.00	0.00	0.00	0.00	0.00	0.00	0.00	0.00
0.00	0.00	0.00	0.00	0.00	0.00	0.00	0.00
0.00	0.00	0.00	0.00	0.00	0.00	0.00	0.00
0.07	0.08	0.08	0.08	0.07	0.08	0.07	0.10
3.09	3.09	3.09	3.09	3.08	3.09	3.08	3.11
0.04	0.04	0.04	0.04	0.04	0.04	0.04	0.05
3.05	3.05	3.05	3.05	3.04	3.05	3.04	3.06
0.897	0.880	0.885	0.887	0.911	0.892	0.900	0.888
0.075	0.084	0.083	0.085	0.073	0.082	0.073	0.100

›32	Ttn34		Ttn40		Ttn42	
›ned	unzoned		unzoned		unzoned	
56	57	58	61	62	63	64
rim	core	rim	core	rim	core	rim
30.36	30.40	30.30	30.26	30.20	30.22	30.28
35.37	36.64	36.93	35.27	34.82	34.64	35.96
2.71	2.04	1.83	2.79	2.89	2.83	2.27
0.36	0.27	0.27	0.32	0.36	0.36	0.34
0.39	0.30	0.30	0.35	0.40	0.40	0.38
0.09	0.06	0.05	0.04	0.10	0.06	0.08
28.16	28.48	28.28	27.86	27.99	27.98	27.99
0.00	0.00	0.01	0.01	0.01	0.01	0.01
0.04	0.01	0.01	0.04	0.04	0.00	0.05
0.18	0.00	0.01	0.21	0.21	0.27	0.02
0.18	0.08	0.08	0.11	0.12	0.08	0.11
0.01	0.03	0.05	0.02	0.08	0.03	0.07
0.02	0.03	0.07	0.21	0.23	0.25	0.17
0.08	0.05	0.13	0.11	0.18	0.20	0.08
0.01	0.00	0.01	0.00	0.01	0.00	0.01
0.77	0.68	0.66	0.85	0.81	0.79	0.73
98.33	98.78	98.67	98.09	98.03	97.72	98.15
0.33	0.29	0.28	0.36	0.34	0.33	0.31
98.01	98.49	98.39	97.73	97.69	97.39	97.85
1.00	1.00	1.00	1.00	1.00	1.01	1.00
0.88	0.91	0.92	0.88	0.87	0.87	0.90
0.11	0.08	0.07	0.11	0.11	0.11	0.09
0.01	0.01	0.01	0.01	0.01	0.01	0.01
0.00	0.00	0.00	0.00	0.00	0.00	0.00
1.00	1.01	1.00	0.99	1.00	1.00	0.99
0.00	0.00	0.00	0.00	0.00	0.00	0.00
0.00	0.00	0.00	0.00	0.00	0.00	0.00
0.00	0.00	0.00	0.00	0.00	0.00	0.00
0.00	0.00	0.00	0.00	0.00	0.00	0.00
0.00	0.00	0.00	0.00	0.00	0.00	0.00
0.00	0.00	0.00	0.00	0.00	0.00	0.00
0.00	0.00	0.00	0.00	0.00	0.00	0.00
0.00	0.00	0.00	0.00	0.00	0.00	0.00
0.08	0.07	0.07	0.09	0.08	0.08	0.08
3.09	3.08	3.07	3.09	3.10	3.10	3.08
0.04	0.04	0.03	0.04	0.04	0.04	0.04
3.05	3.04	3.04	3.05	3.05	3.05	3.04
0.884	0.913	0.921	0.882	0.876	0.878	0.901
0.081	0.071	0.069	0.089	0.085	0.084	0.077

average	std.dev
30.3	0.1
35.9	0.7
2.5	0.3
0.3	0.0
0.34	0.04
0.1	0.0
28.2	0.2
0.01	0.01
0.03	0.02
0.18	0.18
0.09	0.03
0.04	0.02
0.13	0.07
0.09	0.05
0.00	0.01
0.76	0.07
98.5	0.4
0.3	0.0
98.2	0.4
1.0	0.0
0.9	0.0
0.1	0.0
0.0	0.0
0.0	0.0
1.0	0.0
0.0	0.0
0.0	0.0
0.0	0.0
0.0	0.0
0.0	0.0
0.0	0.0
0.0	0.0
0.0	0.0
0.1	0.0
3.1	0.0
0.0	0.0
3.0	0.0
0.90	0.01
0.08	0.01

LA-ICP-MS U-(Th-)Pb data analytical details

Laboratory & Sample Preparation	
Laboratory name	CNR-Istituto di Geoscienze e Georisorse U.O. Pavia (Italy)
Sample type/mineral	Monazite and titanite
Sample preparation	Polished thin section with a thickness of 30μm and/or 50μm.
Imaging	BSE images with normal brightness/contrast setting and highly contrasted, MIRA3 TESCAN FE-SEM, 20kV, 16-17mm working distance
Laser ablation system	
Make, Model & type	Geolas 102 from Microlas
Ablation cell & volume	In-house built low volume cell, volume ca. 4 cm^3
Laser wavelength (nm)	193 nm
Pulse width (ns)	4 ns
Fluence ($J.cm^{-2}$)	7 $J.cm^{-2}$
Repetition rate (Hz)	3 Hz for monazite; 5 Hz for titanite
Ablation duration (secs)	40 secs
Ablation pit depth / ablation rate	Not measured
Spot diameter (□m) nominal/actual	10 □m for monazite; 25 or 35 □m for titanite
Sampling mode / pattern	Static spot ablation
Carrier gas	100% He in the cell, Ar make-up gas combined using a Y-piece 50% along the sample transport line to the torch.
Cell carrier gas flow (l/min)	0.44 l/min
ICP-MS Instrument	
Make, Model & type	Agilent 8900 ICP-MS
Sample introduction	Ablation aerosol (sample + He + Ar)
RF power (W)	1250W
Make-up gas flow (l/min)	0.44 l/min He + 0.91 l/min Ar
Detection system	Single quadrupole, dual detection, no-gas mode

Masses measured	Monazite: 202-208, 232, 238; titanite: 27, 29, 31, 43, 44, 49, 51, 55, 57, 89, 90, 93, 139, 140, 141, 146, 149, 151, 157, 159, 163, 165, 167, 169, 173, 175, 177, 198, 202-208, 232, 238 for titanite
Integration time per peak/dwell times (ms); quadrupole settling time between mass jumps	Monazite: ^{202}Hg (50), ^{204}Pb (150), ^{206}Pb (20), ^{207}Pb (40), ^{208}Pb (10), ^{232}Th (2), and ^{238}U (20); titanite: Al^{27}(3), Si^{29}(3), P^{31}(3), Ca^{43}(3), Ca^{44}(3), Ti^{49}(3), V^{51}(3), Mn^{55}(3), Fe^{57}(3), Y^{89}(5), Zr^{90}(5), Nb^{93}(5), La^{139}(5), Ce^{140}(5), Pr^{141}(5), Nd^{146}(5), Sm^{149}(5), Eu^{151}(5), Gd^{157}(5), Tb^{159}(5), Dy^{163}(5), Ho^{165}(5), Er^{167}(5), Tm^{169}(5), Yb^{173}(5), Lu^{175}(5), Hf^{177}(5), Hg^{198}(5), Hg^{202}(5), Pb^{204}(5), Pb^{206}(30), Pb^{207}(45), Pb^{208}(15), Th^{232}(10), U^{238}(10).
Total integration time per output datapoint (secs)	~0.4secs for monazite; ~0.3secs for titanite *(N.B. this should represent the time resolution of the data)*
'Sensitivity'	9000 cps of Th on NIST612
IC Dead time (ns)	
Data Processing	
Gas blank	30 second before and after ablation
Calibration strategy	MOACIR and MKED-1 were used as primary reference materials for monazite and titanite dating, respectively. 44069 monazite (Aleinikoff et al., 2006; Liu et al., 2012) was analysed as secondary/validation standard. Titanite trace elements: NIST610 was used as primary reference materials for titanite trace element characterization MKED-1 and TTN150 (Klemme et al., 2008) were analysed as secondaries/validation
Reference Material info	MOACIR monazite: Cruz et al. 1996; Seydoux-Guillaume et al. (2002a, b); considering the values, re-calibrated for isotopic disequilibrium, reported by Gasquet et al. (2010). 44069 monazite: Aleinikoff et al. (2006) with the ^{208}Pb/^{232}Th values after Liu et al. (2012); MKED-1 titanite: Spandler et al. (2016); Bear Lake and Khan River titanite: Mazoz et al. (2022).
Data processing package used / Correction for LIEF	GLITTER ® (van Achterbergh et al., 2001)
Mass discrimination	Standard-sample bracketing with ^{207}Pb/^{206}Pb, ^{206}Pb/^{238}U and ^{208}Pb/^{232}Th normalized to reference material
Common-Pb correction,	No common-Pb correction applied to the data.

composition and uncertainty	
Uncertainty level & propagation	Ages are quoted at 2sigma absolute, propagation is by quadratic addition according to Horstwood et al. (2003). Reproducibility and age uncertainty of reference material are propagated.
Quality control / Validation	44069 monazite (Aleinikoff et al., 2006): average ratio ± 1sigma; precision(%); accuracy(%) $^{207}Pb/^{206}Pb$: 0,0538±0,0014; 2.2%; $^{207}Pb/^{235}U$: 0,5070±0,0132; 2.1%; 2.45%[a] $^{206}Pb/^{238}U$: 0,0683±0,0007; 1.4%; 0.33%[a] $^{208}Pb/^{232}Th$: 0,0219±0,0002; 3.6%; 4.88%[b] Data for the accuracy are from Aleinikoff et al. (2006) for [a] and Liu et al. (2012) for [b]. Precision: 2.2% Wtd ave $^{206}Pb/^{238}U$ age = 338 ± 3 (2*s*, MSWD = 0.9, n=8) GJ-1 – Wtd ave $^{206}Pb/^{238}U$ age = 602 ± 5 (2*s*, MSWD = 1.1, n=7) Systematic uncertainty for propagation is 2% (2*s*). Bear Lake titanite: average ratio ± 1sigma; precision (%); accuracy (%). Accuracy is measured with respect to the reference value proposed by Mazoz et al. (2022). $^{207}Pb/^{206}Pb$: 0.11314±0.00148; 1.31%; 1.19%; $^{207}Pb/^{235}U$: 3.08732±0.08049; 2.61%; -3.57% $^{206}Pb/^{238}U$: 0.19792±0,00434; 2.19%; -4.94% Khan River titanite: average ratio ± 1sigma; precision (%); accuracy (%). Accuracy is measured with respect to the reference value proposed by Mazoz et al. (2022). $^{207}Pb/^{206}Pb$: 0.06118±0.005255; 8.59%; -1.28%; $^{207}Pb/^{235}U$: 0.73966±0.087656; 11.85%; -6.24% $^{206}Pb/^{238}U$: 0.08752±0.003556; 4.06%; -4.69%
Other information	

Aleinikoff, J.N.; Schenck, W.S.; Plank, M.O.; Srogi, L.; Fanning, C.M.; Kamo, S.L.; Bosbyshell, H. 2005. Deciphering igneous and metamorphic events in high-grade rocks of the wilmington complex, delaware: Morphology, cathodoluminescence and backscattered electron zoning, and shrimp u-pb geochronology of zircon and monazite. Geol. Soc. Am. Bull., 118, 39–64.

Cruz, M.J., Cunha, J.C., Merlet, C., Sabatè, P. 1996. Datação pontual das monazitas da região de Itambé, Bahia, através da microssonda electronica XXXIX Congresso Brasileiro de Geologia, vol 2, Sociedade Brasileira de Geologià-Núcleo, Bahià-Segipe, pp 206–209

Gasquet, D., Bertrand, J.M., Paquette, J.L., Lehmann, J., Ratzoy, G., De Ascencão Guedes, R., Tiepolo, M., Boullier, A.M., Scaillet, S., Nomade, S. 2010. Miocene to Messinian deformation and hydrothermal activity in a pre-Alpine basement massif of the French western Alps: new U–Th–Pb and argon ages from the Lauzière massif. Bulletin de la Société Géologique de France 181: 227–241

Horstwood, M.S.A., Foster, G.L., Parrish, R.R., Noble, S.R., Nowell, G.M. 2003. Common-Pb corrected in situ U-Pb accessory mineral geochronology by LA-MCICP-MS. J Anal At Spectrom 18:837–846

Klemme S., Prowatke, S., Münker, C., Magee, C. W., Lahaye, Y., Zack, T., Kasemann, S.A., Cabato, E.J.A., Kaeser, B., 2008. Synthesis and Preliminary Characterisation of New Silicate, Phosphate and Titanite Reference Glasses. Geostandards and Geoanalytical Research, 32, 39-54. DOI: 10.1111/j.1751-908X.2008.00873.x

Liu, Z.-C.; Wu, F.-Y.; Yang, Y.-H.; Yang, J.-H.; Wilde, S.A., 2012. Neodymium isotopic compositions of the standard monazites used in uthpb geochronology. Chem. Geol., 334, 221–239.

Mazoz, A., Goncalves, G.O., Lana, C., Buick I.S., Corfu, F., Kama, S.L., Wang, H., Yang, Y-H, Scholz, R., Queiroga, G., Fu, B., Martins, L., Schannor, M., Tropia de Abreu, A., Babinski, M., Peixoto, E., Ventura Santos, R., 2022. Khan River and Bear Lake: Two Natural Titanite Reference Materials for High-Spatial Resolution U-Pb Microanalysis. Geostandards and Geoanalytical Research, doi: 10.1111/ggr.12444

Seydoux-Guillaume, A.M., Paquette, J.L., Wiedenbeck, M., Montel, J.M., Heinrich, W. 2002a. Experimental resetting of the U–Th–Pb system in monazite. Chem Geol 191:165–181

Seydoux-Guillaume, A.M., Wirth, R., Nasdala, L., Gottschalk, M., Montel, J.M., Heinrich, W., 2002b. XRD, TEM and Raman study of experimental annealing of natural monazite. Phys Chem Miner 29: 240–253

Spandler, C., Hammerli, J., Sha, P., Hilbert-Wolf, H., Hu, Yi, Roberts, Eric, Schmitz, Mark, 2016. MKED1: A new titanite standard for in situ analysis of Sm–Nd isotopes and U–Pb geochronology. Chemical Geology 425, 110–126. https://doi.org/10.1016/j.chemgeo.2016.01.002.

Table S4 - U-Th-Pb data of monazite

RUN#	Date	Identifier	Mnz#	Textural position
RUN1	11/18/2021	007SMPL	4	foliation
RUN1	11/18/2021	008SMPL	4	foliation
RUN1	11/18/2021	009SMPL	4	foliation
RUN1	11/18/2021	010SMPL	4	foliation
RUN1	11/18/2021	011SMPL	4	foliation
RUN1	11/18/2021	012SMPL	4	foliation
RUN1	11/18/2021	013SMPL	6	*
RUN1	11/18/2021	014SMPL	6	*
RUN1	11/18/2021	015SMPL	5	foliation
RUN1	11/18/2021	016SMPL	5	foliation
RUN1	11/18/2021	017SMPL	5	foliation
RUN1	11/18/2021	018SMPL	12	foliation
RUN1	11/18/2021	019SMPL	12	foliation
RUN1	11/18/2021	020SMPL	12	foliation
RUN1	11/18/2021	021SMPL	12	foliation
RUN1	11/18/2021	022SMPL	12	foliation
RUN1	11/18/2021	023SMPL	11	foliation
RUN1	11/18/2021	024SMPL	11	foliation
RUN1	11/18/2021	025SMPL	11	foliation
RUN1	11/18/2021	028SMPL	8	foliation
RUN1	11/18/2021	029SMPL	8	foliation
RUN1	11/18/2021	030SMPL	10	foliation
RUN1	11/18/2021	031SMPL	10	foliation
RUN1	11/18/2021	032SMPL	10	foliation
RUN1	11/18/2021	033SMPL	10	foliation
RUN2	11/18/2021	006SMPL	9	foliation
RUN2	11/18/2021	007SMPL	9	foliation
RUN2	11/18/2021	008SMPL	9	foliation
RUN2	11/18/2021	009SMPL	9	foliation
RUN2	11/18/2021	010SMPL	14	*
RUN2	11/18/2021	011SMPL	14	*
RUN2	11/18/2021	012SMPL	14	*
RUN2	11/18/2021	013SMPL	14	*
RUN2	11/18/2021	014SMPL	14	*
RUN2	11/18/2021	015SMPL	14	*
RUN2	11/18/2021	016SMPL	14	*
RUN2	11/18/2021	017SMPL	14	*
RUN2	11/18/2021	018SMPL	15	within garnet
RUN2	11/18/2021	019SMPL	15	within garnet
RUN2	11/18/2021	020SMPL	15	within garnet

RUN2	11/18/2021	021SMPL	15	within garnet
				*contact/partially enc

			Data f	
Y-content (wt%)	$^{207}Pb/^{206}Pb$	1s abs	$^{207}Pb/^{235}U$	1s abs
1.96	0.05418	0.00213	0.25779	0.00966
1.97	0.05280	0.00142	0.26163	0.00675
2.07	0.05348	0.00149	0.27783	0.00742
1.8	0.05233	0.00206	0.23278	0.00874
2.12	0.05019	0.00180	0.23807	0.00816
2.81	0.05327	0.00150	0.27146	0.00731
0.47	0.05262	0.00168	0.29873	0.00910
0.15	0.05196	0.00184	0.31983	0.01084
0.67	0.05723	0.00161	0.29683	0.00795
2.06	0.05217	0.00146	0.27061	0.00723
2.61	0.05273	0.00175	0.27289	0.00863
0.84	0.05091	0.00187	0.23576	0.00828
0.84	0.05384	0.00186	0.26130	0.00859
1.34	0.05599	0.00296	0.26619	0.01348
1.34	0.05473	0.00231	0.26012	0.01050
1.05	0.05212	0.00261	0.22862	0.01096
0.8	0.05148	0.00163	0.24747	0.00749
2.43	0.05081	0.00166	0.26715	0.00834
0.4	0.05222	0.00200	0.25667	0.00936
0.18	0.05311	0.00220	0.30061	0.01190
0.43	0.05555	0.00222	0.28205	0.01074
0.31	0.05110	0.00280	0.24409	0.01283
2.6	0.05052	0.00195	0.26426	0.00969
2.6	0.05088	0.00271	0.27445	0.01401
0.4	0.05403	0.00206	0.27028	0.00980
1	0.05094	0.00177	0.22522	0.00672
1.01	0.05189	0.00169	0.29033	0.00801
1.59	0.06209	0.00207	0.43109	0.01216
1.21	0.05064	0.00221	0.20652	0.00806
0.98	0.05114	0.00185	0.26459	0.00832
0.32	0.06123	0.00198	0.38276	0.01040
0.32	0.07197	0.00356	0.36102	0.01603
0.32	0.05988	0.00273	0.28744	0.01176
0.32	0.05336	0.00196	0.25346	0.00809
0.25	0.05767	0.00183	0.37943	0.01006
0.22	0.05389	0.00182	0.29287	0.00840
0.98	0.05398	0.00192	0.24703	0.00755
2.82	0.04875	0.00166	0.23581	0.00685
0.52	0.05211	0.00174	0.33443	0.00948
1.46	0.05464	0.00175	0.34525	0.00924

2.39	0.04983	0.00195	0.24921	0.00858

:losed within garnet

or Wetherill plot[3]					
$^{206}Pb/^{238}U$	1s abs	Rho	$^{208}Pb/^{232}Th$	1s abs	$^{207}Pb/^{206}Pb$
0.03460	0.00047	0.0	0.01080	0.00013	379
0.03594	0.00036	0.1	0.01112	0.00013	320
0.03768	0.00039	0.1	0.01116	0.00013	349
0.03230	0.00043	0.0	0.00995	0.00012	300
0.03442	0.00043	0.1	0.01107	0.00013	204
0.03697	0.00039	0.1	0.01173	0.00014	340
0.04118	0.00047	0.1	0.01291	0.00015	312
0.04465	0.00056	0.1	0.01386	0.00016	284
0.03762	0.00040	0.1	0.01176	0.00014	500
0.03763	0.00039	0.1	0.01184	0.00014	293
0.03754	0.00045	0.1	0.01138	0.00014	317
0.03360	0.00042	0.1	0.01130	0.00014	237
0.03521	0.00044	0.1	0.01148	0.00014	364
0.03449	0.00062	0.0	0.01112	0.00013	452
0.03448	0.00050	0.0	0.01084	0.00013	401
0.03185	0.00054	0.0	0.00999	0.00012	291
0.03487	0.00040	0.1	0.01105	0.00013	262
0.03814	0.00045	0.1	0.01167	0.00014	232
0.03565	0.00048	0.1	0.01105	0.00013	295
0.04106	0.00061	0.1	0.01362	0.00017	333
0.03682	0.00052	0.0	0.01116	0.00013	434
0.03466	0.00065	0.1	0.01156	0.00015	245
0.03794	0.00052	0.1	0.01216	0.00015	219
0.03914	0.00071	0.1	0.01181	0.00015	235
0.03629	0.00049	0.1	0.01156	0.00014	372
0.03208	0.00033	0.0	0.01037	0.00010	238
0.04060	0.00039	0.0	0.01279	0.00012	281
0.05038	0.00051	0.0	0.01459	0.00014	677
0.02958	0.00040	0.0	0.00957	0.00010	224
0.03754	0.00041	0.0	0.01141	0.00011	247
0.04536	0.00044	0.0	0.01440	0.00014	647
0.03640	0.00061	0.0	0.01127	0.00011	985
0.03483	0.00050	0.0	0.01057	0.00010	599
0.03448	0.00038	0.0	0.01093	0.00010	344
0.04774	0.00045	0.0	0.01499	0.00014	517
0.03944	0.00040	0.0	0.01233	0.00012	366
0.03321	0.00035	0.0	0.01028	0.00010	370
0.03510	0.00035	0.1	0.01102	0.00011	136
0.04658	0.00046	0.0	0.01457	0.00014	290
0.04584	0.00043	0.0	0.01450	0.00014	398

0.03629	0.00044	0.1	0.01138	0.00011	187

Ages[3]				
1s abs	$^{207}Pb/^{235}U$	1s abs	$^{206}Pb/^{238}U$	1s abs
15	233	9	219	3
9	236	6	228	2
10	249	7	238	2
12	212	8	205	3
7	217	7	218	3
10	244	7	234	2
10	265	8	260	3
10	282	10	282	4
14	264	7	238	3
8	243	6	238	2
11	245	8	238	3
9	215	8	213	3
13	236	8	223	3
24	240	12	219	4
17	235	9	219	3
15	209	10	202	3
8	225	7	221	3
8	240	8	241	3
11	232	8	226	3
14	267	11	259	4
17	252	10	233	3
13	222	12	220	4
8	238	9	240	3
13	246	13	248	4
14	243	9	230	3
8	206	6	204	2
9	259	7	257	2
23	364	10	317	3
10	191	7	188	3
9	238	7	238	3
21	329	9	286	3
49	313	14	230	4
27	257	10	221	3
13	229	7	219	2
16	327	9	301	3
12	261	7	249	3
13	224	7	211	2
5	215	6	222	2
10	293	8	293	3
13	301	8	289	3

7	226	8	230	3

$^{208}Pb/^{232}Th$	1s abs	% U-Pb disc[1]	-Pb vs Th-Pb disc[2]
217	3	5.8	1.0
224	3	3.5	1.8
224	3	4.2	5.9
200	2	3.6	2.3
223	3	-0.6	-2.0
236	3	4.0	-0.7
259	3	2.0	0.3
278	3	0.1	1.2
236	3	9.8	0.7
238	3	2.1	0.1
229	3	3.0	3.7
227	3	0.9	-6.6
231	3	5.4	-3.4
224	3	8.8	-2.3
218	3	6.9	0.3
201	2	3.3	0.6
222	3	1.6	-0.5
235	3	-0.4	2.8
222	3	2.7	1.6
273	3	2.8	-5.4
224	3	7.6	3.8
232	3	1.0	-5.8
244	3	-0.8	-1.8
237	3	-0.5	4.1
232	3	5.4	-1.1
209	2	1.3	-2.4
257	2	0.9	-0.1
293	3	12.9	7.6
193	2	1.4	-2.4
229	2	0.3	3.5
289	3	13.1	-1.1
227	2	26.4	1.7
213	2	14.0	3.7
220	2	4.7	-0.5
301	3	8.0	0.0
248	2	4.4	0.7
207	2	6.0	1.8
222	2	-3.4	0.4
292	3	-0.2	0.4
291	3	4.1	-0.7

229	2	-1.7	0.5

1 Discordance calculated as (1-(206Pb/238U a
2 Discordance calculated as (1-(206Pb/238U a

age/207Pb/235U age))*100
age/208Pb/232Th age))*100

Table S4 - U-Th-Pb data of monazite

RUN#	Date	Identifier	Mnz#	Textural position
RUN1	11/30/2021	006SMPL	10	foliation
RUN1	11/30/2021	007SMPL	10	foliation
RUN1	11/30/2021	008SMPL	10	foliation
RUN1	11/30/2021	009SMPL	10	foliation
RUN1	11/30/2021	010SMPL	10	foliation
RUN1	11/30/2021	011SMPL	11	foliation
RUN1	11/30/2021	012SMPL	11	foliation
RUN1	11/30/2021	013SMPL	11	foliation
RUN1	11/30/2021	014SMPL	11	foliation
RUN1	11/30/2021	015SMPL	11	foliation
RUN1	11/30/2021	016SMPL	11	foliation
RUN1	11/30/2021	017SMPL	11	foliation
RUN1	11/30/2021	018SMPL	11	foliation
RUN1	11/30/2021	019SMPL	15	foliation
RUN1	11/30/2021	020SMPL	15	foliation
RUN1	11/30/2021	021SMPL	15	foliation
RUN1	11/30/2021	022SMPL	7	foliation
RUN1	11/30/2021	023SMPL	7	foliation
RUN1	11/30/2021	024SMPL	7	foliation
RUN1	11/30/2021	025SMPL	7	foliation
RUN1	11/30/2021	026SMPL	7	foliation

			Data for Wetherill p	
Y-content (wt%)	$^{207}Pb/^{206}Pb$	1s abs	$^{207}Pb/^{235}U$	1s abs
1.09	0.05415	0.00110	0.27734	0.00570
3.01	0.05143	0.00122	0.27030	0.00642
3.01	0.04999	0.00116	0.26450	0.00613
1.05	0.05046	0.00112	0.25774	0.00572
1.32	0.05075	0.00102	0.24976	0.00507
1.13	0.05148	0.00122	0.26543	0.00628
0.71	0.05347	0.00144	0.27498	0.00729
0.71	0.05029	0.00132	0.26143	0.00678
2.28	0.05006	0.00098	0.25675	0.00512
2.6	0.05102	0.00101	0.26215	0.00525
2.88	0.04892	0.00107	0.25538	0.00556
2.88	0.05117	0.00103	0.26447	0.00538
1.13	0.05994	0.00136	0.31257	0.00707
0.63	0.04989	0.00106	0.25333	0.00542
1.97	0.05421	0.00140	0.29559	0.00753
1.08	0.05087	0.00173	0.25288	0.00839
0.71	0.05393	0.00170	0.28448	0.00875
0.34	0.04880	0.00141	0.25918	0.00738
0.16	0.05035	0.00115	0.25981	0.00593
1.92	0.05207	0.00146	0.27781	0.00763
0.63	0.05206	0.00183	0.28017	0.00957

plot[3]					
$^{206}Pb/^{238}U$	1s abs	Rho	$^{208}Pb/^{232}Th$	1s abs	$^{207}Pb/^{206}Pb$
0.03715	0.00040	0.1	0.01155	0.00009	377
0.03812	0.00043	0.1	0.01198	0.00009	260
0.03837	0.00043	0.1	0.01172	0.00009	195
0.03705	0.00041	0.1	0.01185	0.00009	216
0.03569	0.00038	0.1	0.01134	0.00008	229
0.03740	0.00042	0.1	0.01158	0.00009	262
0.03730	0.00045	0.1	0.01181	0.00009	349
0.03770	0.00045	0.1	0.01183	0.00009	208
0.03720	0.00039	0.1	0.01152	0.00009	198
0.03727	0.00039	0.1	0.01191	0.00009	242
0.03786	0.00041	0.1	0.01188	0.00009	144
0.03749	0.00040	0.1	0.01206	0.00009	248
0.03783	0.00043	0.1	0.01150	0.00009	601
0.03683	0.00040	0.1	0.01168	0.00009	190
0.03955	0.00047	0.1	0.01175	0.00009	380
0.03606	0.00050	0.1	0.01147	0.00009	235
0.03826	0.00051	0.1	0.01166	0.00009	368
0.03852	0.00047	0.1	0.01187	0.00009	138
0.03743	0.00041	0.1	0.01194	0.00009	211
0.03869	0.00048	0.1	0.01224	0.00009	288
0.03903	0.00054	0.1	0.01194	0.00009	288

		Ages[3]		
1s abs	$^{207}Pb/^{235}U$	1s abs	$^{206}Pb/^{238}U$	1s abs
8	249	5	235	3
6	243	6	241	3
5	238	6	243	3
5	233	5	235	3
5	226	5	226	2
6	239	6	237	3
9	247	7	236	3
5	236	6	239	3
4	232	5	235	2
5	236	5	236	2
3	231	5	240	3
5	238	5	237	3
14	276	6	239	3
4	229	5	233	3
10	263	7	250	3
8	229	8	228	3
12	254	8	242	3
4	234	7	244	3
5	235	5	237	3
8	249	7	245	3
10	251	9	247	3

$^{208}Pb/^{232}Th$	1s abs	% U-Pb disc[1]	J-Pb vs Th-Pb disc[2]	
232	2	5.4	1.3	
241	2	0.7	0.2	
236	2	-1.9	3.0	
238	2	-0.7	-1.5	
228	2	0.1	-0.8	
233	2	1.0	1.7	
237	2	4.3	-0.5	
238	2	-1.2	0.4	
232	2	-1.5	1.7	
239	2	0.2	-1.4	
239	2	-3.7	0.4	
242	2	0.4	-2.1	
231	2	13.3	3.4	
235	2	-1.7	-0.7	
236	2	4.9	5.6	
231	2	0.2	-0.9	
234	2	4.8	3.2	
239	2	-4.1	2.1	
240	2	-1.0	-1.3	
246	2	1.7	-0.5	
240	2	1.6	2.8	

1 Discordance calculated as (1-(206Pb/238U a

2 Discordance calculated as (1-(206Pb/238U a

age/207Pb/235U age))*100
age/208Pb/232Th age))*100

Table S4 - U-Th-Pb data of monazite

RUN#	Date	Identifier	Mnz#	Textural positior
RUN2	11/17/2021	006SMPL	2	Foliation
RUN2	11/17/2021	007SMPL	2	Foliation
RUN2	11/17/2021	008SMPL	2	Foliation
RUN2	11/17/2021	009SMPL	1	Foliation
RUN2	11/17/2021	010SMPL	1	Foliation
RUN2	11/17/2021	011SMPL	7	Foliation
RUN2	11/17/2021	012SMPL	7	Foliation
RUN2	11/17/2021	013SMPL	7	Foliation
RUN2	11/17/2021	014SMPL	7	Foliation
RUN2	11/17/2021	015SMPL	8	Foliation
RUN2	11/17/2021	016SMPL	8	Foliation
RUN2	11/17/2021	017SMPL	8	Foliation
RUN2	11/17/2021	018SMPL	8	Foliation
RUN2	11/17/2021	019SMPL	9	Foliation
RUN2	11/17/2021	020SMPL	9	Foliation
RUN2	11/17/2021	021SMPL	9	Foliation
RUN2	11/17/2021	022SMPL	9	Foliation
RUN2	11/17/2021	026SMPL	6	Foliation
RUN2	11/17/2021	027SMPL	6	Foliation
RUN2	11/17/2021	028SMPL	6	Foliation
RUN2	11/17/2021	029SMPL	6	Foliation
RUN2	11/17/2021	030SMPL	6	Foliation
RUN2	11/17/2021	031SMPL	6	Foliation
RUN2	11/17/2021	036SMPL	5	Foliation
RUN2	11/17/2021	037SMPL	5	Foliation
RUN2	11/17/2021	038SMPL	5	Foliation
RUN2	11/17/2021	039SMPL	4	Foliation
RUN2	11/17/2021	040SMPL	4	Foliation
RUN2	11/17/2021	041SMPL	10	Foliation
RUN2	11/17/2021	032SMPL	3	Within garnet
RUN2	11/17/2021	033SMPL	3	Within garnet
RUN2	11/17/2021	034SMPL	3	Within garnet
RUN2	11/17/2021	035SMPL	3	Within garnet

			Data f	
Y-content (wt%)	$^{207}Pb/^{206}Pb$	1s abs	$^{207}Pb/^{235}U$	1s abs
0.25	0.04986	0.00136	0.21866	0.00565
0.74	0.04667	0.00145	0.23615	0.00694
0.38	0.05027	0.00148	0.22041	0.00613
0.5	0.04859	0.00137	0.23176	0.00618
0.22	0.05164	0.00146	0.30736	0.00817
0.6	0.04855	0.00231	0.20901	0.00934
0.34	0.04954	0.00201	0.28629	0.01085
0.18	0.05197	0.00213	0.28739	0.01098
0.41	0.05064	0.00182	0.24529	0.00824
0.43	0.08558	0.00565	0.37535	0.02290
0.43	0.04975	0.00271	0.21720	0.01097
0.92	0.04968	0.00288	0.21557	0.01164
2.15	0.05137	0.00328	0.24898	0.01480
1.86	0.04816	0.00254	0.21773	0.01068
0.15	0.05029	0.00254	0.21374	0.01003
0.36	0.05584	0.00284	0.22231	0.01050
0.27	0.05579	0.00366	0.24103	0.01472
0.13	0.05068	0.00359	0.32194	0.02112
0.12	0.06742	0.00460	0.42125	0.02659
1.37	0.05225	0.00390	0.22983	0.01596
0.67	0.05063	0.00291	0.22906	0.01225
1.07	0.05100	0.00342	0.23904	0.01492
2.52	0.05029	0.00345	0.24963	0.01593
0.65	0.04915	0.00437	0.25845	0.02159
2.08	0.05842	0.00537	0.37491	0.03258
0.33	0.05952	0.00462	0.31570	0.02331
no data	0.04930	0.00539	0.28452	0.02972
no data	0.05023	0.00590	0.35336	0.03991
no data	0.05031	0.00543	0.28300	0.02936
no data	0.05085	0.00408	0.25693	0.01922
no data	0.06235	0.00483	0.39903	0.02892
no data	0.05244	0.00451	0.31339	0.02525
no data	0.04797	0.00440	0.23779	0.02050

or Wetherill plot[3]					
$^{206}Pb/^{238}U$	1s abs	Rho	$^{208}Pb/^{232}Th$	1s abs	$^{207}Pb/^{206}Pb$
0.03180	0.00034	0.1	0.01020	0.00008	188
0.03667	0.00043	0.1	0.01112	0.00009	32
0.03179	0.00036	0.1	0.01028	0.00008	207
0.03458	0.00037	0.1	0.01075	0.00008	128
0.04315	0.00047	0.1	0.01336	0.00010	270
0.03118	0.00052	0.1	0.00975	0.00008	126
0.04187	0.00061	0.1	0.01292	0.00011	173
0.04008	0.00059	0.1	0.01222	0.00010	284
0.03511	0.00046	0.1	0.01145	0.00009	224
0.03175	0.00074	0.0	0.00836	0.00008	1329
0.03163	0.00059	0.1	0.01011	0.00008	183
0.03146	0.00062	0.1	0.00975	0.00008	180
0.03514	0.00076	0.1	0.01118	0.00010	257
0.03278	0.00060	0.1	0.01002	0.00008	107
0.03082	0.00054	0.1	0.00971	0.00008	208
0.02887	0.00051	0.0	0.00901	0.00007	446
0.03133	0.00070	0.0	0.01005	0.00009	444
0.04608	0.00110	0.1	0.01403	0.00012	226
0.04532	0.00105	0.0	0.01165	0.00010	851
0.03191	0.00080	0.1	0.01038	0.00009	296
0.03283	0.00065	0.1	0.01010	0.00008	224
0.03400	0.00077	0.1	0.01035	0.00009	241
0.03602	0.00083	0.1	0.01131	0.00010	208
0.03815	0.00114	0.1	0.01092	0.00011	155
0.04655	0.00145	0.0	0.01255	0.00012	546
0.03848	0.00103	0.0	0.01173	0.00011	586
0.04186	0.00157	0.1	0.01290	0.00014	162
0.05103	0.00207	0.1	0.01486	0.00017	206
0.04080	0.00148	0.1	0.01399	0.00019	209
0.03666	0.00099	0.1	0.01109	0.00010	234
0.04642	0.00122	0.0	0.01386	0.00013	686
0.04335	0.00126	0.0	0.01208	0.00012	305
0.03596	0.00112	0.1	0.01037	0.00011	98

	Ages[3]			
1s abs	$^{207}Pb/^{235}U$	1s abs	$^{206}Pb/^{238}U$	1s abs
5	201	5	202	2
1	215	6	232	3
6	202	6	202	2
4	212	6	219	2
8	272	7	272	3
6	193	9	198	3
7	256	10	264	4
12	257	10	253	4
8	223	7	222	3
88	324	20	201	5
10	200	10	201	4
10	198	11	200	4
16	226	13	223	5
6	200	10	208	4
11	197	9	196	3
23	204	10	183	3
29	219	13	199	4
16	283	19	290	7
58	357	23	286	7
22	210	15	202	5
13	209	11	208	4
16	218	14	216	5
14	226	14	228	5
14	233	20	241	7
50	323	28	293	9
46	279	21	243	7
18	254	27	264	10
24	307	35	321	13
23	253	26	258	9
19	232	17	232	6
53	341	25	293	8
26	277	22	274	8
9	217	19	228	7

$^{208}Pb/^{232}Th$	1s abs	% U-Pb disc[1]	J-Pb vs Th-Pb disc[2]	
205	2	-0.5	-1.6	
224	2	-7.8	3.7	
207	2	0.3	-2.5	
216	2	-3.5	1.4	
268	2	-0.1	1.5	
196	2	-2.7	0.9	
259	2	-3.4	1.9	
245	2	1.2	3.1	
230	2	0.1	-3.4	
168	2	37.7	16.5	
203	2	-0.6	-1.3	
196	2	-0.7	1.8	
225	2	1.4	-0.9	
202	2	-4.0	3.1	
195	2	0.5	0.2	
181	1	10.0	1.2	
202	2	9.3	-1.6	
282	2	-2.5	3.0	
234	2	20.0	18.1	
209	2	3.6	-3.1	
203	2	0.6	2.5	
208	2	1.0	3.4	
227	2	-0.8	0.4	
220	2	-3.4	9.0	
252	2	9.3	14.1	
236	2	12.6	3.2	
259	3	-4.0	2.0	
298	3	-4.4	7.1	
281	4	-1.9	-8.9	
223	2	0.0	4.0	
278	3	14.2	4.9	
243	2	1.2	11.3	
209	2	-5.1	8.4	

1 Discordance calculated as (1-(206Pb/238U a
2 Discordance calculated as (1-(206Pb/238U a

age/207Pb/235U age))*100
age/208Pb/232Th age))*100

Table S4 - U-Th-Pb data of monazite

RUN#	Date	Identifier	Mnz#	Textural position
RUN2	16/11721	006SMPL	1a	Foliation
RUN2	16/11721	007SMPL	1a	Foliation
RUN2	16/11721	008SMPL	1a	Foliation
RUN2	16/11721	009SMPL	1a	Foliation
RUN2	16/11721	010SMPL	1a	Foliation
RUN2	16/11721	011SMPL	1a	Foliation
RUN2	16/11721	012SMPL	1a	Foliation
RUN2	16/11721	013SMPL	1a	Foliation
RUN2	16/11721	014SMPL	1a	Foliation
RUN2	16/11721	015SMPL	4a	Foliation
RUN2	16/11721	016SMPL	4a	Foliation
RUN2	16/11721	017SMPL	4a	Foliation
RUN2	16/11721	018SMPL	4a	Foliation
RUN2	16/11721	019SMPL	4a	Foliation
RUN2	16/11721	020SMPL	4a	Foliation
RUN2	16/11721	021SMPL	4a	Foliation
RUN2	16/11721	022SMPL	6a	Foliation
RUN2	16/11721	023SMPL	6a	Foliation
RUN2	16/11721	024SMPL	6a	Foliation
RUN2	16/11721	025SMPL	6a	Foliation
RUN2	16/11721	026SMPL	6a	Foliation
RUN2	16/11721	027SMPL	6b	Foliation
RUN2	16/11721	028SMPL	6b	Foliation
RUN2	16/11721	029SMPL	6b	Foliation
RUN2	16/11721	030SMPL	6b	Foliation

			Data for Wetherill p	
Y-content (wt%)	$^{207}Pb/^{206}Pb$	1s abs	$^{207}Pb/^{235}U$	1s abs
0.39	0.05241	0.00142	0.31872	0.00997
0.21	0.06196	0.00200	0.37836	0.01336
0.15	0.05406	0.00148	0.31008	0.00977
0.15	0.05869	0.00171	0.34893	0.01145
0.08	0.05051	0.00153	0.29493	0.00995
0.02	0.05251	0.00148	0.32251	0.01035
0.13	0.05119	0.00145	0.30553	0.00986
0.06	0.05246	0.00167	0.31356	0.01102
0.13	0.05503	0.00169	0.31342	0.01069
0.79	0.05326	0.00170	0.33351	0.01169
0.82	0.05297	0.00137	0.26020	0.00789
0.36	0.05235	0.00206	0.20887	0.00864
1.14	0.05658	0.00250	0.22864	0.01040
0.25	0.06165	0.00196	0.25367	0.00884
0.05	0.05587	0.00168	0.27799	0.00935
0.61	0.05759	0.00162	0.34405	0.01100
0.38	0.05435	0.00168	0.32358	0.01111
0.38	0.05314	0.00161	0.31472	0.01062
0.12	0.05216	0.00154	0.29152	0.00968
0.05	0.05752	0.00179	0.34049	0.01169
0.15	0.05074	0.00161	0.29863	0.01045
0.11	0.04895	0.00149	0.29822	0.01009
0.13	0.05290	0.00176	0.30743	0.01112
0.15	0.05072	0.00162	0.28341	0.00992
0.17	0.05249	0.00173	0.28847	0.01039

plot[3]					
$^{206}Pb/^{238}U$	1s abs	Rho	$^{208}Pb/^{232}Th$	1s abs	$^{207}Pb/^{206}Pb$
0.04412	0.00047	0.0	0.01406	0.00027	303
0.04429	0.00056	0.0	0.01367	0.00027	673
0.04161	0.00045	0.0	0.01279	0.00025	374
0.04312	0.00049	0.0	0.01303	0.00025	556
0.04235	0.00049	0.0	0.01304	0.00025	219
0.04455	0.00050	0.0	0.01386	0.00027	308
0.04329	0.00048	0.0	0.01362	0.00026	249
0.04336	0.00052	0.0	0.01375	0.00027	306
0.04131	0.00049	0.0	0.01266	0.00025	413
0.04538	0.00056	0.0	0.01366	0.00027	340
0.03562	0.00038	0.0	0.01111	0.00022	328
0.02892	0.00041	0.0	0.00897	0.00018	301
0.02930	0.00046	0.0	0.00904	0.00018	475
0.02984	0.00037	0.0	0.00944	0.00018	662
0.03609	0.00042	0.0	0.01084	0.00021	447
0.04333	0.00048	0.0	0.01362	0.00026	514
0.04319	0.00052	0.0	0.01338	0.00026	386
0.04296	0.00050	0.0	0.01348	0.00026	335
0.04054	0.00047	0.0	0.01252	0.00024	292
0.04294	0.00051	0.0	0.01324	0.00026	512
0.04270	0.00051	0.0	0.01383	0.00027	229
0.04419	0.00051	0.1	0.01332	0.00026	145
0.04215	0.00052	0.0	0.01365	0.00027	325
0.04053	0.00049	0.0	0.01264	0.00024	228
0.03986	0.00049	0.0	0.01179	0.00023	307

Ages[3]				
1s abs	$^{207}Pb/^{235}U$	1s abs	$^{206}Pb/^{238}U$	1s abs
8	281	9	278	3
22	326	12	279	4
10	274	9	263	3
16	304	10	272	3
7	262	9	267	3
9	284	9	281	3
7	271	9	273	3
10	277	10	274	3
13	277	9	261	3
11	292	10	286	4
8	235	7	226	2
12	193	8	184	3
21	209	10	186	3
21	230	8	190	2
13	249	8	229	3
14	300	10	273	3
12	285	10	273	3
10	278	9	271	3
9	260	9	256	3
16	298	10	271	3
7	265	9	270	3
4	265	9	279	3
11	272	10	266	3
7	253	9	256	3
10	257	9	252	3

$^{208}Pb/^{232}Th$	1s abs	% U-Pb disc[1]	J-Pb vs Th-Pb disc[2]	
282	5	0.9	-1.4	
274	5	14.3	1.8	
257	5	4.2	2.3	
262	5	10.5	3.9	
262	5	-1.9	2.1	
278	5	1.0	1.0	
273	5	-0.9	-0.1	
276	5	1.2	-0.9	
254	5	5.7	2.6	
274	5	2.1	4.1	
223	4	3.9	1.0	
180	4	4.6	1.8	
182	4	11.0	2.3	
190	4	17.4	-0.2	
218	4	8.2	4.7	
273	5	8.9	0.0	
269	5	4.2	1.4	
271	5	2.4	0.2	
251	5	1.4	1.8	
266	5	8.9	1.9	
278	5	-1.6	-3.0	
267	5	-5.2	4.1	
274	5	2.2	-3.0	
254	5	-1.1	0.9	
237	5	2.1	6.0	

1 Discordance calculated as (1-(206Pb/238U a
2 Discordance calculated as (1-(206Pb/238U a

age/207Pb/235U age))*100
age/208Pb/232Th age))*100

Table S4 - U-Th-Pb data of monazite

RUN#	Date	Identifier	Mnz#	Textural position
Run1	11/16/2021	006SMPL	8a	Foliation
Run1	11/16/2021	007SMPL	8a	Foliation
Run1	11/16/2021	008SMPL	8a	Foliation
Run1	11/16/2021	009SMPL	8a	Foliation
Run1	11/16/2021	010SMPL	8a	Foliation
Run1	11/16/2021	011SMPL	8c	Foliation
Run1	11/16/2021	012SMPL	8c	Foliation
Run1	11/16/2021	013SMPL	8c	Foliation
Run1	11/16/2021	014SMPL	8b	Foliation
Run1	11/16/2021	015SMPL	8b	Foliation
Run1	11/16/2021	016SMPL	8b	Foliation
Run1	11/16/2021	017SMPL	8b	Foliation
Run1	11/16/2021	018SMPL	8b	Foliation
Run1	11/16/2021	019SMPL	8b	Foliation
Run1	11/16/2021	020SMPL	8b	Foliation
Run1	11/16/2021	021SMPL	8b	Foliation
Run1	11/16/2021	022SMPL	8b	Foliation
Run1	11/16/2021	023SMPL	8b	Foliation
Run1	11/16/2021	024SMPL	8b	Foliation
Run1	11/16/2021	025SMPL	8b	Foliation

			Data f	
Y-content (wt%)	$^{207}Pb/^{206}Pb$	1s abs	$^{207}Pb/^{235}U$	1s abs
0.62	0.05130	0.00143	0.28492	0.00826
0.09	0.05131	0.00104	0.33697	0.00756
1.42	0.05360	0.00166	0.33589	0.01069
0.01	0.05135	0.00090	0.34711	0.00705
0.04	0.05175	0.00115	0.28371	0.00684
0.46	0.04733	0.00117	0.23495	0.00620
0.73	0.04801	0.00104	0.22439	0.00531
0.58	0.05049	0.00112	0.26405	0.00638
0.07	0.05113	0.00107	0.35195	0.00810
0.36	0.05035	0.00115	0.24426	0.00599
0.5	0.05110	0.00088	0.34474	0.00691
0.63	0.05103	0.00089	0.34878	0.00701
0.5	0.05010	0.00088	0.34296	0.00693
0.47	0.04973	0.00117	0.23660	0.00595
0	0.05052	0.00253	0.34112	0.01681
0	0.05303	0.00263	0.35187	0.01708
0.18	0.05241	0.00113	0.32803	0.00771
0.18	0.05114	0.00095	0.32702	0.00688
0.64	0.05175	0.00136	0.30210	0.00827
0.44	0.05134	0.00107	0.32546	0.00743

·or Wetherill plot[3]					
$^{206}Pb/^{238}U$	1s abs	Rho	$^{208}Pb/^{232}Th$	1s abs	$^{207}Pb/^{206}Pb$
0.04027	0.00048	0.1	0.01248	0.00014	254
0.04762	0.00049	0.1	0.01484	0.00017	255
0.04544	0.00058	0.1	0.01396	0.00016	354
0.04902	0.00048	0.1	0.01502	0.00017	257
0.03975	0.00043	0.1	0.01242	0.00014	274
0.03599	0.00040	0.1	0.01112	0.00013	66
0.03390	0.00035	0.1	0.01046	0.00012	100
0.03792	0.00040	0.1	0.01156	0.00013	218
0.04989	0.00052	0.1	0.01536	0.00018	247
0.03518	0.00037	0.1	0.01084	0.00012	211
0.04892	0.00047	0.1	0.01486	0.00017	245
0.04956	0.00048	0.1	0.01530	0.00017	242
0.04964	0.00048	0.1	0.01465	0.00017	200
0.03449	0.00038	0.1	0.01056	0.00012	182
0.04894	0.00087	0.1	0.01421	0.00017	219
0.04810	0.00086	0.1	0.01347	0.00016	330
0.04539	0.00048	0.1	0.01378	0.00016	303
0.04637	0.00046	0.1	0.01426	0.00016	247
0.04234	0.00049	0.1	0.01062	0.00013	274
0.04597	0.00047	0.1	0.01326	0.00015	256

		Ages[3]		
1s abs	$^{207}Pb/^{235}U$	1s abs	$^{206}Pb/^{238}U$	1s abs
7	255	7	255	3
5	295	7	300	3
11	294	9	286	4
5	303	6	309	3
6	254	6	251	3
2	214	6	228	3
2	206	5	215	2
5	238	6	240	3
5	306	7	314	3
5	222	5	223	2
4	301	6	308	3
4	304	6	312	3
4	299	6	312	3
4	216	5	219	2
11	298	15	308	5
16	306	15	303	5
7	288	7	286	3
5	287	6	292	3
7	268	7	267	3
5	286	7	290	3

$^{208}Pb/^{232}Th$	1s abs	% U-Pb disc[1]	J-Pb vs Th-Pb disc[2]
251	3	0.0	1.5
298	3	-1.7	0.7
280	3	2.6	2.2
301	3	-2.0	2.3
249	3	0.9	0.7
224	3	-6.4	1.9
210	2	-4.6	2.1
232	3	-0.8	3.2
308	4	-2.5	1.8
218	3	-0.4	2.2
298	3	-2.4	3.2
307	3	-2.6	1.6
294	3	-4.3	5.9
212	2	-1.4	2.9
285	3	-3.4	7.4
270	3	1.1	10.7
277	3	0.7	3.3
286	3	-1.7	2.1
214	3	0.3	20.1
266	3	-1.3	8.1

1 Discordance calculated as (1-(206Pb/238U a
2 Discordance calculated as (1-(206Pb/238U a

age/207Pb/235U age))*100
age/208Pb/232Th age))*100

Table S4 - U-Th-Pb data of monazite

RUN#	Date	Identifier	Mnz#	Textural position
RUN1	11/17/2021	006SMPL	6c	Foliation
RUN1	11/17/2021	007SMPL	6c	Foliation
RUN1	11/17/2021	008SMPL	6c	Foliation
RUN1	11/17/2021	009SMPL	6c	Foliation
RUN1	11/17/2021	010SMPL	6c	Foliation
RUN1	11/17/2021	011SMPL	6c	Foliation
RUN1	11/17/2021	012SMPL	6c	Foliation
RUN1	11/17/2021	013SMPL	6c	Foliation
RUN1	11/17/2021	014SMPL	6c	Foliation
RUN1	11/17/2021	015SMPL	6c	Foliation
RUN1	11/17/2021	016SMPL	6c	Foliation
RUN1	11/17/2021	017SMPL	6c	Foliation
RUN1	11/17/2021	018SMPL	6c	Foliation
RUN1	11/17/2021	019SMPL	6b	Foliation
RUN1	11/17/2021	020SMPL	6b	Foliation
RUN1	11/17/2021	021SMPL	6b	Foliation
RUN1	11/17/2021	022SMPL	6b	Foliation
RUN1	11/17/2021	026SMPL	6b	Foliation
RUN1	11/17/2021	027SMPL	6b	Foliation
RUN1	11/17/2021	028SMPL	6b	Foliation
RUN1	11/17/2021	029SMPL	6b	Foliation
RUN1	11/17/2021	030SMPL	6b	Foliation
RUN1	11/17/2021	031SMPL	6b	Foliation
RUN1	11/17/2021	032SMPL	6b	Foliation
RUN1	11/17/2021	033SMPL	6a	Foliation
RUN1	11/17/2021	034SMPL	6a	Foliation
RUN1	11/17/2021	035SMPL	6a	Foliation
RUN1	11/17/2021	036SMPL	6a	Foliation
RUN1	11/17/2021	037SMPL	6a	Foliation
RUN1	11/17/2021	038SMPL	6a	Foliation
RUN1	11/17/2021	039SMPL	6a	Foliation
RUN1	11/17/2021	040SMPL	6a	Foliation
RUN1	11/17/2021	041SMPL	6a	Foliation
RUN1	11/17/2021	042SMPL	6a	Foliation
RUN1	11/17/2021	043SMPL	7a	within garnet
RUN1	11/17/2021	044SMPL	7a	within garnet
RUN1	11/17/2021	045SMPL	7a	within garnet
RUN1	11/17/2021	046SMPL	7a	within garnet
RUN1	11/17/2021	047SMPL	7a	within garnet
RUN1	11/17/2021	048SMPL	7a	within garnet
RUN1	11/17/2021	049SMPL	7a	within garnet
RUN1	11/17/2021	055SMPL	7b	Foliation
RUN1	11/17/2021	056SMPL	7b	Foliation

RUN1	11/17/2021	057SMPL	7b	Foliation
RUN1	11/17/2021	058SMPL	7b	Foliation
RUN1	11/17/2021	059SMPL	7b	Foliation
RUN1	11/17/2021	060SMPL	7b	Foliation
RUN1	11/17/2021	061SMPL	7b	Foliation
RUN1	11/17/2021	062SMPL	2a	Foliation
RUN1	11/17/2021	063SMPL	2a	Foliation
RUN1	11/17/2021	065SMPL	2a	Foliation

				Data f
Y-content (wt%)	$^{207}Pb/^{206}Pb$	1s abs	$^{207}Pb/^{235}U$	1s abs
0.03	0.05367	0.00168	0.24465	0.00740
0.06	0.05832	0.00188	0.34918	0.01086
0.11	0.05105	0.00161	0.27536	0.00840
0.11	0.05174	0.00234	0.28623	0.01252
0.54	0.05028	0.00159	0.23120	0.00711
0.54	0.05053	0.00151	0.26667	0.00774
0.23	0.05647	0.00218	0.28990	0.01075
0.54	0.05362	0.00198	0.24409	0.00873
0.46	0.05107	0.00171	0.26080	0.00847
0.28	0.05379	0.00203	0.24987	0.00912
no data	0.05322	0.00198	0.22203	0.00799
no data	0.05260	0.00186	0.21400	0.00730
no data	0.05423	0.00192	0.22419	0.00769
0.37	0.05123	0.00161	0.24631	0.00751
0.37	0.05252	0.00162	0.25961	0.00773
0.09	0.05248	0.00174	0.31893	0.01025
0.00	0.05392	0.00244	0.32469	0.01412
0.18	0.05018	0.00197	0.31012	0.01169
0.13	0.05485	0.00220	0.32811	0.01267
0.38	0.05292	0.00193	0.25327	0.00888
0.38	0.05130	0.00196	0.23394	0.00862
0.36	0.05232	0.00209	0.25113	0.00964
1.75	0.05087	0.00190	0.25119	0.00904
0.32	0.05009	0.00203	0.23559	0.00916
0.34	0.05267	0.00338	0.20056	0.01223
0.34	0.05122	0.00199	0.24519	0.00911
0.00	0.05183	0.00246	0.28732	0.01309
0.06	0.05707	0.00316	0.32042	0.01689
0.28	0.05193	0.00224	0.24684	0.01016
0.13	0.05245	0.00251	0.31603	0.01440
0.00	0.05167	0.00273	0.30592	0.01543
0.00	0.05082	0.00281	0.31330	0.01648
0.27	0.05001	0.00263	0.24824	0.01235
0.49	0.05342	0.00316	0.25480	0.01420
1.43	0.05159	0.00264	0.32872	0.01581
0.46	0.05551	0.00292	0.34824	0.01717
0.40	0.05185	0.00231	0.34187	0.01436
0.88	0.05290	0.00238	0.35162	0.01487
0.68	0.05178	0.00238	0.34031	0.01467
0.33	0.05124	0.00253	0.31879	0.01477
0.02	0.05135	0.00249	0.31876	0.01452
1.60	0.04969	0.00311	0.20545	0.01196
1.88	0.05107	0.00283	0.28540	0.01464

0.94	0.05118	0.00314	0.34789	0.01974
0.31	0.05161	0.00294	0.34196	0.01801
0.75	0.05210	0.00298	0.33892	0.01792
0.15	0.05197	0.00452	0.28236	0.02257
1.60	0.05119	0.00310	0.33258	0.01856
0.28	0.05809	0.00521	0.25111	0.02082
0.23	0.05369	0.00539	0.25725	0.02386
0.06	0.05118	0.00654	0.26810	0.03127

or Wetherill plot[3]					
$^{206}Pb/^{238}U$	1s abs	Rho	$^{208}Pb/^{232}Th$	1s abs	$^{207}Pb/^{206}Pb$
0.03306	0.00048	0.1	0.01058	0.00008	357
0.04343	0.00065	0.1	0.01325	0.00010	542
0.03912	0.00057	0.1	0.01248	0.00009	243
0.04013	0.00071	0.1	0.01234	0.00009	274
0.03336	0.00049	0.1	0.01065	0.00008	208
0.03828	0.00054	0.1	0.01165	0.00008	219
0.03724	0.00061	0.1	0.01147	0.00008	471
0.03301	0.00053	0.1	0.01117	0.00008	355
0.03705	0.00056	0.1	0.01159	0.00008	244
0.03369	0.00055	0.1	0.01056	0.00008	362
0.03026	0.00048	0.1	0.00925	0.00007	338
0.02951	0.00046	0.1	0.00904	0.00007	312
0.02999	0.00047	0.1	0.00940	0.00007	381
0.03487	0.00051	0.1	0.01077	0.00008	251
0.03584	0.00052	0.1	0.01214	0.00009	308
0.04408	0.00067	0.1	0.01350	0.00010	306
0.04369	0.00079	0.1	0.01351	0.00010	368
0.04485	0.00074	0.1	0.01340	0.00010	203
0.04339	0.00073	0.1	0.01331	0.00010	406
0.03473	0.00055	0.1	0.01092	0.00008	325
0.03309	0.00053	0.1	0.01043	0.00008	254
0.03483	0.00058	0.1	0.01061	0.00008	299
0.03583	0.00058	0.1	0.01085	0.00008	235
0.03413	0.00057	0.1	0.01056	0.00008	199
0.02763	0.00064	0.1	0.00855	0.00007	315
0.03473	0.00057	0.1	0.01092	0.00008	251
0.04023	0.00075	0.1	0.01216	0.00009	278
0.04075	0.00086	0.1	0.01282	0.00010	494
0.03449	0.00061	0.1	0.01123	0.00009	282
0.04373	0.00083	0.1	0.01332	0.00010	305
0.04296	0.00086	0.1	0.01372	0.00011	271
0.04475	0.00092	0.1	0.01322	0.00010	233
0.03602	0.00072	0.1	0.01171	0.00010	195
0.03461	0.00076	0.1	0.01094	0.00009	347
0.04624	0.00091	0.1	0.01435	0.00012	267
0.04552	0.00092	0.1	0.01467	0.00012	433
0.04784	0.00085	0.1	0.01476	0.00012	279
0.04824	0.00087	0.1	0.01583	0.00012	325
0.04769	0.00087	0.1	0.01508	0.00012	276
0.04515	0.00087	0.1	0.01462	0.00012	252
0.04505	0.00085	0.1	0.01415	0.00011	257
0.03000	0.00069	0.1	0.01027	0.00009	181
0.04055	0.00084	0.1	0.01322	0.00011	244

0.04934	0.00111	0.1	0.01625	0.00014	249
0.04808	0.00102	0.1	0.01574	0.00014	268
0.04720	0.00101	0.1	0.01569	0.00013	290
0.03942	0.00118	0.1	0.01292	0.00013	284
0.04715	0.00105	0.1	0.01521	0.00013	249
0.03137	0.00096	0.0	0.01044	0.00011	533
0.03477	0.00116	0.0	0.01392	0.00014	358
0.03800	0.00159	0.1	0.01274	0.00015	249

Ages[3]				
1s abs	$^{207}Pb/^{235}U$	1s abs	$^{206}Pb/^{238}U$	1s abs
11	222	7	210	3
17	304	9	274	4
8	247	8	247	4
12	256	11	254	5
7	211	6	212	3
7	240	7	242	3
18	258	10	236	4
13	222	8	209	3
8	235	8	235	4
14	226	8	214	3
13	204	7	192	3
11	197	7	187	3
14	205	7	190	3
8	224	7	221	3
9	234	7	227	3
10	281	9	278	4
17	286	12	276	5
8	274	10	283	5
16	288	11	274	5
12	229	8	220	4
10	213	8	210	3
12	227	9	221	4
9	228	8	227	4
8	215	8	216	4
20	186	11	176	4
10	223	8	220	4
13	256	12	254	5
27	282	15	257	5
12	224	9	219	4
15	279	13	276	5
14	271	14	271	5
13	277	15	282	6
10	225	11	228	5
21	230	13	219	5
14	289	14	291	6
23	303	15	287	6
12	299	13	301	5
15	306	13	304	5
13	297	13	300	5
12	281	13	285	5
12	281	13	284	5
11	190	11	191	4
14	255	13	256	5

15	303	17	310	7
15	299	16	303	6
17	296	16	297	6
25	253	20	249	7
15	292	16	297	7
48	227	19	199	6
36	232	22	220	7
32	241	28	240	10

$^{208}Pb/^{232}Th$	1s abs	% U-Pb disc[1]	U-Pb vs Th-Pb disc[2]
213	2	5.6	-1.5
266	2	9.9	2.9
251	2	-0.2	-1.3
248	2	0.8	2.3
214	2	-0.2	-1.2
234	2	-0.9	3.3
231	2	8.8	2.2
225	2	5.6	-7.2
233	2	0.3	0.7
212	2	5.7	0.6
186	1	5.6	3.2
182	1	4.8	3.0
189	1	7.3	0.7
217	2	1.2	2.0
244	2	3.1	-7.4
271	2	1.1	2.5
271	2	3.4	1.6
269	2	-3.1	4.9
267	2	5.0	2.4
220	2	4.0	0.3
210	2	1.7	0.1
213	2	3.0	3.3
218	2	0.3	3.9
212	2	-0.7	1.9
172	1	5.3	2.1
220	2	1.2	0.3
244	2	0.9	3.9
257	2	8.8	0.0
226	2	2.4	-3.3
267	2	1.1	3.1
275	2	-0.1	-1.6
265	2	-2.0	5.9
235	2	-1.3	-3.2
220	2	4.8	-0.3
288	2	-1.0	1.2
294	2	5.4	-2.6
296	2	-0.9	1.7
317	2	0.7	-4.5
303	2	-1.0	-0.7
293	2	-1.3	-3.1
284	2	-1.1	0.0
207	2	-0.4	-8.4
265	2	-0.5	-3.6

326	3	-2.4	-4.9
316	3	-1.4	-4.3
315	3	-0.3	-5.8
259	3	1.3	-4.1
305	3	-1.9	-2.7
210	2	12.5	-5.4
279	3	5.2	-26.8
256	3	0.3	-6.4

1 Discordance calculated as (1-(206Pb/238U a

2 Discordance calculated as (1-(206Pb/238U a

age/207Pb/235U age))*100
age/208Pb/232Th age))*100

Table S5 - Titanite Trace elements and U-Pb

Titanite type	Run name	Spot dimension (microns)	Identifier
Type Z	RUN2	35	006SMPL
Type Z	RUN2	35	007SMPL
Type Z	RUN2	35	008SMPL
Type Z	RUN2	35	009SMPL
Type Z	RUN2	35	010SMPL
Type Z	RUN2	35	011SMPL
Type Z	RUN2	35	012SMPL
Type Z	RUN2	35	013SMPL
Type Z	RUN2	35	014SMPL
Type Z	RUN2	35	015SMPL
Type Z	RUN2	35	016SMPL
Type Z	RUN2	35	017SMPL
Type Z	RUN2	35	018SMPL
Type Z	RUN2	35	019SMPL
Type Z	RUN2	35	020SMPL
Type Z	RUN2	35	021SMPL
Type Z	RUN2	35	022SMPL
Type Z	RUN2	35	029SMPL
Type Z	RUN2	35	030SMPL
Type Z	RUN2	35	031SMPL
Type Z	RUN2	35	032SMPL
Type Z	RUN2	35	033SMPL
Type Z	RUN2	35	034SMPL
Type Z	RUN2	35	035SMPL
Type Z	RUN1	25	006SMPL
Type Z	RUN1	25	007SMPL
Type Z	RUN1	25	008SMPL
Type Z	RUN1	25	009SMPL
Type Z	RUN1	25	010SMPL
Type Z	RUN1	25	011SMPL
Type Z	RUN1	25	012SMPL
Type Z	RUN1	25	013SMPL
Type Z	RUN1	25	014SMPL
Type Z	RUN1	25	015SMPL
Type Z	RUN1	25	016SMPL
Type Z	RUN1	25	017SMPL

Ttn#	Textural position	Zoning feature	(ppm)
Ttn2	rim	dark	3197.87
Ttn2	rim	dark	6495.5
Ttn2	core	bright	26738.61
Ttn2	core	bright	26425.26
Ttn2	core	bright	25490.92
Ttn2	core	bright	21784.52
Ttn2	core	bright	30554.8
Ttn2	core	bright	27431.51
Ttn2	rim	dark/bright	25744.34
Ttn7	rim	dark	3446.25
Ttn7	rim	dark/bright	21737.94
Ttn7	rim	dark	3654.21
Ttn7	core	bright	23372.63
Ttn7	core	bright	22746.63
Ttn7	core	bright	20533.66
Ttn7	core	bright	20091.69
Ttn7	rim	dark	7483.53
Ttn10	rim	dark	12436.62
Ttn10	core	bright	29877.02
Ttn10	core	bright	27505.22
Ttn10	core	bright	28236.41
Ttn10	core	bright	25624.22
Ttn10	core	bright	25304.42
Ttn10	core	bright	19011.8
Ttn3a	core	bright	22608.57
Ttn3a	core	bright	29196.06
Ttn3a	rim	dark	10862.15
Ttn4b	rim	dark	10308.28
Ttn4b	core	bright	11701.61
Ttn4b	core	bright	8323.18
Ttn4b	core	bright	13253.08
Ttn4b	core	bright	11846.44
Ttn5c	rim	dark	3909.82
Ttn5c	core	bright	14385.07
Ttn5c	core	bright	12695.78
Ttn5c	rim	dark	1835.54

		Data for Wetherill plot			
$^{207}Pb/^{206}Pb$	1s	$^{207}Pb/^{235}U$	1s	$^{206}Pb/^{238}U$	1s
0.36702	0.01738	**2.48979**	**0.11699**	**0.04923**	**0.00163**
0.41303	0.01564	**3.24608**	**0.13103**	**0.05702**	**0.00160**
0.16405	0.00562	**0.98495**	**0.03807**	**0.04356**	**0.00106**
0.13926	0.00473	**0.81421**	**0.03137**	**0.04243**	**0.00103**
0.12032	0.00421	**0.68522**	**0.02697**	**0.04134**	**0.00100**
0.23752	0.00770	**1.64362**	**0.06108**	**0.05022**	**0.00122**
0.12358	0.00498	**0.68086**	**0.02964**	**0.03998**	**0.00103**
0.17822	0.00608	**1.07253**	**0.04128**	**0.04367**	**0.00107**
0.34263	0.01145	**2.76385**	**0.10423**	**0.05858**	**0.00148**
0.63396	0.02176	**10.10473**	**0.38547**	**0.11568**	**0.00316**
0.40537	0.01363	**3.50418**	**0.13205**	**0.06272**	**0.00161**
0.25446	0.01447	**1.38472**	**0.07647**	**0.03950**	**0.00140**
0.12966	0.00634	**0.68635**	**0.03466**	**0.03844**	**0.00110**
0.31265	0.01329	**2.06660**	**0.09117**	**0.04799**	**0.00141**
0.15558	0.00738	**0.88122**	**0.04319**	**0.04115**	**0.00118**
0.16339	0.00628	**0.97400**	**0.04074**	**0.04326**	**0.00112**
0.48959	0.02018	**5.62497**	**0.24046**	**0.08354**	**0.00259**
0.19182	0.01162	**0.95945**	**0.05677**	**0.03637**	**0.00127**
0.11533	0.00522	**0.63294**	**0.03020**	**0.03988**	**0.00107**
0.12057	0.00500	**0.64814**	**0.02885**	**0.03903**	**0.00102**
0.11643	0.00509	**0.61535**	**0.02855**	**0.03835**	**0.00102**
0.10899	0.00466	**0.62554**	**0.02860**	**0.04167**	**0.00109**
0.11982	0.00481	**0.68442**	**0.02976**	**0.04148**	**0.00106**
0.14965	0.00662	**0.83133**	**0.03865**	**0.04034**	**0.00111**
0.13209	0.00907	**0.65590**	**0.04296**	**0.03601**	**0.00104**
0.16873	0.00843	**0.84959**	**0.04085**	**0.03653**	**0.00081**
0.25826	0.01224	**1.62456**	**0.07308**	**0.04562**	**0.00107**
0.17532	0.01482	**0.88225**	**0.06924**	**0.03650**	**0.00143**
0.12634	0.00647	**0.71960**	**0.03582**	**0.04131**	**0.00087**
0.19496	0.01258	**1.09911**	**0.06640**	**0.04092**	**0.00126**
0.13552	0.00676	**0.77073**	**0.03729**	**0.04125**	**0.00086**
0.38270	0.01985	**3.41415**	**0.16468**	**0.06471**	**0.00189**
0.37306	0.02315	**2.98868**	**0.16751**	**0.05811**	**0.00212**
0.14473	0.00824	**0.81828**	**0.04464**	**0.04101**	**0.00101**
0.37604	0.01627	**2.99150**	**0.12344**	**0.05771**	**0.00132**
0.50083	0.02876	**4.00373**	**0.20424**	**0.05803**	**0.00208**

	MICROSTRUCTURES (EBSD	
Rho	**comment**	**observation**
0.0	High-distortion	twins
0.0	no-distortion	twins
0.0	no-distortion	twins
0.0	no-distortion	twins
0.0	no-distortion	twins
0.0	low-distortion	twins
0.0	no-distortion	twins
0.0	no-distortion	twins
0.0	moderate-distortion	twins
0.0	High-distortion	twins
0.0	High-distortion	twins
0.0	low-distortion	twins
0.0	no-distortion	twins
0.0	no-distortion	twins
0.0	no-distortion	twins
0.0	no-distortion	twins
0.0	low-distortion	twins
0.0	moderate-distortion	twins
0.0	no-distortion	twins
0.0	no-distortion	twins
0.0	no-distortion	twins
0.0	low-distortion	twins
0.0	low-distortion	twins
0.0	High-distortion	twins
0.0	High-distortion	
0.0	moderate-distortion	
0.0	moderate-distortion	
0.0	low-distortion	
0.0	low-distortion	
0.0	low-distortion	
0.0	low-distortion	
0.0	low-distortion	
0.0	moderate-distortion	
0.0	low-distortion	
0.0	no-distortion	
0.0	low-distortion	

D DATA) WBV magnitude microns-1
0.001601
0.000160
0.000304
0.000184
0.000110
0.000551
0.000428
0.000045
0.000691
0.000968
0.000561
0.000273
0.000078
0.000512
0.003977
0.00017
0.002525
0.002682
0.006775
0.004124
0.003646
0.004069
0.001635
0.008995
0.000608
0.001308
0.000328
0.036794
0.040976
0.001919
0.037729
0.000392
0.004823
0.001567
0.003892
0.000847

Titanite type	Run name	Spot dimension (microns)	Identifier	Ttn#	Textural position
Type H	RUN2	35	036SMPL	Ttn18	core
Type H	RUN2	35	037SMPL	Ttn18	core
Type H	RUN2	35	038SMPL	Ttn18	core
Type H	RUN2	35	039SMPL	Ttn18	core
Type H	RUN2	35	040SMPL	Ttn19	rim
Type H	RUN2	35	041SMPL	Ttn19	core
Type H	RUN2	35	042SMPL	Ttn19	core
Type H	RUN2	35	043SMPL	Ttn19	rim
Type H	RUN2	35	050SMPL	Ttn16	rim
Type H	RUN2	35	051SMPL	Ttn16	core
Type H	RUN2	35	052SMPL	Ttn16	core
Type H	RUN2	35	053SMPL	Ttn16	core
Type H	RUN2	35	054SMPL	Ttn16	core
Type H	RUN2	35	055SMPL	Ttn24	rim
Type H	RUN2	35	056SMPL	Ttn24	core
Type H	RUN2	35	057SMPL	Ttn24	core
Type H	RUN2	35	058SMPL	Ttn24	core
Type H	RUN2	35	059SMPL	Ttn24	rim
Type H	RUN2	35	060SMPL	Ttn34	rim
Type H	RUN2	35	061SMPL	Ttn34	core
Type H	RUN2	35	062SMPL	Ttn34	core
Type H	RUN2	35	063SMPL	Ttn34	core
Type H	RUN2	35	064SMPL	Ttn34	core
Type H	RUN2	35	065SMPL	Ttn34	core
Type H	RUN2	35	066SMPL	Ttn34	rim
Type H	RUN1	25	024SMPL	Ttn28a	rim
Type H	RUN1	25	025SMPL	Ttn28a	core
Type H	RUN1	25	026SMPL	Ttn28a	rim
Type H	RUN1	25	027SMPL	Ttn29a	rim
Type H	RUN1	25	028SMPL	Ttn29a	core
Type H	RUN1	25	029SMPL	Ttn29a	core
Type H	RUN1	25	030SMPL	Ttn29a	rim
Type H	RUN1	25	031SMPL	Ttn29a	rim
Type H	RUN1	25	032SMPL	Ttn23a	core
Type H	RUN1	25	033SMPL	Ttn23a	core
Type H	RUN1	25	034SMPL	Ttn23a	core
Type H	RUN1	25	035SMPL	Ttn23a	core

Zoning feature	(ppm)	$^{207}Pb/^{206}Pb$
homogeneous	4650.51	0.07710
homogeneous	4271.46	0.08845
homogeneous	3910.71	0.08008
homogeneous	4455.07	0.06956
homogeneous	1413.26	0.06427
homogeneous	1657.19	0.06396
homogeneous	1352.36	0.06357
homogeneous	2038.4	0.06780
homogeneous	1434.58	0.11737
homogeneous	2353.54	0.10728
homogeneous	2719.76	0.13312
homogeneous	2503.05	0.65903
homogeneous	2299.72	0.07996
homogeneous	2511.15	0.10312
homogeneous	3840.43	0.08139
homogeneous	3419.48	0.11306
homogeneous	2763.82	0.10311
homogeneous	1804.08	0.16289
homogeneous	1354.86	0.12216
homogeneous	1328.53	0.14322
homogeneous	2307.89	0.07771
homogeneous	2340.5	0.07569
homogeneous	1199.14	0.17902
homogeneous	889.28	0.13878
homogeneous	1761.97	0.09290
homogeneous	2590.68	0.08005
homogeneous	2139.4	0.06272
homogeneous	2074.09	0.08920
homogeneous	2405.85	0.14563
homogeneous	2126.65	0.14093
homogeneous	1978.32	0.06546
homogeneous	1788.8	0.12784
homogeneous	1374.85	0.16464
homogeneous	3153.15	0.51090
homogeneous	4783.85	0.31354
homogeneous	3487.29	0.35077
homogeneous	3261.63	0.36099

Data for Wetherill plot					
1s	$^{207}Pb/^{235}U$	1s	$^{206}Pb/^{238}U$	1s	Rho
0.00362	**0.38483**	**0.01908**	**0.03625**	**0.00095**	**0.0**
0.00407	**0.42914**	**0.02090**	**0.03522**	**0.00093**	**0.0**
0.00381	**0.42173**	**0.02109**	**0.03823**	**0.00101**	**0.0**
0.00469	**0.35066**	**0.02383**	**0.03673**	**0.00112**	**0.0**
0.00258	**0.32956**	**0.01449**	**0.03723**	**0.00092**	**0.1**
0.00418	**0.30597**	**0.02033**	**0.03473**	**0.00104**	**0.1**
0.00278	**0.32239**	**0.01518**	**0.03685**	**0.00093**	**0.1**
0.00299	**0.37695**	**0.01783**	**0.04035**	**0.00102**	**0.1**
0.01086	**0.58735**	**0.05243**	**0.03642**	**0.00156**	**0.0**
0.00578	**0.51514**	**0.02839**	**0.03492**	**0.00102**	**0.0**
0.00673	**0.70210**	**0.03643**	**0.03830**	**0.00111**	**0.0**
0.02084	**11.99885**	**0.43972**	**0.13217**	**0.00327**	**0.0**
0.00384	**0.37695**	**0.01905**	**0.03424**	**0.00091**	**0.0**
0.00554	**0.55206**	**0.03040**	**0.03890**	**0.00112**	**0.0**
0.00394	**0.46117**	**0.02347**	**0.04112**	**0.00110**	**0.0**
0.00502	**0.62255**	**0.02928**	**0.04000**	**0.00107**	**0.0**
0.00527	**0.55128**	**0.02914**	**0.03889**	**0.00110**	**0.0**
0.00830	**0.86936**	**0.04511**	**0.03879**	**0.00117**	**0.0**
0.00605	**0.52715**	**0.02696**	**0.03132**	**0.00088**	**0.0**
0.00908	**0.71958**	**0.04505**	**0.03644**	**0.00124**	**0.0**
0.00328	**0.38075**	**0.01733**	**0.03556**	**0.00090**	**0.1**
0.00332	**0.36238**	**0.01703**	**0.03475**	**0.00089**	**0.1**
0.01134	**0.94792**	**0.05869**	**0.03840**	**0.00136**	**0.0**
0.00891	**0.66056**	**0.04185**	**0.03460**	**0.00117**	**0.0**
0.00464	**0.41142**	**0.02137**	**0.03213**	**0.00088**	**0.0**
0.00509	**0.41294**	**0.02556**	**0.03742**	**0.00085**	**0.0**
0.00392	**0.31128**	**0.01914**	**0.03600**	**0.00074**	**0.0**
0.00518	**0.46753**	**0.02650**	**0.03802**	**0.00082**	**0.0**
0.00850	**0.75805**	**0.04244**	**0.03776**	**0.00095**	**0.0**
0.00794	**0.76378**	**0.04159**	**0.03929**	**0.00095**	**0.0**
0.00432	**0.30748**	**0.01989**	**0.03407**	**0.00076**	**0.0**
0.00767	**0.55730**	**0.03217**	**0.03162**	**0.00078**	**0.0**
0.01129	**0.77932**	**0.05042**	**0.03434**	**0.00106**	**0.0**
0.04888	**4.67814**	**0.38143**	**0.06638**	**0.00432**	**0.0**
0.02370	**2.06074**	**0.14010**	**0.04768**	**0.00203**	**0.0**
0.03076	**2.70288**	**0.20754**	**0.05595**	**0.00298**	**0.0**
0.02906	**2.25146**	**0.15935**	**0.04523**	**0.00216**	**0.0**

MICROSTRUCTURES (EBSD DATA)		
		WBV magnitude
comment	**observation**	**microns-1**
no-distortion	twins	0.000461
moderate-distortion	twins	0.001064
low-distortion	twins	0.000675
moderate-distortion	twins	0.002613
moderate-distortion	twins	0.000989
low-distortion	twins	0.00063
low-distortion	twins	0.000449
moderate-distortion	twins	0.014736
moderate-distortion	deformation bands	0.000445
moderate-distortion	deformation bands	0.000245
low-distortion	deformation bands	0.000573
moderate-distortion	deformation bands	0.001216
High-distortion	deformation bands	0.002981
moderate-distortion	twins	0.000252
low-distortion	twins	0.000508
moderate-distortion	twins	0.000419
low-distortion	twins	0.000129
High-distortion	twins	0.000388
moderate-distortion	twins-2set	0.001027
moderate-distortion	twins-2set	0.000208
moderate-distortion	twins-2set	0.002913
moderate-distortion	twins-2set	0.001198
moderate-distortion	twins-2set	0.000337
moderate-distortion	twins-2set	0.003467
moderate-distortion	twins-2set	0.008543
n.a.		
n.a.		
n.a.		
n.a.		
n.a.		
n.a.		
n.a.		
n.a.		
High-distortion	twins	0.003463
moderate-distortion	twins	0.001542
moderate-distortion	twins	0.001954
moderate-distortion	twins	0.001441

	1	2	3	4
	RUN2	RUN2	RUN2	RUN2
	35 microns	35 microns	35 microns	35 microns
	Ttn2	Ttn2	Ttn2	Ttn2
spot name	**A1**	**A2**	**A3**	**A4**
identifier	**006SMPL**	**007SMPL**	**008SMPL**	**009SMPL**
zoning				
Spot position	**rim**	**rim**	**core**	**core**
zoning	**dark**	**dark**	**bright**	**bright**
EBDS data	**ligh-distortio**	**no-distortion**	**no-distortion**	**no-distortion**
Al27	9234.4	10133.03	10446.28	10538.22
P31	354.61	488.44	516.88	587.63
Ca44	238080.28	222387.02	221840.47	220033.95
Ti49	285773.06	307488.38	278869.44	281372.25
V51	980.67	1373.54	1194.76	1234.54
Mn55	847.07	1069.17	826.3	764.17
Fe57	**3131.64**	**3792.56**	**4136.78**	**3771.6**
Y89	1151.76	1737.79	2660.08	2632.16
Zr90	**191.25**	**250.85**	**974.59**	**969.5**
Nb93	1306.34	1814.55	1429.6	1270.29
La139	**64.31**	**187.18**	**2650.88**	**2750.15**
Ce140	605.08	1571.8	11746.56	11958.27
Pr141	187.01	406.19	1660.65	1665.87
Nd146	1537.33	2860.3	8319.14	7888.15
Sm149	804.14	1470.03	2361.38	2162.82
Eu151	104.26	147.93	130.5	126.06
Gd157	679.6	1138.07	1551.55	1369.83
Tb159	95.42	147.75	194.43	176.79
Dy163	380.74	611.85	823.82	748.28
Ho165	48.31	80.54	121.69	112.92
Er167	95.61	151.16	249.09	249.33
Tm169	10.87	16.15	29.03	30.7
Yb173	61.74	83.84	153.93	170.24
Lu175	5.43	6.71	15.21	18.42
Hf177	18.76	28.75	53.95	51.56
Pb208	6.3	16.77	28.04	27.92
Th232	**15.69**	**47.77**	**946.12**	**982.72**
U238	88.06	139.39	390.08	391.8
	0.18	0.34	2.43	2.51
Al/Fe	**2.95**	**2.67**	**2.53**	**2.79**
LREE=(La-Sm)	**3197.87**	**6495.50**	**26738.61**	**26425.26**
Zr/Y	**0.17**	**0.14**	**0.37**	**0.37**
Y/(Dy/Yb)	**186.77**	**238.12**	**497.03**	**598.84**
Dy/Yb Normalizzati	**6.17**	**7.30**	**5.35**	**4.40**
HREE	1377.72	2236.07	3138.75	2876.51
T°C	741.32	755.91	835.69	835.36

5	**6**	**7**	**8**	**9**	**10**
RUN2	**RUN2**	**RUN2**	**RUN2**	**RUN2**	**RUN1**
35 microns	**35 microns**	**35 microns**	**35 microns**	**35 microns**	**25 microns**
Ttn2	**Ttn2**	**Ttn2**	**Ttn2**	**Ttn2**	**Ttn3**
A5	**A6**	**A7**	**A8**	**A9**	**A1**
010SMPL	**011SMPL**	**012SMPL**	**013SMPL**	**014SMPL**	**006SMPL**
core	**core**	**core**	**core**	**core**	**core**
bright	**bright**	**bright**	**bright**	**dark/bright**	**bright**
no-distortion	**ow-distortio**	**no-distortion**	**no-distortion**	**derate-distor**	**igh-distortio**
10211.05	11316.55	11633.38	11028.02	9766.91	11487.42
791.23	585.37	681.62	511.48	495.32	847.54
222006.75	213626.17	220451.06	207278.98	213091	236926.94
298257.72	295914.28	300791.75	279367.66	269298.16	250366.7
1125.91	1132.49	1248.54	1161.05	1228.61	993.84
800.8	903.73	884.81	787.19	801.67	733.19
3976.06	**4200.83**	**4282.25**	**4477.2**	**3978.56**	**3409.04**
2683.62	2580.27	2787.58	2628.84	2548.7	2423.76
1040.44	**973.66**	**1002.32**	**990.01**	**932.02**	**893**
1387.89	1319.45	1698.66	1490.74	1532.22	1754.02
2815.67	**2687.12**	**3031.96**	**2729.99**	**2621.41**	**2088.08**
11893.46	10351.87	13756.15	12033.09	11240.46	9342.72
1554.85	1299.43	1791.11	1722.62	1614.2	1419.51
7314	5910.3	9398.74	8552.03	8094.71	7456.37
1912.94	1535.8	2576.84	2393.78	2173.56	2301.89
125.27	116.46	145.1	135.12	130.6	113.18
1246.57	1035.91	1651.54	1584.74	1452.63	1502.96
165.09	143.29	206.82	191.91	179.25	186.95
729.59	657.7	821.27	816.22	773.19	769.95
115.95	104.58	122.19	117.84	114.27	106.47
254.08	236.28	253.84	254.19	232.34	225.28
31.79	30.72	29.45	28.33	29.13	23.59
184.54	187.65	162.51	160.27	155.45	127.98
19.71	20.89	16.81	17.25	16.86	13.76
51	39.17	60.36	53.55	52.48	49.69
26.73	38.51	29	29.95	40.57	16.83
982.17	**889.18**	**1058.73**	**942.27**	**919.71**	**666.09**
425.48	452.02	410.3	393.78	381.74	275.85
2.31	1.97	2.58	2.39	2.41	2.41
2.57	**2.69**	**2.72**	**2.46**	**2.45**	**3.37**
25490.92	**21784.52**	**30554.80**	**27431.51**	**25744.34**	**22608.57**
0.39	**0.38**	**0.36**	**0.38**	**0.37**	**0.37**
678.79	**736.18**	**551.60**	**516.19**	**512.42**	**402.87**
3.95	**3.50**	**5.05**	**5.09**	**4.97**	**6.02**
2747.32	2417.02	3264.43	3170.75	2953.12	2956.94
839.85	835.63	837.47	836.69	832.87	830.18

11	**12**	**13**	**14**	**15**	**16**
RUN1	**RUN1**	**RUN1**	**RUN1**	**RUN1**	**RUN1**
25 microns	**25 microns**	**25 microns**	**25 microns**	**25 microns**	**25 microns**
Ttn3	**Ttn3**	**Ttn4**	**Ttn4**	**Ttn4**	**Ttn4**
A2	**A3**	**B1**	**B2**	**B3**	**B4**
007SMPL	**008SMPL**	**009SMPL**	**010SMPL**	**011SMPL**	**012SMPL**
core	**rim**	**rim**	**core**	**core**	**core**
bright	**dark**	**dark**	**bright**	**bright**	**bright**
derate-distort	**lerate-distor**	**ow-distortio**	**ow-distortio**	**ow-distortio**	**ow-distortior**
12086.68	9749.03	11212.75	12456.6	10992.92	10398.16
1024.84	<681.25	<489.14	<657.97	829.47	1046.01
261188.91	266499	288121.19	254615.08	251573.42	239842.44
277219.97	251568.91	290089.94	241944.48	239923.58	236940.22
1113.18	1178.31	1437.36	1618.39	1432.77	1324.4
762.46	818.31	793.1	1591.25	1445.1	1317.07
4123.41	**2986.74**	**3274.01**	**3057.7**	**3033.65**	**3158.69**
2701.97	1725.89	1434.15	1891.53	1603.72	1783.33
1031.52	**392.51**	**453.41**	**456.27**	**416.16**	**514.89**
1920.2	2327.95	1140.69	259.92	530.18	661.97
2643.57	**504.64**	**953.81**	**1115.83**	**657.01**	**1320.74**
11942.26	3066.13	3547.98	4170.53	2748.76	4849.36
1880.04	766.58	703.42	770.01	555.7	876.67
9861.63	4795.94	3820.47	4298.73	3211.58	4706.34
2868.56	1728.86	1282.6	1346.51	1150.13	1499.97
136.29	134.18	170.53	155.2	168.45	154.15
1959.86	1286.51	955.05	983.88	888.74	1035.78
221.3	150.07	113.51	125.77	110.31	122.63
913.37	581.4	445.03	526.28	449.2	509.52
127.01	77.78	62.12	78.89	66.59	74.03
262.9	148.65	120.35	177.07	138.68	162.49
25.56	16.4	14.69	21.87	18.38	19.39
133.78	87.9	75.61	138.46	109.01	122.2
14.37	8.83	9.4	16.69	12.86	13.24
62.97	37.01	38.82	47	32.16	40.65
24.1	10.5	5.46	5.36	7.8	5.84
878.66	**104.47**	**99.01**	**94.59**	**42.33**	**109.68**
331.47	152.03	168.36	183.68	167.81	200.22
2.65	0.69	0.59	0.51	0.25	0.55
2.93	**3.26**	**3.42**	**4.07**	**3.62**	**3.29**
29196.06	**10862.15**	**10308.28**	**11701.61**	**8323.18**	**13253.08**
0.38	**0.23**	**0.32**	**0.24**	**0.26**	**0.29**
395.75	**260.93**	**243.66**	**497.65**	**389.18**	**427.70**
6.83	**6.61**	**5.89**	**3.80**	**4.12**	**4.17**
3658.15	2357.54	1795.76	2068.91	1793.77	2059.28
839.30	780.93	789.25	789.62	784.29	796.70

17	**18**	**19**	**20**	**21**	**22**
RUN1	**RUN1**	**RUN1**	**RUN1**	**RUN1**	**RUN2**
25 microns	**25 microns**	**25 microns**	**25 microns**	**25 microns**	**35 microns**
Ttn4	**Ttn5**	**Ttn5**	**Ttn5**	**Ttn5**	**Ttn7**
B5	**C1**	**C2**	**C3**	**C4**	**A1**
013SMPL	**014SMPL**	**015SMPL**	**016SMPL**	**017SMPL**	**015SMPL**
core	**rim**	**core**	**core**	**rim**	**rim**
bright	**dark**	**bright**	**bright**	**dark**	**dark**
ow-distortio	**ow-distortio**	**ow-distortio**	**ow-distortion**	**derate-distort**	**High-distortion**
9912.72	13299.73	12201.41	10843.64	9745.7	11974.86
1028.68	<434.80	694.59	<445.94	428.71	614.07
249244.73	261036.31	259246.09	231807.3	279687.31	255547.31
248076.61	252343.72	258294.3	235937.45	250364.23	310932.03
1430.23	1480.58	1192.27	1104.42	2222.51	1516.56
962.47	828.28	677.12	634.8	776.46	865.81
3169.9	**4037.24**	**3540.34**	**3413.48**	**3790.1**	**3775.79**
1510.02	1032.16	2013.35	1778.94	1177.68	1217.41
450.67	**379.67**	**1549.17**	**1381.62**	**224.26**	**337.49**
717.86	1030.94	980.71	974.32	716.22	1289.96
1163.07	**283.06**	**2418.39**	**2060.79**	**66.01**	**156.56**
4175.55	1293.23	6564.04	5628.66	452.78	958.78
794.52	265.21	839.02	760.11	121.07	225.73
4355.12	1525.75	3679.5	3443.01	790.3	1495.94
1358.18	542.57	884.12	803.21	405.38	609.24
172.79	112.53	104.89	96.87	87.77	133.99
988.69	444.17	655	616.97	383.06	520.23
114.57	59.89	92.86	83.68	56.09	72.68
470.7	274.3	497.15	424.84	283.36	330.8
67.13	42.79	81.46	73.86	47.53	48.97
134.87	89.78	202.98	173.93	102.76	104.41
15.87	10.69	25.24	22.39	13.7	11.54
90.85	56	161.29	132.26	68.78	67.28
10.29	5.97	18.44	15.01	6.78	7.09
40.91	28.34	59.38	62.6	20.53	34.51
21.91	9.31	16.64	26.81	8.16	39.24
109.83	**104.47**	**721.26**	**622.83**	**12.23**	**59.37**
168.67	93.46	196.7	169.56	67.47	122.15
0.65	1.12	3.67	3.67	0.18	0.49
3.13	**3.29**	**3.45**	**3.18**	**2.57**	**3.17**
11846.44	**3909.82**	**14385.07**	**12695.78**	**1835.54**	**3446.25**
0.30	**0.37**	**0.77**	**0.78**	**0.19**	**0.28**
291.45	**210.72**	**653.19**	**553.81**	**285.86**	**247.60**
5.18	**4.90**	**3.08**	**3.21**	**4.12**	**4.92**
1892.97	983.59	1734.42	1542.94	962.06	1163.00
788.90	779.03	865.84	858.25	749.84	772.36

23	**24**	**25**	**26**	**27**	**28**
RUN2	**RUN2**	**RUN2**	**RUN2**	**RUN2**	**RUN2**
35 microns	**35 microns**	**35 microns**	**35 microns**	**35 microns**	**35 microns**
Ttn7	**Ttn7**	**Ttn7**	**Ttn7**	**Ttn7**	**Ttn7**
A2	**A3**	**A4**	**A5**	**A6**	**A7**
016SMPL	**017SMPL**	**018SMPL**	**019SMPL**	**020SMPL**	**021SMPL**
rim/core	**rim**	**core**	**core**	**core**	**core**
dark/bright	**dark**	**bright**	**bright**	**bright**	**bright**
ligh-distortio	**ow-distortio**	**no-distortion**	**no-distortion**	**no-distortion**	**no-distortion**
12394.9	10262.87	12130.84	12405.19	11389.96	11300.41
772.42	490.3	764.09	576.72	733.78	752.13
222377.94	222820.59	238947.05	222711.91	207998.19	212146.11
293319.06	318812.69	311782.28	310296.5	269722.31	277068.81
1196.03	1521.07	1306.79	1220.57	1062.42	1096.44
674.99	742.45	716.55	697.48	633.98	674.88
4468.28	**3011.14**	**4304.83**	**3847.16**	**3883.03**	**3761.11**
1763.38	918.86	2065.62	1919.64	1957.5	1868.59
1223.29	**344.6**	**1407.26**	**1260.83**	**1236.26**	**1166.94**
2165.09	1279.7	1454.27	1692.83	1233.6	1657.88
3110.28	**201.74**	**3389.26**	**3212.28**	**2900.29**	**2989.08**
10326.42	1030.26	11033.68	10924.53	9838.46	9418.46
1238.44	235.06	1352.91	1304.22	1166.45	1161.16
5768.95	1542.88	6141.06	5960.54	5411.5	5296.12
1293.85	644.27	1455.72	1345.06	1216.96	1226.87
113.2	147.61	122.93	119.26	110.2	104.26
905.28	535.69	1008.44	951.74	856.87	866.18
113.28	68.92	127.8	121.67	116.09	114.4
506.21	279.94	567.55	535.71	544.49	519.18
78.07	38.35	94.72	87.4	88.69	85.24
161.45	68.3	199.26	173.47	184.89	175.32
16.3	8.09	20.88	19.67	20.32	19.83
78.42	41.88	109.18	94.08	108.22	100.95
7.22	4.11	10.23	9.42	10.39	9.68
73.52	37.49	70.97	73.22	67.85	70.33
49.2	7.13	30.56	42.86	29.86	26.6
1160	**52.2**	**1359.85**	**1212.89**	**1157.93**	**996.76**
271.37	141.34	357.89	328.53	313.53	279.63
4.27	0.37	3.80	3.69	3.69	3.56
2.77	**3.41**	**2.82**	**3.22**	**2.93**	**3.00**
21737.94	**3654.21**	**23372.63**	**22746.63**	**20533.66**	**20091.69**
0.69	**0.38**	**0.68**	**0.66**	**0.63**	**0.62**
273.18	**137.46**	**397.36**	**337.12**	**389.06**	**363.33**
6.46	**6.68**	**5.20**	**5.69**	**5.03**	**5.14**
1866.23	1045.28	2138.06	1993.16	1929.96	1890.78
850.28	773.53	859.46	852.24	850.96	847.22

29	**30**	**31**	**32**	**33**	**34**
RUN2	**RUN2**	**RUN2**	**RUN2**	**RUN2**	**RUN2**
35 microns	**35 microns**	**35 microns**	**35 microns**	**35 microns**	**35 microns**
Ttn7	**Ttn10**	**Ttn10**	**Ttn10**	**Ttn10**	**Ttn10**
A8	**A1**	**A2**	**A3**	**A4**	**A5**
022SMPL	**029SMPL**	**030SMPL**	**031SMPL**	**032SMPL**	**033SMPL**
rim	**rim**	**core**	**core**	**core**	**core**
dark	**dark**	**bright**	**bright**	**bright**	**bright**
ow-distortion	**lerate-distor**	**no-distortion**	**no-distortion**	**no-distortion**	**ow-distortion**
12327.72	11880.15	11998	11766.89	11937.18	11687.51
583.5	930.79	1355.04	1177.26	1183.48	1350.91
234709.58	212950.55	203445.27	208881.03	220107.33	207994.69
300795.72	270572.59	265847.69	250140.59	262082.88	247918.17
1163.08	1453.93	1147.28	1078.71	1092.4	996.77
717.39	739.05	782.94	767.43	736.49	855.74
2938.28	**2823.9**	**4108.63**	**3938.36**	**3762.28**	**3963.38**
771.52	2614.92	2802.11	2669.56	2741.91	2515.18
438.74	**375.76**	**1008.51**	**999.46**	**983.25**	**1067.69**
1123.13	2422.93	2697.33	2173.37	2224.73	1853.45
776.56	**325.23**	**2711.98**	**2509.83**	**2491.63**	**2563.68**
2762.92	2873.51	12428.1	11260	11689.17	10888.01
498.68	848.53	1918.79	1764.88	1810	1607.27
2642.17	5915.98	9995.77	9286.98	9507.15	8260.78
803.2	2473.37	2822.38	2683.53	2738.46	2304.48
154.51	124.38	121.89	117.37	121.53	106.16
520.8	1733.22	1868.25	1711.39	1805.83	1542.31
61.26	206.91	216.34	202.64	210.48	181.17
257.62	801.15	799.69	797.29	822.54	734.86
34.22	113.48	114.94	116.86	119.44	105.46
56.51	223.41	241.28	241.64	242.57	224.22
6.08	24.82	28.29	28.78	29.32	27.27
33.5	137.35	157.16	163.48	166.9	156.47
3.1	13.36	17.7	18.1	18.31	18.09
37.74	40.58	61.45	59.99	54.82	55.2
27.23	5.87	20.99	21.19	18.31	20.86
125.22	**119.19**	**899.41**	**875.97**	**770.87**	**828.32**
148.56	150.43	349.26	330.85	344.47	348.13
0.84	0.79	2.58	2.65	2.24	2.38
4.20	**4.21**	**2.92**	**2.99**	**3.17**	**2.95**
7483.53	**12436.62**	**29877.02**	**27505.22**	**28236.41**	**25624.22**
0.57	**0.14**	**0.36**	**0.37**	**0.36**	**0.42**
100.33	**448.30**	**550.69**	**547.38**	**556.36**	**535.54**
7.69	**5.83**	**5.09**	**4.88**	**4.93**	**4.70**
973.09	3253.70	3443.65	3280.18	3415.39	2989.85
787.34	778.44	837.86	837.29	836.25	841.50

35	**36**				
RUN2	**RUN2**				
35 microns	**35 microns**				
Ttn10	**Ttn10**				
A6	**A7**				
034SMPL	**035SMPL**				
core	**core**				
bright	**bright**	**Bright inner domains**			**Dark (**
ow-distortio	**igh-distortion**				
		Average	**St.dev.**	**R.S.D.**	**Average**
11795.67	11343.05	11305.1	828.6	7.3%	10982.0
1333.77	1103.52	849.6	281.9	33.2%	555.8
205771.05	214360.97	225207.6	17578.3	7.8%	248183.9
246755.89	263741.09	268909.2	22521.6	8.4%	283874.1
992.87	1065.86	1185.9	144.3	12.2%	1432.8
818.72	729.61	843.8	235.6	27.9%	819.7
3838.11	**3983.12**	3835.8	408.4	10.6%	3356.1
2421.27	2418.68	2293.3	414.0	18.1%	1378.2
951.34	**745.72**	983.6	282.8	28.7%	338.9
2310.25	1941.37	1513.5	578.0	38.2%	1445.2
2330.94	**1569.73**	2413.2	687.1	28.5%	351.9
10379.98	7183.12	9593.0	2981.8	31.1%	1816.2
1611.42	1207.72	1369.0	394.4	28.8%	425.7
8528.79	6866.51	6874.4	2085.9	30.3%	2692.7
2453.29	2184.72	1897.4	633.5	33.4%	1076.4
106.01	105.52	125.6	19.7	15.7%	131.8
1576.3	1548.96	1282.2	385.8	30.1%	819.6
181.51	183.08	157.9	41.7	26.4%	103.3
705.25	717.61	665.0	145.5	21.9%	424.6
104.37	104.48	100.0	18.8	18.8%	59.4
223.67	214.81	211.9	38.2	18.0%	116.1
26.34	24.9	24.9	4.8	19.1%	13.3
156.83	140.38	139.9	29.5	21.1%	71.4
18.26	15.88	15.2	3.6	23.9%	7.1
50.14	47.76	55.4	10.7	19.2%	32.3
17.6	13.42	25.1	11.0	44.0%	13.6
632.96	**486.86**	787.7	351.8	44.7%	74.0
334.44	242.59	311.9	85.7	27.5%	127.1
1.89	2.01	2.4	1.1	43.0%	0.6
3.07	**2.85**	3.0	0.4	12.7%	3.3
25304.42	**19011.80**	22146.9	6283.0	28.4%	6363.0
0.39	**0.31**	0.4	0.2	36.3%	0.3
538.43	**473.15**	488.0	113.6	23.3%	236.0
4.50	**5.11**	4.8	0.9	18.3%	6.0
2992.53	2950.10	2597.0	639.0	24.6%	1614.8
834.16	818.99	833.5	21.1	2.5%	770.8

outer domains

St.dev.	R.S.D.
1348.6	12%
187.2	34%
25768.4	10%
26197.3	9%
331.1	23%
100.4	12%
445.9	13%
537.4	39%
89.3	26%
561.9	39%
302.5	86%
1134.7	62%
264.5	62%
1672.8	62%
655.2	61%
25.1	19%
445.1	54%
50.6	49%
183.8	43%
24.6	41%
48.4	42%
5.2	39%
28.8	40%
2.9	41%
7.8	24%
11.2	82%
41.8	57%
33.2	26%
0.3	55%
0.5	17%
3746.8	59%
0.1	48%
94.0	40%
1.1	19%
780.1	48%
16.3	2%

	RUN2	RUN2	RUN2	RUN2
	35 microns	35 microns	35 microns	35 microns
	Ttn16	Ttn16	Ttn16	Ttn16
spot name	A1	A2	A3	A4
identifier	050SMPL	051SMPL	052SMPL	053SMPL
zoning				
Spot position	rim	core	core	core
zoning	dark	bright	bright	bright
EBDS data	derate-distort	derate-distor	ow-distortior	derate-distort
Al27	11954.2	13668.06	11358.77	13654.32
P31	343.4	<234.95	346.66	<228.89
Ca44	215954.19	208734.53	192974.23	192856.88
Ti49	245509	223439.22	215476.64	205249.34
V51	871.88	1096.45	1268.86	1112.81
Mn55	399.55	458	364.47	565.96
Fe57	3201.13	7526.35	3079.11	11306.66
Y89	477.69	675.76	943.24	824.54
Zr90	308.2	803.91	523.5	482.31
Nb93	615.15	639.77	592.95	575.06
La139	91.07	227.31	241.02	223.5
Ce140	448.27	906.16	987.63	894.25
Pr141	94.7	154.51	188.29	169.72
Nd146	595.59	824.15	1003.61	945.63
Sm149	204.95	241.41	299.21	269.95
Eu151	50.76	48.36	56.49	53.55
Gd157	182.76	203.21	248.87	230.26
Tb159	27.23	32.07	39.89	35.27
Dy163	129.62	166.43	220.5	195.76
Ho165	19.07	27.5	40.78	35.44
Er167	38.94	62.1	99.09	81.51
Tm169	4.19	8.57	12.72	10.26
Yb173	22.43	43.54	73.01	61.99
Lu175	2.24	4.8	7.25	6.26
Hf177	22.81	42.18	34.77	31.8
Pb208	1.85	6.58	2.64	64.26
Th232	16.35	257.05	22.27	24.92
U238	123	194.76	170.02	174.89
	0.13	1.32	0.13	0.14
Al/Fe	3.73	1.82	3.69	1.21
LREE=(La-Sm)	1434.58	2353.54	2719.76	2503.05
Zr/Y	0.65	1.19	0.56	0.58
Y/(Dy/Yb)	82.66	176.79	312.32	261.10
Dy/Yb Normalizzati	5.78	3.82	3.02	3.16
HREE	426.48	548.22	742.11	656.75
T°C	767.27	823.63	797.68	792.86

RUN2	RUN2	RUN2	RUN2	RUN2	RUN2
35 microns	35 microns	35 microns	35 microns	35 microns	35 microns
Ttn16	Ttn18	Ttn18	Ttn18	Ttn18	Ttn19
A5	A1	A2	A3	A4	A1
054SMPL	036SMPL	037SMPL	038SMPL	039SMPL	040SMPL
core	core	core	core	core	rim
bright	ıomogeneou:	ıomogeneou:	ıomogeneou:	ıomogeneou:	ıomogeneou:
ligh-distortio	no-distortion	derate-distor	low-distortior	derate-distort	derate-distort
14348.09	15020.01	14172.68	14148.02	14281.94	14601.66
277.03	<238.10	407.51	273.56	756.4	539.49
211861.44	225120.88	203790.89	216064.53	197908.14	202106.44
216074.34	227391.58	214479.3	215277.02	221071.3	213581.41
1093.45	1330.77	1085.45	1088.01	1105.79	884.28
417.22	402.57	412.75	466.5	409.13	405.14
2329.73	2600.09	3104.73	3352.57	2625.22	2663.02
773	1330.85	1282.78	1248.63	1273.1	683.47
2837.63	2623.61	2489.64	2155.51	2257.24	2932.38
582.93	800.66	812.3	716.26	790.62	754.98
262.75	688.75	607.29	547.13	654.96	166.65
930.89	2031.72	1846.52	1706.25	1956.45	552.5
153.23	295.92	270.91	250.37	284.07	96.75
757.54	1327.75	1253.02	1135.59	1257.84	460
195.31	306.37	293.72	271.37	301.75	137.36
38.21	53.14	49.27	48.7	51.24	32.83
165.1	272.86	255.75	243.76	255.44	124.5
28.5	44.45	45.79	41.5	44.3	23.19
162.47	267.88	251.67	249.46	252.98	140.58
32.33	51.87	52.25	49.66	49.47	26.6
78.25	136.25	134.77	132.85	130.09	66.37
11.44	18.77	18.92	18.39	18.25	9.33
66.42	118.65	115.91	121.1	115.8	57.59
7.37	14.52	13.73	13.69	13.4	6.29
97.7	78.94	77.08	69.25	63.98	119.45
12.15	13.77	12.31	10.92	13.27	12.32
608.26	675.04	568.1	469.93	612.61	563.17
288.37	283.92	284.52	264.14	272.48	553.44
2.11	2.38	2.00	1.78	2.25	1.02
6.16	5.78	4.56	4.22	5.44	5.48
2299.72	4650.51	4271.46	3910.71	4455.07	1413.26
3.67	1.97	1.94	1.73	1.77	4.29
316.01	589.46	590.80	606.15	582.75	279.99
2.45	2.26	2.17	2.06	2.18	2.44
551.88	925.25	888.79	870.41	879.73	454.45
907.78	902.18	898.46	888.36	891.57	910.15

RUN2	RUN2	RUN2	RUN1	RUN1	RUN1
35 microns	35 microns	35 microns	25 microns	25 microns	25 microns
Ttn19	Ttn19	Ttn19	Ttn23	Ttn23	Ttn23
A2	A3	A4	A1	A2	A3
041SMPL	042SMPL	043SMPL	032SMPL	033SMPL	034SMPL
core	core	rim	rim	core	core
omogeneou	omogeneou	omogeneous	weakly zoned	weakly zoned	weakly zoned
ow-distortior	ow-distortior	derate-distort	ligh-distortio	derate-distort	derate-distort
16222.86	16581.17	12952.1	10702	10486.46	9561.1
260.04	379.34	<233.29	<367.34	587.87	<366.22
234574.63	208134.5	203796.03	186216.5	194251.72	192231.91
255583.77	231072.66	218408.8	207840.75	203469.61	210087.3
1029.54	955.53	1006.6	339.36	390.63	377.41
474.41	453.56	421.24	610.22	621.11	667.42
3172.86	3006.2	3170.5	2120.5	2375.17	2062.04
698.3	565.92	674.28	153.94	330.46	124.97
2479.97	1986.45	2654.48	473.37	284.09	310.63
820.82	778.08	862.47	863.43	856.85	576.48
190.12	161.6	221.63	266.83	332.4	408.05
685.05	538.67	784.07	1028.23	1552.39	1440.38
110.14	89.6	140.09	210.28	326.88	237.07
511.08	434.72	684.71	1265.67	1958.34	1136.13
160.8	127.77	207.9	382.14	613.84	265.66
37.7	32.97	40.47	33.75	97.3	52.04
143.9	110.11	173.29	209.58	375.58	134.97
24.18	20.91	29.65	20.16	37.39	11.84
139.41	118.26	162.57	65.64	127.29	41.69
27.1	22.26	27.83	6.27	14.3	4.53
66	58.97	67.33	10.67	20.07	7.9
9.05	7.72	8.62	1.15	1.94	0.83
56.33	48.98	49.64	7.97	9.16	4.44
6.25	5.52	5.12	0.71	0.76	0.402
92.25	75	119.01	16.62	15.28	10.96
13.62	12.41	9.63	3.19	3.78	4.38
600.65	556.67	410.84	35.88	63.93	83.3
628.31	607.87	379.11	21.3	45.57	26.86
0.96	0.92	1.08	1.68	1.40	3.10
5.11	5.52	4.09	5.05	4.42	4.64
1657.19	1352.36	2038.40	3153.15	4783.85	3487.29
3.55	3.51	3.94	3.08	0.86	2.49
282.16	234.39	205.89	18.69	23.78	13.31
2.47	2.41	3.27	8.24	13.90	9.39
472.22	392.73	524.05	322.15	586.49	206.60
898.18	882.71	903.01	791.76	762.75	767.71

RUN1	**RUN2**	**RUN2**	**RUN2**	**RUN2**	**RUN2**
25 microns	**35 microns**	**35 microns**	**35 microns**	**35 microns**	**35 microns**
Ttn23	**Ttn24**	**Ttn24**	**Ttn24**	**Ttn24**	**Ttn24**
A4	**A1**	**A2**	**A3**	**A4**	**A5**
035SMPL	**055SMPL**	**056SMPL**	**057SMPL**	**058SMPL**	**059SMPL**
core	**rim**	**core**	**core**	**core**	**rim**
weakly zoned	**dark**	**bright**	**bright**	**bright**	**dark**
derate-distort	**derate-distor**	**ow-distortior**	**derate-distor**	**ow-distortior**	**igh-distortio**
8287.3	12116.3	13771.71	14134.35	12621.64	10228.78
<328.62	409.15	305.64	227.07	468.26	489.25
177352.11	204825.25	198003.06	195890.73	195638.36	188386.97
189886.75	214982.72	204510.63	194742.8	206921.28	203590.83
355.34	1267.24	1331.82	986.81	1386.58	1271.78
532.53	434.78	331.21	338.14	341.31	366.99
1612.73	3496.35	2649.22	3607.76	2576.85	2560.06
239.1	870.08	858.48	885.76	890.12	782.69
208.77	558.66	3312.09	1562.02	915.66	416.64
632.04	616.64	632.86	621.89	619.69	615.76
278.64	237.77	539.04	494.44	292.08	130.26
1120.19	949.51	1675.73	1492.78	1098.36	622.98
226.9	172.48	244.34	213.24	183.86	123
1245.93	904.41	1131.12	983.88	942.92	706.1
389.97	246.98	250.2	235.14	246.6	221.74
64.59	51.58	40.2	40.78	51.3	49.46
230.97	203.6	203.34	191.59	208.41	190.41
24	34.08	32.71	31.46	34.31	30.97
84.22	194.93	191.82	182.15	191.86	170.17
9.88	36.9	35.74	36	36.45	32.23
14.16	87.55	89.74	93	90.47	82.2
1.73	12.04	12.82	12.75	12.69	10.68
10.42	80.79	81.96	79.67	81.61	69.13
0.86	9.42	9.43	9.29	9.76	8.24
9.52	34.39	109.11	43.97	42.21	28.53
3.49	2.35	15.39	13.38	6.2	3.27
47.2	40.18	634.36	524.85	210.25	25.57
34.96	151.58	219.45	213.08	173.5	143.14
1.35	0.27	2.89	2.46	1.21	0.18
5.14	3.47	5.20	3.92	4.90	4.00
3261.63	2511.15	3840.43	3419.48	2763.82	1804.08
0.87	0.64	3.86	1.76	1.03	0.53
29.58	360.61	366.81	387.42	378.62	317.96
8.08	2.41	2.34	2.29	2.35	2.46
376.24	659.31	657.56	635.91	665.56	594.03
745.99	801.53	919.00	866.40	831.75	784.36

RUN1	**RUN1**	**RUN1**	**RUN1**	**RUN1**	**RUN1**
25 microns	**25 microns**	**25 microns**	**25 microns**	**25 microns**	**25 microns**
Ttn28	**Ttn28**	**Ttn28**	**Ttn29**	**Ttn29**	**Ttn29**
A1	**A2**	**A3**	**A1**	**A2**	**A3**
024SMPL	**025SMPL**	**026SMPL**	**027SMPL**	**028SMPL**	**029SMPL**
rim	**core**	**core**	**rim**	**core**	**core**
omogeneous	**omogeneous**	**omogeneous**	**omogeneous**	**omogeneous**	**omogeneous**
no data	**no data**	**no data**	**no data**	**no data**	**no data**
10285.69	14085.95	12480.23	10379	14669.15	13466.6
<456.15	835.12	<494.06	<437.92	<452.91	<458.11
212951.98	195954.97	199574.59	199470.48	193914.63	183948.61
210816.44	186702.38	193836.67	206611.25	184442.63	182048.3
1332.61	1248.66	1193.21	1226.57	1142.78	1102.33
432.53	397.89	455.28	422.11	432.12	389.68
2314.01	2387.94	2630.69	2564.76	3806.86	1985.37
978.64	773.09	766.36	905.2	747.65	744.87
621.54	2692.93	2477.83	575.29	2385.45	2216.84
623.5	586.16	620.92	644.68	681.63	616.62
237.85	235.21	223.06	223.09	245.67	220.58
978.44	852.29	809.71	875.9	835.19	776.34
179.99	139.87	144.43	166	143.74	134
920.07	722.95	701.82	883.55	708.34	670.87
274.33	189.08	195.07	257.31	193.71	176.53
51.83	31.8	34.31	50.04	34.2	33.95
242.48	165.02	175.63	234.94	159.61	167.39
39.46	27.81	29.87	35.44	27.1	27.09
217.83	165.28	171.39	207.97	162.48	157.59
40.65	34.39	30.78	40	31.85	31.13
96.94	84.04	80.56	87.36	78.06	77.39
12.53	11.07	11.01	11.36	10.87	10.21
67.12	72.2	64.32	71.25	64.24	67.11
7.22	7.4	7.29	7.23	6.64	6.94
37.82	95.72	91.15	39.1	64.2	71.16
2.49	18.27	12.14	7.03	18	14.11
54.58	813.37	442.29	75.98	671.98	714.29
230.31	340.15	264.66	247.58	335.31	313.22
0.24	2.39	1.67	0.31	2.00	2.28
4.44	5.90	4.74	4.05	3.85	6.78
2590.68	2139.40	2074.09	2405.85	2126.65	1978.32
0.64	3.48	3.23	0.64	3.19	2.98
301.55	337.71	287.60	310.12	295.60	317.20
3.24538141	2.28919668	2.66	2.92	2.53	2.35
724.23	567.21	570.85	695.55	540.85	544.85
807.91	904.04	898.12	803.28	895.44	890.31

RUN1	**RUN1**	**RUN2**	**RUN2**	**RUN2**	**RUN2**
25 microns	**25 microns**	**35 microns**	**35 microns**	**35 microns**	**35 microns**
Ttn29	**Ttn29**	**Ttn34**	**Ttn34**	**Ttn34**	**Ttn34**
A4	**A5**	**A1**	**A2**	**A3**	**A4**
030SMPL	**031SMPL**	**060SMPL**	**061SMPL**	**062SMPL**	**063SMPL**
rim	**rim**	**rim**	**core**	**core**	**core**
omogeneous	**omogeneous**	**omogeneous**	**omogeneous**	**omogeneous**	**omogeneous**
no data	**no data**	**derate-distort**	**derate-distort**	**derate-distort**	**derate-distort**
9599.48	11193.62	10518.52	10700.17	10881.15	10548.73
418.98	663.76	509.86	338.25	524.43	413.06
206881.3	233587.34	196380.11	201322.75	197558.09	198558.03
213262.11	246335.63	216838.8	210206.5	198326.89	200104.69
1109.99	990.86	1113.82	1130	1137.52	1156.37
433.36	466.29	410.97	415.87	409.35	404.79
2946.13	2752.39	2747.89	2177.22	2023.11	2027.56
851.05	1183.81	786.32	745.39	713.5	714.56
1229.22	204.72	255.01	286.75	528.3	529.28
749.39	865.86	656.86	655.42	638.17	644.07
145.69	52.49	86.16	93.63	241.16	245.93
626.21	335.44	401.25	413.62	893.9	900.05
122.92	82.86	89.97	88.35	155.58	159.6
680.07	618.54	568.25	533.93	796.5	805.96
213.91	285.52	209.23	199	220.75	228.96
45.96	69.63	47.49	43.17	41.87	41.32
205.31	288.17	199.1	185.85	189.54	187.72
34.03	45.65	35.05	32.36	31.73	30.9
185.82	273.39	197.19	184.16	174.37	172.22
36.44	51.82	35.22	32.72	32.5	31.88
82.44	113.07	79.27	70.43	70.37	70.89
10.97	15.79	9.23	9.04	9.04	8.79
66.82	82.52	50.18	47.79	49.47	47.28
6.24	5.92	4.88	4.61	4.96	4.98
44.86	16.74	19.02	20.85	35.1	35.03
6.84	3.76	2.29	1.45	7.71	7.76
235.46	12.66	18.45	8.21	363.07	352.34
272.13	185.83	174.8	89.19	303.69	308.99
0.87	0.07	0.11	0.09	1.20	1.14
3.26	4.07	3.83	4.91	5.38	5.20
1788.80	1374.85	1354.86	1328.53	2307.89	2340.50
1.44	0.17	0.32	0.38	0.74	0.74
306.03	357.32	200.10	193.43	202.42	196.17
2.78	3.31	3.93	3.85	3.52	3.64
628.07	876.33	610.12	566.96	561.98	554.66
850.59	744.95	756.81	763.26	798.22	798.32

RUN2	**RUN2**	**RUN2**			
35 microns	**35 microns**	**35 microns**			
Ttn34	**Ttn34**	**Ttn34**			
A5	**A6**	**A7**			
064SMPL	**065SMPL**	**066SMPL**			
core	**core**	**rim**			
omogeneous	**omogeneous**	**omogeneous**	**Inner domains**		
derate-distort	**derate-distort**	**derate-distortion**			
10486.93	10324.72	8722.66	12798.5	2161.1	17%
359.87	496.18	435.74	426.8	170.9	40%
200428.5	193059.47	194467.77	200388.3	12073.8	6%
206717.73	208676.22	193736.11	208231.8	16319.3	8%
1169.97	998.51	986.15	1051.0	276.1	26%
411.5	386.64	381.97	438.4	82.6	19%
2133.32	2072.13	2299.76	3129.3	2043.7	65%
710.25	645.53	955.29	780.2	295.8	38%
279.42	227.93	262.24	1474.3	1061.1	72%
673.85	650.48	697.51	672.7	86.1	13%
83.77	50.16	113.93	311.5	178.2	57%
374.4	249.71	544.06	1078.7	502.2	47%
79.47	58.79	117.86	180.1	72.1	40%
480.95	371.29	709.45	905.7	354.9	39%
180.55	159.33	276.67	248.5	96.1	39%
39.87	37.47	55.97	46.2	13.6	30%
172.3	156.93	252.51	201.4	55.1	27%
30.28	28.58	43.25	31.8	7.8	24%
175.87	158.83	238.38	174.6	51.3	29%
30.63	27.88	41.35	32.4	11.7	36%
69.31	61.9	93.48	78.3	33.5	43%
8.87	7.83	11.43	10.5	4.8	46%
47.23	39.47	59.33	63.5	31.9	50%
4.61	3.86	5.83	7.0	3.9	56%
21.96	17.17	21.91	53.9	30.7	57%
1.14	1.39	1.92	11.6	12.2	105%
2.56	5.7	29.3	373.3	274.5	74%
56.42	76.75	217.47	238.8	151.8	64%
0.05	0.07	0.13	1.5	0.9	61%
4.92	4.98	3.79	4.7	1.2	25%
1199.14	889.28	1761.97	2724.5	1125.1	41%
0.39	0.35	0.27	1.9	1.2	66%
190.74	160.42	237.76	293.3	168.0	57%
3.72	4.02	4.02	3.7	2.8	74%
539.10	485.28	745.56	599.5	167.3	28%
761.83	750.71	758.34	841.5	61.2	7%

Outer domains

11104.5	1589.9	14%
476.2	98.2	21%
203752.0	12932.6	6%
215959.5	15501.2	7%
1033.4	267.2	26%
432.1	61.9	14%
2736.4	409.1	15%
775.2	263.8	34%
874.3	938.1	107%
713.9	102.6	14%
164.5	71.4	43%
678.9	238.0	35%
133.1	41.0	31%
749.7	214.8	29%
243.2	60.1	25%
48.3	9.8	20%
208.9	42.2	20%
33.2	7.6	23%
182.0	54.3	30%
32.9	11.8	36%
75.5	27.4	36%
9.8	3.9	39%
57.1	22.3	39%
5.8	2.4	42%
43.4	36.6	84%
4.7	3.4	72%
126.5	181.7	144%
225.0	135.7	60%
0.5	0.5	103%
4.1	0.6	15%
1969.3	580.4	29%
1.4	1.5	108%
248.2	106.5	43%
3.7	1.7	46%
605.0	153.9	25%
806.7	54.7	7%

Table S6 - Monazite textural features for the studied sam

Grain	Size (μm^2)	Position
Mnz2a	8000	in foliation
Mnz6a	74000	in foliation
Mnz6b	84000	in foliation
Mnz6c	22000	in foliation
Mnz7b	21000	in sillimanite
Mnz7a	21000	In garnet
Mnz8a	4000	in foliation
Mnz8b	14000	in foliation
Mnz8c	5000	in foliation
Mnz6a	9000	in foliation
Mnz6b	4000	in foliation
Mnz4a	7000	in foliation
Mnz1a	11000	in foliation
Mnz9	6000	contact with garnet
Mnz1	3000	contact with garnet
Mnz2	4000	in foliation
Mnz8	5000	in garnet
Mnz6	8000	in garnet
Mnz7	7000	in foliation
Mnz10	7000	in foliation
Mnz5	3000	in strain shadow
Mnz10	12000	in foliation
Mnz11	11000	in foliation
Mnz15	3000	in foliation
Mnz6	3000	in foliation
Mnz7	17000	in strain shadow
Mnz14	76000	contact with garnet
Mnz5	3000	contact with garnet
Mnz9	7000	in foliation
Mnz8	3000	in foliation
Mnz6	2000	in foliation
Mnz12	6000	in foliation
Mnz4	13000	in foliation
Mnz15	13000	in foliation
Mnz11	4000	in foliation
Mnz10	6000	in foliation

ıples

Litology	Fabric	Sample
Bt-rich paragneiss	Protomylonitic	VSDO-13A1
Bt-rich paragneiss	Protomylonitic	VSDO-13A1
Bt-rich paragneiss	Protomylonitic	VSDO-13A1
Bt-rich paragneiss	Protomylonitic	VSDO-13A1
Bt-rich paragneiss	Protomylonitic	VSDO-13A1
Bt-rich paragneiss	Protomylonitic	VSDO-13A1
Bt-rich paragneiss	Protomylonitic	VSDO-13A2
Bt-rich paragneiss	Protomylonitic	VSDO-13A2
Bt-rich paragneiss	Protomylonitic	VSDO-13A2
Bt-poor paragneiss	Protomylonitic	VSDO-13B1
Bt-poor paragneiss	Protomylonitic	VSDO-13B1
Bt-poor paragneiss	Protomylonitic	VSDO-13B1
Bt-poor paragneiss	Protomylonitic	VSDO-13B1
paragneiss	Mylonitic	VSDO-13M1
paragneiss	Mylonitic	VSDO-13M1
paragneiss	Mylonitic	VSDO-13M1
paragneiss	Mylonitic	VSDO-13M1
paragneiss	Mylonitic	VSDO-13M1
paragneiss	Mylonitic	VSDO-13M1
paragneiss	Mylonitic	VSDO-13M1
paragneiss	Mylonitic	VSDO-13M1
paragneiss	Mylonitic	VSDO-13M2
paragneiss	Mylonitic	VSDO-13M2
paragneiss	Mylonitic	VSDO-13M2
paragneiss	Mylonitic	VSDO-13M2
paragneiss	Mylonitic	VSDO-13M2
paragneiss	Mylonitic	VSDO-13M4
paragneiss	Mylonitic	VSDO-13M4
paragneiss	Mylonitic	VSDO-13M4
paragneiss	Mylonitic	VSDO-13M4
paragneiss	Mylonitic	VSDO-13M4
paragneiss	Mylonitic	VSDO-13M4
paragneiss	Mylonitic	VSDO-13M4
paragneiss	Mylonitic	VSDO-13M4
paragneiss	Mylonitic	VSDO-13M4
paragneiss	Mylonitic	VSDO-13M4

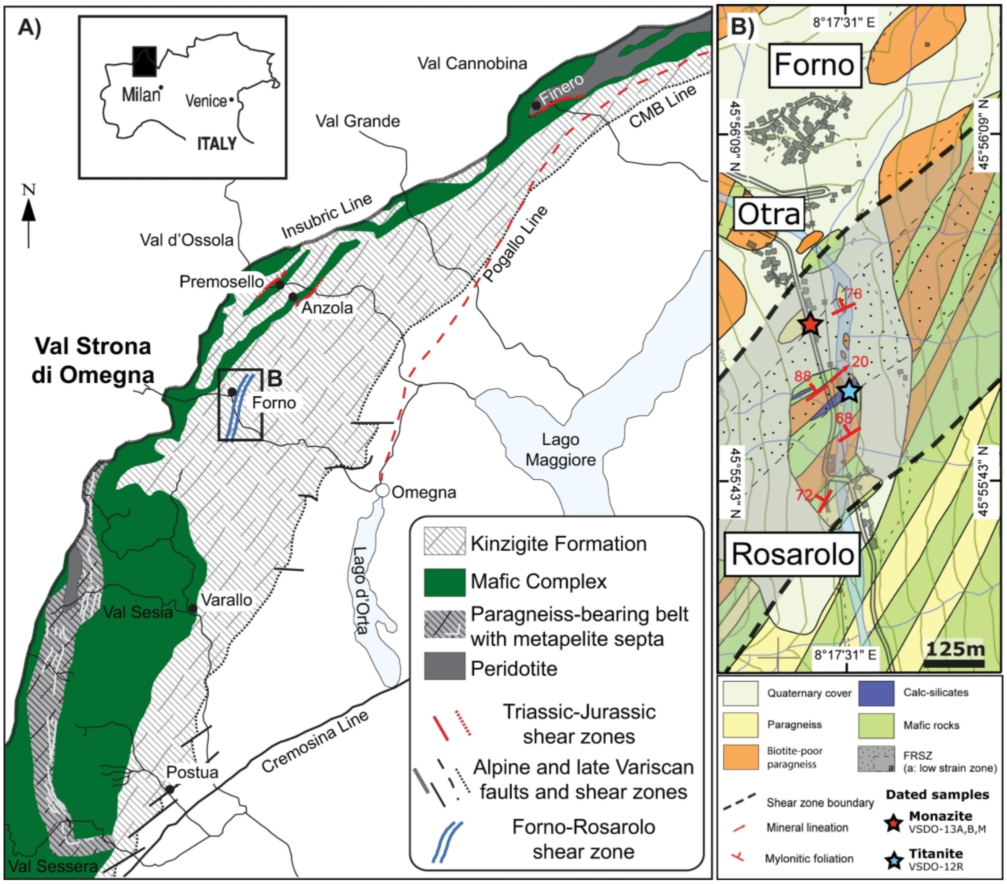

270x236mm (300 x 300 DPI)

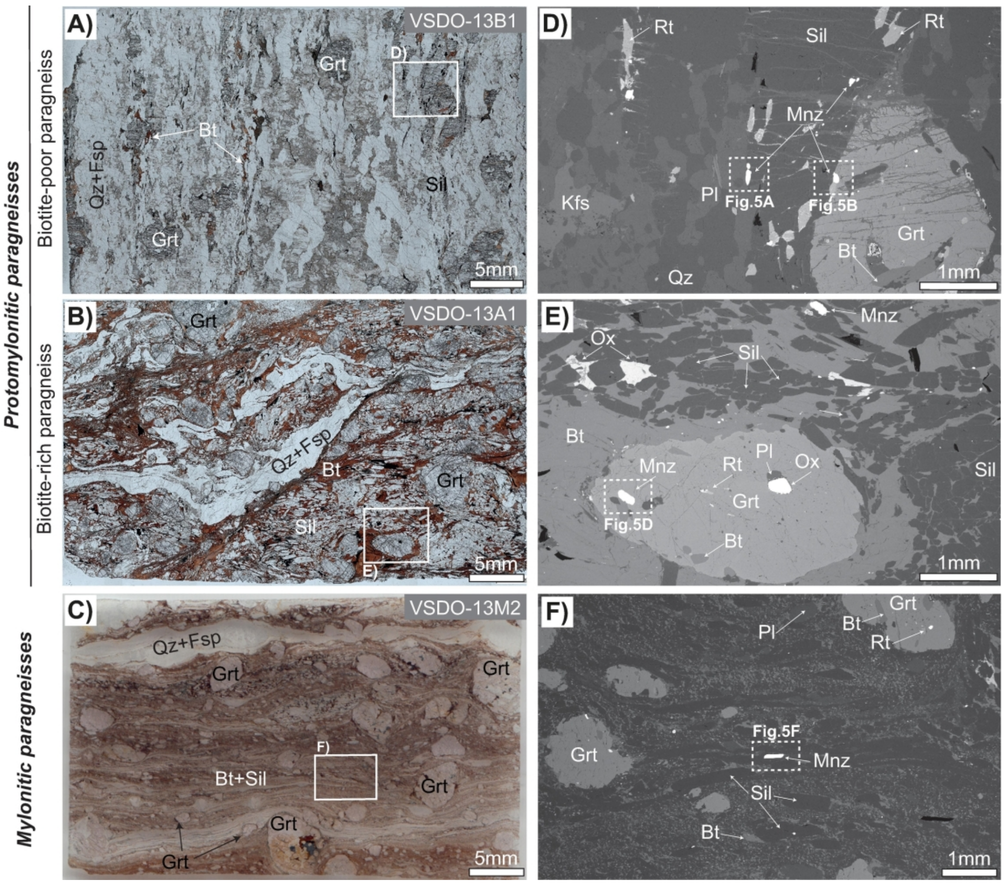

201x176mm (300 x 300 DPI)

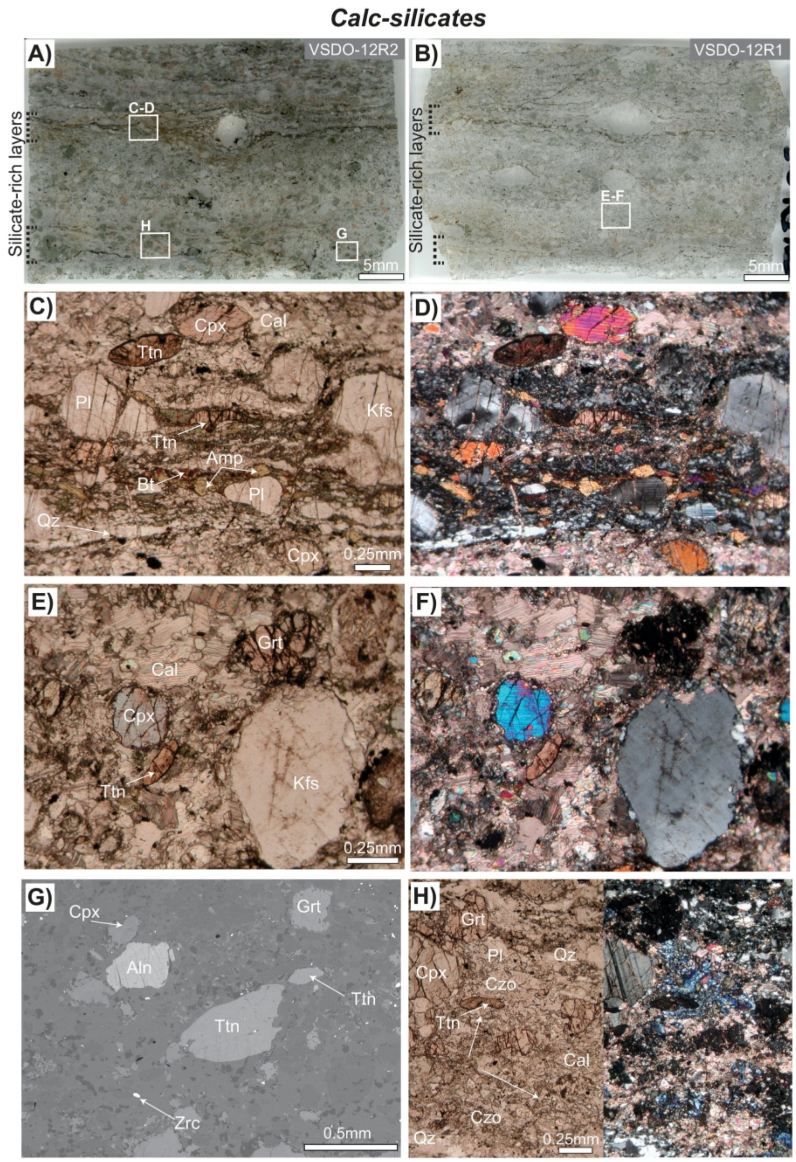

192x281mm (300 x 300 DPI)

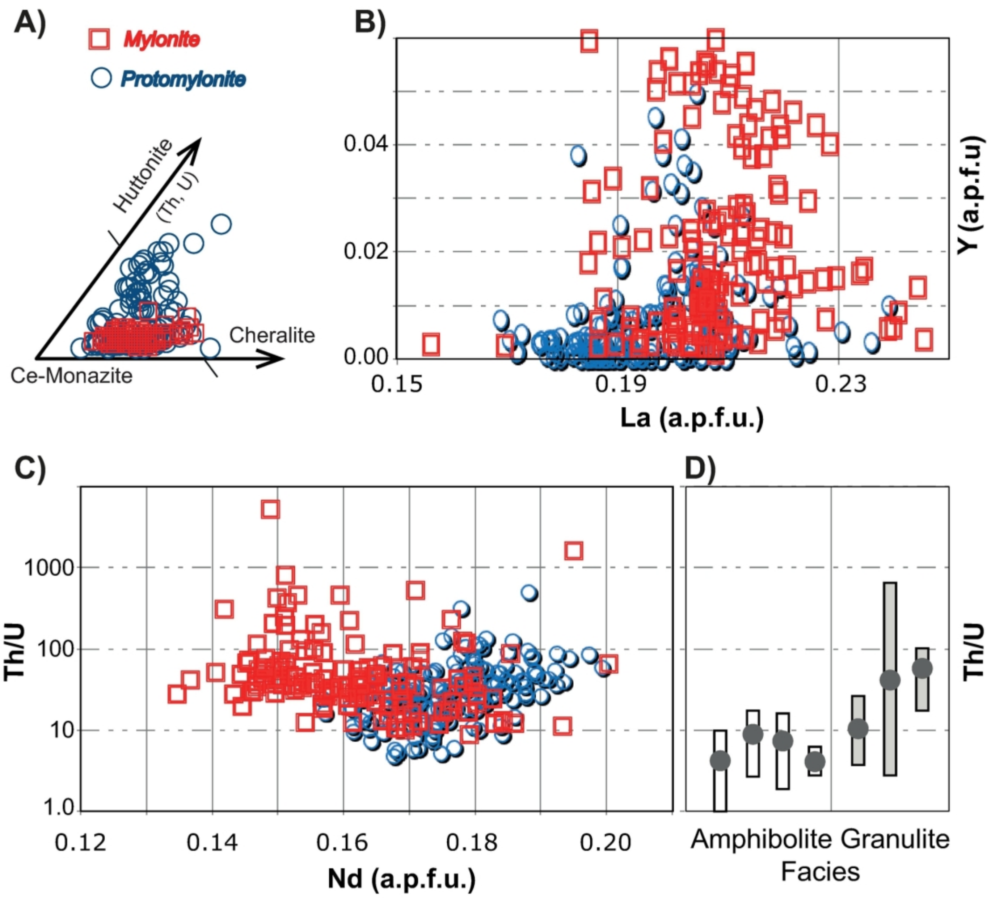

173x155mm (300 x 300 DPI)

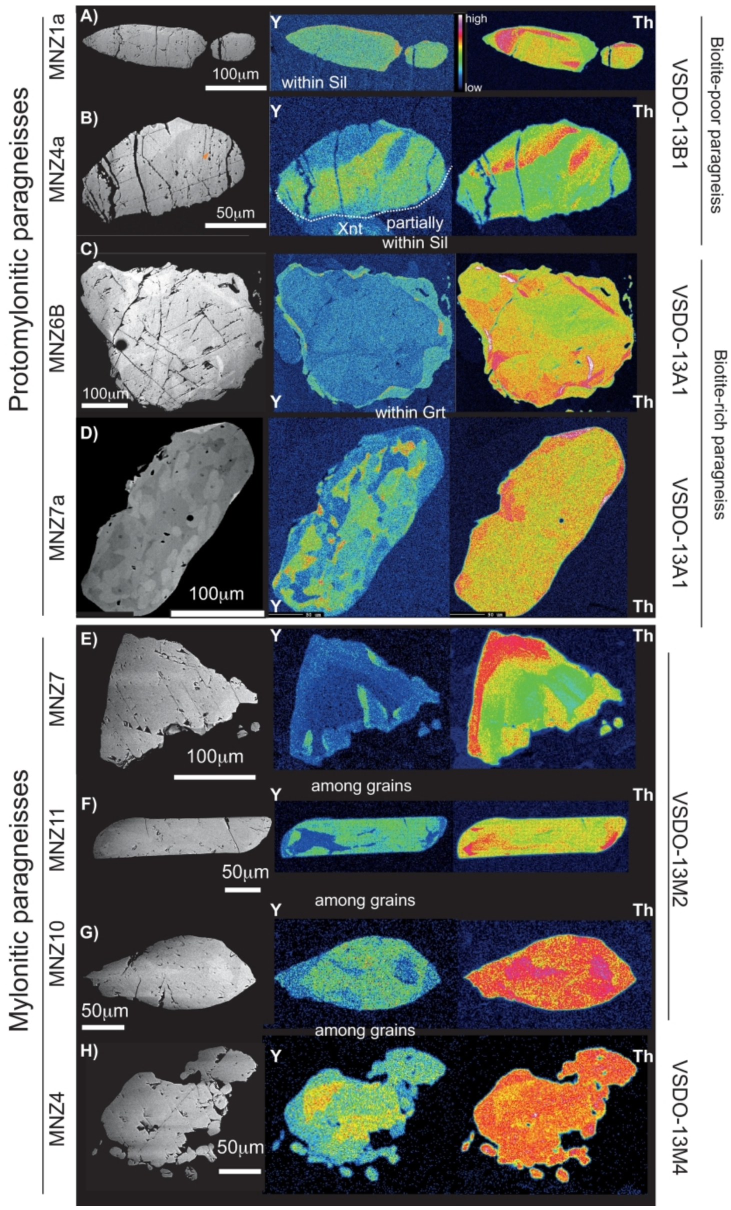

175x289mm (300 x 300 DPI)

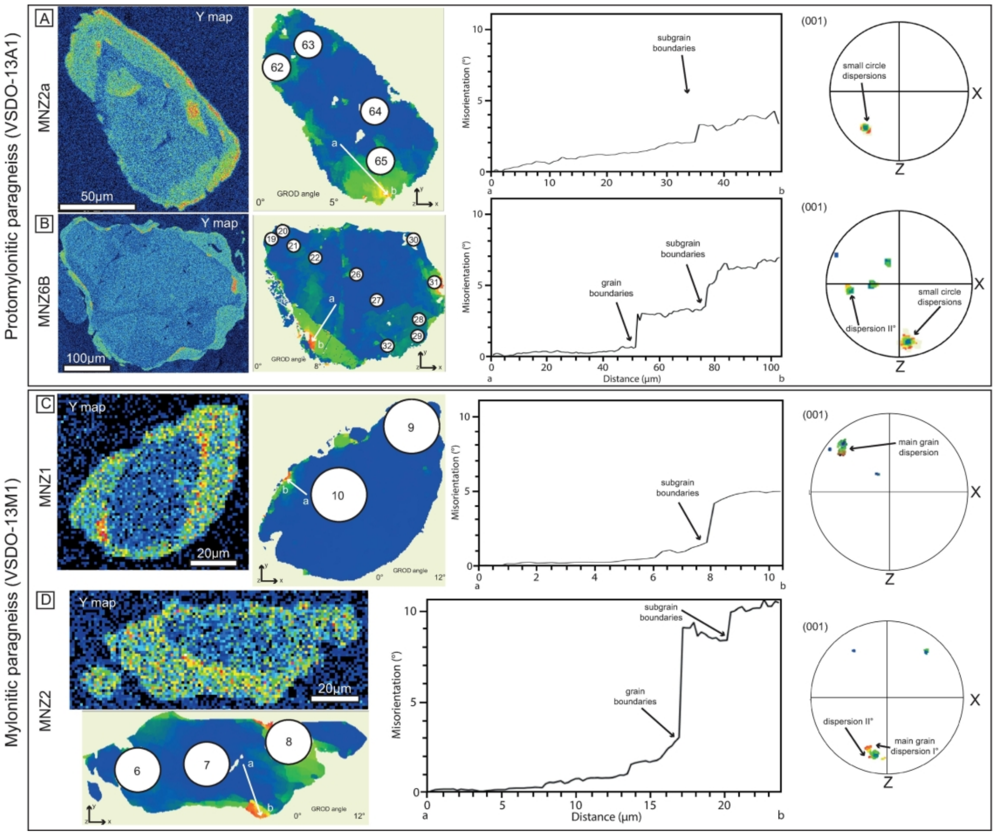

201x166mm (300 x 300 DPI)

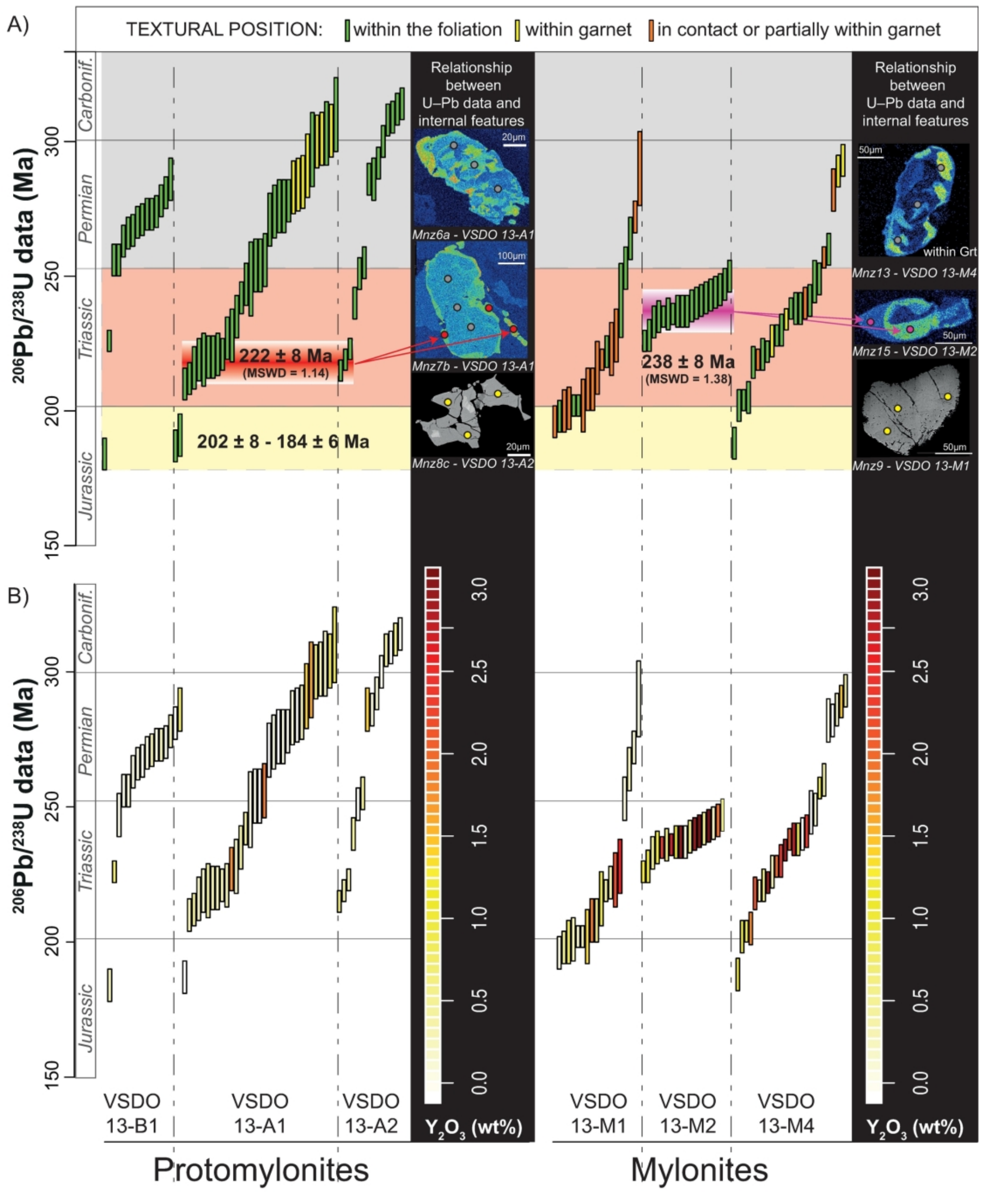

203x248mm (300 x 300 DPI)

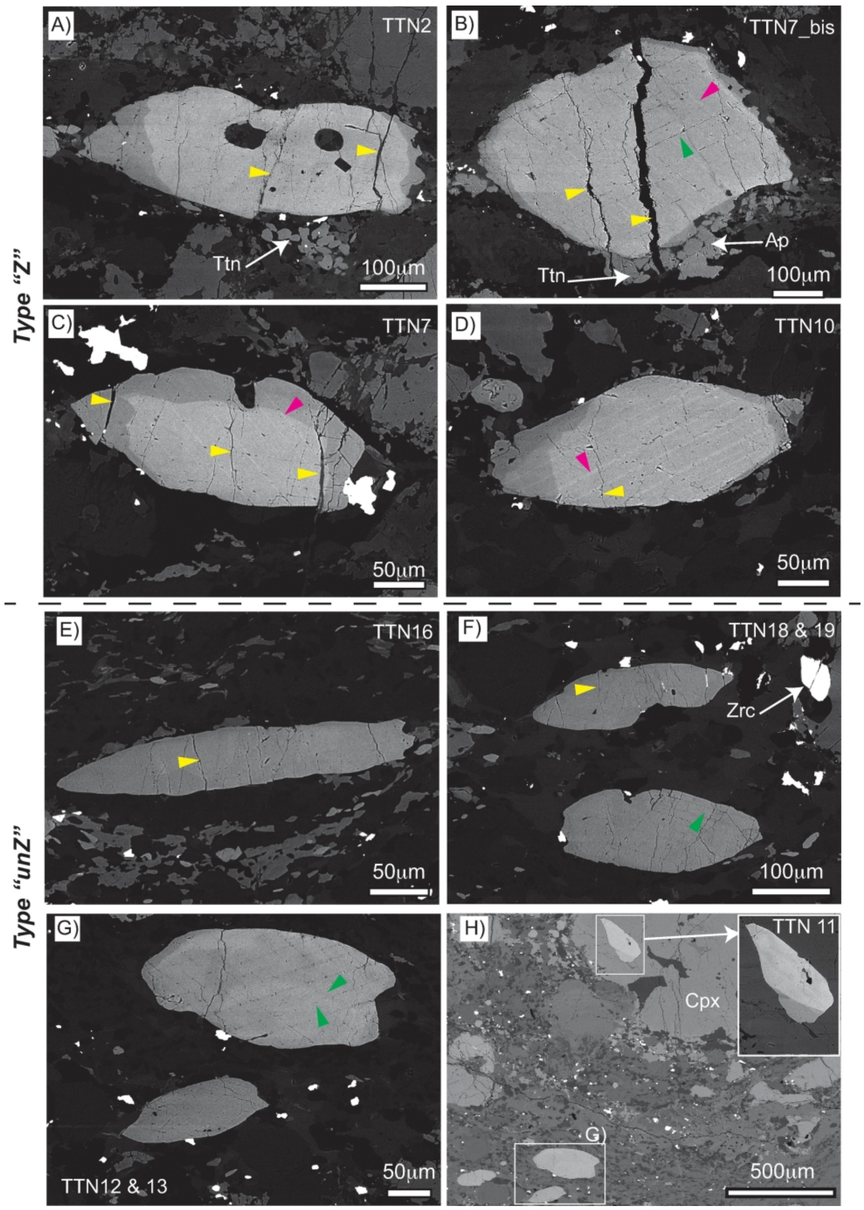

158x221mm (300 x 300 DPI)

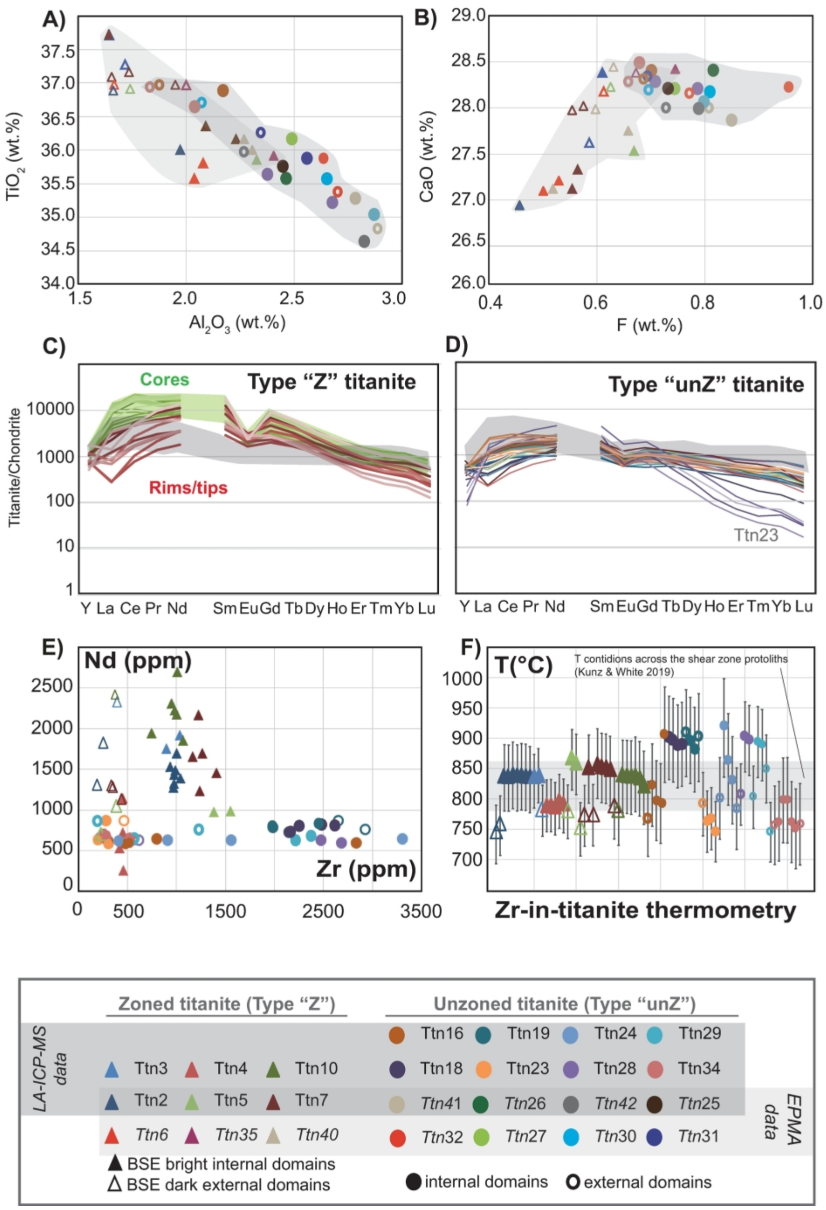

186x271mm (300 x 300 DPI)

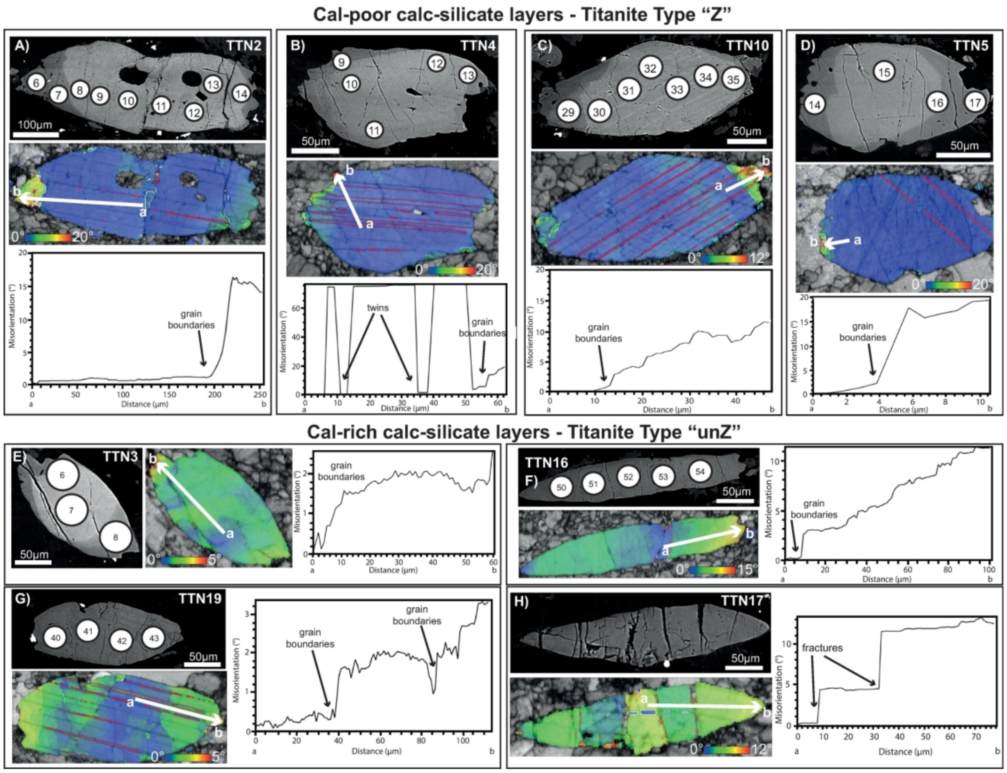

204x156mm (300 x 300 DPI)

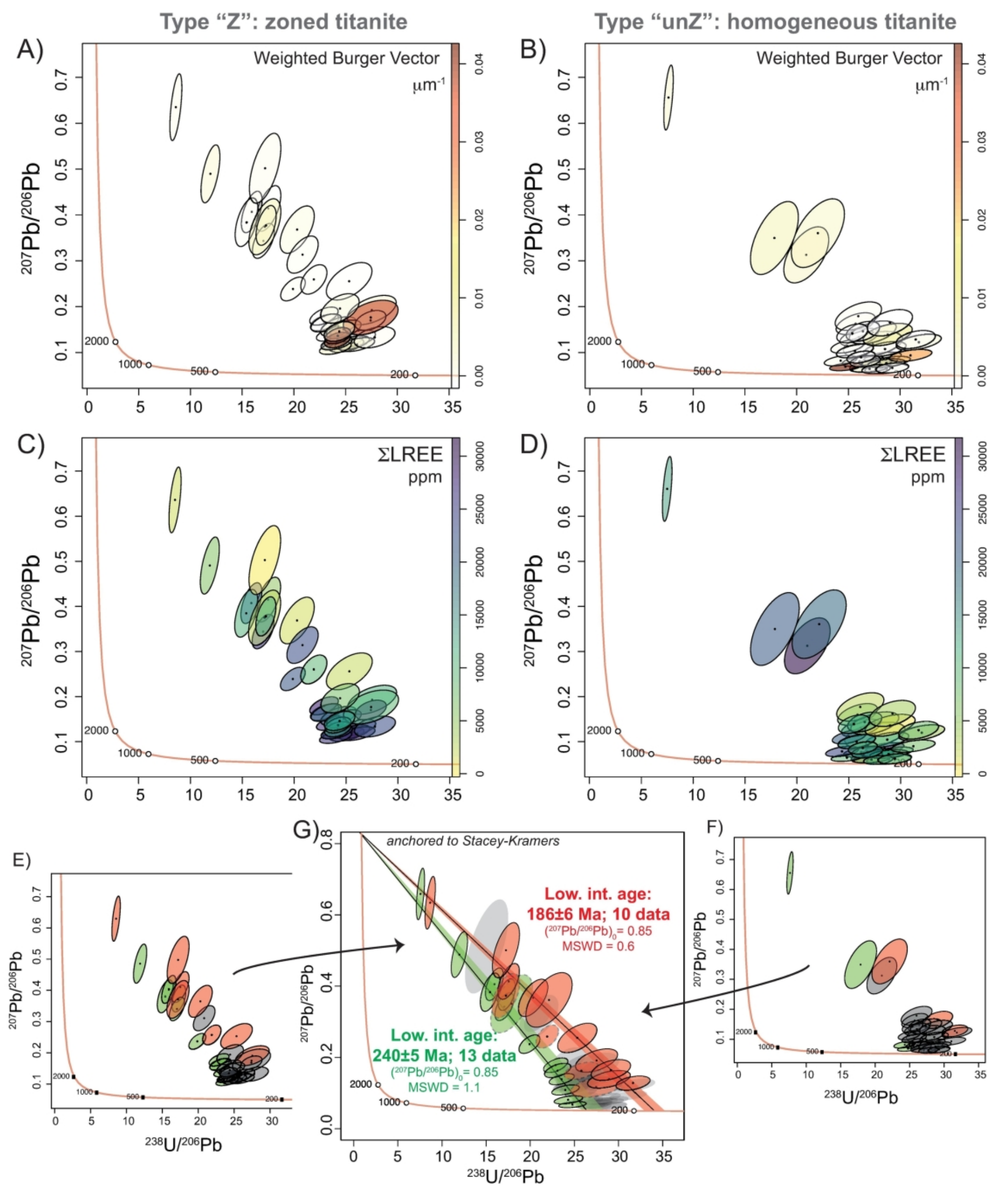

207x244mm (300 x 300 DPI)

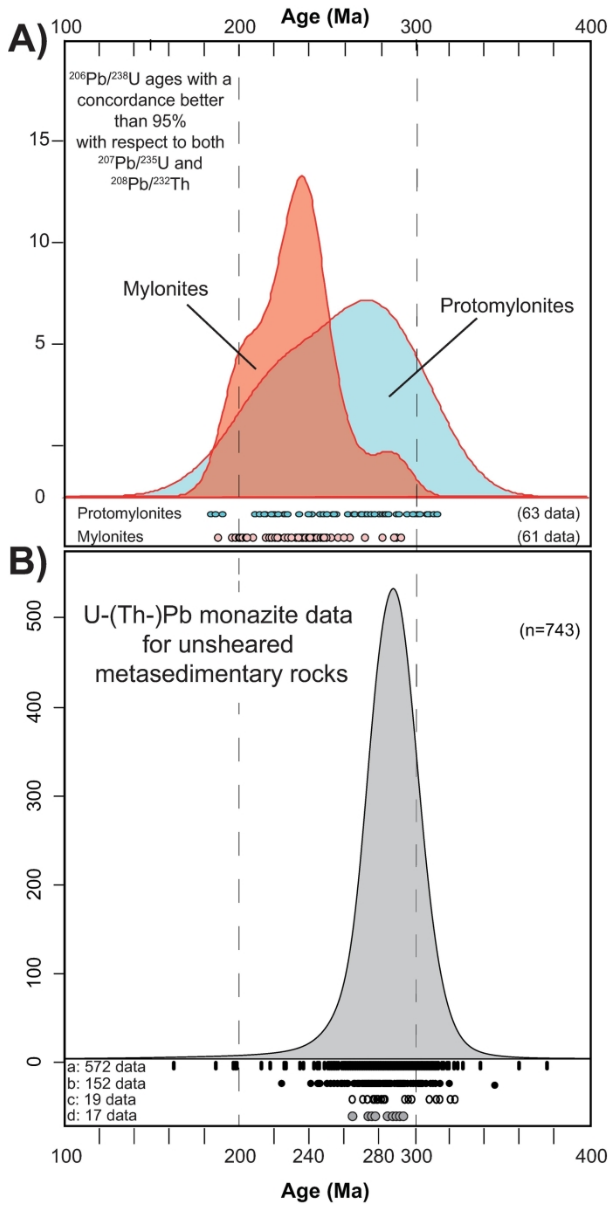

120x241mm (300 x 300 DPI)

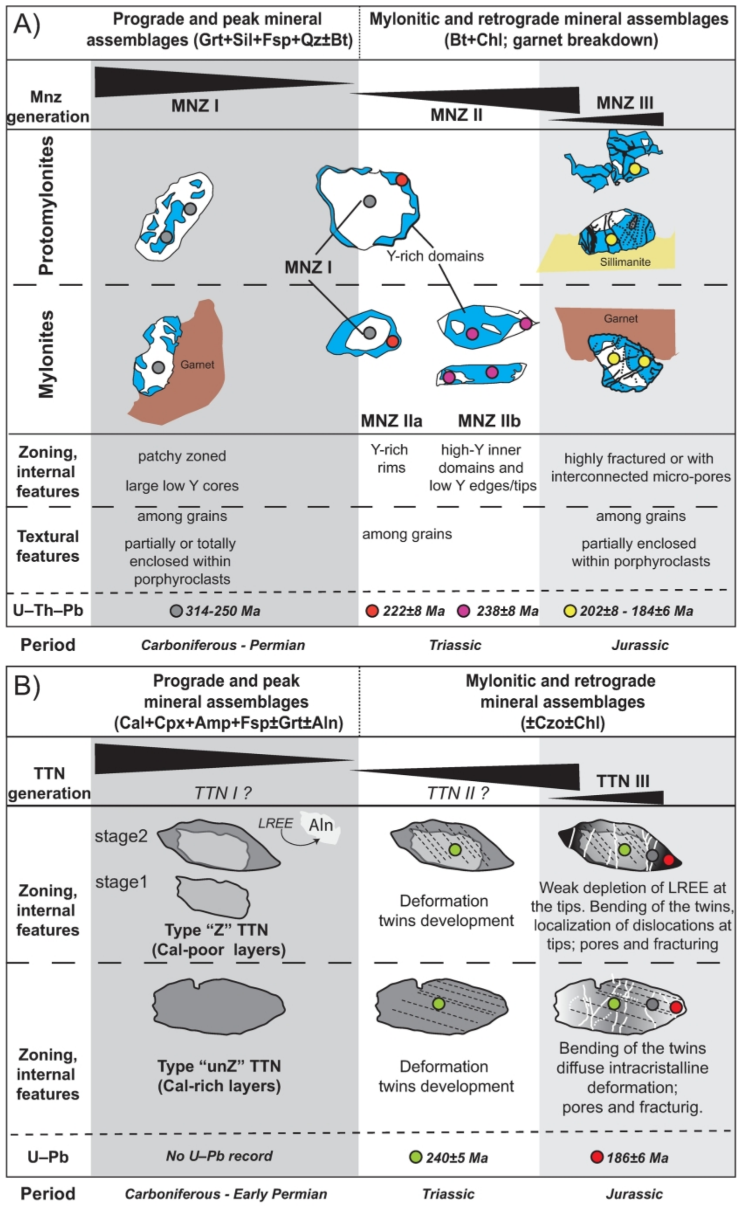

179x284mm (300 x 300 DPI)

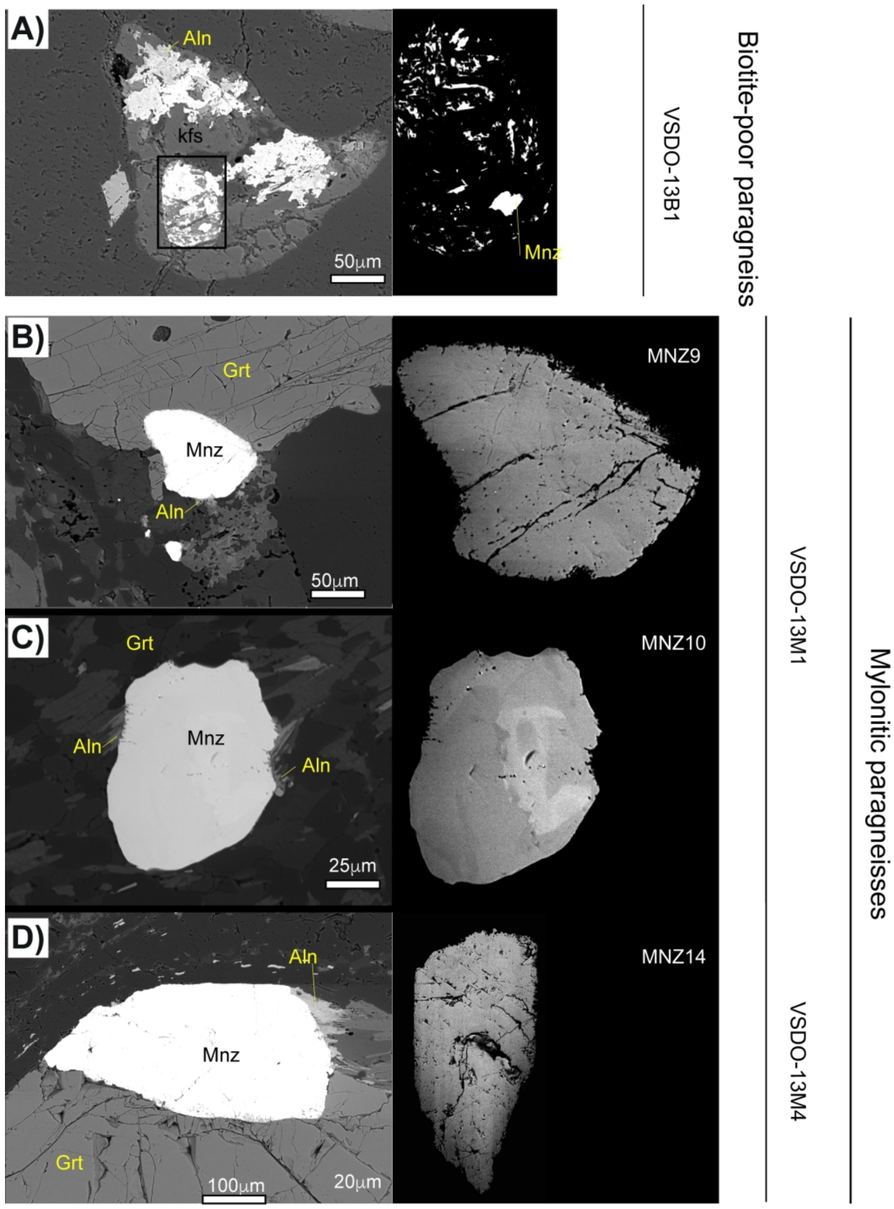

149x201mm (300 x 300 DPI)

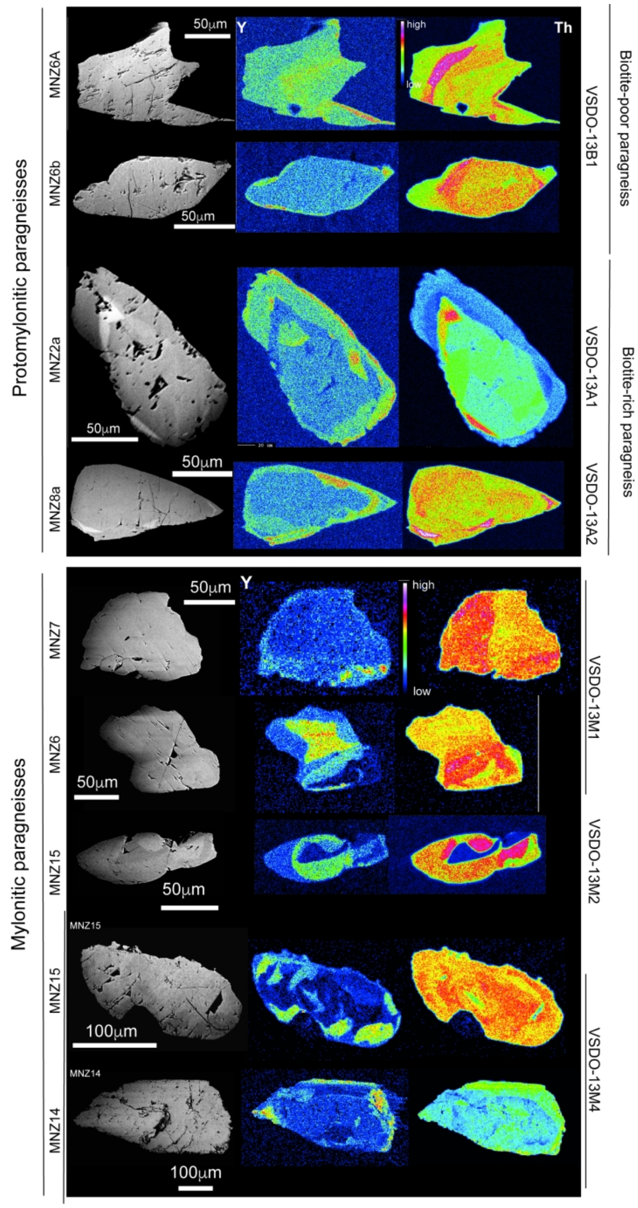

149x284mm (300 x 300 DPI)

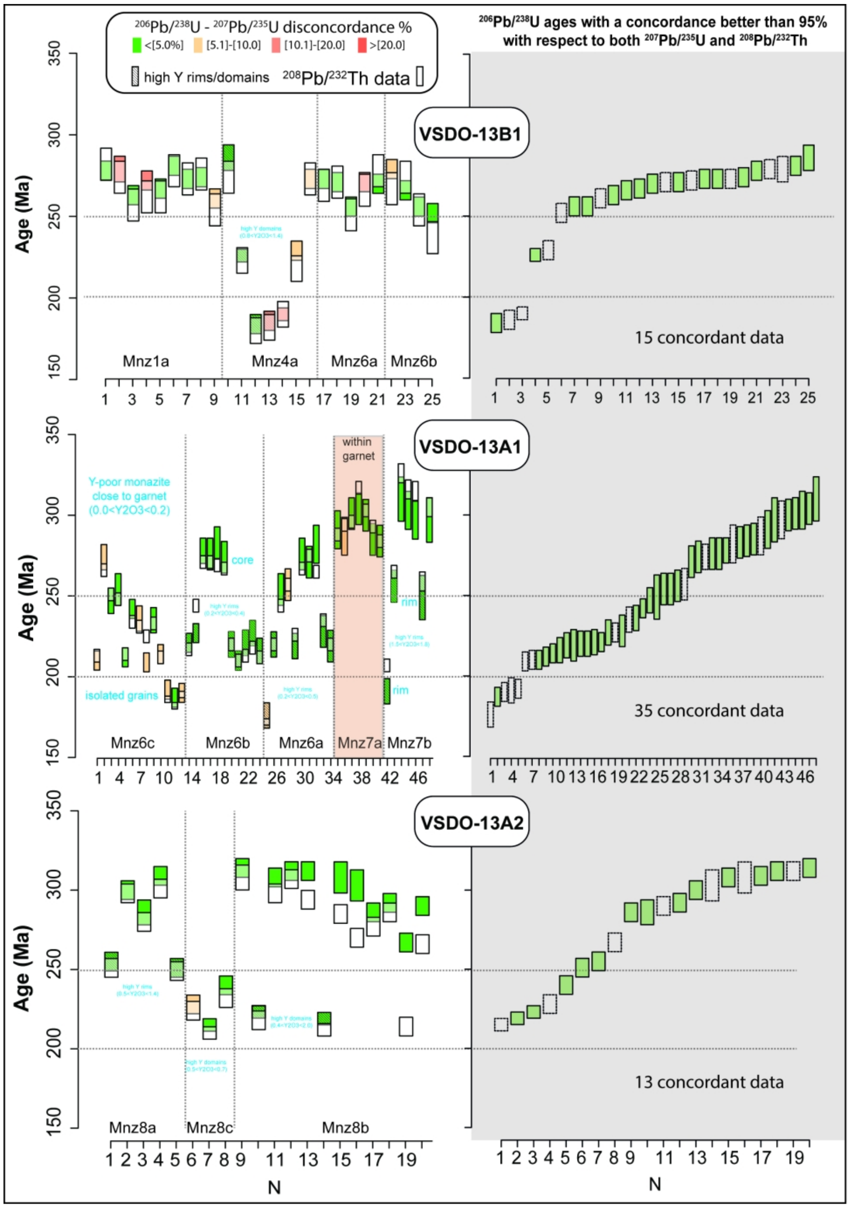

198x273mm (300 x 300 DPI)

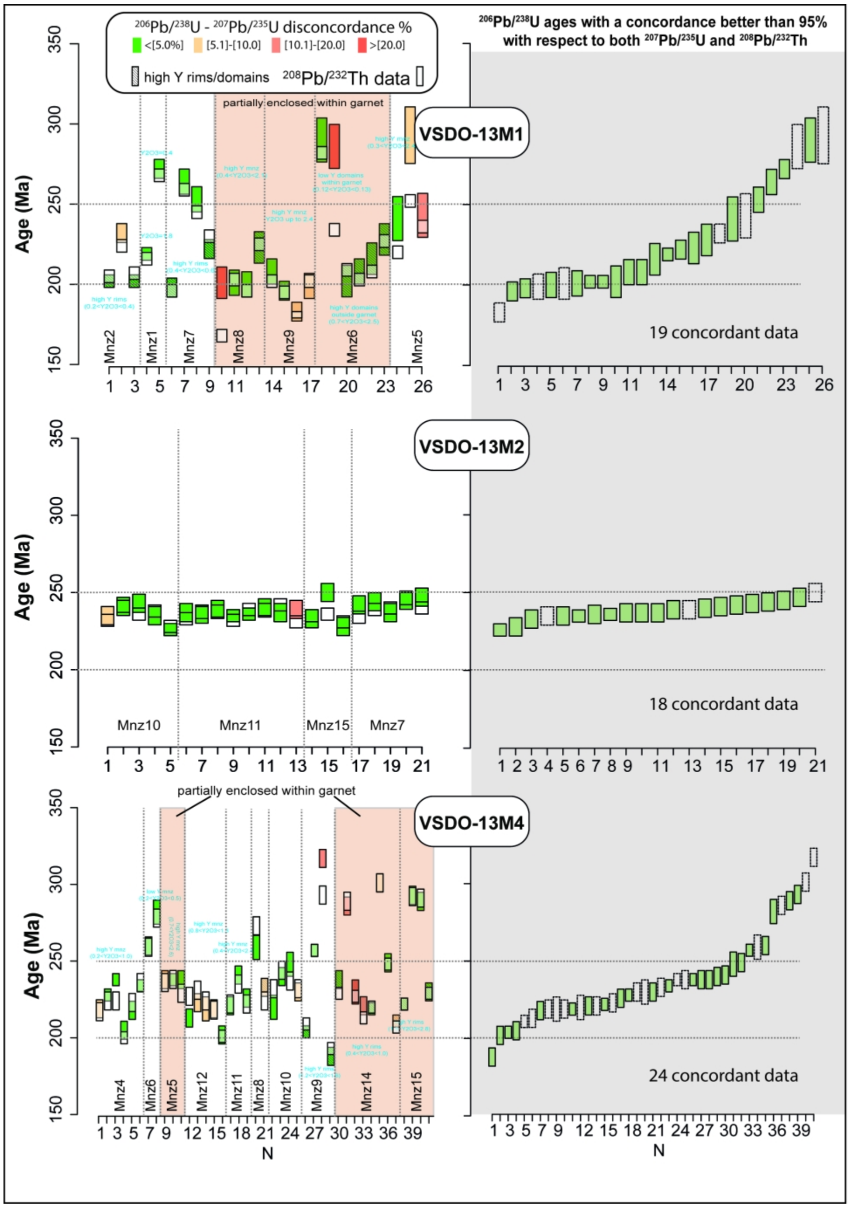

198x273mm (300 x 300 DPI)

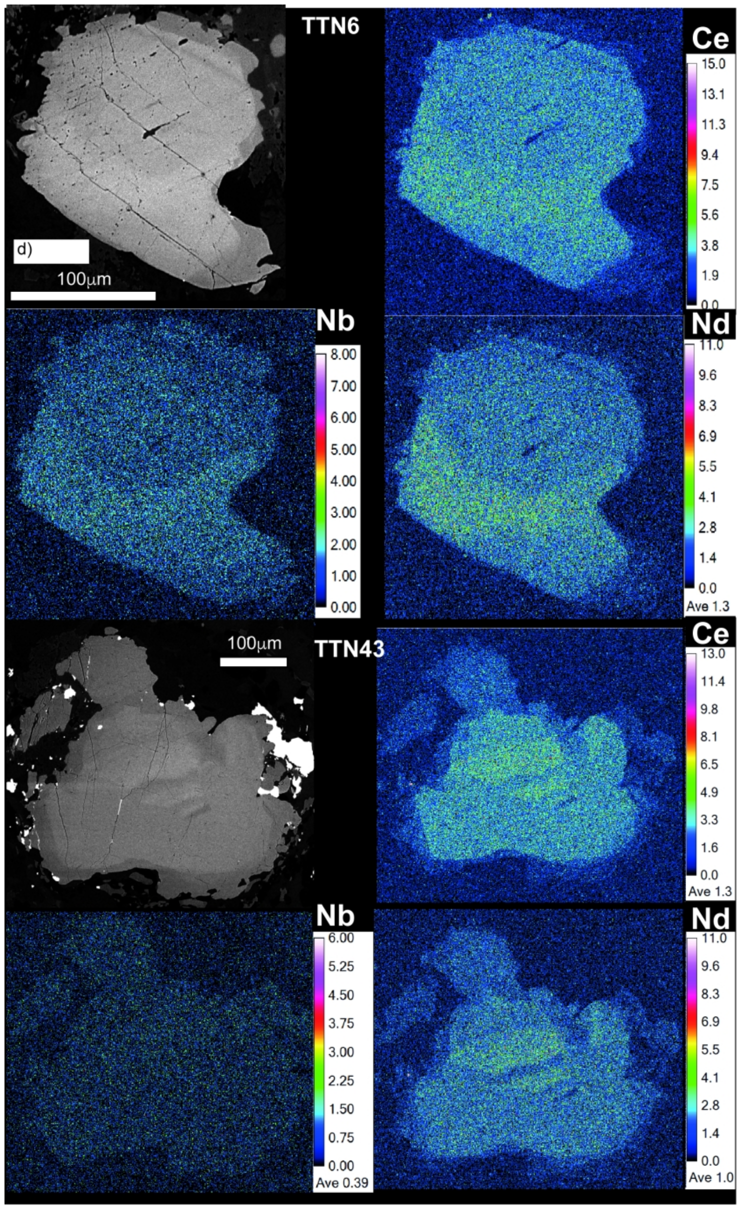

159x260mm (300 x 300 DPI)

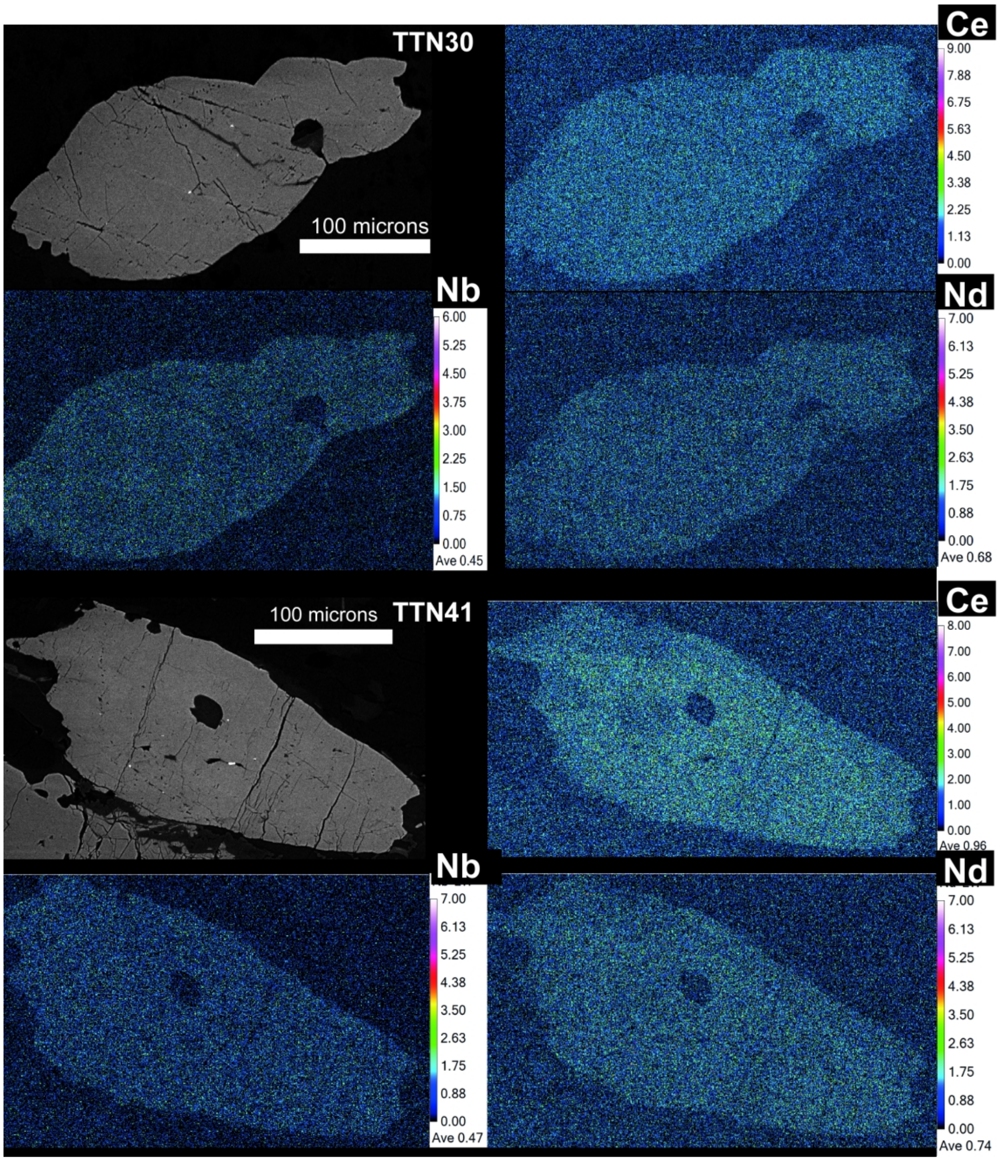

189x218mm (300 x 300 DPI)